



INFLUENCE OF SOME ELEMENTS FROM ANODE COPPER ON CATHODE COPPER QUALITY

Branislav ČADJENOVIĆ, Radmila MARKOVIĆ, Aleksandra MILOSAVLJEVIĆ

IRM, Mining and Metallurgy Institute Bor
33-35 Zeleni Bulevar, 19210 Bor, SERBIA

ABSTRACT

In the sites of TIR BOR, electrolytic refining process of the fire refined copper is used for obtaining the cathode copper quality according to the Standard BS6017.

Defined parameter values of electrolytic refining process of anode copper as well as process realization according to the Standard JUS ISO 9001, defined procedures and instructions, present the basic precondition for cathode copper production of suitable quality.

The aim of this work was to determine the influence of some chemical elements that were present in anode copper considerably over permitted limits, predicted by suitable JUS ISO 9001 Standard on chemical quality of cathode copper. The investigations have showed that the increased values of oxygen (up to 1 500 ppm) and nickel (up to 800 ppm) in anode have no important effect on quality of cathode copper, what was confirmed by production of 91.14 % cathode copper of BS6017 quality from total production in the observed period.



ELECTROCHEMICAL BEHAVIOR OF COPPER WITH NON-STANDARD IMPURITIES CONTENT

¹. Radmila MARKOVIĆ, ². Bernd FRIEDRICH, ³. Jasmina STEVANOVIĆ, ⁴. Bore JEGDIĆ

¹. IRM, Mining and Metallurgy Institute Bor, 33-35 Zeleni bulevar, 19210 Bor, SERBIA

². IME Process Metallurgy and Metal Recycling, Aachen, DEUTCHLAND

³. ICTM, Institute of Electrochemistry Beograd, 12 Njegoseva, 11000 Beograd, SERBIA

⁴. "GOŠA" Institute, Milana Rakića 35, 11000 Beograd, SERBIA

Abstract

This paper presents the results of electrochemical behavior of copper recycling anode with non-standard impurities content in sulphuric acid solution. The anodes were obtained by casting the waste material formed in Cu refining processes and contained the next alloying elements: Ni in concentration up to 10 % and Sn and Pb in concentration of some percentage. The present impurities remain the various problems on electrochemical behavior of anode material.

The obtained results showed that the pasivation of recycling anode during the electrolytic process in sulphuric acid solution is not registered. Copper is dissolved from the anode and deposited on cathode by using the direct current. In the same time, nickel is dissolved from anode and retained in electrolyte. The possibility of nickel separation and production from this solution in a form of salts using chemical method or pure metal form of electrochemical deposition is feasible according to concentration increasing.

For better understanding the electrochemical behavior of recycled anodes, the corrosive behavior of anodes was studied in a three arrangement cell. Sulphuric acid solution was used as electrolyte, and the method of linear potential change was used in defining the phase content.

Key words:

recycling anode, Cu, Ni, Sn, Pb, electrochemical process

1. INTRODUCTION

Large amounts of waste materials from the copper smelting process are used for recycling. Selection of recycling methods depends on material type for recycling.

The most often used method for Cu, Ni, Sn and Pb production from various types of waste materials is the electrolytic refining process. It is known that Ni presence in anode material, higher than about 3 %, results into anode passivation in the sulphuric acid solution.(1,2). For better understanding the electrochemical behavior of recycled anodes, the various electrochemical measuring were done.

2. EXPERIMENTAL PROCEDURE

The copper and nickel bearing waste materials obtained in copper refinement processes are used for the production of materials which could be use in electrolytic process for copper cathode production in the one side and on the other side, for the nickel transferring in solution form aim to further valorization.

According to this request, it was done multiphase experiment in a three electrode arrangement cell, according to the industrial parameters:

- ✚ Material which was used as anode material was prepared from pure metals: copper, nickel, tin and lead. Copper was main component, nickel was added in content up to 10 % and tin and lead in content up to 1 %.

An induction furnace (Balzers) with melting power of 10 - 15 kW is used for casting. The crucible made of graphite; with volume of 1.8 l. Smelting and casting process does not carry out by the use of pressure or vacuum. When temperature of 1300°C is reached, alloying elements are added. Graphite sticks are utilized for oxygen reduction in melt. Oxygen content was measured before casting by the use of Electro- Niter oxygen measuring system. Glass pipettes were used for sampling and determination of oxygen content. Reduction process is stopped when the oxygen content was achievement the value of under the 200 ppm. an melt is cast at approx. 1300°C. After the self-adsorbtion cooling, anodes are preparing for the electrolytic treatment by mechanical removal of 2 mm surface area.

Chemical analyses were performed using an optical emission spectrometry (OES) on apparatus OES ARL 4460.

Electrochemical measurements were conducted in 3 electrode arrangement cell where the working anode was pure Cu, pure Ni or some copper bearing alloys. The saturated Callomel electrode (SCE) was used as reference electrode and Pt with the same area as so as working anode. Polarization curves and measurements by anodic liner sweep voltammetry (ALSV) method are done on potentiostat PAR 273 A, on voltage scan rate of 2 mV/s. Electrolyte of concentration of 172 g/dm³ was prepared by using the 98 % sulphuric acid p.a quality and bidestilated water.

3. RESULT AND DISCUSSION

The results of chemical analyses:

1st sample: Cu - purity of 99.95 %

2nd sample: Ni - purity of 99.9 %

3rd sample: Alloy Cu-Ni with 5 % Ni and up to 1 % of Sn and Pb

4th sample: Alloy Cu-Ni with 7.5 % Ni and up to 1 % of Sn and Pb

5th sample: Alloy Cu-Ni with 10 % Ni and up to 1 % of Sn and Pb

The corrosion property of different samples is presented on Figure 1.

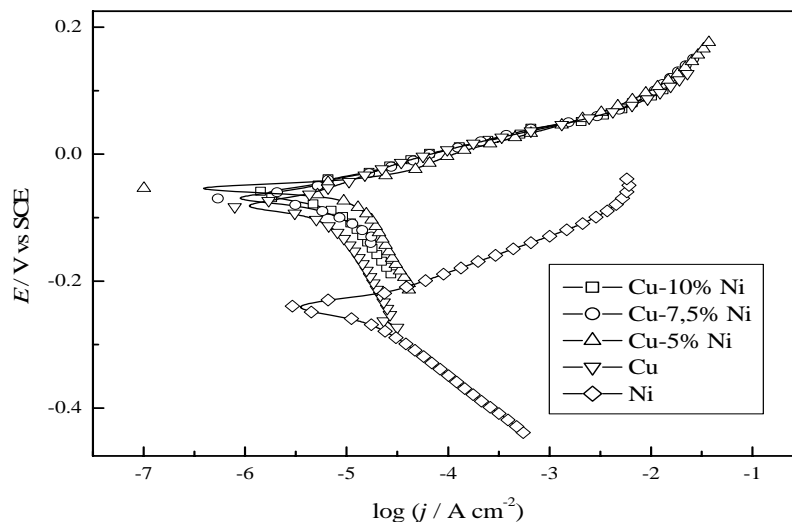


Figure 1. Corrosion behavior of pure Ni, pure copper and Cu-Ni alloys with 5 % Ni, 7.5% Ni and 10% Ni in sulphuric acid solution.

From the diagram on Figure 1, the values of corrosion potential as so as the values of corrosion current for pure Ni, pure Cu and Cu-Ni alloys could be readout. It could be seen that the corrosion current value of pure Ni is lower than corrosion current value of pure Cu. Also, the corrosion current value for pure Ni is lower than values for Cu-Ni alloys. The value for corrosion potential for pure Ni is 200 mV more negative regard to corrosion potential for pure Cu and Cu-Ni alloys.

The corrosion current values, as so as the anode and cathode Taffel inclinations was determinate aim to define this recycling anode stability in sulphuric acid solution. The results are presented in Table 1.

Table 1. Corrosion current and Tafel inclinations

Description	$b_{\text{cath.}}$ (V dec ⁻¹)	$b_{\text{anod.}}$ (V dec ⁻¹)	Corrosion ($\mu\text{A cm}^{-2}$)
Cu-Ni, 10 % Ni	0.080	0.050	6.0
Cu-Ni, 7.5% Ni	0.090	0.040	3.0
Cu-Ni, 5% Ni	0.200	0.040	6.0
Pure Cu	0.260	0.045	5.0
Pure Ni	0.120	0.060	12.5

The next values are obtained:

1. The values for Tafel inclination for anode reaction on pure Cu and alloys were about 0.040 V dec⁻¹ and. Those values are enough stabile. In a case of pure Ni, the obtained value was 0.060 V dec⁻¹.
2. The values for Tafel inclination for cathode reaction were in range from 0.080 to 0.260 V dec⁻¹. It was explanation by high potential of hydrogen evolution reaction on pure copper and copper alloys. This value is decreased with nickel content increasing. For the pure nickel this value is 0.120 V dec⁻¹.
3. All alloys have got the very low corrosion current values, up to 10 $\mu\text{A cm}^{-2}$.

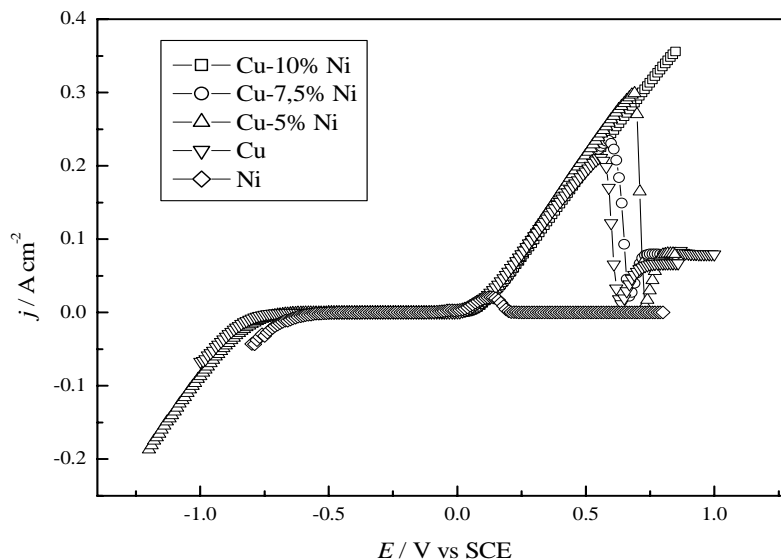


Figure 2. Current density versus voltage curve at a voltage scan rate of 2 mV/s

From the diagrams on Figure 2, could be seen that dissolution of pure Ni started before all other materials. For dissolution of pure is characteristic that the electric arc charge is the minimal and the area of active dissolution is terminated on potential of 0,2 vs SCE. The dissolution of pure copper started on more positive potential regarding to value of pure nickel potential. The quantity of electric arc charge is higher than for pure nickel. The electrolytic dissolution process of alloys: first started alloy with 5 % Ni, than alloy with 7.5 % Ni and than alloy with 10 % Ni. The characteristic of Cu-Ni alloy where the Ni content was 10 % is the highest quantity of electric arc charge and the value for potential on which started passivation is the most positive regarding to other materials.

4. CONCLUSION

Based on literature data, it is known that copper alloys with nickel content higher than 3 % become passivity in sulphuric acid solution.

The results of experimental investigation (Figure 2) are indicated that copper bearing alloys with nickel content from 5 to 10 % Ni and other alloying elements up to 1 % were not passivated in sulphuric acid solution. The results of the investigations also indicated that the values of electrolytic dissolution could be up to 200 mA/cm².

REFERENCE

- [1] G.Jarjoura and G.J.Kipouros, “Electrochemical Studies on the Effect of Nickel on Copper Sulphate Solutin” Canadian Metallurgical Quarterly, Vol 45, No 3, pp 283-294, 2006
- [2] G.Jarjoura and G.J.Kipouros, "Effect of nickel on copper anode passivation in a copper sulfate solution by impedance spectroscopy", Journal of Applied Electrochemistry, Vol 36, pp 691-701 (2006).
- [3] V. Jović, R. Zejnilović, A. Despić, J. Stevanović, Characterization of electrochemically formed thin layers of binary alloys by linear sweep voltammetry, Journal of Applied Electrochemistry, Vol. 18, No. 4. (1988), pp. 511-520



SYNTHESIS AND CHARACTERIZATION OF A CATALYST FORMED BY DIRECT INCORPORATION OF SOME HETEROPOLYACIDS INTO MESOPOROUS MATERIALS

Alexandru POPA, Viorel SASCA, Catalin IANASI,
Orsina VERDES, Livia AVRAM

Institute of Chemistry Timișoara, ROMANIA

ABSTRACT

The effect of incorporation of heteropolyacids species into organized mesoporous silica by using non-ionic and cationic surfactants were studied. The structure and texture of $H_3PMo_{12}O_{40}$ included on mesoporous silica were studied by XRD, FT-IR, BET and pore size distribution. The synthesis of silica molecular sieve containing HPAs was carried out in acidic media by using a mixture of cationic and non-ionic surfactants. FT-IR studies showed that HPAs anions preserved their Keggin structure after incorporation on molecular sieves supports. The values of specific surface area of HPAs were increased by deposition on molecular sieve supports.

1. INTRODUCTION

Heteropolyacids have attracted considerable attention as they present high acidity and favourable redox behaviour. Especially Keggin type heteropolyacids (HPAs) have been used extensively in acid-catalysed reactions as well as oxidation reactions both in the heterogeneous and homogeneous systems. Pure HPAs generally show low catalytic reactivity owing to their small surface area. In order to be more effective for catalytic reactions, HPAs are usually impregnated or incorporation on different porous materials with high surface area [1-6].

Direct incorporation of heteropolyacids (HPAs) $H_3PMo_{12}O_{40}$ (HPM) into mesoporous silica molecular sieve during the synthesis was studied. The synthesis of silica molecular sieve containing HPAs was carried out in acidic media by using a mixture of cationic and non-ionic surfactants, such as cetyltrimethylammonium bromide ($C_{16}TMABr$) and Triton (TX-100) or Tween 100 [7]. The obtained mesoporous materials were characterised by FTIR spectrometry, X-ray diffraction at low angles, thermal analysis (TG-DTA) and N_2 adsorption-desorption measurements.

FT-IR studies showed that HPAs anions preserved their Keggin structure after incorporation on molecular sieves materials. X-ray diffraction studies confirmed the uniformity of the distribution of active phase in the silica molecular sieve composites.

2. MATERIALS and METHODS

Molybdo phosphoric acid, $H_3[PMo_{12}O_{40}] \cdot 12H_2O$ (HPM) was purchased from Merck. The silicon source was tetraethoxysilane (TEOS) from Fluka. Two types of non-ionic surfactants were used in this study: polyethyleneglycol-4-tert-octylphenylether with 9-10 ethoxy groups (Triton X-100) from Fluka and polyethylene sorbitan-monostearate (Tween 60) from Merck. The cationic surfactant used is cetyltrimethylammonium bromide $C_{16}H_{33}(CH_3)_3 NBr$ (CTMABr) from Fluka. As mineralizing agent it was employed sodium fluoride NaF, from Fluka.

Mesoporous molecular sieves-included HPAs (denoted HPA-in-TX 100 or Tween 60) with 15 % HPA loading, were prepared by the hydrolysis of tetraethyl orthosilicate using non-ionic and cationic surfactants. The procedure described by Toufaily et. al. [7] was applied

with some modifications. In first synthesis we used a mixture of TX-100 and CTMABr surfactants, while in the second we used as surfactant only Tween 60.

First synthesis was performed with the following molar composition: $1\text{SiO}_2:0.22\text{TX100}:0.04\text{CTMABr}:0.04\text{NaF}:0.006\text{HPM}:168\text{H}_2\text{O}$. In a first step, 7.4 g of TX-100 and 0.82 g of CTMABr were dissolved in 160 ml distilled water containing 4 ml of hydrochloric acid (HCl 37 wt.%). Then, after a clear solution was obtained, 11 g of TEOS were added and stirred until complete dissolution. Then a solution of 0.57 g HPM in 30 ml acidified (HCl) distilled water was added to first solution and stirred for 4 hours at room temperature. The solution was aged for 24 h at room temperature without stirring. A small amount of sodium fluoride (0.1 g) was then added in order to promote the hydrolysis of TEOS. The solution was furthermore aged at 60°C for 48h. The solid product was filtered, washed with distilled water and dried in air for 6h. Calcination for template surfactants removal was carried out under air by increasing temperature from 25 to 350°C with a rate of 2°C/min and heating at 350°C for 4h.

The second synthesis was performed by the same procedure but with Tween 60 as non-ionic surfactant. The following molar composition was used: $1\text{SiO}_2:0.067\text{Tween 60}:0.04\text{NaF}:0.006\text{HPM}:148\text{H}_2\text{O}$. The structure and texture of HPM and HPVM included on molecular sieves were studied by XRD, FT-IR and low temperature nitrogen adsorption technique. Powder X-ray diffraction data were obtained with a XD 8 Advanced Bruker diffractometer using the Cu K_α radiation in the range $2\theta = 0.5-5^\circ$ at low angles and $2\theta = 5-60^\circ$.

Textural characteristics of the outgassed samples were obtained from nitrogen physisorption using a Quantachrome instrument, Nova 2000 series. The specific surface area S_{BET} , mean cylindrical pore diameters d_p and adsorption pore volume V_{pN_2} were determined. Prior to the measurements the samples were degassed to 10^{-5}Pa at 250°C. The BET specific surface area was calculated by using the standard Brunauer, Emmett and Teller method on the basis of the adsorption data. The pore size distributions were calculated applying the Barrett-Joyner-Halenda (BJH) method to the desorption branches of the isotherms. The IUPAC classification of pores and isotherms were used in this study.

The IR absorption spectra were recorded with a Jasco 430 spectrometer (spectral range 4000-400 cm^{-1} range, 256 scans, and resolution 2 cm^{-1}) using KBr pellets.

3. RESULTS AND DISCUSSION

For all synthesized materials the N_2 adsorption-desorption isotherms exhibit a type IV isotherm (Fig. 1 a, b). The specific surface area, pore volume and pore diameter determined from the isotherm using the BJH method are given in Table 1.

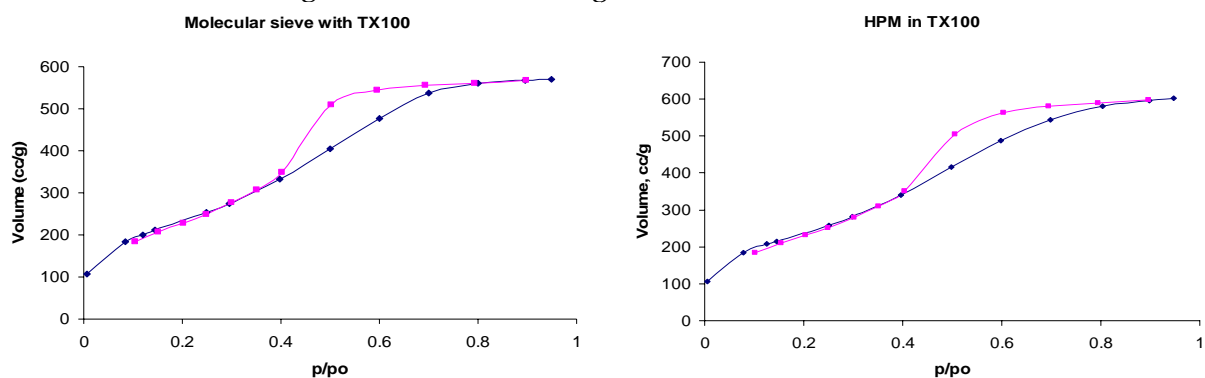


Figure 1. Nitrogen adsorption-desorption plot of molecular sieve with TX 100 (a) and HPM included on TX 100 (b)

Table 1 Textural properties of molecular sieves and included HPM

Sample	Specific surface area (m^2/g)	Pore volume BJH_{Des} (cc/g)	Average pore diameter BJH_{Des} (nm)
TX 100	841.65	0.881	3.66
Tween 60	877.67	1.012	3.64
HPM in TX100	857.04	0.931	3.67
HPM in Tween 60	762.01	0.867	3.66

The pore size distribution curves of parent molecular sieves with TX 100 plus CTMABr and Tween 60 respectively, have narrow pore size distribution within mesopore range with a maximum at 37 Å and 36 Å, respectively.

After HPM incorporation in molecular sieves matrix, the pore volumes of samples decreased with the increase of the concentration of active phase and also the surface area decreased with the increase in HPAs loading. The pore size distribution curves of HPM included on molecular sieves with TX 100 plus CTMABr and Tween 60 respectively, have one maximum within mesopore range at approximately the same values as in the case of pure molecular sieves.

The XRD patterns at low angles for the initial molecular sieves show a broad diffraction peak below 2.5° (2θ) for both materials prepared with TX 100 plus CTMABr and Tween 60, respectively (not shown).

For the two HPM included on molecular sieves the diffraction peaks at low angles are presented but with diminished intensity. The diffraction peak of included HPM appears like a shoulder. It can be asserted that the long – range order of molecular sieve is decreased evidently even for loading of 15 wt. % HPAs.

In order to confirm the presence of the Keggin anion on silica-HPA composites, the samples were analysed by FTIR. The $\text{PMo}_{12}\text{O}_{40}^{3-}$ Keggin ion structure consists of a PO_4 tetrahedron surrounding by four Mo_3O_{13} formed by edge-sharing octahedra. These groups are connected each other by corner-sharing oxygen. This structure give rise to four types of oxygen, being responsible for the fingerprints bands of Keggin anion between 1200 cm^{-1} and 700 cm^{-1} .

The pure HPAs show an IR spectrum with the specific lines of the Keggin structure containing the main absorption bands at 1064 cm^{-1} , 965 cm^{-1} , 864 cm^{-1} , 785 cm^{-1} assigned to the stretching vibrations $\nu_{\text{as}} \text{P}-\text{O}$, $\nu_{\text{as}} \text{Mo}=\text{O}_t$, $\nu_{\text{as}} \text{Mo}-\text{O}_e-\text{Mo}$ and $\nu_{\text{as}} \text{Mo}-\text{O}_e-\text{Mo}$ [4, 5]. These bands are preserved on the molecular sieves - HPA composites, but they are broadened and partially obscured because of the strong absorption bands of silica (1090, 812 and 456 cm^{-1}) (Figure 2).

The introduction of heteropolyacids into the silica matrix slightly influenced the structure of resulted composite (Figure 2). The vibration band at ca. 1090 cm^{-1} can be assigned to $\nu_{\text{as}}(\text{Si}-\text{O}-\text{Si})$ and decreased to 1072 cm^{-1} by incorporation of HPAs into the structure of the silica. The band at ca. 966 cm^{-1} present in the spectrum of included HPM sample can be assigned to the $\nu_{\text{as}} \text{Mo}=\text{O}_t$ stretching vibration. The bands at 812 and 454 cm^{-1} can be assigned to $\nu_s(\text{Si}-\text{O}-\text{Si})$ and $\delta(\text{Si}-\text{O}-\text{Si})$ bonds, respectively [6].

The bands of HPAs included on silica in the 1300-400 cm^{-1} region are partially or completely overlapped by the bands of the silica matrix. The band assigned to the P –O asymmetric stretching vibration at 1064 cm^{-1} is completely overlapped by the strong band at 1090 cm^{-1} of the silica.

Two IR bands in the spectra of included HPM appeared at 966 and 660 cm^{-1} , which can be assigned to the $\nu_{\text{as}} \text{Mo}=\text{O}_t$ stretching vibration and to $\delta(\text{O}-\text{P}-\text{O})$ of the HPAs.

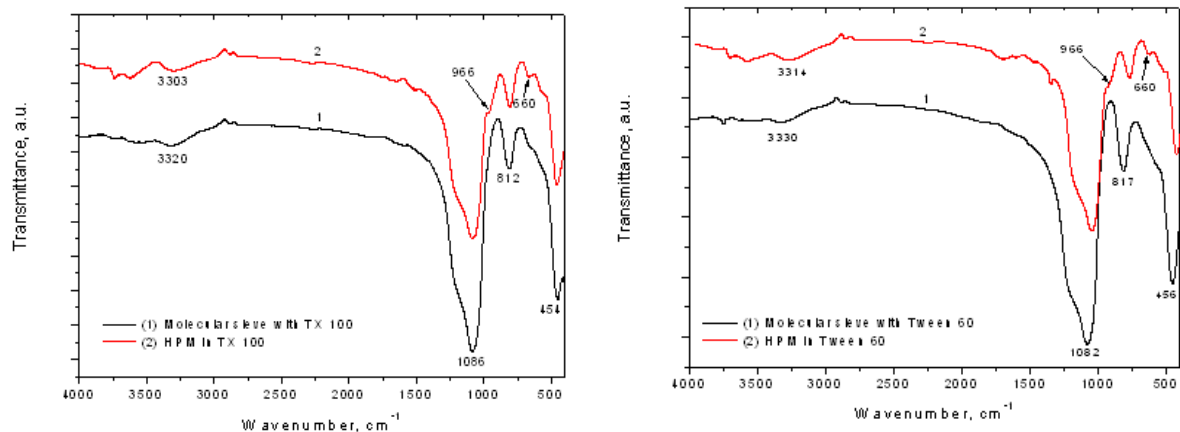


Fig. 2 FTIR spectra of molecular sieves - heteropolyacids composites

4. CONCLUSIONS

The HPAs anions preserved their Keggin structure on the surface of molecular sieves-HPA composites and forms finely dispersed HPAs species. The molecular sieves-HPM composites exhibit differential pore size distribution in the mesoporosity range.

It can be asserted that the long – range order of molecular sieve is decreased evidently even for loading of 15 wt. % HPAs.

The favourable effect of HPAs incorporation on silica molecular sieve is the increasing of pore volume and specific surface area, which in fact make the silica-HPA composites proper for heterogeneous catalysis.

LIST OF REFERENCES

- [1] F.Cavani, Catal. Today 41, (1998) 73-86
- [2] Alexandru Popa, V. Sasca and J. Halasz, Applied Surface Science, 255 (5 PART I), (2008)1830-1835
- [3] Alexandru Popa, V. Sasca, E.E. Kiš, R. Marinkovic-Neducin and J. Halasz, J. Optoelectron. Adv. Mater., 10(6), (2008) 1401-1407
- [4] A.Molnar, C. Keresszegi, B. Torok - Appl. Catal. A: General, 189 (1999) 217 - 224.
- [5] A.Kukovecz, Zs.Balogi, Z.Konya, M.Toba, P.Lentz, S.-I.Niwa, F.Mizukami, A.Molnar, J.B.Nagy, I.Kiricsi, Appl. Catal. A:General 5921 (2002) 1-12.
- [6] S.C. Laha, P.Mukherjee, S.R. Sainkar, R.Kumar, J.Catal.. 207 (2002) 213 -220
- [7] J.Toufaily, M.Soulard, J-L.Guth, J.Patarin, L.Delmonte, T.Hamieh, M.Kodeih, D.Naoufal, H.Hamad, Colloids and Surfaces A: Phys.Eng. Aspects, 316 (2008) 285-291
- [8] A.J.Bridgeman, Chem Phys. 287 (2003) 55-69



THE HEAVY METALS MONITORING IN CANNED VEGETABLES MIX

I. DAVID¹, F. BERBENTEA¹, M. ȘTEFANUȚ², L. GEORGESCU¹,
G.BUJANĂ¹, T.TRAȘCĂ¹, M.DANCI¹, Oana DANCI¹

¹U.S.A.M.V.B., Banat University of Agricultural Sciences and Veterinary Medicine, Faculty of Food Processing Technologies, Calea Aradului 199, Timisoara, ROMANIA

²INCEMC, National Research-Development Institute for Electrochemistry and Condensed Matter, str. Aurel Paunescu Podeanu 144, Timisoara, ROMANIA

Abstract

The paper proposes some possibilities for heavy metals detection in canned vegetables mix: Cr, Fe, Pb, Cd, Sn, Al, Zn, As. The heavy metals concentrations have been determined by AA spectrometry and electrochemical methods: cyclic voltammetry. The monitoring of heavy metals in canned vegetables mix can help evaluate and improve the insufficiently developed technology.

Key words:

vegetables mix, heavy metals, AA spectroscopy, cyclic voltammetry

1. INTRODUCTION

Vegetables mix and similar products are widely used for taste enhancement of various food products. Apart from their taste properties they also have a high nutritive value due to the content of easily retainable sugars, vitamin C, carotenoids and mineral salts.

Vegetables mix is a produce conserved through decrease in humidity, thus preventing the evolution of microorganisms. Microorganisms require a certain minimum amount of water to develop; bacteria require 35%, yeasts 25% and molds only need 10%.

2. EXPERIMENTAL

2.1. Samples preparation

Vegetables mix products have been weighed and treated by concentrated nitric acid (67%, Merck, heavy metals free). Samples digestion has been achieved in a 1000W MWS-2 – Berghof type microwave oven using a three-step program: $T_1=160^{\circ}\text{C}$, $t_1=15$ min., $P_1=40-60\%$ from total power, $T_2=210^{\circ}\text{C}$, $t_2=15$ min., $P_2=60-80\%$, $T_3=210^{\circ}\text{C} \rightarrow 100^{\circ}\text{C}$, $t_3=15$ min., $P_3=0\%$. Thus resulted solutions have been completed with ultrapure water (RO System Operating Barnstead apparatus) to equal volumes in 25 ml calibrated flasks.

2.2. Methods of analysis

2.2.1. AA Spectrometry

The heavy metals content has been determined by AA spectrometry (International Standard ISO 15586:2003) and cyclic voltammetry (Koryta, 1993), $i=f(E)$. AA spectrometry has been achieved with novAA 400 G type spectrometer - Analytik Jena - Germany, equipped with graphite furnace, WinAAS 3.17.0 software for evaluation, control and result presentation, a so-called cookbook, for every element, and a HS 55-1 hydride generator. Calibration curves have been plotted using standard solutions of metals in search.

2.2.2. Electrochemical Methods

Heavy metals such as Sn, Fe, Zn at the electrode surface are affected by characteristic redox phenomena which can be used to determine their concentration. The voltammograms $i=f(E)$ are obtained using PGZ 402 Voltalab, with VoltaMaster 4, version 7 software (User's manual, *Voltalab*®, 2008). A 50 cm³ BEC/EDI X51 V001 electrochemical cell, from Radiometer Copenhagen is part of the Voltalab system. Platinum electrodes ($S_{work}=7.85$ mm², $S_{aux}=50$ mm²) and standard calomel electrode (SCE) with 0.1M HNO₃ support electrolyte have been used in experiments. Recording speed was 50 mV/min. at an apparatus sensitivity of 10 nA. Calibration curves for Fe and Sn have been plotted using metals standard solutions as $I_{peak}=f(\text{conc.})$.

3. RESULTS AND DISCUSSIONS

Vegetables mix products are obtained through processing of fully mature tomatoes, beans, onions, papricas. Vegetables concentrates are used in the food industry to enhance the taste and nutritive value of various products. There are three phases in the vegetables mix production technology: obtaining the brute vegetables mix, conditioning and packaging the product (HOTARARE nr.1197, 2002; ORDIN 1050, 2006). When packaging into metallic cans the heavy metals content may exceed the safety limits, and in turn may be detrimental to public health. The two proposed analysis methods have the advantage of being fast and reliable (result accuracy). Five types of these products have been studied, both local and imported: four of them packaged in metallic cans and one in glass bottle, for reference.

The heavy metal concentrations in vegetables mix determined by AA spectroscopy are presented in Table 1. High values are noted in the case of Fe (which although beneficial to the human body may become an energetic catalyst for some chemical or biochemical processes), of Sn and of Al, especially in the Italian products.

Table 1. The heavy metal concentrations

No.	Sample	Concentration, ppm							
		Cr	Fe	Pb	Cd	Sn	Al	Zn	As
1.	Vegetables mix <i>Sultan</i> (Romanian product, Turkish licence, metallic can)	0.20	29.5	0.02	0.009	4.45	33.45	7.1	**
2.	Vegetables mix <i>Conserv frig</i> (Romanian product, metallic can)*	0.15	218.0 0	0.20	0.034	70.78	36.1	4.03	**
3.	Vegetable mix <i>Mib</i> (Romanian product, metallic can)	0.13	16.93	**	0.003	12.5	23.1	6.5	**
4.	Vegetable mix <i>Maxim's</i> , (Italian product, metallic can)*	0.18	41.31	1.9	0.109	14.8	80.2	9.0	**
5.	Vegetables mix <i>BuŃtea</i> (Romanian product, glass bottle)	0.26	27.61	0.16	0.017	8.24	48.56	8.79	**

* before the samples were taken the vegetables mix was homogenized at 1500 rpm with an IKA-LABORTECHNIK stirrer, with adjustable rotations and display unit observation

** under limit detection

It has been remarked the high Cd concentration in *Maxim's* vegetables mix (Italian product).

For the determination of heavy metals by electrochemical methods, the first step was plotting the calibration curves. The methods used for Fe and Sn by means of cyclic voltametry $i=f(E)$ are presented in Fig.1., Fig.2., Fig.3. and Fig.4.

The electrochemical method has only been applied for the higher concentration of metals Fe and Sn. Extracting Fe from the vegetables mix products using this method has had no results. (Fig. 5.). Note that the Fe voltamogram is lower than the base line of the support electrolyte.

Sn, on the other hand, is present in the Italian vegetables mix canned in high concentrations Fig.6 and Fig.7. (samples were taken from right next to where the can is welded, for all samples).

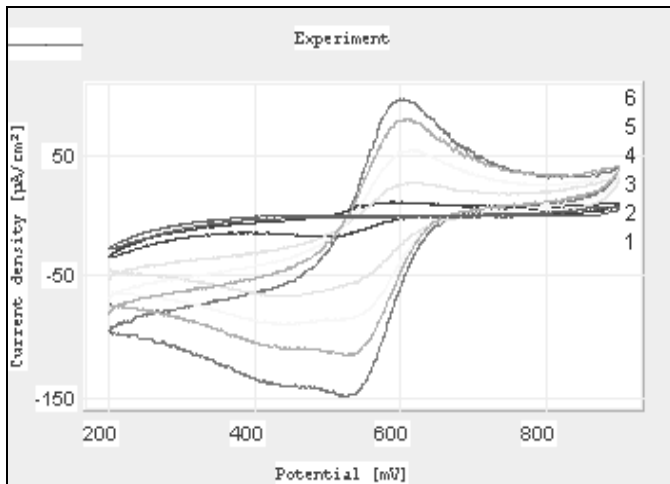


Fig.1. Cyclic voltammograms for equilibrium $Fe^{3+} + e^{-} \rightarrow Fe^{2+}$. 1 – support electrolyte HNO_3 0.1 M; 2 - $c=25.64$ mg/L; 3 - $c=50.00$ mg/L; 4 - $c=95.24$ mg/L; 5 - $c=136.36$ mg/L; 6 - $c=173.91$ mg/L

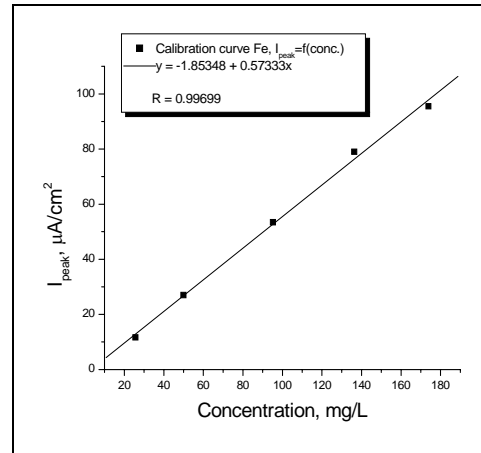


Fig.2. Calibration curve for iron concentration determination in canned vegetables mix, $I_{peak}=f(\text{conc.})$, $E_{ESC} = 608$ mV

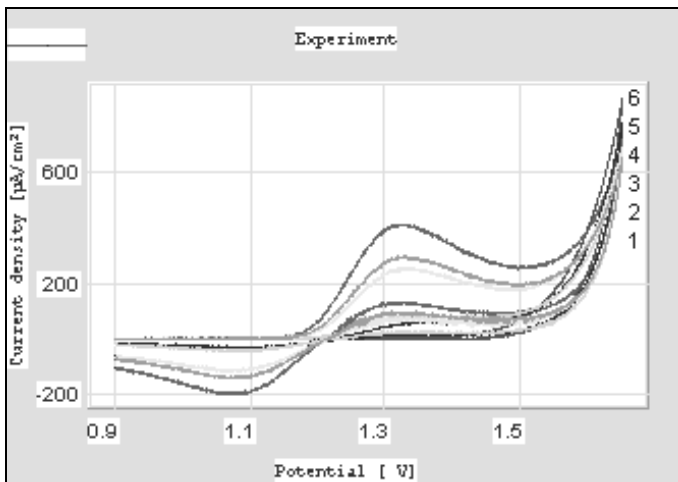


Fig.3. Cyclic voltammograms for equilibrium $Sn^{4+} + 2e^{-} \rightarrow Sn^{2+}$. 1 – support electrolyte HNO_3 0.1 M; 2 - $c=6.8333$ mg/L; 3 - $c=13.5257$ mg/L; 4 - $c=20.0816$ mg/L; 5 - $c=26.5050$ mg/L; 6 - $c=32.8000$ mg/L

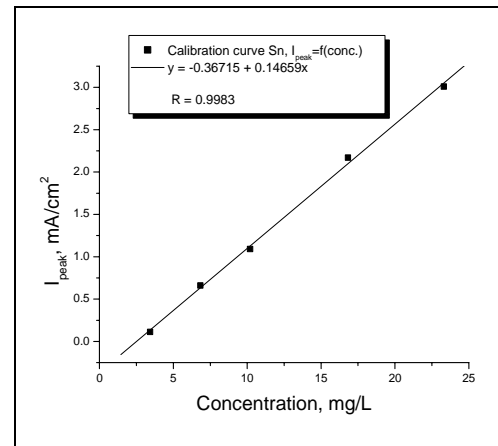


Fig.4. Calibration curve for tin concentration determination in canned vegetables mix, $I_{peak}=f(\text{conc.})$, $E_{ESC} = 1.375$ V

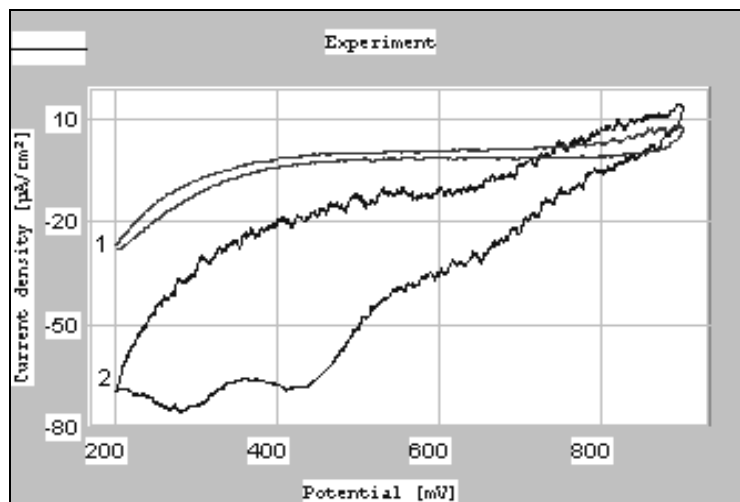


Fig.5. Fe determination in *Conserv frig* (vegetables mix)

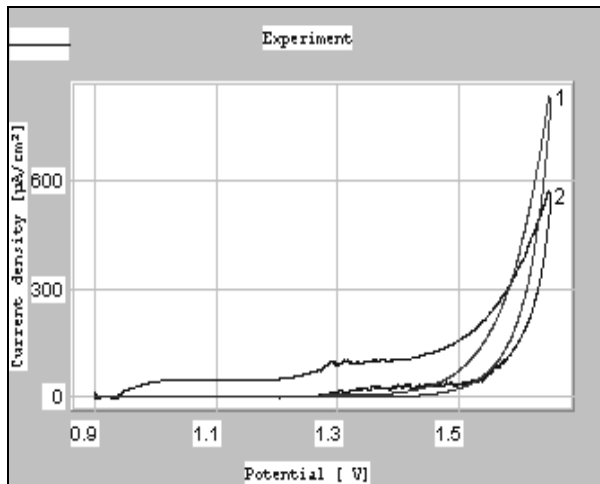


Fig.6. Sn determination in *Conserva frig* (vegetables mix), $E_{ESC} = 1.375$ V

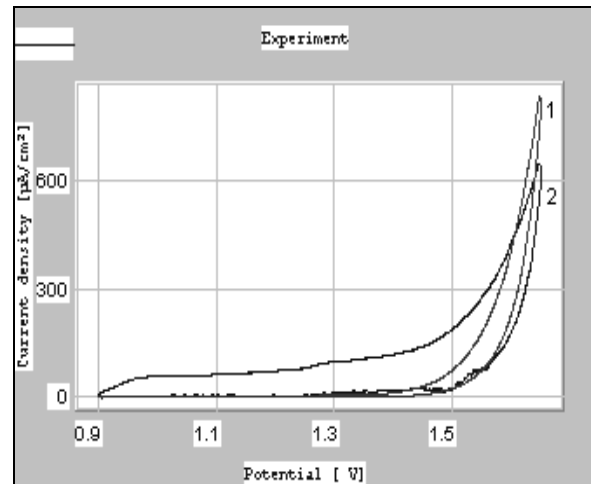


Fig.7. Sn determination in *Maxim's* (vegetables mix), $E_{ESC} = 1.375$ V

The values obtained using the electrochemical method are $c = 3.60$ ppm Sn for *Conserva frig* ($I_{peak} = 0.1589$ mA/cm²) and $c = 3.40$ ppm Sn for *Maxim's* ($I_{peak} = 0.1367$ mA/cm²). There are obvious errors in using this method due to all the metal ions which can influence the electrochemical behavior.

4. CONCLUSIONS

The environment pollution with heavy metals (Cr, Ni, Pb, Zn, Al, As, Cd, etc.) is due mainly to the activity of humans. Two heavy metals (Sn and Al) showed higher concentrations than legally admitted in canned vegetables mix. Concentration of heavy metals from the polluted environment in vegetables is influenced by different factors and stopped through several mechanisms. The monitoring of heavy metals in canned vegetables mix can help to evaluate and improve the insufficiently developed technology.

REFERENCES

- [1] HOTARARE nr. 1197 /24 octombrie 2002 pentru aprobarea Normelor privind materialele si obiectele care vin in contact cu alimentele (*Romanian specific standard*).
- [2] * * * International Standard ISO 15586:2003 (E), Water quality – Determination of trace elements using atomic absorption spectrometry with graphite furnace.
- [3] Koryta J., Dvorak J., Kavan L., „Principles of Electrochemistry”, Wiley, Chichester, 1993, p.191.
- [4] ORDIN 1050 /21.12.2006 privind aprobarea Normei sanitare veterinare si pentru siguranta alimentelor privind anumiti contaminanti din alimentele de origine animala si nonanimala (*Romanian specific standard*).
- [5] * * * User's manual, *VoltaLab® system with VMA*, Radiometer analytical, 2008.



BIOCOMPATIBLE MATERIALS REALIZED BY PLASMA THERMAL SPRAYING OF HYDROXYAPATITE ON METALLIC SUPPORTS

Radu ROSU, Doru Romulus PASCU, Ioana SAVIN

ISIM Timisoara, ROMANIA

Abstract

In this paper is presented the thermal spraying process of the oxidic ceramic (hydroxyapatite) on metallic supports to obtain biocompatible materials with application in general medicine. Two main applications are obtained by realizing of titanium base implants, dental and orthopedic. The samples were examined by optical and electronic microscopy, finally the ceramic layers presented the roughness between 8 and 9 μm and the layer thickness between 90 și 330 μm . No defects can be reported. The samples obtained by plasma thermal spraying were corrosion tested in simulated body fluid (SBF with pH 7,4 la 37°C).

Key words:

thermal spraying, biocompatible materials, oxidic ceramic, SBF

1. INTRODUCTION

The best materials used to the prosthesis fabrication in dental and orthopedic medicine are those which are similar with the composition of the humane bone, the repairing mechanism of the bone is the natural regenerations.

One approach to provide a strong, long-lasting adhesive interface between a bone replacement implant and the surrounding tissue involves the use of bioactive materials.

Hydroxyapatite (HA) is the most well known bioactive ceramic materials used in medicine. The inorganic constituent of bone is made up of biological apatites, which provide strength to the skeleton and act as a storehouse for calcium, phosphorus, sodium, and magnesium.

2. MATERIALS USED

For biocompatible layers deposition hydroxyapatite powders were used with the dimension of the particles between 10-30 μm and Ti-Mo-Al titanium alloy as substrate. The chemical composition of the titanium alloy is presented in table 1. The chemical composition of the two samples (substrates) is conform ASTM grade 11.

Table 1 The chemical composition of the titanium alloy used as substrate

No. sample	Chemical composition %					
	Ti	Mo	Al	Mn	V	Fe
1	97,70	1,641	0,3245	0,1048	0,0921	< 0,032
2	97,75	1,626	0,2989	0,1060	0,0847	< 0,034

In figure 1 and 2 the biphasic structure is presented (solid solution α enriched in titanium and intermetallic compounds of Ti-Mo, Ti-Al) of the titanium alloy used as substrate (BM) for the deposition of the hydroxyapatite layers by plasma thermal spraying. In the base metal (BM) were developed fine macles due to the hot plastic deformation process of the Ti-Mo-Al alloy.

Hydroxyapatite $\text{Ca}_{10}(\text{PO}_4)_6(\text{OH})_2$ is a oxidic ceramic which is used to realize the biocompatible layers by plasma thermal spraying or by other methods.

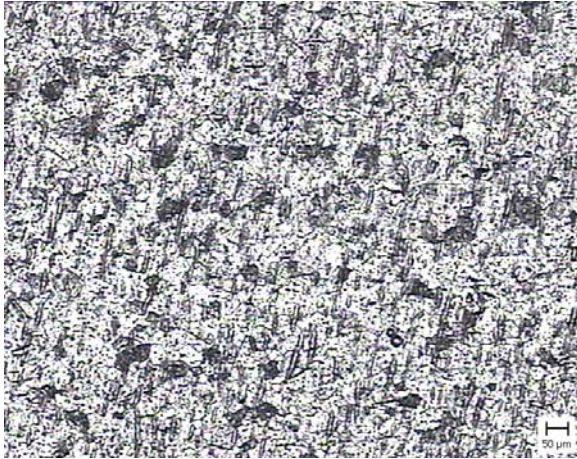


Figure 1. Titanium alloy substrate BM (cupric solution, 50 x)



Figure 2. Titanium alloy substrate BM (cupric solution, 100 x)

3. SAMPLES PREPARATION

Before thermal spraying, the titanium samples were blasted with electrocorindon with the granulation between 0,8 – 2 mm and the air pressure of 5 bar. The blasting distance was 50±5 mm.



Figure 3 The thermal spraying gun 3MB of the plasma thermal spraying installation

Because the powders presented a high agglomeration tendency the dehydration of the powder (heating to 60 °C, time 12 h) was necessary.

The deposition of the hydroxyapatite powder on titanium alloy substrate was realized with the plasma thermal spraying installation from ISIM – Timisoara. In figure 3 is presented the thermal spraying gun 3MB of the installation.

The plasma spraying process was made in horizontal position the spraying gun position was perpendicularly on the titanium alloy support. In figure 4 is presented image from the plasma thermal spraying process.

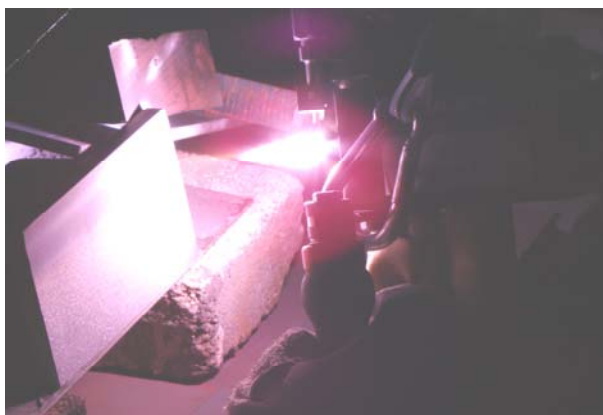


Figure 4. Image form plasma spraying process

In plasma spraying process of the hydroxyapatite the distance between the titanium surface and spraying gun was 100 mm .

The plasma spraying parameters used for the hydroxyapatite deposition are presented in table 2.

With the parameters from table 2 were made two samples:

- ✚ A sample (M1) with one hydroxyapatite layer, using Ti-Mo-Al alloy
- ✚ A sample (M2) with three hydroxyapatite layers, using Ti-Mo-Al alloy

Table 2. The plasma spraying parameters

I _p A	U _a V	Q _p l/min	Q _{tr} l/min	m _p g/min	d _p mm	N _n	Cooling
500	60	40	6	15	100	3	air
500	60	40	6	15	100	1+1+1	air

4. EXPERIMENTAL RESULT AND INTERPRETATION

The macroscopic examinations show the deposited layers aspect of different thickness (table 3). The determination of the hydroxyapatite layer thickness was made with Leptoskop Pocket device from ISIM – Timisoara. On the examined surfaces no defects were observed.

Table 3. Layer thickness plasma sprayed

No. Sample	No. Layers	Layer thickness [μm]	
		Individual values, g	Average value, \bar{g}
M1	1	90, 100, 111, 160, 120, 132, 122, 92, 101, 120	127,8
M2	3	310, 310, 320, 330, 315, 318, 321, 310, 315, 318	316,7

Analyzing the thickness values of the sprayed layers is observed that the values of the sample M1 vary between 90 și 160 μm and presents a high dispersion on the values with the average 127,8 μm , the sample M2 present values between 310 și 330 μm with the average 316,7 μm , which attest a high compacting of the layers deposited by thermal spraying. The average roughness of the deposited layers measured with SJ-201P device is maximum 8,50 μm .

Microscopic examinations made according EN1321 show the microstructure of the deposited layers by plasma thermal spraying process, which consist from globular and acicular particles of apatite with the hardness 5 on Mohr hardness scale (figure 5, 6). On the examined sections by optical microscopy no defects were observed (pores, microcracks).

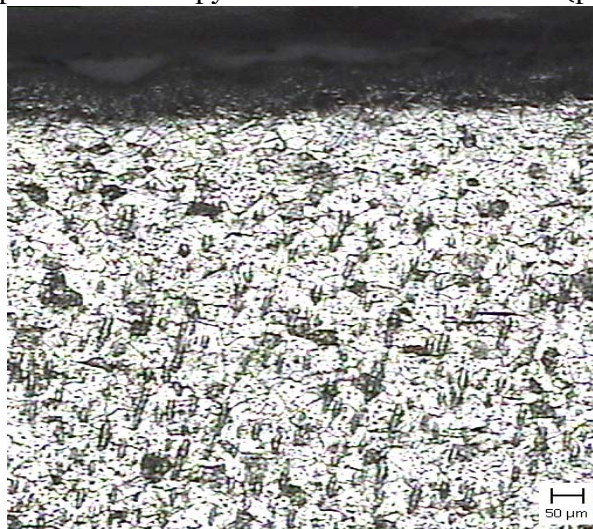


Figure 5 The microstructure of the hydroxyapatite ayer deposited by plasma thermal spraying (ferric chloride , 50 x)

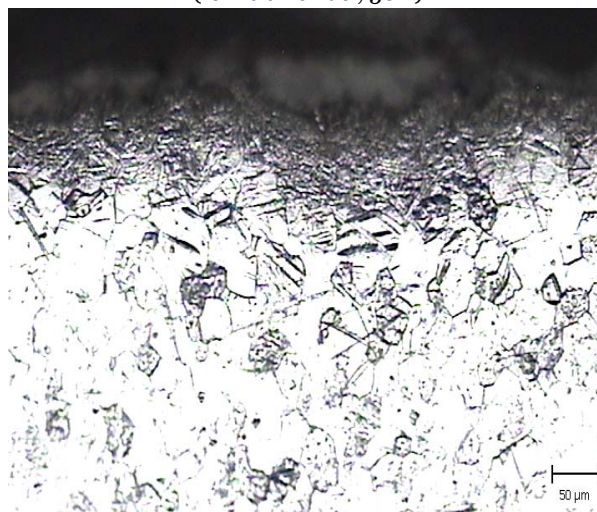


Figure 5 The microstructure of the hydroxyapatite layer deposited by plasma thermal spraying (ferric chloride , 100 x)

In figure 7 and 8 are presented the images of the deposited layer by plasma thermal spraying of the hydroxyapatite powder on titanium alloy substrate using SEM (scanning electronic microscopy).

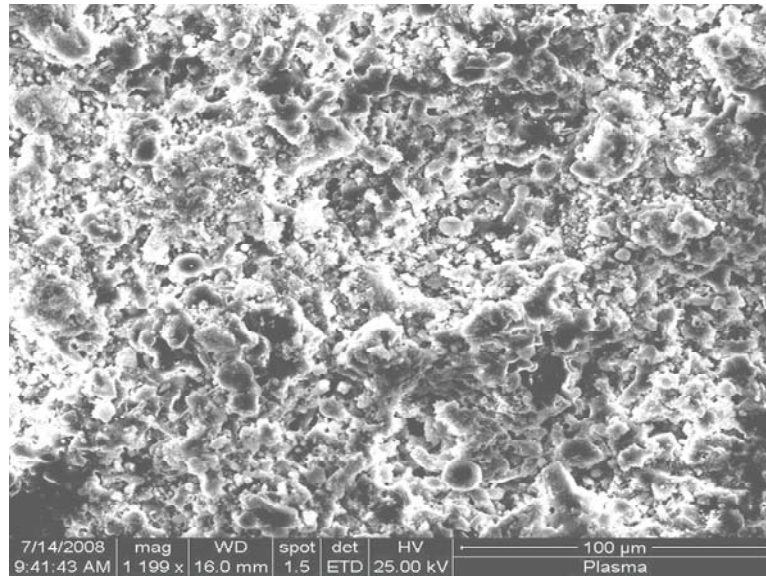


Figure 7. SEM image of the deposited layer (1200 x)

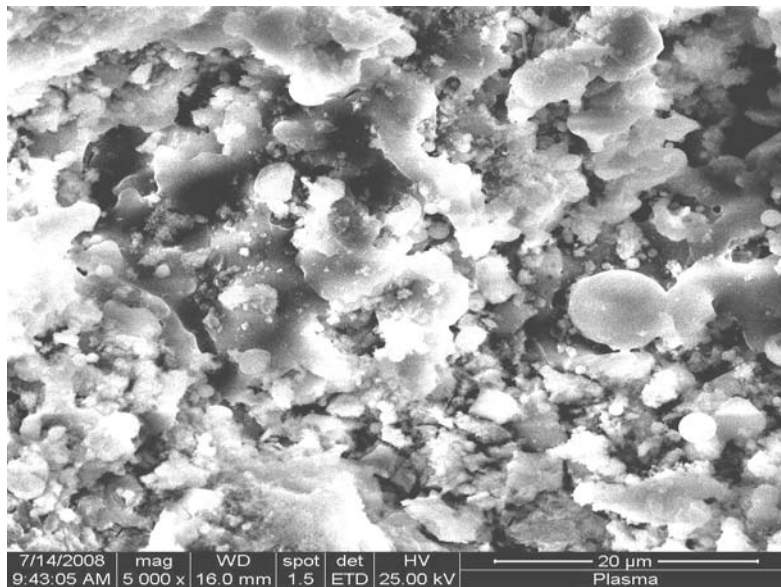


Figure 8. SEM image of the deposited layer (5000 x)

The SEM analysis of the deposited layer by plasma thermal spraying shows a characteristic morphology of the deposited layer by plasma thermal spraying with fine and big particles disposed uniformly on the surface.

5. CORROSION TESTS

The samples for corrosion tests deposited with hydroxyapatite layers have the aspect presented in figures 9 and 10.

Before the corrosion test the samples were weighed with an analytic balance and presented the values:

$$M_1 = 9,8973 \text{ g}$$

$$M_2 = 11,7419 \text{ g}$$

The test samples were introduced in simulated body fluid (SBF). In table 3 is presented the chemical composition of the corrosion testing solution.



Figure 9. Sample M1

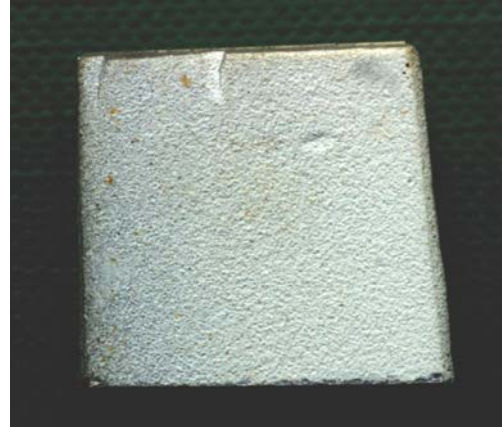


Figure 10. Sample M2

Table 3 Regents for preparing SBF (pH7.4, 1l)

Order	Reagent	Amount
1	NaCl	7.996 g
2	NaHCO ₃	0.350 g
3	KCl	0.224 g
4	K ₂ HPO ₄ ·3H ₂ O	0.228 g
5	MgCl ₂ ·6H ₂ O	0.305 g
6	1M-HCl	40 mL
(About 90 % of total amount of HCl to be added)		
7	CaCl ₂	0.278 g
8	Na ₂ SO ₄	0.071 g
9	(CH ₂ OH) ₃ CNH ₂	6.057 g

The corrosion test is realized on 28 days, after every 7 days is verified the mass losing of the samples. In the first step was not observed cracks on the surface of the tested samples.

6. CONCLUSIONS

6.1 The best materials used to the prosthesis fabrication in dental and orthopedic medicine are those which are similar the composition of the humane bone, and the repairing mechanism of the bone is the natural regenerations. One approach to providing a strong, long-lasting adhesive interface between a bone replacement implant and the surrounding tissue involves the use of bioactive materials.

6.2 Macro and microscopic examinations of the realized combination show specific structure of the materials used, without plasma spraying defects (pores, cracks, microcraks).

6.3 The generalized corrosion tests are made in simulated body fluid (SBF) by the determination of the mass losing in the tests cycles. The test results confirm the corrosion resistance of the investigated specimens.

BIBLIOGRAPHY

- [1] Ladislav Bardos, Hana Barankova: Plasma processes at atmospheric and low pressures, Plasma processes at atmospheric and low pressures, Vacuum, 2008
- [2] Zafer Evis, Metin Usta, Isil Kutbay: Improvement in sinterability and phase stability of hydroxyapatite and partially stabilized zirconia composites, 2008

- [3] Akira Kobayashi, Wei Jiang: Properties of titania/hydroxyapatite nanostructured coating produced by gas tunnel type plasma spraying, Vacuum, 2008
- [4] S. Zhang, Y.S. Wang: Evaluation of adhesion strength and toughness of fluoridated hydroxyapatite coatings, Thin Solid Films, 2008
- [5] CAO Ning, BAI Yun-qiang, MA Quan-sheng, SUI Jin-ling, LI Mu-sen: Biological behavior of hydroxyapatite coatings on carbon/carbon composites produced by plasma spraying, New Carbon Materials, 2008
- [6] A. Dey, A.K. Mukhopadhyay, S. Gangadharan, M.K. Sinha, D. Basu, N.R. Bandyopadhyay: Nanoindentation study of microplasma sprayed hydroxyapatite coating, Ceramics International, 2009



THERMAL SHOCK BEHAVIOR OF THE COATS DEPOSITED BY PLASMA SPRAYING OF THE TiO₂

Maria Laura BENEĂ

“Politehnica” University of Timișoara, Engineering Faculty of Hunedoara, ROMANIA

ABSTRACT

For the coats made by using the TiO₂ powder (type Metco 102) on a martensitic stainless steel substrate, the thermal shock testing conditions consist in: fast heating to 800°C (or 500°C) (10s) and water cooling without maintaining to maximum temperature.

After 20 cycles to a maximum temperature of 800°C we noticed the appearance of pattern fine cracks, which is developed along the next 20 cycles but with no scorching.

For a maximum temperature of the 500°C of the thermal shock, after 180 cycles we not observed the appearance of the scorches on the coats surface.

KEYWORDS

Thermal Shock, TiO₂ coatings, plasma deposition

1. INTRODUCTION

Plasma spraying of materials such as ceramics and non-metallic, which have high melting points, has there fore become well established as a commercial process. Such coatings are increasingly used in aerospace, automobile, textile, medical, printing and electrical industries to impart proprieties such as corrosion resistance, thermal resistance, wear resistance, etc [1,2].

One of the most important characteristics of thermal barrier coatings is the ability to undergo fast temperature changes without failing; the so called thermal shock resistance.

The thermal shock resistance is defined as the number of thermal shock a thermal barrier coating withstands without failing.

This paper describes the results of tests conducted to determine the thermal shock behavior of the coats deposited by plasma spraying of the TiO₂.

2. EXPERIMENTAL PART

2.1. Experimental conditions at the TiO₂ coatings spraying in plasma

The substrate is the martensitic stainless steel Z12CNDV12.

The powder used is Metco 102, with 99% TiO₂ and particle size between 7,8 and 88 μm.

The coatings have been made using plasma generator GPPR-400 equipment.

There have been working using the following parameters:

- ⚡ intensity of the current at the generator: 500 A;
- ⚡ voltage: 70 V;
- ⚡ spraying distance: 50 mm;
- ⚡ plasma gas flow: 36,6 l/h;
- ⚡ coating thickness: 0,3 mm;

Thermal shock testing

For the coats made by using Metco 102 powder on a martensitic stainless steel substrate, the thermal shock testing consist in: fast heating to 800°C or 500°C (10 s) and water cooling (600°C/s) without maintaining to maximum temperature.

3. RESULTS AND DISCUSION

Some results of the experimental determination are shown in table 1.

TABLE 1. RESULTS OF THE THERMAL SHOCK DETERMINATION

Cod sample	The number of thermal cycles	The maximum temperature cycle [°C]	Cooling medium	Observation
48	20	800	water	The appearance of scorches
50	30	800	water	The appearance of scorches
54	25	800	water	The appearance of scorches
Medium		59		
3	180	500	water	No cracks, No scorches

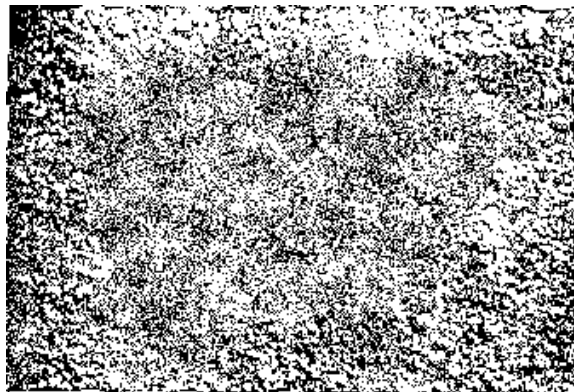
Figure 1 shows some images for the coats made using Metco 102 powder, in a different moments of the determination.

Samples were examined by optical microscopy using a stereo microscope

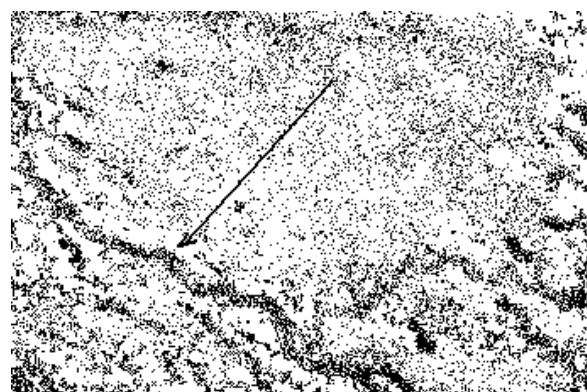
As was expected, the evidence submitted TiO_2 have a reduced resistance to heat shock at 800°C (25 cycles).

Layers, in its original state, have a characteristic ceramic deposition, with a pronounced roughness without visible cracks to the naked eye or to the optical microscope at low zoom. The images in Figure 1 reveals the fact that a smooth network of cracks is formed after the first set of 22 set of cycles. The cracks increase is fast, showing in this way the extended cracks and the exfoliations detected on the sample number 54. The breaking surface is highlighted by the glossy appearance of the detachment surface limits. The observed cracks have the propagation way perpendicular to the longitudinal axis of the sample, highlighting the direction with maximum stretching tensions during the experiment. Also, the cracks orientation on the layer thickness is from the substrate towards the deposit surface determed by the tensions in the substrate during the experiment.

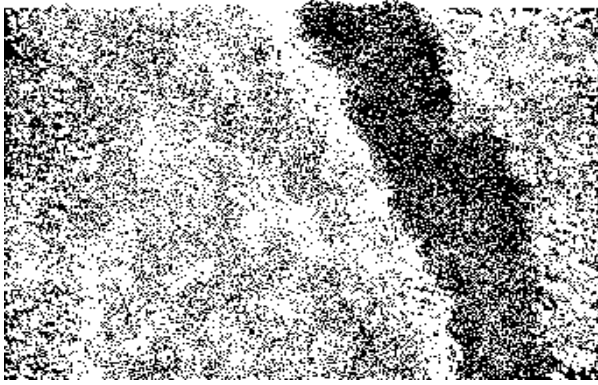
Because the treatment chose in the first step was considered excessively harsh for the ability of TiO_2 to take thermal shocks, the experiment was resumed on a new set of samples covered in the same conditions at a maximum temperature of the thermal cycle 500°C with a cooling speed of 600°C/s. After running 180 cycles do not show any exfoliations. The network of cracks appears to form at a higher number of cycles (54) and extends slowly, increasing the number of cycles. The number of cracks expands significantly at over 135 cycles. At the limit of 180 cycles the apparition of the first dislocation of the coverage layer on the limits of the cracks can be notified. Images for the coats made by using the Metco 102 powder at the thermal shock are presented in following samples.



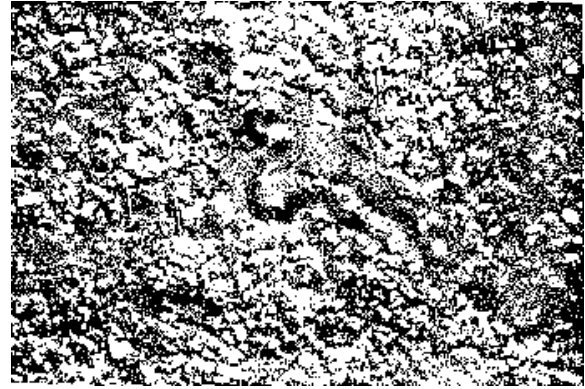
Sample 50, 40x, Initial state



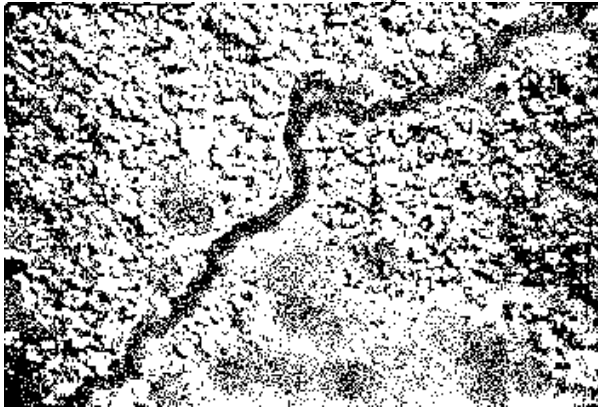
Sample 50, 800°C/water/322 cycles Cracks



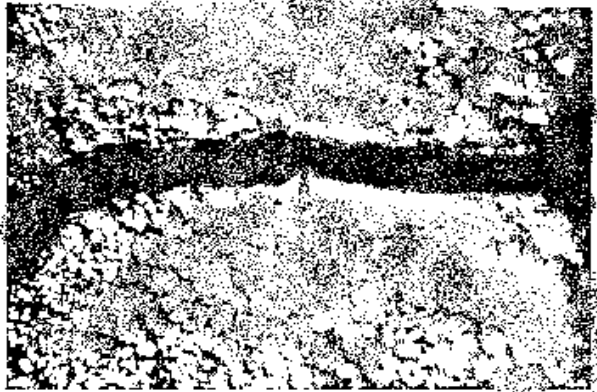
Sample 50 (70x), 800°C/ water / 19 cycles
 Detachment layer



Sample 50 (70x), 800°C/ water / 31 cycles
 Cracks



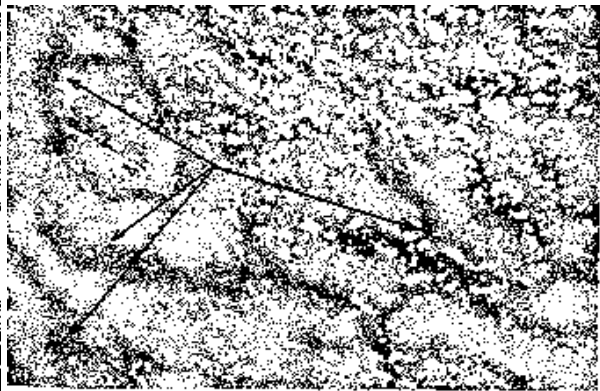
Sample 54 (70x), 800°C / water / 25 cycles
 Cracks



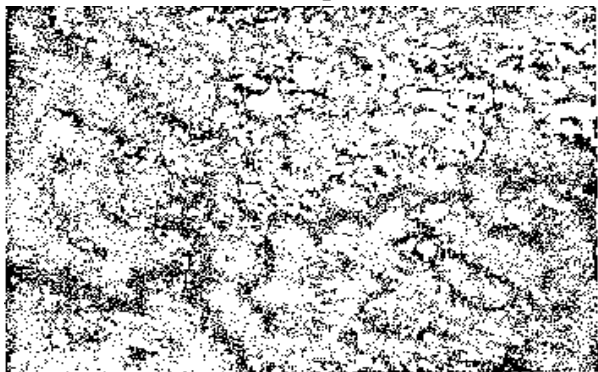
Sample 54 (70x), 800°C / water / 31 cycles
 Detachment layer



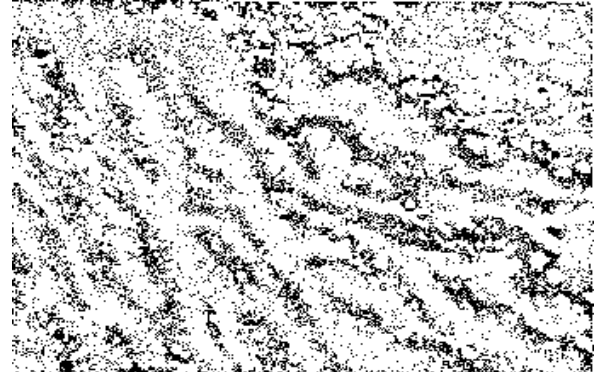
Sample 54 (70x), 800°C / water / 31 cycles
 Detachment (per section)



Sample 3 (70x), 500°C/ water/104 cycles
 Cracks



Sample 3 (70x), 500°C/ water/130 cycles
 Cracks



Sample 3 (70x), 500°C/ water/156 cycles
 Network of cracks



Sample 3 (70x), 500°C/water/180 cycles
Cracks and layer displacement

glossy limits of the detachment surface;

- ✚ The cracks that have been seen have the sense of propagation perpendicular to the longitudinal axis of the sample attempted at 800°C, highlighting the maximum stretch tension during the experiment;
- ✚ The orientation of the cracks on the coating layer thickness tested at 800°C is from the substrate to the surface the deposit, this is determined by the tension of substrate during the experiment;
- ✚ Particularly in the first stage of the experiment is considered over harsh for TiO₂'s capacity to take heat shock;
- ✚ At a maximum temperature of thermal cycle of 500°C and a cooling of 600°C/s after running a number 180 cycles, no samples presented peeling;
- ✚ The network of cracks is formed from a larger number of cycles and expands slowly when increasing the number of cycles;
- ✚ The maximum temperature of thermal cycle of 500°C, the cracks are not extending significantly at more than 135 cycles;
- ✚ The apparition of the first displacement of coverage layer on the edge of the cracks is notified at the limit of the 180 cycles with the maximum temperature of 500°C.

4. CONCLUSIONS

Conclusions that results from analyzing the results of determination the resistance to thermal shock of the TiO₂ layers are:

- ✚ The TiO₂ samples have a low resistance at thermal shock at 800°C (25 cycles);
- ✚ It has already formed a network of cracks after the first set of 22 cycles performed at 800°C;
- ✚ The growth of cracks is rapid, revealing the extended cracks and the exfoliation uncovered on the sample number 54;
- ✚ The breaking surface is highlighted by the

REFERENCES

- [1] Nicoll, A.R., “Protective Coatings and their Processing – Thermal spray”, Plasma Technik, AG,Wohlen, Switzerland, Publ.No.86002E.
- [2] Calosso, W.F., Nicoll, A.R., “Process requirements for plasma sprayed coatings for internal combustion engine components”, Proc. Energy – Surface Technology Conerence and Exhibition, ASME,1987.
- [3] Benea, M.L., “Contribuții teoretice și experimentale asupra acoperirilor ceramice superrefractare realizate în jet de plasmă”, Teză de doctorat, Timișoara, 2003



PREPARATION AND CHARACTERIZATION OF GOLD NANOCCLUSERS WITH COADSORBED METALS

János KISS, András BERKÓ, László ÓVÁRI,
László BUGYI, Zsolt MAJZIK, Nándor BALÁZS

Reaction Kinetics Research Laboratory of CRC of Hungarian Academy of Sciences,
University of Szeged, HUNGARY

ABSTRACT

Au and their coadsorbed layers with Mo and Rh were produced on titania surfaces and characterized by LEIS, XPS, AES and STM. The data indicated that the deposition of Au on the Mo-covered TiO₂(110) surface enhanced the dispersion of gold. The driving force for the disruption is that Au-Mo bond energy is larger than the Au-Au bond energy. In case of Au-Rh bimetallic system, Au disruption was not observed. Rh atoms impinged onto Au clusters pregrown on TiO₂(110) became covered by by gold atoms by place exchange. The incorporation of rhodium led to an enlargement of gold clusters.

KEYWORDS

nanocluster, gold, molybdenum, rhodium, TiO₂, bimetal

1. INTRODUCTION

The preparation and characterization of metal nanoparticles on oxide surfaces is of great technological importance in catalysis, gas-sensorics and in different fields of material science. TiO₂ has excellent properties as a support material, affecting the catalytic activity of the supported particles in an advantageous way in many cases. Both the metal-support electronic interaction, and particle restructuring can influence the reactivity [1-3].

The presence of a second metallic component can significantly improve the catalytic performance in several cases, assigned frequently to “ensemble” or “ligand” effects [4], as it was experienced for example in the catalytic reduction of NO on supported Rh-Ag [5], in the steam reforming of methane on supported Ni-Au [6] or for the oxidation of CO on Pd-Au/TiO₂ [7]. Segregation or dissolution of surface atoms are key issues in bimetallic systems. Low energy ion scattering spectroscopy (LEIS), applied in the present work with He ions, is particularly useful to follow the surface composition, because it gives information only about the outermost atomic layer.

Previous studies concluded that the growth of gold and rhodium adlayers on clean TiO₂ followed Volmer-Weber mechanism, while XPS measurements showed that there is no chemical interaction between stoichiometric TiO₂ and the gold or rhodium particles [2-3, 8-10]. In the case of Mo growth on TiO₂(110), we found that the outermost atomic layer comprises of considerable amount of molybdenum and oxygen both at low and high metal coverages [11]. The reaction between TiO₂ and Mo is also evidenced by the shift in the Ti2p and Mo3d XPS lines, revealing that Ti is reduced, while Mo is oxidized. The oxidation state for titanium was 4, 3 and 2, in harmony with previous findings [12].

In our former study it was demonstrated by scanning tunneling microscopy (STM) and LEIS that addition of Mo to Au/TiO₂(110) resulted in the disruption of gold nanoparticles [11]. This led to the increase in the dispersion of gold. In the present work we compare the behavior of Au-Mo system with that of Au-Rh system, both on TiO₂(110). Note that the interaction of rhodium with titania is much weaker than that of Mo, corresponding to the lower activity of Rh towards oxygen.

2. EXPERIMENTAL

The experiments were performed in two separate ultrahigh vacuum (UHV) systems (base pressure <5 ×10⁻⁸ Pa). One chamber was equipped with facilities for LEIS, AES, and XPS measurements. In the second one, STM and AES techniques were applied.

A Specs IQE ion source was used for LEIS. He⁺ ions of 800 eV kinetic energy were applied at a low ion flux. The ions and electrons were analyzed by a Leybold hemispherical energy analyzer. The STM imaging was performed by electrochemically etched W-tips conditioned in situ by voltage pulses in a commercial room temperature STM system (WA-Techology).

The rutile TiO₂(110) single crystals were products of PI-KEM. The samples were attached to a Ta plate with a UHV compatible oxide glue (AREMCO, ceramobond 571), and could be heated with a filament placed behind the Ta plate. The sample temperature was measured by a chromel–alumel thermocouple, attached to the side of the sample with the same adhesive material. The cleanliness, composition and morphology of the surface were controlled by AES, LEIS, XPS and STM methods.

Rh, Mo and Au were deposited by an EGN4 e-beam evaporator of Oxford Applied Research at a substrate temperature of 300 K. The amount of the deposited metals is expressed in equivalent monolayers (eqML). In the STM chamber, the surface concentrations of the deposited metals were estimated from the volume of the nanoparticles separated clearly from each other.

3. RESULTS AND DISCUSSION

Rh formed predominantly two dimensional (2D) clusters on titania at small coverages ($\Theta_{Rh} \leq 0.2$ - 0.3 ML) at room temperature according to STM and LEIS results, while 3D nanoparticles were formed at higher amounts of Rh (with a typical diameter of 1.8 nm and a height of 0.5 nm at $\Theta_{Rh} = 0.5$ ML). Gold clusters were significantly larger (diameter of 3.2 nm at $\Theta_{Au} = 0.5$ ML). Deposition of Rh on the Au/TiO₂(110) surface led to a decrease in the Ti and O LEIS peaks due to the shadowing effect of Rh. In contrary, a significant *increase* in the LEIS signal was detected for Au, which means that the number of Au atoms on the topmost layer of the metal clusters was enhanced (figure 1A). It was observed in a broad coverage range ($\Theta_{Au} = 0.25$ - 0.8 ML), the effect being somewhat stronger at higher gold concentrations. Deposition of Mo on Au/TiO₂ resulted in rather similar changes in LEIS spectra (figure 1B).

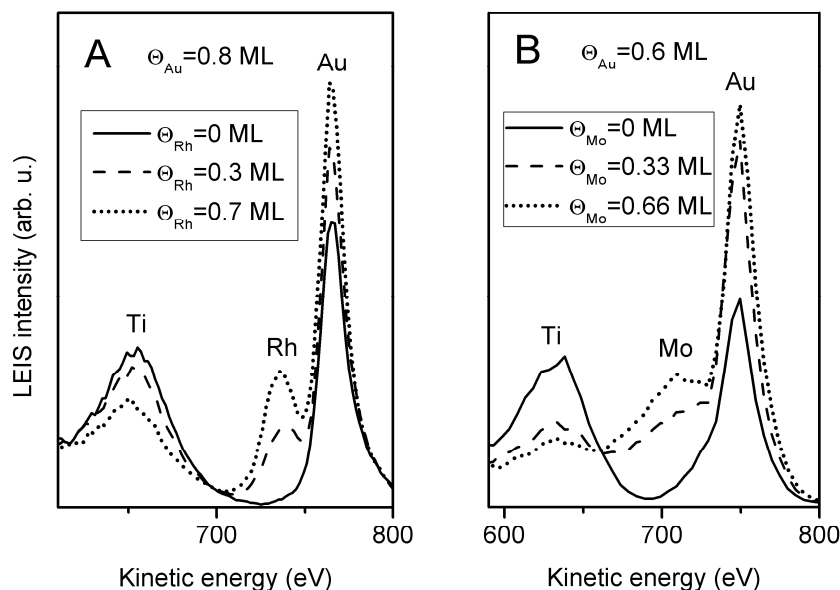


Fig.1 (A) Ti, Rh and Au LEIS signals as a function of Rh deposition time and (B) Ti, Mo and Au LEIS signals as a function of Mo deposition time, both recorded on Au-precovered titania.

STM measurements indicated that in the case of similar coverages (\square_{Au} and \square_{Rh} appr. 0.5 ML) the number of Au nanoparticles did not change on the effect of the deposition of Rh. Gold clusters became larger after Rh deposition (figure 2 A, B, C), in contrary to what was observed for post-deposition of Mo on Au/TiO₂ (figure 2 D, E, F). The statistical evaluation, in which a raised attention was paid to tip-shape effects, exhibited an average increase of the volume of the Au particles by 60-80 % on the effect of Rh post-deposition. According to the analysis of the images, a simple attachment of Rh atoms landing on Au nanoparticles during evaporation can account for an increase in the volume of the Au particles by only 20-25 %. The unexpected enhancement of the average volume suggests that a fraction of rhodium atoms impinging on the free oxide surface in the vicinity of Au clusters is trapped by gold nanoparticles, while the rest of Rh forms separate rhodium clusters. Comparing LEIS and STM data, the increase in the Au LEIS peak indicates that a part of rhodium atoms evaporated on top of the gold clusters, moved to subsurface sites of gold particles. One plausible mechanism is place

exchange. Both thermal and non-thermal place exchange was previously observed, when Rh was deposited on Au(111) [13,14], resulting also in the, formation of subsurface Rh atoms, though the two metals are immiscible in bulk. Note that the surface energy of Au is much smaller than that of Rh. Alternatively, it seems probable that those rhodium atoms on the surface of gold clusters, which do not take part in place exchange can be covered by Au atoms diffusing on the cluster surface. Both mechanisms involve the incorporation of rhodium into the gold clusters and lead to an increase in the cluster diameter, and a concomitant enhancement in the Au LEIS signal.

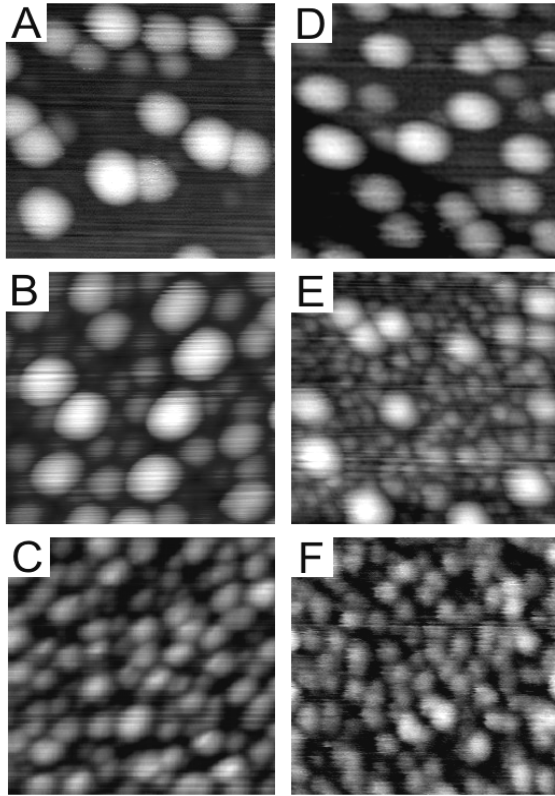


Fig.2: STM images recorded after deposition of (A) 0.6 ML of Au; (B) 0.6 ML of Au followed by 0.6 ML Rh; (C) 0.6 ML of Rh; (D) 0.6 ML of Au; (E) 0.6 ML of Au followed by 0.3 ML Mo; (F) 0.4 ML of Mo. The size of the images: 20 x 20 nm².

and STM techniques is very effective to explore the fine details of the supported bimetallic systems.

ACKNOWLEDGEMENT

Support by OTKA NI69327, K69200 and by the National Office for Research and Technology, Pázmány Péter Programme RET-07/2005 is gratefully acknowledged. In this scientific program plaid significant role the Hungarian Academy of Sciences.

REFERENCES

- [1] C.R. Henry: *Surf. Sci. Rep.*, **31**, 231 (1998) – and references therein
- [2] U. Diebold: *Surf. Sci. Rep.*, **48**, 53 (2003) – and references therein
- [3] Q. Fu, T. Wagner: *Surf. Sci. Rep.*, **62**, 431 (2007) – and references therein
- [4] J.A. Rodriguez: *Surf. Sci. Rep.*, **24**, 223 (1996)– and references therein
- [5] O.R. Inderwildi, S.J. Jenkins, D.A. King: *Surf. Sci.*, **601**, L103 (2007)
- [6] J.H. Larsen, I. Chorkendorff: *Surf. Sci. Rep.*, **35**, 163 (1999) – and references therein
- [7] L. Guzzi: *Catal. Today*, **101**, 53 (2005) – and references therein
- [8] A.M. Kiss, M. Svec, A. Berkó: *Surf. Sci.*, **600**, 3352 (2006)
- [9] L. Óvári, J. Kiss: *Appl. Surf. Sci.*, **252**, 8624, (2006)

- [10] F. Cosandey, T.E. Madey: Surf.Rev.Lett., **8**, 73 (2001)– and references therein
- [11] L. Bugyi, A. Berkó, L. Óvári, A.M. Kiss, J. Kiss: Surf. Sci., **602**, 1650 (2008)
- [12] S. Pétigny, B. Domenichini, H. Mostéfa-Sba, E. Lesniewska, A. Steinbrunn, S. Bourgeois: Appl. Surf. Sci., **142**, 114 (1999)
- [13] I. Chado, F. Scheurer, J.P. Bucher: Phys. Rev. B, **64**, 094410 (2001)
- [14] E.I. Altman, R.J. Colton: Surf. Sci., **304**, L400 (1994)
- [15] S. Curtarolo, D. Morgan, G. Ceder: Computer Coupling of Phase Diagrams and Thermochemistry, **29**, 163, (2005)
- [16] L.Z. Mezey, J. Giber: Jpn. J. Appl. Phys., **21**, 1569 (1982)



POSSIBLE USE OF METAL COMPLEXES OF POLYAMINOPOLYPHOSPHONIC ACIDS

Imre LABADI¹, Károly MOGYORÓSI¹, Ecaterina PRINCZ²

¹ University of Szeged, Department of Inorganic & Analytical Chemistry, Szeged, HUNGARY

² Institute for Chemistry of Timisoara of Romanian Academy, Timisoara, ROMANIA

Abstract

The development of nuclear resonance (NMR) imaging techniques as a clinical diagnostic modality has prompted the need of compounds, which enhance the image contrast between normal and diseased tissue and/or indicate the status of organ or blood flow. Complexes of paramagnetic transition metal and lanthanide ions with polyamino-polycarboxylic acids have been studied earlier in this respect in detail.

Owing to the structural similarities between the polyamino-polycarboxylic acids and polyamino-polyphosphonic acids, the lanthanide and transition metal complexes of the later ones were prepared and studied. The ethylenediamino-tetramethylene-phosphonic acid (EDTMP) and 1,3-propanediamine-tetramethylene-phosphonic acid (PDTMP) were chosen as ligand, and lanthanide ions (Eu(III), La(III), Gd(III), Sm(III)) or transition metal ions (Fe(III), Zn(II), Cu(II), Ni(II), Mn(II), VO(II)) used for preparation of metal complexes. The preparation of complexes were performed at different pH (pH= 1, 3 and 5). The composition of the complexes was determined by metal ion analysis and the complexes were studied by thermal analysis and IR spectroscopy.

The thermal behaviour of the transition metal complexes of EDTMP and PDTMP permit a suggestion for their use as a precursor compound to prepare different phosphate compounds, having interesting magnetic properties.

Keywords:

polyamino-polyphosphonates, lanthanide complexes, transition metal complexes, MRI agents, precursors for metal phosphates

1. INTRODUCTION

Throughout history, metals and metal compounds have been used in medicine to treat a variety of ailments. An even more recent development is the use of paramagnetic metal complexes for enhancing contrast of magnetic resonance imaging (MRI) in the non-invasive diagnostics of diseases and tumours. Paramagnetic metal ions function as contrast agents by increasing the relaxation rates of the observed water protons near the ion, through interactions between the electron spins of the paramagnetic centre and the nuclei of the water hydrogens [1–2].

Numerous complexes with polyaminopolycarboxylic acids have been studied as potential contrast agents [3–10]. The structural similarities between the polyamino-polycarboxylic and polyaminopolyposphonic acids determined the study of these ligands as chelating agents. Replacement of the carboxylic groups by organophosphonic acid groups determines the specific nature of the polyamino-polyphosphonic acids due to the presence of tetrahedral phosphonic group as compared to planar carboxylic group and greater polarisability of the PO bond [11, 12].

Our studies had been focused to the synthesis and characterization of some lanthanide and transition metal complexes with two of the polyamino-polyphosphonic acids (EDTMP, PDTMP), because exchange reactions between the lanthanide complexes used as contrast agents in MRI and end transmetalation by transition metal ions may place in the human body. By this way a dangerous free lanthanide ions could be appeared [13-14] and owing to

this phenomenon the use of lanthanide complexes of the EDTMP and PDTMP, as an MRI agents reagents, will forms a new problem.

An another practical importance of the polyamino-polyphosphonic acids and their metal complexes is the use of them as a precursor of different metalpolyphosphates. For instance in the last 10-20 years an increased interest could be observed against the new iron phosphates, pyrophosphates, alkali-iron phosphates- pyrophosphates as compounds having special magnetic properties. The metal complexes of polyamino-polyphosphonic acids were proofed as a candidate as precursors for preparation of the above mentioned metal phosphates, pyrophosphates[15].

In the present work the complexes of different lanthanide-, transition metal complexes of EDTMP and PDTMP were isolated from solution having different pH and their IR spectra and thermal stabilities were studied in order to determine their compositions, their stability and the binding mode of the water molecules in the complexes.

2. EXPERIMENTAL

Preparation of the ligands

The investigated polyamino-polyphosphonic acids (EDTMP and PDTMP) were synthesized by us via a Mannich reaction of 1,2-ethylenediamine or 1,3-propanediamine with phosphorous acid and formaldehyde, as described earlier [16, 17].

pK values of the ligands(EDTMP, PDTMP)

The protonation constants and the complex stability constants were determined by potentiometric titration [20]. The pK values of the ligands determine the possible composition of the metal complexes prepared at different pH and different ligand metal ratio. At low pH (1-3), 2-5 proton could be replaced by sodium and other metal-ion. At higher pH all proton could be replaced by sodium ion and different metal-ion.

Table 1.

pK values of the EDTMP and PDTMP (H₈L) determined by us [18].

The pK values of the EDTMP[] and PDTMP [18]

Ligand	pK ₁	pK ₂	pK ₃	pK ₄	pK ₅	pK ₆	pK ₇	pK ₈
EDTMP	<1	1.5	3.02	5.2	6.4	7.85	10.00	11.00
PDTMP	<2	<2	4.05	5.10	5.89	6.85	10.00	11.40

Preparation of the metal complexes

The preparation of the complexes was performed as followings:

The ligands (EDTMP and PDTMP) was mixed with the appropriate metal nitrate or acetate in ratio 1:1, 1:2 and the pH of the solution was adjusted by adding sodium hydroxide solution. The formed precipitate was filtered, washed, dried and stored in exsiccator. The metal-ion and sodium contents of the complexes were determined.

The composition of the complexes

The composition of the investigated complexes is shown in Table 2. Comparing the pK values of the ligands and the pH values of the preparation of the complexes, the gained composition of the complexes could be interpret easily.

Table 2.

The general composition of the investigated metal complexes of EDTMP and PDTMP[18,19]

Ligand (L)	Composition	Metal ions (M)
EDTMP	M ₄ (H ₄ L) ₃ xH ₂ O	La(III), Sm(III)
EDTMP	MH ₅ L xH ₂ O	La(III), Sm(III)
EDTMP	MNa ₅ L xH ₂ O	La(III), Sm(III)
PDTMP	MNa ₅ L xH ₂ O	Eu(III), La(III), Gd(III), Sm(III)
EDTMP PDTMP	MH ₅ L xH ₂ O, MNa ₂ H ₃ L xH ₂ O MNa ₅ L xH ₂ O	Fe(III)
EDTMP, PDTMP	MH ₆ L xH ₂ O M ₂ H ₄ L xH ₂ O	Co(II), Ni(II), Zn(II), Cu(II), VO(II)

The IR spectra of the ligands and of the metal complexes

The characteristic bands of the ligands are presented in Table 3-4.

Table 3

Characteristic bands of EDTMP and their assignation [18]

Band maximum(cm ⁻¹)	Assignation
3402s, 3246s	v(OH, water)
3026s,3014s	v(≡NH ⁺)
2954s, 2924vs, 2854s	v _{as} and v _{sym} of CH ₂
2767m, 2611m, 2308m	v (OH, POH)
1653m, broad	δHOH
1461m, 1438m, 1413w, 1379, 1321w	δCH ₂ or/and v(C-N)
1261s,1207s, 1121vs,1008vs, 953vs	v (P=O, P-O(H))
838w, 792w, 776w,748w	v(C-P)
573m, 532m, 487m	v (OH, POH)

Table 4

Characteristic bands of PDTMP and their assignation [19]

Band maximum(cm ⁻¹)	Assignation
3372s	v(OH, water)
3024s,3005s	v(≡NH ⁺)
2950s, 2921vs, 2849s	v _{as} and v _{sym} of CH ₂
2773m, 2612m, 2288m	v (OH, POH)
1657m, broad	δHOH
1485m, 1437m, 1411w, 1344	δCH ₂ or/and v(C-N)
1248s,1167s, 1050s, 980s, 944s	v (P=O, P-O(H))
838w, 792w, 776w,748w	v(C-P)
602m, 585m, 548m, 512m, 482m	v (OH, POH)

The IR spectra, characteristic bands of metal complexes changed, related to the IR spectra of the ligands, showing the formation of complex between the metal ion and ligands [18, 19].

3. THE THERMAL BEHAVIOUR OF THE EDTMP, PDTMP AND THEIR METAL COMPLEXES

Both the EDTMP and PDTMP ligands have 2 water molecules, as a crystal water, which release the solid material on heating in two steps (below 150 °C and between 150 and 200 °C, 1.5 and 0.5 mole water, respectively) [16,17].

The thermoanalytical studies of the metal complexes of EDTMP, PDTMP show that the complexes of EDTMP, PDTMP contain two types of water molecules. This fact is very important from point of view of possible medicinal use of these complexes.

From the thermal decomposition of the metal complexes of EDTMP, PDTMP several conclusions could be drawn:

1. One of the final decomposition products is the metal-pyrophosphate, sodium-pyrophosphate.
2. The free OH groups of the EDTMP, PDTMP losses water molecules on heating, so they form polyphosphates with different composition and probably with different structure.

REFERENCES

- [1] D. E. Reichert, J. S. Lewis and C. J. Anderson, Coord. Chem. Rev., 184 (1999) 3
- [2] L. Thunus, and R. Lejeune, Coord. Chem Rev. 184 (1999) 125
- [3] R.B. Lauffer : Chem. Rev., 87 (1987) 901.

- [4] L.Thunus, R.Lejeune: *Coord.Chem.Rev.*, 184(1999) 125.
- [5] S. Aime, M. Botta, M. Fasano, E. Terreno, *Chem. Soc. Rev.*, 27 (1998) 19.
- [6] R. Ruloff, R. N. Muller, D. Pubanz, A. E. Merbach, *Inorg. Chim. Acta*, 275-276 (1998) 15.
- [7] S. Jurisson, D. Berning, Wei Jia and Dangshe Ma: *Chem. Rev.*, 93 (1993) 1137.
- [8] A. N. Pudovik: *Chemistry of Organophosphorus Compounds*, MIR Publishers, Moscow, 1983, 150
- [9] K. Sawada, T. Miyagawa, T. Sahaguchi, K. Doi, *J. Chem. Soc. Dalton Trans.*, 1993, 3777.
- [10] L. V. Ruzajkina, B. A. Rjabuhin, A. N. Jermakov, I. N. Marov, L. S. Davidova, E. B. Krutko, *Zh. Neorg. Khim* **25** (1980) 3254
- [11] I.V. Tananaiev, E.N. Bereznev, G. S. Terjosin, O. B. Kuznecova, L.V.Goeva, *Zh. Neorg.Khim.*,26(1981) 278-280
- [12] T.S. Terjosin, L.K Gharitonova, N. N. Novikova, M. V. Rudomino, *Zh. Neorg. Khim* 22(1977) 2115
- [13] M. I. Kabachnik, N. M. Djatlova, T. Ya. Medvegy, Yu. F. Belugin, V. V. Sidorenko, *Dokl. AN* **175** (1967) 351
- [14] B. V. Zhadanov and N. M. Djatlova, *Zh. Fiz. Khim* 48 (1969) 744
- [15] Z. Rzacynska and A. Bartyzel, *J. Therm. Anal. Cal.* 68 (2002) 937
- [16] N. Palta, B. V. Rao, S. N. Dubey and D. M. Puri; *Polyhedron* 3 (1984) 527.
- [17] E.N. Rizkalla, *Rev. Inorg. Chem.* 5 1983(2231
- [18] E. Princz, I. Szilágyi, K. Mogyorosi and I Labadi, *J. Therm. Anal. and Calorimetry* 69(2002), 427-439
- [19] E. Printz, K. Mogyorosi and I. Labadi, *J. Thermal Anal. and Calorimetry* 77 (2004) 767-776
- [20] I. Labadi to be published



DEGRADATION OF PURE AND WASTE PVC AND PET IN THE PRESENCE OF MODIFIED POROUS CATALYSTS

János HALÁSZ, Kinga VŐNEKI, Judit KRAJKÓ

Department of Applied and Environmental Chemistry,
University of Szeged, Rerrich tér 1, H-6720 Szeged, HUNGARY

ABSTRACT

The catalytic degradation of pure and mixed polymers such as poly-(vinylchloride) (PVC) and poly-(ethylterephthalat) (PET) was followed by thermal analytical method (TA) and was performed in a laboratory batch system (LBS) using modified ZSM-5, MCM-41 and hydrotalcites based catalysts. In degradation of PET, the acidic H-ZSM-5 resulted in less liquid products and more gaseous components than the other, transition metal containing catalysts. The degradation of PVC takes place in two steps, the first is the departure of HCl at about 300 °C followed by formation of aromatic hydrocarbons. Minimal residue could be obtained over Fe,Mg,Al-hydrotalcites and mixed oxide catalyst. From the results obtained it can be concluded that not only the catalyst structure but also the polymer structure determines the activity of a micro- or mesoporous material in the catalytic degradation of plastics or plastic wastes. Therefore, different optimal conditions (catalyst and reaction temperature) can be applied for each plastics studied (pure, mixed and waste) in thermal treatment.

Keywords:

plastic pyrolysis, porous catalysts, degradation, polymer waste, PVC, PET

1. INTRODUCTION

The total amount of plastic wastes generated by our society is growing rapidly. The main source of plastic is the municipal solid waste. Plastics contained in the municipal solid wastes can be estimated about 10% of total waste by weight and the amount goes up to 20% when consider in volume. The low biodegradability of different plastics creates a serious environmental problem that is directing the governments and environmental organizations and enterprises to propose a hierarchy to solve the problem of plastic wastes based on source reduction re-use and recycling. Up to now and considering the case of European Union only ~10 wt.% of plastic wastes have been recycled, while ~73 wt.% have gone to landfills and ~17 wt% have been incinerated [1].

While incineration can be used to recover the waste as energy, the loss of a potential chemical source and negative public acceptance limit the extend of this solution. If we accept that landfill storage is not a rational solution and can only be considered as provisional, then one is left with the most desired primary and secondary waste recycling. The primary recycling however, are limited to pure thermoplastics, therefore secondary technologies used for treatment of mixed plastic wastes is of growing importance. In this way plastic wastes are converted into monomers, fuels or valuable chemicals for petrochemistry [2].

Traditional thermal cracking, i.e. pyrolysis can be applied to transform both thermoplastics and thermosets into gases, liquid hydrocarbons and solid residue [3]. Thermal cracking and hydrocracking have been studied at laboratory and pilot plant level, and some commercial installation have been built for treatment of mixed plastic wastes, even those containing chlorine [4]. However, thermal cracking yields low value unstable hydrocarbons within a very broad range of molecular weight. Catalytic degradation can operate at lower temperatures and can produce products with better quality (much narrower boiling point distribution and much higher stability) [5].

A large number of laboratory studies have been conducted for direct catalytic degradation of polymers, especially for pyrolysis of polyolefins, however, there are a lot of study deal with the degradation of PET and PVC. A high variety of catalysts have been used that even if performing well, they can be uneconomical due to the price of catalyst and to the high energy demand. Among the catalysts studied acidic zeolites and mesoporous materials performed special activity in the temperature range of 300-500 °C [6-10].

The objective of this work is to study the potential of modified ZSM-5 zeolite, MCM-41 mesoporous silica, hydrotalcites (HD) and HD originated mixed oxides as catalysts for degradation of PET and PVC using thermal analytical measurements and laboratory reactor experiments.

Table 1: Properties of catalysts

Prepared catalyst sample	Structure (XRD, IR, TEM)	BET surface area, m ² /g
CaCO ₃ *	-	3.3
CaO*	-	1.5
Na-ZSM-5	ZSM-5	360
H-ZSM-5	ZSM-5	385
Fe-ZSM5	ZSM-5	346
Cu-ZSM-5	ZSM-5	352
Ni-ZSM-5	ZSM-5	370
Fe-MCM-41	MCM-41	890
Ti-MCM-41	MCM-41	1010
Cr-MCM-41	MCM-41	960
Mg-Al-LDH	hydrotalcite	20
Fe-Mg-Al-LDH	hydrotalcite	25
Cr-Mg-Al-LDH	hydrotalcite	12
Cu-Mg-Al-LDH	hydrotalcite	32
Ca-Mg-Al-LDH	hydrotalcite	16
Mg-Al-MO	Mg- + Al-oxide	40
Fe-Mg-Al-MO	Mg- + Al- + Fe(III)-oxide	42
Cr-Mg-Al-MO	Mg- + Al- + Cr(III)-oxide	50
Cu-Mg-Al-MO	Mg- + Al- + Cu(II)-oxide	27
Ca-Mg-Al-MO	Mg- + Al- + Ca-oxide	21

*commercial product (MOLAR RT, Hungary)

2. EXPERIMENTAL SECTION

Catalysts

The catalyst samples were prepared in our laboratory except CaCO₃ or CaO (MOLAR RT, Hungary).

The synthesized Na-ZSM-5 zeolite was modified by conventional or solid state ion-exchange to form H-, Fe-, Cu-, Ni- and Ti-ZSM5 samples [11].

The Ti- or Fe-MCM-41 specimen was prepared from sodium silicate, CTMA-Br and Ti(SO₄)₂ or Fe(NO₃)₃ solution at pH 12 [12]. The crystallization was carried out at 373 K for 2 days followed by calcination at 823 K for six hours.

The Fe/Al/Mg-hydrotalcite (M^{II}/M^{III} = 2, and M^{III}: 0.9 Al and 0.1 Fe) was prepared by coprecipitation at constant pH = 10 ± 0.2 of an aqueous solution of Mg(NO₃)₂, Al(NO₃)₃ and Fe(NO₃)₃ with a solution of NaOH and Na₂CO₃ [13].

The structure of the catalysts was characterized by X-ray diffraction, IR-spectroscopy and transmission electron microscopy, their thermal stability was followed by thermal analytical method. The specific surface area and pore size distribution of the samples were determined by nitrogen adsorption isotherms.

The properties of the samples have corresponded to the data of literature. The physical characteristics of the catalysts used are shown in Table 1.

Methods

Commercial plastics: HDPE, PP, PET and PVC in granulate form have been used as model feed. The degradation of pure polymers was followed using either by utilizing of thermoanalytical method (*MOM Derivatograph Q, Hungary*) or in a laboratory batch reactor system with gaschromatographic product analysis (*Shimadzu GC2010, Japan*).

3. RESULTS AND DISCUSSIONS

TG experiments

The TG analysis for pure PET - as it is shown in Fig. 1 - proves a relatively sharp, one steep weightloss with a maximum in the DTG curve placed at 480 °C. This behavior corresponds with the thermal degradation of this polyester of narrow molecular mass distribution. Figures 2 and 3 show TG analysis of PET/H-ZSM5 and PET/Ti-MCM41 catalyst mixture with 10 % catalyst content.

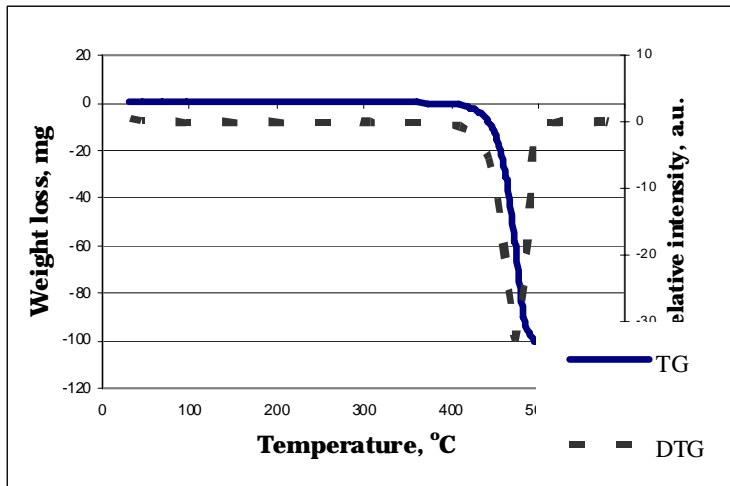


Figure 1: Thermal analytical study of PET degradation without catalyst

In the case of the PET/catalyst mixture it is clearly observed that the polymer degradation takes place at a quite lower temperature, due to the polymer catalytic cracking. In the presence of this catalyst, the weight loss starts at temperatures between 400 and 425 °C, indicating that a significant reduction occurs in the threshold temperature compared to the pure thermal degradation (with DTG maxima as characteristic temperature at 485 and 480 °C, respectively). Moreover, clear differences could be observed in regards to this temperature among the catalysts; the data can be seen in Table 2.

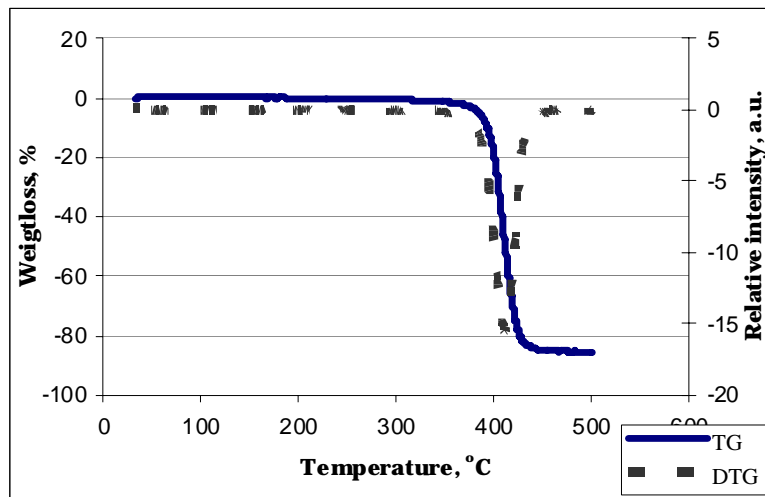


Figure 2: Thermal analytical study of PET degradation over H-ZSM-5 catalyst

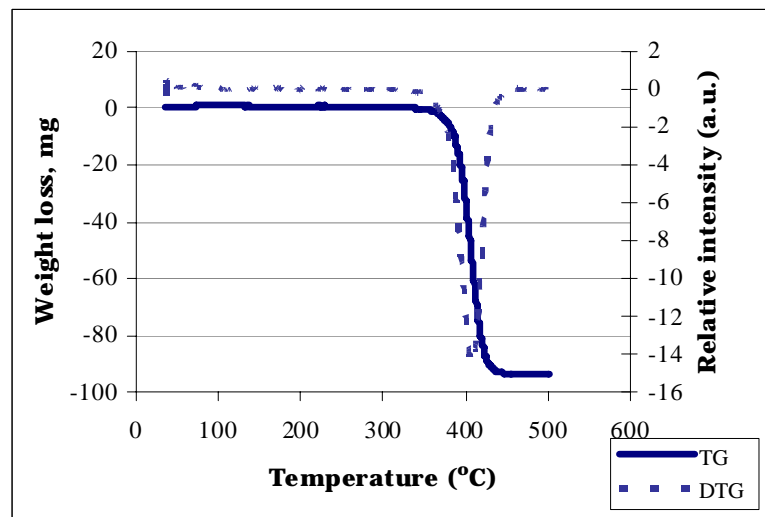


Figure 3: Thermal analytical study of PET degradation over Ti-MCM-41 catalyst

The difference of the PET and the PVC in the catalytic degradation can be seen in Figs. 4 and 5. The decomposition of PVC takes place at least in two steps, the first is due to the release of HCl with ~ 300 °C characteristic temperature, the second peak corresponds to the pyrolysis of the residual hydrocarbon framework (440 - 470 °C temperature range).

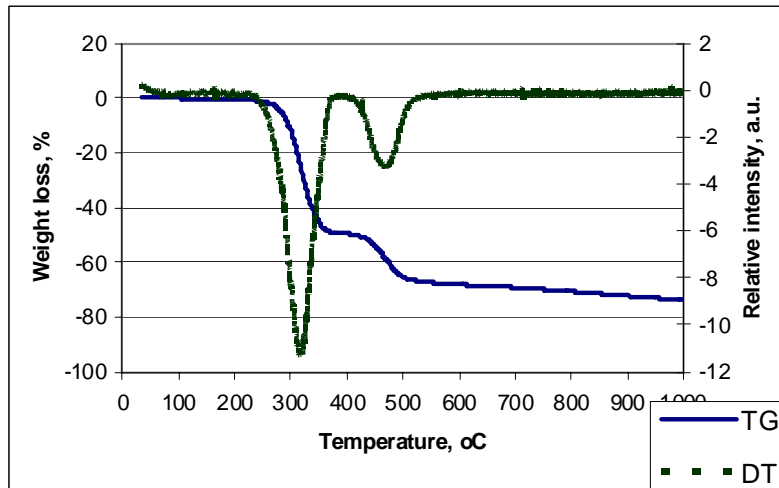


Figure 4: Thermal analytical study of PVC degradation over Fe-ZSM-5 catalyst

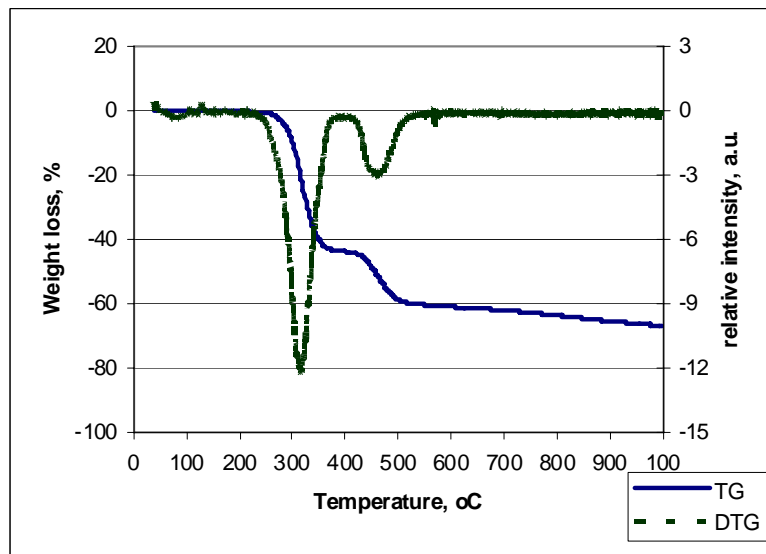


Figure 5: Thermal analytical study of PVC degradation over Ti-MCM-41 catalyst

Table 2: Characteristic temperature of plastic decomposition (DTG peak maxima)

Catalyst	DTG peak maximum, °C	
	PET	PVC*
none	473	320, 478
CaO	-	310, 459
CaCO ₃	-	313, 460
Na-ZSM-5	465	316, 470
H-ZSM-5	412	313, 423
Fe-ZSM-5	423	310, 452
Cu-ZSM-5	-	312, 460
Ti-ZSM-5	-	305, 456
Fe-MCM-41	461	269, 443
Ti-MCM-41	458	275, 450
Mg,Al-oxide	452	281, 475
Fe,Mg,Al-oxide	447	292, 471
Cr,Mg,Al-oxide	445	310, 456
Cu,Mg-Al-,oxide	456	304, 442
Ca,Mg,Al-oxide	-	290, 445

*for PVC two peaks can be identified to characteristics

4. CATALYTIC DECOMPOSITION OF PET AND PVC IN THE BATCH REACTOR

Considering the solid residual (in mass %) determined at 400 °C at the end of the reactions (after two hours) could be calculated the nominal conversion and the relative amounts of gaseous (crack), liquid (oil) and solid (residue) products. These data can serve for characterization of the process and there are collected in Table 3. In the case of PVC the amount of HCl collected in a trap with NaOH solution can be seen in this Table, as well.

Table 3: Conversion of plastic decomposition in the different catalysts at 400 °C

	PET				PVC				
	conv.	crack %	oil %	resi- due %	conv.	crack %	oil %	resi- due %	HCl %
none	0.853	23.1	36.7	40.2	0.726	3.0	28.5	58.5	72.9
CaO	-	-	-	-	0.894	4.5	52.8	42.7	36.6
CaCO ₃	-	-	-	-	0.896	6.3	55.7	38.0	27.4
Na-ZSM-5	0.733	18.7	43.4	37.9	0.872	6.8	36.4	43.2	76.8
H-ZSM-5	0.882	55.5	22.7	21.8	0.875	43.7	33.8	22.5	53.5
Fe-ZSM-5	0.836	23.4	46.7	29.9	0.965	30.1	44.2	25.7	63.9
Ti-ZSM-5	0.874	34.6	43.2	22.2	0.909	24.2	46.1	29.7	52.9
Fe-MCM-41	0.756	32.6	46.6	20.8	0.889	11.4	56.9	32.7	62.9
Ti-MCM-41	0.873	28.5	44.4	27.1	0.842	16.8	44.9	38.3	65.8
Mg,Al-oxide	0.740	32.0	35.2	32.8	0.936	10.1	62.7	27.2	37.3
Fe,Mg,Al-oxide	0.943	20.3	47.5	32.2	0.843	16.6	54.7	28.7	65.6
Cr,Mg,Al-oxide	0.866	37.1	42.4	20.5	0.912	21.3	60.1	18.6	60.3
Cu,Mg,Al-oxide	0.857	26.2	56.4	17.4	0.886	-	-	-	-
Ca,Mg,Al-oxide	0.953	-	-	-	0.826	-	-	-	-

The H-ZSM-5 catalyst possessing strong acid sites resulted in less liquid products and more gaseous components than the other, transition metal containing catalysts. These results are in agreement with the fact that acidic sites catalyze the degradation/cracking of heavier hydrocarbons.

The Cl balance can be calculated from the relative amount of HCl, and it is clearly seen that the basic catalysts react with the HCl formed in the pyrolysis. This reaction could result in the deactivation of the catalyst, however, its importance is the possible mineralization of chlorine.

The effect of the temperature for the reaction of PET in the presence of Al-Mg-oxide catalyst can be seen on Fig. 6. On higher temperatures the formation of gaseous products are preferential.

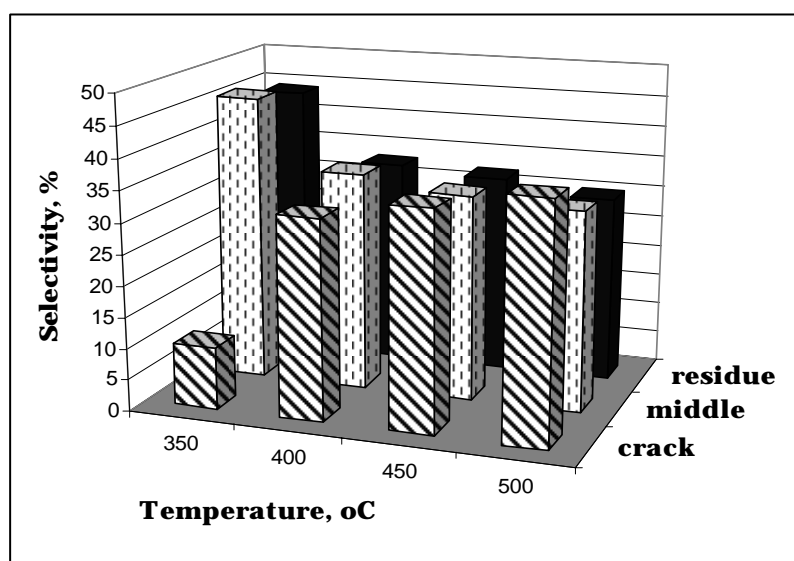


Figure 6: Product distribution in PET degradation at different temperatures in the presence of Al-Mg-oxide catalyst

5. CONCLUSIONS

For PET degradation the non-acidic Na-ZSM-5 and the Fe-ZSM-5 samples product liquid hydrocarbons with yields about 90 % which is higher than that of non-catalytic thermal degradation. while the H-ZSM-5 sample enhances the formation of low molecular weight (gaseous) products.

The catalytic degradation of PVC takes place at least in two steps: the first one is the leaving of HCl. In this reaction. The catalysts with basic character (CaO, CaCO₃, hydrotalcites and Mg-Al-mixed oxides) have definite activity, principally due to the stabilization of the system by the reaction with the releasing HCl.

From the results obtained it can be concluded that not only the catalyst framework but also the polymer structure determinate the activity of porous materials in the catalytic degradation of plastic wastes. The polymer chain ends are able to penetrate into the pore system of the catalyst, reaching the active sites into the channel system.

Polymer with aromatic ring. i.e. PET show lower activity in the case of catalysts with smaller pore sizes (ZSM-5). By other hand, the higher pore size resulted in higher initial reactivity, but the coke deposition was improved in the catalysts of large pores, can lead to a fast deactivation.

Acknowledgement

This work was supported by the Hungarian National Office of Research and Technology (NKTH) and the Agency for Research Fund Management and Research Exploitation (KPI) under contract no. RET-07/2005.

REFERENCES

- [1] S.C. Cardona and A. Corma, *Kinetic study of the catalytic cracking of polypropylene in a semibatch stirred reactor*, Catal. Today., 75, 239-246 (2002).
- [2] M. Azhar-Uddin, Y. Sakata, A. Muto, Y. Shiraga, K. Koizumi, Y. Kanada and K. Murata, *Catalytic degradation of polyethylene and polypropylene into liquid hydrocarbons with mesoporous silica.*, Micropor. & Mesopor. Mater., 21, 557-564 (1998).
- [3] I.H. Metcan, A.R. Ozkan, R. Isler, J. Yanik, M. Saglam and M. Yuksel, *Naphtha derived from polyolefins*, Fuel, 84, 619-628 (2005).
- [4] Q. Zhou, C. Tang, Y-Z. Wang and L. Zheng, *Catalytic degradation and dechlorination of PVC-containing mixed plastics via Al-Mg composite oxide catalysts*, Fuel 83, 1727-1732 (2004).
- [5] A. Marcilla, A. Gomez, S. Menargues and R. Ruiz, *Pyrolysis of polymers in the presence of a commercial clay*. Polymer Degrad. and Stab., 88, 456-460 (2005).
- [6] B. Saha and A.K. Ghoshal, *Thermal degradation kinetics of poly(ethylene terephthalate) from waste soft drinks bottles*, Chem. Engin. J., 111 (2005) 39-43.
- [7] S.C. Cardona and A. Corma, *Tertiary recycling of polypropylene by catalytic cracking in a semibatch stirred reactor, Use spent equilibrium FCC commercial catalyst*, Appl. Catal. B: Environ., 25, 151-162 (2000).
- [8] J. Halász, Z. Kónya, Z.T. Faragó, K. Siegert and I. Kiricsi, *Degradation of pure and waste polyolefins and PVC in the presence of modified porous catalysts*, Stud. Surf. Sci. Catal., 174, 1021-1026 (2008).
- [9] C. Tang, Y.-Z. Wang, Q. Zhou and L. Zheng, *Catalytic effect of Al-Zn composite catalyst on the degradation of PVC-containing polymer mixtures into pyrolysis oil*, Polymer Degrad. Stab., 81, 89-94 (2003).
- [10] D. Braun, *Recycling of PVC*, Prog. Polym. Sci., 27, 2171-2195 (2002).
- [11] J. Varga, Á. Fudala, J. Halász, G. Schöbel and I. Kiricsi, *ZSM-5 zeolites modified by solid-state ion-exchange for NO decomposition*, Stud. Surf. Sci. Catal., 94, 665-672 (1995).
- [12] D. Méhn, Z. Kónya, J. Halász, J. B.Nagy, B. Rác, Á. Molnár and I. Kiricsi, *Flexibility of the MCM-41 structure: A novel way to catalyst design and production*, Applied Catal. A: General, 232, 67-76 (2002).
- [13] F. Cavani, F. Trifirio and A. Vaccari, *Hydrotalcite-type anionic clays: Preparation. properties and applications*, Catal. Today, 11, 173-301 (1991).



STEAM REFORMING OF ETHANOL ON ALUMINA SUPPORTED NOBLE METAL CATALYSTS

Márta DÖMÖK, Kornélia BAÁN, István SARUSI,
Albert OSZKÓ, András ERDŐHELYI

Institute of Solid State and Radiochemistry,
University of Szeged, H-6701 Szeged, HUNGARY

ABSTRACT

The increasing demand for alternative energy sources drew a great attention to the steam reforming of ethanol to produce H_2 . From environmental point of view the use of ethanol is preferred because it can be readily produced from renewable biomass

Recently it has been found that supported noble metals are active catalysts of H_2 production in the ethanol reforming. It was found that while the selectivity of hydrogen decreased in time, the formation of ethylene increased parallel to it on all alumina supported noble metals at 723 K. This trend was resumed by increasing the following parameters: water concentration, metal loading and reaction temperature. By means of infrared spectroscopy and TPD measurements it was found that after the ethanol adsorption not only different types of ethoxy species but significant amount of adsorbed CO and acetate group were present on the surface. The latter species were stable even above 700 K. During the reaction at 723 K not only acetate but adsorbed CO was found. It is surprising to detect CO well above its desorption temperature. It means that the formation rate of the CO is higher than its desorption or further reaction rate.

It was presumed that the surface acetate species bonded mainly to the support. In spite of the location of these species we stated that the surface acetate hindered the reaction to hydrogen on the metal.



DIODE LASER BASED PHOTOACOUSTIC INSTRUMENT FOR AMMONIA CONCENTRATION AND FLUX MONITORING

A. POGÁNY⁽¹⁾, Á. MOHÁCSI⁽²⁾, Z. GALBÁCS⁽⁴⁾, T. WEIDINGER⁽⁶⁾,
L. HORVÁTH⁽⁵⁾, A. VARGA⁽³⁾, Z. BOZÓKI⁽²⁾, G. SZABÓ⁽¹⁾

⁽¹⁾Department of Optics and Quantum Electronics, University of Szeged, HUNGARY

⁽²⁾Research Group on Laser Physics of the Hungarian Academy of Sciences, HUNGARY

⁽³⁾Hilase Developing, Producing, Servicing and Trading Ltd.,

⁽⁴⁾Department of Inorganic and Analytical Chemistry, University of Szeged, HUNGARY

⁽⁵⁾Hungarian Meteorological Service Budapest, HUNGARY

⁽⁶⁾Lorand Eotvos Univ, Dept Meteorol, Budapest, HUNGARY

ABSTRACT

A diode laser based near infrared (1532 nm) photoacoustic ammonia monitoring instrument was combined with a preconcentration unit in order to reach sub-ppb detection limit with a compact, automatic measuring instrument. The system has no measurable cross-sensitivity to common atmospheric gases, most importantly to water vapor and carbon dioxide. The minimum detectable amount of ammonia is 2.9 ng, which means a minimum detectable concentration of 0.5 ppb with a 30-minute measurement time. The instrument was calibrated with the widely accepted, wet-chemical AMANDA instrument, and was tested in several inter-comparison campaigns with various instruments. Results of the inter-comparison campaigns show that the instrument is highly reliable even under harsh field conditions and accurate enough for environmental ammonia concentration monitoring. The instrument can be operated with three sampling inlets and thus can be used for ammonia flux measurements with the gradient method. The instrument was successfully tested in a measurement campaign on an agricultural field near a cattle farm, the purpose of which was to quantify ammonia load to the field originating from the cattle farm, taking use of the wide dynamic range of the instrument. In a second campaign, long term flux measurements were carried out for several months above semi-natural grassland, where the stability of the instrument was tested. In this campaign, ammonia emission was observed during the day (with a typical maximum of about 220 $\mu\text{gN}/\text{m}^2\cdot\text{h}$) and deposition during the night (-10 $\mu\text{gN}/\text{m}^2\cdot\text{h}$ on average), and the measured flux values were within the theoretically estimated range.

Keywords

ammonia, concentration, flux, photoacoustic spectroscopy, preconcentration

1. INTRODUCTION

Ammonia is the most important alkaline gas in the troposphere, therefore plays a crucial role in atmospheric acid-base chemistry. Increased ammonia load might alter the pH of soil and water and thereby damage sensitive ecosystems. Besides this, ammonia is the third-most abundant nitrogen-containing compound in the atmosphere, which means that higher amounts of ammonia mean an increased nitrogen load and might cause eutrophication. Furthermore, ammonia contributes to atmospheric fine aerosol formation, through its reactions with sulfur and nitrogen oxides, and effect global radiation budgets and has adverse effects on human health.

Due to the above mentioned facts, ammonia is considered as an air pollutant; however its importance has been discovered only recently. The Gothenburg Protocol of the UN Convention on Long-Range Transboundary Air Pollution in Europe was the first international convention regulating ammonia emissions.

Besides its concentration, fluxes of ammonia are also important from the environmental point of view, since this provides information about the direction and magnitude of ammonia exchange between the atmosphere and biosphere.

Several ammonia monitoring instruments have been developed in the past few decades, however, none of them is ideal for long-term ammonia flux monitoring in the field, therefore developing ammonia monitoring instrument remains an unsolved problem.

We have developed a compact, automatic instrument based on diode laser based photoacoustic spectroscopy, combined with chemical preconcentration of the sampled air, which ensures the high sensitivity and selectivity. The instrument can be supplemented with more sampling inlets which make it suitable for flux measurements based on gradient methods.

2. EXPERIMENTAL

We have combined a near-infrared diode laser based photoacoustic ammonia monitoring system described in Ref. 1 with preconcentration sampling (Ref. 2). The instrument can be supplemented with more sampling inlets and therefore used in flux measurements. The main characteristics of the instrument are the following: detection limit of 0.5 ppb, time resolution between 5 and 30 minutes, no measurable cross sensitivity to water vapor, carbon dioxide and aerosol particles, compact design and capability of unattended, automatic operation.

3. RESULTS

Long term ammonia flux measurements were carried out with the instrument in Bugac, above semi-natural grassland in the Hungarian Great Plain. A cattle farm is located near the monitoring station that causes relatively high ammonia concentration during the day.

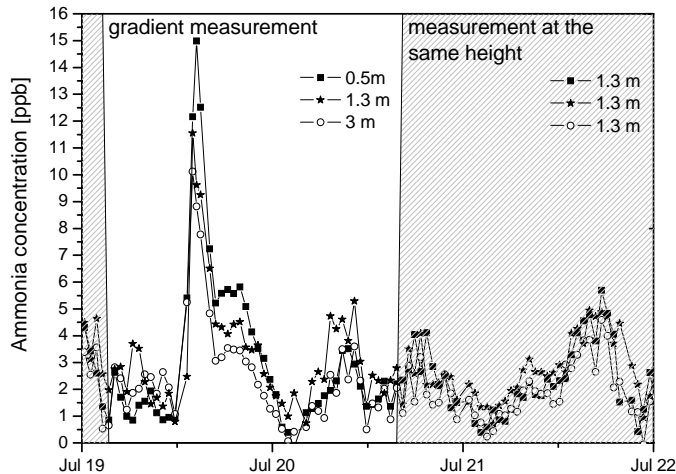


Figure 2: Ammonia concentration measured by the three inlets of the photoacoustic instrument in Bugac. Shading indicates when all three inlets were placed at the same height

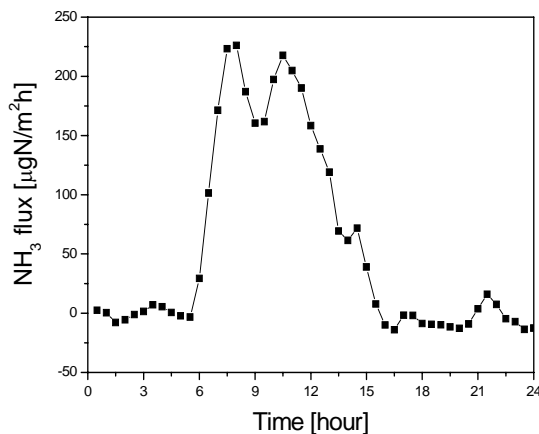


Figure 3: Average daily variation of ammonia flux, calculated from the measurement data from three different heights for the period between 2nd July and 5th October, 2008

Figure 2 shows a 3-day part of the measurements. White area indicates when the three sampling inlets of the instrument were placed at 0.5, 1.3 and 3 m, respectively for gradient measurements. Shading indicated when the inlets were brought to a common height (1.3 m) for self-checking and determination of correction factors if necessary. The Figure shows that in case of gradient measurements higher concentrations were observed closer to the ground, which indicates emission of ammonia.

Ammonia fluxes were calculated from the concentration data measured at three different heights using the aerodynamic gradient method. Fluxes were averaged to determine the average daily variation of the ammonia flux. Figure 3 shows this daily variation for the period 2nd July – 5th October, 2008.

The Figure shows that ammonia is emitted during the day and weakly deposited during night. The net balance of ammonia is positive, the site is an emission source of ammonia, which is a result of the nearby cattle farm.

4. CONCLUSION

We have developed a novel ammonia monitoring instrument that is suitable for measuring ammonia concentration at three different heights simultaneously. The obtained data can be used for ammonia flux calculation based on the gradient method. Several months of test measurements show that the instrument is well suited for long-term environmental monitoring.

REFERENCES

- [1] Helga Huszár, Andrea Pogány, Zoltán Bozóki, Árpád Mohácsi, László Horváth, Gábor Szabó: Ammonia monitoring at ppb level using photoacoustic spectroscopy for environmental application. *Sensors and Actuators B*. 1027-1033 134 (2008).
- [2] A. Pogány, Á. Mohácsi, A. Varga, Z. Bozóki, Z. Galbács, L. Horváth, G. Szabó A compact ammonia detector with sub-ppb accuracy using near-infrared photoacoustic spectroscopy and preconcentration sampling *Env. Sci. Technol.* 826-830, 43 (3), 2009
- [3] www.photoacoustics.hu



DEMONSTRATION OF THE APPLICABILITY OF NOVEL PHOTOACOUSTIC AEROSOL MONITOR FOR OPTICAL ABSORPTION COEFFICIENT DETERMINATION – LABORATORY AND FIELD TEST

T.AJTAI ⁽¹⁾, M. SCHNAITER ⁽²⁾, C. LINKE ⁽²⁾, M. VRAGEL, Á. FILEP ⁽¹⁾,
LAJOS FÖDI ⁽¹⁾, GÁBOR MOTIKA ⁽⁴⁾, Z. BOZÓKI ⁽³⁾, G. SZABÓ ⁽¹⁾

⁽¹⁾ Department of Optics and Quantum Electronics, University of Szeged, HUNGARY

⁽²⁾ Institute of Meteorology and Climate Research, forschungszentrum Karlsruhe, GERMANY

⁽³⁾ Research Group on Laser Physics of the Hungarian Academy of Science,
University of Szeged, HUNGARY

⁽⁴⁾ Lower Tisza Valley Environmental Inspectorate, Szeged, HUNGARY

ABSTRACT

Despite of its importance, the possibilities to determine the direct radiative forcing by atmospheric aerosols is very limited due to lack of the reliable on-line instruments. Therefore there is an increasing concern for novel methods promising more accurate and reliable results in this field. The accuracy and reliability of the available on-line instruments like SP2 (Single Particle Soot Photometer), MAAP (Multi Angle Absorption Photometer), are limited by the weakness of the spectral resolution or the sampling artefact of filter matrix during the light attenuation measurement on the deposited filter. These methods neither suitable for direct determination of the light absorption by aerosols nor dispose the capability of the source apportionment.

In this work we present a novel photoacoustic based instrument for direct light absorption measurements in the atmosphere and demonstrate the suitability of that both in laboratory and field circumstances.

We have developed a novel Multi Wavelength PhotoAcoustic System (WaSul-MuWaPas) based on the diode laser pumped, high repetition rate, Q-switched Nd:YAG laser and its frequency converted harmonics for direct determination of light absorption by aerosols.

This instrument has designed to make *in situ* measurements at four different wavelengths simultaneously from the NIR to the UV wavelength range (1064nm, 532nm, 355nm, 266nm). The Wasul-MuWaPas measures directly the optical absorption coefficient on airborne particles, not belong to the integrated plate type technique (filter-free operation), operating at wide wavelength range (source apportionment possibilities), due to the possibilities of the wavelength independent cell constant determination the measurement method is absolute. Because of these the Wasul-MuWaPas system may become one of the best candidates for absorption measurements of various atmospheric aerosols such as black carbon, mineral dust, and secondary organic and inorganic aerosols as well as for source apportionment studies.

The present system was successfully tested both under the laboratory and field circumstances. The results of these studied, demonstrated here, is shown excellent agreements with reference methods and presents the main characteristic performances of the system verifying the potential of Wasul-MuWaPas to characterizing the spectral properties of atmospheric aerosols.

These researches were funded by Hungarian Ministry of Economy and Transport NKFP_07_A4_AEROS_EU.



ENVIRONMENTAL IMPACTS OF NITRATE AND NITRITE

Gábor NAGY¹, Zoltán GALBÁCS¹

¹Department of Inorganic and Analytical Chemistry, University of Szeged
H-6720 Dóm tér 7, Szeged, HUNGARY

Abstract:

The natural nitrogen cycle is significantly influenced by the human activity – principally by agriculture and transport. The excessive fertilizing, the organic matter content of sewage waters, and the emission of nitrogen oxides to the atmosphere – caused by vehicles and industrial activities – are unsettling the biosphere's nitrogen balance. The anthropogenic nitrogen surplus in soils, water bases and atmosphere means great problem, and its indirect effect is observable in our environment and daily life. Nitrite and nitrate pollutions are important and serious risks in spite of being relegated to the background in global environmental protection.

Keywords:

nitrate, nitrite, fertilizer, eutrophication, methemoglobin

1. SIGNIFICANCE OF NITROGEN

The nitrogen is present in the environment in many various forms and considerable amount. Nitrogen compounds are especially important from environmental, ecological and physiological aspect because they are indispensable constituents of e.g. proteins, nucleic acids or humus; they can be found in the atmosphere, in soils or in any living organism. The wide interval of nitrogen's oxidation state (-3 - +5) indicates the high number of the – essential, toxic, neutral or anthropogenic - components nitrogen can form. Among these numerous compounds nitrate and nitrite mean significant environmental risk and can cause long-term natural damages.

2. THE NITROGEN CYCLE

The elemental nitrogen of the atmosphere – because of its inert structure – highly resists chemical reactions; hence the most of organisms are disable to use it for biological processes. Only some microorganisms (e. g. Rhizobium, Azotobacter, Clostridium) can fix and convert nitrogen to accessible form for plants (ammonia, ammonium). Ammonia is oxidized by Nitrosomonas and Nitrococcus bacteria to nitrite which is converted to nitrate by Nitrococcus and Nitrobacter species during the nitrification process. These nitrogen forms are also available for the flora. Nitrogen compounds of organic residues are converted to ammonia in the course of ammonification then nitrified as well. A part of nitrite/nitrate content of the soil is returned to the atmosphere as elemental nitrogen and dinitrogen oxide by the activities of e.g. Pseudomonas, Paracoccus species (denitrification) (Figure 1).

Accordingly the presence of nitrate and nitrite in the soil is evident; these forms are the main nitrogen sources of plants and indirectly animals and mankind too. However natural nitrogen cycle is significantly influenced by human activities – principally by traffic and agriculture. The biosphere's nitrogen balance is affected by the overfertilizing, the high organic matter content of sewage or nitrogen oxide emissions of traffic and industry. Anthropogenic nitrogen surplus in the soils, water bases and atmosphere are both sources of environmental problems; the impact to the nature is clearly noticeable.

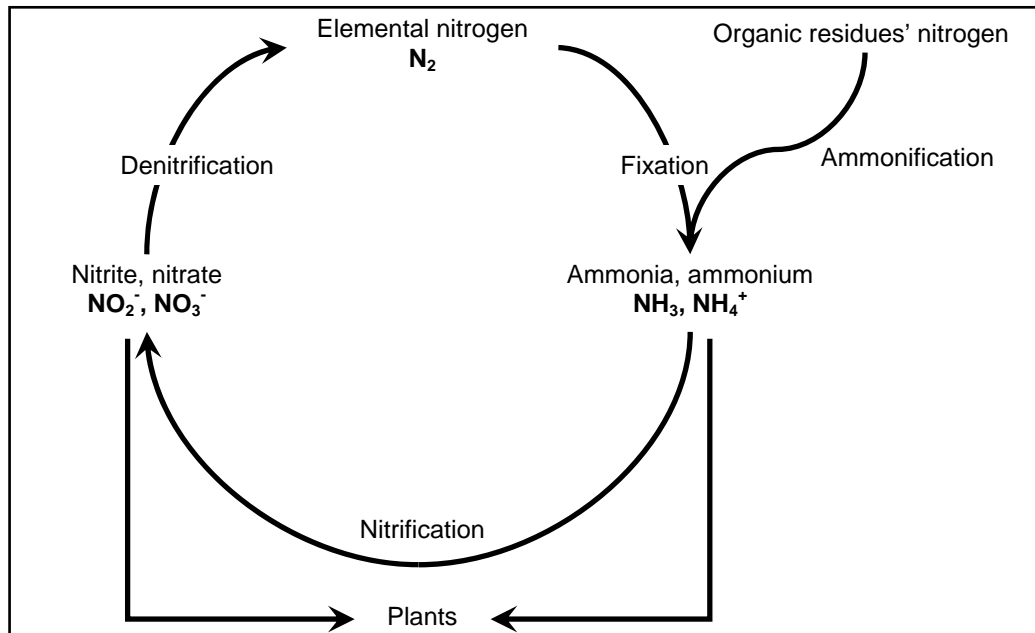


Figure 1. The nitrogen cycle

3. FERTILIZERS

Usually the nutrient content of soils does not correspond with the demands of cultivated plants; hence fertilizers are basic materials in nowadays' agriculture to increase the crop yields. However added nutrients influence the ion mobility and chemical attributes in soils and the components of soil water, the considered and responsible application of fertilizers not necessarily endangers the environment. Besides proportional nutrient supply can be ensured for the plants with fertilizers, some soil parameters can be optimized, such as alkalinity or structure.

However the irresponsible usage of fertilizers can entail serious environmental and financial risks; incorrect dosaging can disturb the existing balance of nutrients, can cause the elements' immobilization and might reduce the product's quality and yield. Soil accepts and stores nutrients only in limited rate; if it is encumbered with fertilizers beyond this limit, nutrients will concentrate in the soil solution, soil water will be polluted and even salt accumulations will evolve. The surplus of organic matter might reach the drinking water bases by erosion, leaking of groundwater or surface runoff and threatens their quality and causes eutrophication.

Nitrogen fertilizers can be especially harmful because of their possibly high solubility; leaching rate of fertilizers' nitrogen content can reach 80% depending on weather, characteristics of soil, amount of fertilizer and vegetation.

Further risk of soil's high nitrogen level is the nitrate accumulation in vegetables. Under optimal circumstances organic acids – derived from oxidation of carbohydrates – form amino acids with ammonia enzymatically reduced from nitrate. These amino acids are essential components of vegetal proteins. If the nitrogen metabolism suffers disturbance, biosynthesis of proteins will slow down and nitrates and amino acids will accumulate in the plant organism. The accumulated nitrate can worsen the vegetable's tissue attributes, lasting and even its taste. High nitrate levels can be measured in e.g. lettuce, kohlrabi, radish, colewort and spinach.

4. NITRATE IN WATERS

Eutrophication of surface waters is caused by increased organic matter content – basically nitrogen and phosphorus compounds – originated from sewage or leaking from fertilized agricultural areas. Great amount of nutrients offsets the balance between photosynthesis and plant breathing: the water's oxygen concentration rises and the flora

starts to proliferate. The multiplied species of fitoplanctons and algae further increase the nutrient amount of water however during their degradation processes the water's dissolved oxygen resource is consumed. Finally the lack of oxygen leads to almost complete disappearance of flora and fauna, decreasing biodiversity and the water loses its self-cleaning capability (Figure 2). Under natural conditions eutrophication occurs much more slowly (e.g. lake succession); the intensive organic matter input significantly speeds up the process.

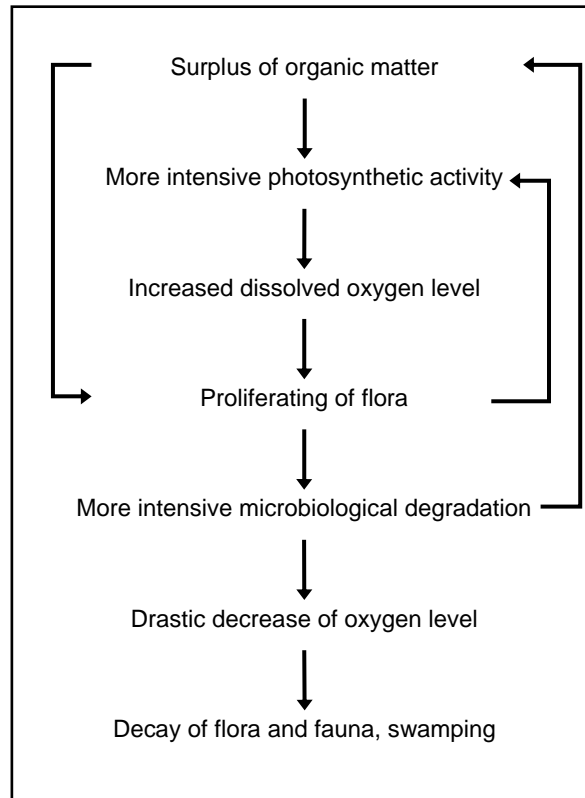


Figure 2. Process of eutrophication

High nitrite and nitrate content means direct risk where drinking water is supplied from polluted water bases. Leaked to groundwater, nitrogen compounds of fertilizers endanger the water quality of drilled wells and other water sources. The amount of nitrate ions stays unchanged during the conventional water cleaning processes; hence the nitrate content of consumed water is equivalent with the water base's.

5. NITROGEN COMPOUNDS AS AIR POLLUTANTS

Besides elemental nitrogen other nitrogen compounds are formed in the course of denitrification that harm the atmosphere. The gas phase losses of fertilizers can get to the atmosphere as nitrogen oxides (e.g. N_2O , NO_x) and take part in generating acid rains and tropospheric smog and thinning ozone layer. The great amount of organic matter can make the denitrification more intensive and considerable part of the fertilizer's nitrogen amount can get in the air. Flue gases are main sources of these types of air pollutions; the magnitude of fertilizer's impact is minor, but confirmed and not negligible.

6. NITRATES AND NITRITES IN FOODS

Nitrite and nitrate get in foods partly as a result of not suitable producing or handling processes and partly as additives. Food industry applies nitrite and nitrate components (e.g. E249 – KNO_2 , E250 – $NaNO_2$, E251 – $NaNO_3$, E252 – KNO_3) primarily with conservation purpose. Most of meat products contain added nitrate and/or nitrite preventing appearance of pathogen microorganisms and ensuring the bright color of the meat. As mentioned, some vegetables' nitrate content can be high as well such as dairy products, cheeses, wines or flour.

7. PHYSIOLOGICAL EFFECTS

Nitrate and nitrite content of foods and drinking water can induce various medical problems – however most of these components usually leave human organism fast and without evolving any deleterious effect. Nitrite – reduced from nitrate mainly in stomach and small intestine – can transform to nitrous acid that oxidizes the ferro-ion of hemoglobin and causing methemoglobinemia. In the case of methemoglobinemia blood's oxygen carrying capability decreases and even death can occur. Under normal circumstances 1-2% of human organism's hemoglobin is present in methemoglobin form; if this scale is about 10% symptoms of languor and concentration disturbance will be observable; 50% of methemoglobin is lethal. Nitrite poisoning is really rare in adult population because a special

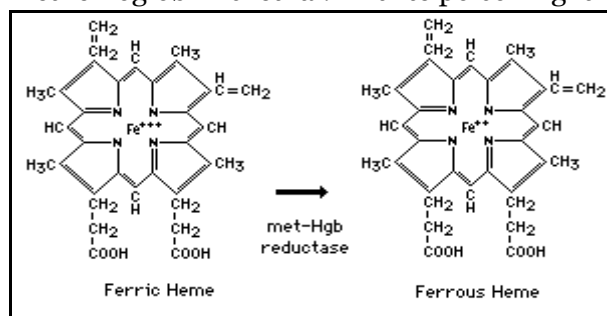


Figure 3. Structure of hemoglobin and methemoglobin [6]

enzyme transforms back the methemoglobin to hemoglobin (Figure 3); however babies are highly endangered because in early age the methemoglobin reductase is not working adequately yet. Therefore the babies' nutrients and drinking water must not include nitrate or nitrite in even trace amount because in lack of medical help anoxic state (“blue baby” disease) is probably deadly.

Another problem related with nitrite presence is the formation of nitrosamines and nitrosamides. These carcinogen N-nitroso compounds are particularly evolved in the acidic media of stomach through reactions of amides and amines with nitrite [2].

8. REGULATIONS

Because of the above environmental and physiological dangers controlling the nitrate and nitrite emissions and monitoring their concentration in foods and waters is important and required. Regulations, decrees and limit values exist to avoid the unnecessary, dangerous or harmful application of these compounds. The directives and regulations of the EU assign fertilizing parameters, limit values for drinking waters, vegetables, meat products etc., and lay emphasis on the protection of nitrate sensitive regions (areas where nitrates can easily reach drinking water bases). Unfortunately national rules not always correspond to the international requirements.

9. CONCLUSIONS

Fast and effective solving of environmental problems caused by anthropogenic nitrite and nitrate is difficult task because of its complexity. The only long-term solutions seem to be the reasonable fertilizing and the adequate wastewater treatment. The environmental and medical risk can only be reduced with controlled emissions and international co-operation. Nitrate and nitrite pollutions are critical however often hidden problems of nowadays that should be taken much more serious.

REFERENCES

- [1] Attila Kerényi, Általános környezetvédelem – globális gondok, lehetséges megoldások, Mozaik Oktatási Stúdió, 1998
- [2] Ghibu G. D., Balint M., Garban Z., Investigations concerning the effects induced by the presence of nitrites and nitrates in the feed of rabbits, Proceedings of the 14th Symposium on Analytical and Environmental Problems, 2007
- [3] N. T. Faithfull, Methods in agricultural chemical analysis, Cabi Publishing, 2002
- [4] R. F. Follett, J. L. Hatfield, Nitrogen in the environment: sources, problems and management, Elsevier, 2001
- [5] Pál Stefanovics, Talajvédelem, környezetvédelem, Mezőgazdasági Kiadó, 1981
- [6] <http://www.med-ed.virginia.edu/courses/path/innes/images/rcdgifs/enzyme3.gif>



NITRATE IN TOBACCO - ANOTHER SOURCE OF DANGER OF SMOKING

Gábor NAGY¹, Zoltán GALBÁCS¹

¹Department of Inorganic and Analytical Chemistry, University of Szeged
H-6720 Dóm tér 7, Szeged, HUNGARY

Abstract:

Despite of the well-known health-damaging consequences, 40-45% of Hungarian adult population is smoking. Numerous publications reported presence of NO_x gases in tobacco smoke [1, 2] that can be transformed to destructive nitric acid in the human organism. The origins of these dangerous gases are the nitrogen compounds of vegetal proteins or – in other opinions – nitrates and nitrites from oxidizer additives. We determined the nitrate content of different types of cigarettes and detected 5-30 mg nitrate in 1 gram tobacco. It is doubtful how nitrate is generated into cigarettes because it is not included on the list of the licensed tobacco additives [3].

Keywords:

nitrate, additive, tobacco, cigarette

1. INTRODUCTION

Tobacco smoke is very complex mixture with over 4000 identified constituents – included lots of hazardous – harmful, toxic, carcinogen and mutagen – compounds. NO_x gases are one fraction of these compounds and by transforming to nitric acid during the burning process they can cause serious injury in the tissues of the lungs and in other mucous membranes. We tried to verify that the sources of these NO_x gases are – at least partly – nitrates and nitrites. We determined nitrate content of 20 different tobacco products according to the Hungarian standards' colorimetric methods [4].

2. MATERIALS AND METHODS

Each sample was made from one cigarette's tobacco amount (~0.5-0.6 g) that was mixed with 20 cm³ distilled water at 300 revolutions per minute then filtered with paper filter. Ideal soaking time (5 minutes) was measured by sharing the tobacco content of a single cigarette to about 0.1 g portions (Figure 1.) because of the relatively high differences between nitrate concentrations of the cigarettes from same box (Figure 2).

The nitrate measurements are based on the reaction of sodium salicylate and nitric acid (issued from the reaction of nitrate and cc. sulphuric acid) that results a yellow nitro-compound of which's absorbance is proportional to nitrate concentration in the sample. During the procedure after 1 cm³ 0.03 M sodium salicylate was added to 5 cm³ of the sample, water was evaporated on water bath at 95°C. The dry residual was wetted with sulphuric acid, and after 10 minutes the solution was diluted with 30 cm³ distilled water, finally the medium was alkalinized with 7 cm³ 10 M sodium-hydroxide. Then the volume was completed to 50 cm³ with distilled water and in one hour we measured the absorbance of the solution spectrophotometric at the wavelength of 410 nm. The exact nitrate concentrations were read from a calibration graph, recorded with different concentrations of potassium nitrate solutions (Figure 3).

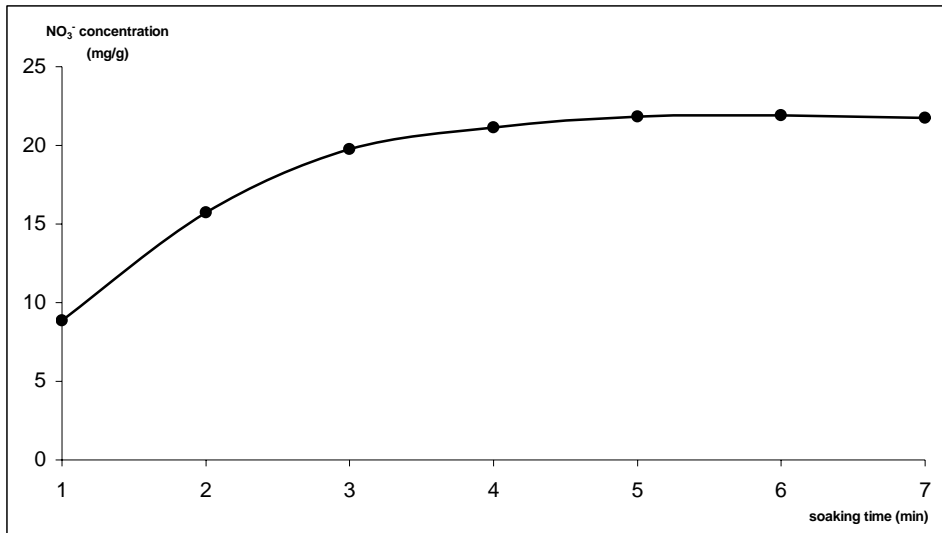


Figure 1. Changing of tobacco’s nitrate content in relation of soaking time (Bond Street, red) – the tobacco content of a single cigarette was shared to 7 portions (~0.1 g).

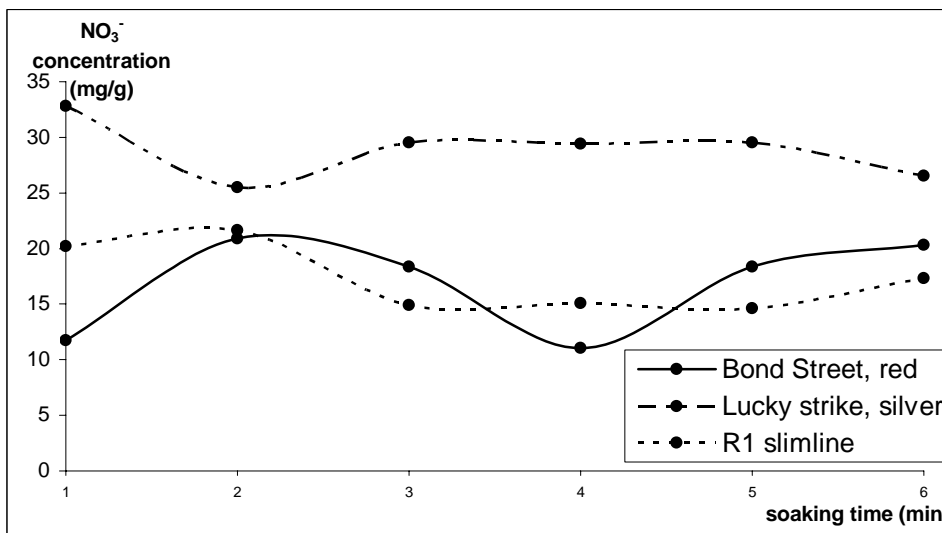


Figure 2. Changing of tobacco’s nitrate content in relation of soaking time – samples were made of entire tobacco content of 6 cigarettes of same brand.

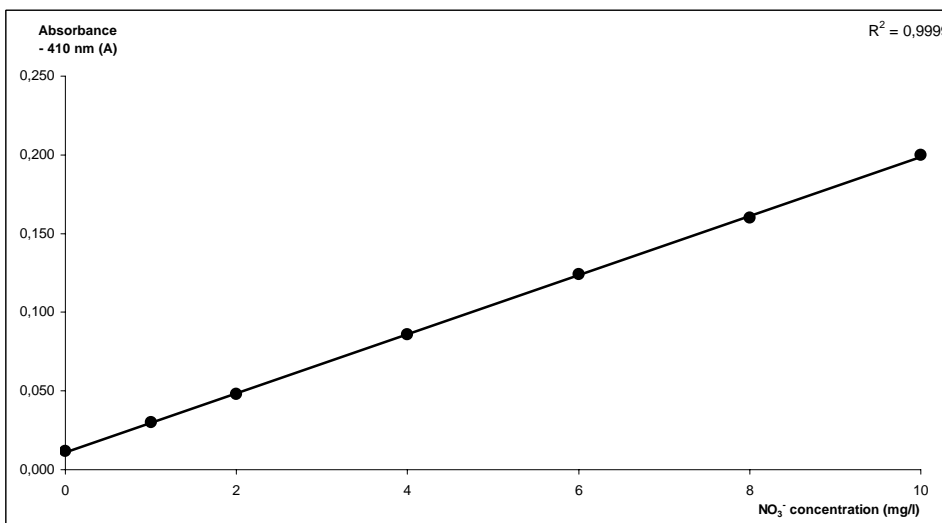


Figure 3. Calibration graph of nitrate determinations

3. RESULTS

However results varied between comparatively wide limits (6.1-29.5 mg/g), presence of nitrate was general; nitrate was detected in every examined tobacco product. One cigarette's average content was 10 mg nitrate. Concentrations of cigar and pipe tobaccos were similar to the cigarettes' results. The results are summarized in Figure 4.

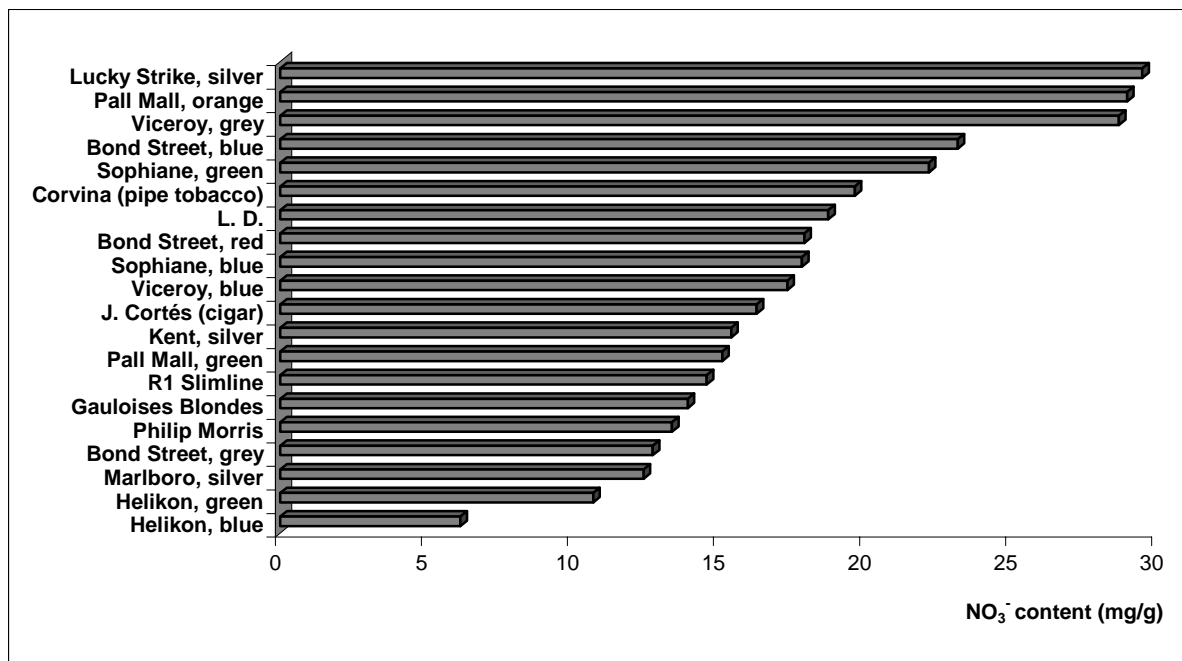


Figure 4. Nitrate content of tobacco products

4. CONCLUSIONS

Both nitrate accumulation (as a consequence of chemical fertilizing) and burning booster additives (e.g. potassium nitrate) are possible sources of the tobacco products' nitrate content. The second assumption seems to be confirmed by the fact that nitrate concentration of tobacco solution is permanent after 5 minute of soaking; nitrate content of the vegetal cell can not be solved so fast without some kind of cell destructive mechanism. This inference can be justified if we examine the nitrate content of the cigarettes from the same box: the high differences (~30%) can be explained with the unbalanced distribution of the oxidizer nitrate compounds sprayed on tobacco leaves or added to the pickle. Considering the above it is very notable that nitrate compounds are not included in the list of permitted additives of tobacco products [3].

REFERENCES

- [1] Dr. Zoltán Galbács, Dr. Norbert Buzás, Dr. Gábor Galbács, Erika Kosik, A dohányfüst káros anyagai, A kémia tanítása 6/1-2, 1998
- [2] Dr. Zoltán Galbács, Dr. Gábor Galbács: Chemical aspects of the dangers of cigarette smoke, Central European Journal of Occupational and Environmental Medicine 8/2-3, 2002
- [3] FVM-ESzCsM-GKM együttes rendelet a dohánytermékek gyártásáról, forgalmazásáról és ellenőrzéséről, 86/2003. (VII. 24.)
- [4] Hungarian standard, MSZ 448/12-82



ROCK EVAL PYROLYSIS AS A TOOL FOR CHARACTERIZATION OF ORGANIC MATTER IN SOIL SAMPLES

Tünde NYILAS¹, Marianna IMRE²

¹Department of Mineralogy, Geochemistry and Petrology, Faculty of Science and Informatics, University of Szeged, HUNGARY

²Department of Geology and Paleontology, Faculty of Science and Informatics, University of Szeged, HUNGARY

Abstract:

Rock-Eval (RE) pyrolysis was designed for petroleum exploration to determine the type and quality of organic matter in rock samples. The aim of our work was to present new fields of application of the RE pyrolysis for assessing the proportion of the organic components of different thermal stabilities, and also to apply this method for characterization of organic matter dynamics in polluted sediments, soil and paleosol profiles.

Keywords:

Rock-Eval pyrolysis, organic matter dynamic, paleosol

1. INTRODUCTION

The geological organic matter is present in the atmosphere, in the water, in the soil, in the recent sediments and in the rocks equally. Organic matter of sediment rocks is studied comprehensively, but we have less knowledge from geochemical of organic matter in soils and recent sediment, although it should be justified because of mass and the important role in the global carbon cycle.

SOM plays a significant role in the CO₂ content of atmosphere and in controlling of global earth temperature. Wearing-away of rocks and pedogenesis processes are influenced by SOM. Adsorption characteristic of organic matter in soils and recent sediments determine the mobility of organic and inorganic pollution thus effects the quality of water in surface and groundwater.

SOM is not homogenous but is a mixture of many organic matters with different chemical compositions and physical qualities. This chemically and kinetically heterogeneous material comprises a mixture of plant and microbial residues of various compositions and with different decomposition rates, as well as their transformation products, in addition to refractory, long-residence-time macromolecular organic substances (kerogen, black carbon). Humification of biopolymers is determined by those environmental parameters (relief, climatic conditions), which define soil types too.

RE pyrolysis was designed for petroleum exploration to determine the type and quality of organic matter in rock samples. Nevertheless, this technique can be used for bulk characterization of the immature organic matter in soil samples and recent sediments.

Either aim of our work was to examine the soil conditions of an archeological site. This study is restricted to introduction of new investigation methods in paleosol examination, using the example of the Neolithic archeological site. For determination of the original soil type of the examined area we adopt sedimentological, micromorphological and pedological investigations as a first step. For supplement this we made an attempt to apply a new method for characterization the soil organic matter.

2. MATERILAS AND METHODS

Samples were collected from the A and B horizons of chernozem braun forest soil from West-Hungary and we analyzed buried paleosoil samples from an archeological site from North-Eastern Hungary. The development of the soil horizon was finished in the Neolithic Age, when the soil was covered so the evolution of the soil horizon broke off. After this period the soil transformed a transition form of soil and sediment. Accordingly reconstruction the original type of the soil is possible only by complex analysis.

We described the soil profile, measured the content and distribution of grain size, the content and relative proportion of organic matter and carbonate. For sedimentological analysis the composition and distribution of grain size we applied Micromeritics SediGraph 5000ET X-ray sedimentograph. Applied method for measure content of organic matter and carbonate was Dean-method the “loss on ignition” [1]. The measured parameters were depicted on profile diagrams for evaluation purposes.

The Rock Eval data of the soil samples were determined with Delsi Oil Show Analyzer (Hetényi et al., 2005). The following parameters can be obtained from one single measurement: **S1** amount of thermovaporized free hydrocarbons - present in the rock as free or adsorbed compounds - expressed in mg HC/g of rock. **S2** the current potential of a rock sample, represents the total amount of oil and gas a source rock can still produce during subsequent complete thermal maturation in an open system. (expressed in mg HC/g of rock). **T_{max}** the temperature (°C) which is recorded for the maximum of the S2 peak varies as a function of the thermal maturity of the organic matter. **TOC** (total organic carbon) content (expressed in weight %) is defined as the sum of the pyrolysed organic carbon content and organic carbon residue content. **HI** (hydrogen index) is defined as carbon normalized S2 and expressed in mg HC/gTOC. **PI** (production index) S_1/S_1+S_2 .

The experimental conditions of Rock-Eval pyrolysis were chosen that all of the hydrocarbonaceous compounds yielded by soil organic matter are recorded as one single peak. Pyrograms of our samples can be described by a combination of four elementary Gaussian components: F1, F2, F3 and F4. These four components are related to major classes of organic constituents differing in origin and their resistance to pyrolysis: labile biological constituents (F1), resistant biological constituents (F2), immature non-biotic constituents (F3) and a mature refractory fraction (F4). F1/F2 ratio illustrate the relative evolution of the two “bio-macromolecule” classes. The $\log[(F1+F2)/F3]$ index quantify the degradation of immature OM [2].

3. MATHEMATICAL DECONVOLUTION

In an immature organic matter, like soil, a wide range of components may be present simultaneously and each of them is represented by a Gaussian curve on the pyrogram (S2 peak) with characteristic mean (M) and standard deviation (σ) values. Each pyrogram is a complicated overlap of several normal distributions curves. In order to define discrete components of the multicomponent mixture, the pyrogram has to be decomposed mathematically. The well-known normal distribution curve is symmetric to the mean having one inflexion point on each side. A composite curve, may exhibit complicated shape with several inflexion points along it. It can be assumed, that in case of this special class of composite curves a mean value of at least one component falls within the interval of the two smallest inflexion points. This feature was utilized during the recursive decomposition algorithm applied in the project.

The first step is smoothing the originally rough pyrogram using moving average method. Moving the window and calculating the means over the whole temperature range result in a smooth data distribution of equal density. After several loops a 5°C interval was found large enough to get pyrogram without unrealistic peaks and ditches.

In the second step of the procedure numerical derivation was fulfilled twice to get the inflexion points of the smoothed composite curve. Without using an effective smoothing algorithm, there is no chance to get inflexions of real meaning. Afterwards, the two smallest inflexion points ($T_{i,1}$, $T_{i,2}$) were chosen, which surround the mean (M_i) in question. In the next

step a two-dimensional search of (M_i, σ_i) was carried out using a Monte Carlo type simulation by computing numerous data pairs so that

$$M_i \in (T_{i,1}, T_{i,2}), \text{ and} \quad (1)$$

$$\sigma_i \in (1/(S2T_{i,1}\sqrt{2\pi}), 1/(S2T_{i,2}\sqrt{2\pi})), \quad (2)$$

where $S2T_{i,j}$ denotes $S2$ values at $T_{i,j}$ temperatures.

Finally, each (M_i, σ_i) pair was used for calculating model $S2$ curves, and a least square best-fit algorithm is applied to get the best M_i and σ_i among them. Best model curve is determined when ε is minimized so that

$$\varepsilon = \sum (S2_{\text{observed}} - S2_{\text{calculated}})^2, \quad (3)$$

where summation goes from 180°C up to $T_{i,1}$ in each case.

After subtracting the model curve from the original $S2$ composite curve, the process was repeated recursively to the residuum from the second step (numerical derivation) [3].

RESULTS AND DISCUSSION

T_{max} values of approximated Gauss curves belong three category: original biopolymers (180-340°C), partially decomposed biopolymers (340-420°C), humic substances (420-600°C). Calculated values are in accord with measured series of stepwise Rock-Eval analyses. Consequently, we can estimating the poportion of original biopolymers well.

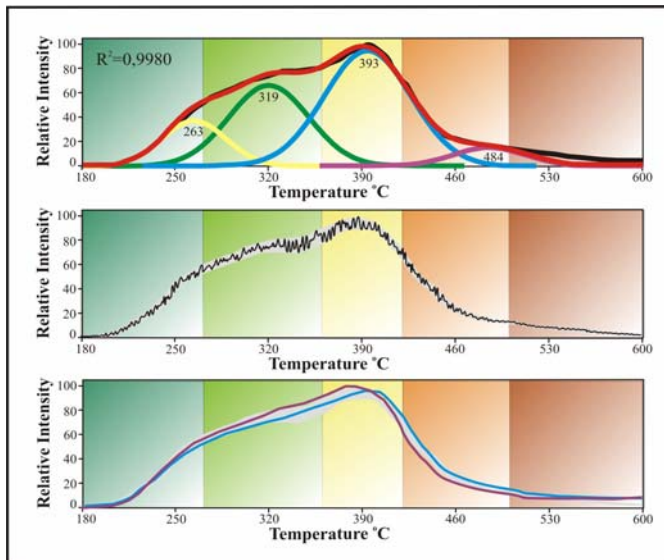


Figure 1. Steps of SOM “fingerprint” analysis

stripe what is the typical “fingerprint” of the SOM in question. We examined four chernozem-brown forest soil samples. We accepted that the unknown sample belongs into the specified soil type if it’s pyrogram concide 90% with the soil type’s envelope (Fig. 1). This method should be suitable for define soil type of „unknown” samples [4].

On buried soil’s study we have to pay attention to the processes which passes off after the coverage of soil. Soil life breaks off; ventilation stops or decreases and the accumulated sediments increase the pressure. These processes are able to change the original properties of the soil therefore only time-independent, steady-state characteristics are adequate for pedological-morphological description. These are texture, type of soil structures, fabric and porosity. We applied Rock-Eval Pyrolysis to get new details of soil organic matter, which can indicate the soil type. Mathematical decomposition of the $S2$ peaks was used to determine the rate of partially decomposed biopolymers, humic substances. The rate of organic carbon accumulation and decomposition rate of biopolymers were interpreted as function of environmental effects.

We use a modified application of Rock-Eval pyrolysis approach for estimating the proportion of the components with different thermal stability and the measure of humification. On a pyrogram each unique organic matter is represented by a normal distribution curve with characteristic mean and standard deviation. As a consequence, a pyrogram is a sum of numerous single Gauss curves what can be decomposed using a proper algorithm. In order to calculate possible composite curves, first the uncertainty of mean and standard deviation of RE measurement was determined by 20 independent runs. On this basis using a Monte Carlo type simulation 1000 different realizations were calculated. The envelope of all these curves defines the

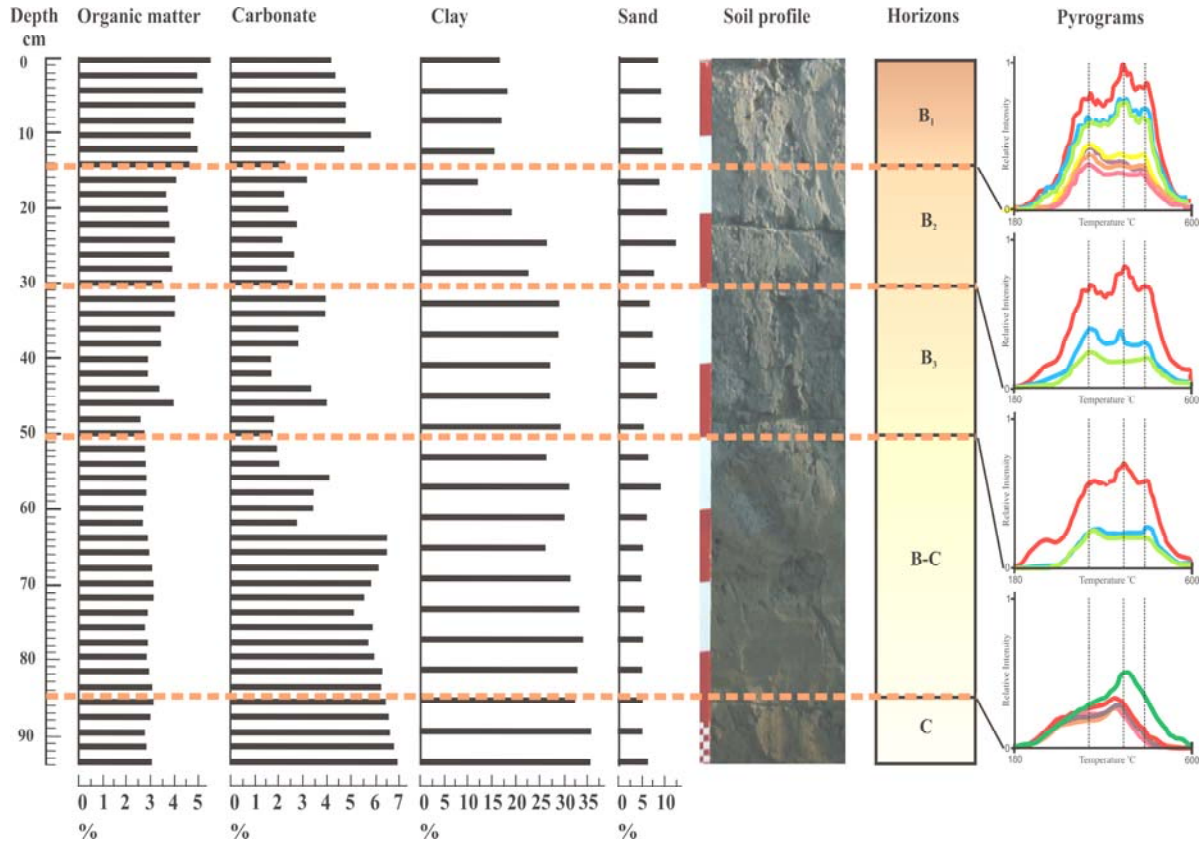


Figure 2. Profile of the monolith and the measured parameters

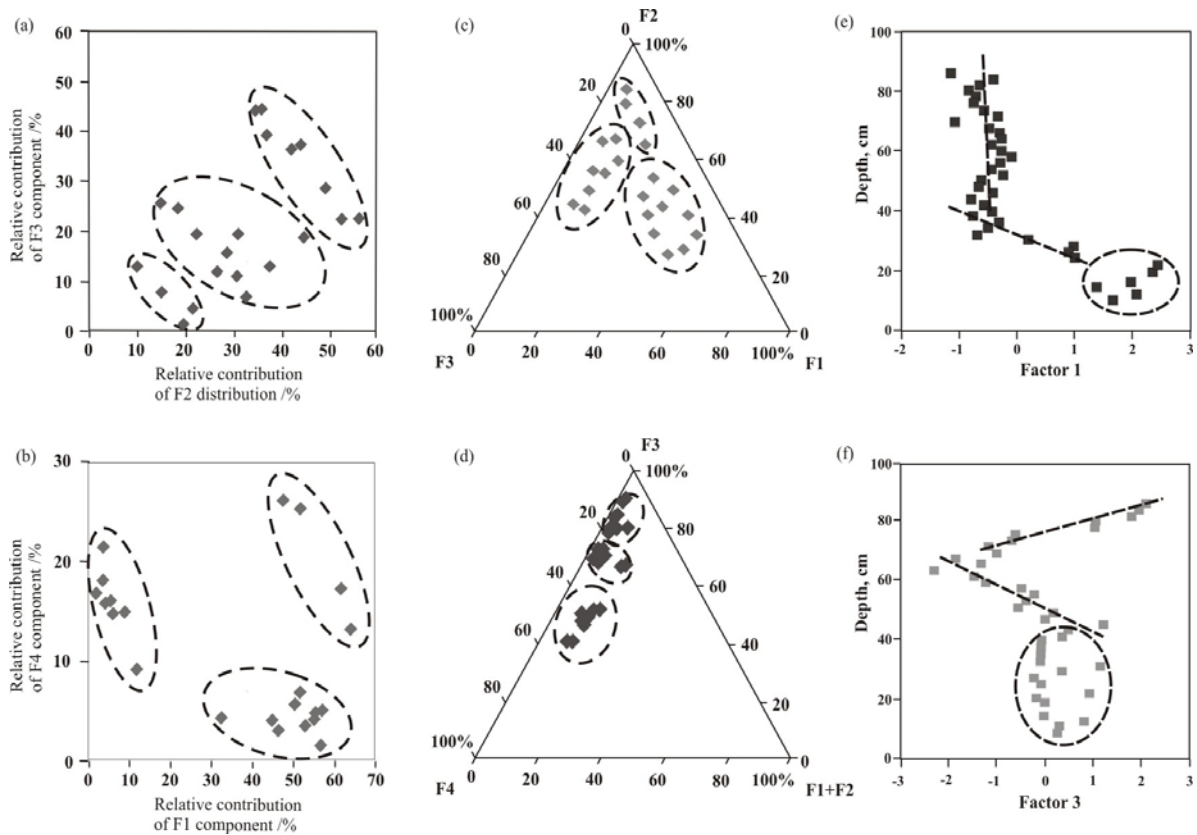


Figure 3. Functionalities of the four constituents (a), (b), (c), (d) and diagrams factors versus depth. (Ellipses do not represent confidence intervals, but are for guidance.)

All measured parameters from RE Pyrolysis and pedological analysis were depicted on profile diagrams for evaluation purposes (Figure 2). The results of the analysis indicate an obvious mobilisation process, which worked downwards the profile, and leads to the formation of a clay accumulation zone within the profile. This shows strong hydromorphic effect in the soil.

According to relationship between (a) stabile bio-macromolecules (F2) and immature geo-macromolecules (F3); (b) labile bio-macromolecules (F1) and refractory geo-macromolecules (F4); (c) relationship between components F1, F2, F3 and (d) F1+F2, F3 and F4 components three zones can be well separated. Consequently the horizons prognosticated by pedological description are identifiable from RE details as well.

Every measured parameters (all measured and calculated values from Rock Eval pyrolysis and pedology routine) were fed into SPSS 11.0 programme. The Factors were composed of strong correlated parameters. As following step we depicted these ones versus depth (put back in the original soil profile). Factor 1 involves clay, S1, S2, T_{max} and organic matter (measured by Dean method); Factor 3 contains sand and HI values (Figure 3). We can separate three point set in this way, which correlate with the pedological details.

We compared pedological details with the results of Rock-Eval analysis. Consequently we can state, that the soil formed in an environment in which the effect of cyclical fluctuating water could influent the soil development. This phenomenon suggests determination the paleosoil as Fluvisol. We established Rock-Eval pyrolysis is suitable to soil classification. We found, it is able to provide new details to explanation paleosoil horizons. However results varied between comparatively wide limits (6.1-29.5 mg/g), presence of nitrate was general; nitrate was detected in every examined tobacco product. One cigarette's average content was 10 mg nitrate. Concentrations of cigar and pipe tobaccos were similar to the cigarettes' results. The results are summarized in Figure 4.

CONCLUSIONS

Rock-Eval pyrolysis proved to be suitable for efficient examination of soil organic matter and estimation the measurement of humification. Further advantages, slight sample need to measure (0.1 g), doesn't require preparation (if the sample is carbonate-free), fast measure (25 min.), and we can detect six parameters from one single measurement (S1, S2, TPI, TOC, Tmax, HI) which we can use perfectly in evaluations. We can escape the lengthy and many chemicals requiring laboratory separates.

Rock-Eval pyrolysis is useable new method for determination paleosoil type, supplements the routinish classical measurement techniques. The method gives us excess-informations compared to traditional organic matter measure. In the course of known type paleosoil pyrolysis can provide new details according to the former details. Rock-Eval pyrolysis is capable define parameters, which help determination of unknown paleosoil type and allow identify minor occurrences within genetical horizons. Statistical evaluation of details assists the complex explanation of the measured values, accordingly determination of paleosoil type.

Acknowledgements

This work was supported by the Hungarian Science Research Found (OTKA T-48325). Thanking for the financial support to the National Research and Development Program NKFP – OM 000248/2002: Paleohistory of Hungary during Holocene.

REFERENCES

- [1] Dean, W. E. Jr., Determination of carbonate and organic matter in calcareous sediments and sedimentary rocks by loss on ignition: Comparison with other methods. J. Sed. Petrol. Vol. 44, p. 242–248, 1974.

- [2] Disnar, J.R. - Guillet, B. - Keravis, D. - Di-Giovanni, C. - Sebag D., Soil organic matter (SOM) characterization by Rock-Eval pyrolysis: scope and limitations. *Organic Geochemistry*, Vol. 34, 327-343, 2003.
- [3] Hetényi, M. - Nyilas, T. - M.Tóth, T., Stepwise Rock Eval pyrolysis as a tool for typing heterogeneous organic matter in soils. *Journal of Analytical and Applied Pyrolysis*, Vol. 74, No. 1-2, 45-54, 2005.
- [4] Nyilas T.,- M. Tóth T., - Hetényi M., Quantification of soil organic matter degradation by Rock-Eval pyrolysis, VII. Alps-Adria Scientific Workshop, Stara Lesna, Slovakia, 2008, DOI: 10.1556/CRC.36.2008.Suppl.1



SUPPORTING THE REASONABLE AGRICULTURAL PRODUCTION WITH A NEWLY FOUNDED ENVIRONMENTAL LABORATORY IN THE SOUTH EASTERN REGION OF HUNGARY

Gábor NAGY, Tünde NYILAS, Szilvia ÖRDÖG, Anita VOLFORD¹

¹SoilChem Laboratory - Homokkert Small-regional Integration Public Company
H-6782 Vállalkozók útja 1/b, Mórahalom, HUNGARY

Abstract:

An agricultural and environmental laboratory was founded within the framework of Baross Gábor Program in the summer of 2008 in Mórahalom, South-East Hungary, South Great Plain region. The primary aim of this initiative is making the countryside's agriculture more effective and environmentally aware, and assisting the dynamic development of the region. The laboratory helps agricultural production – the primary financial source of the region's villages – with analytical measures of soil and water samples, counseling about nutrient dosing, organized presentations, and cooperating with local enterprises and with another laboratory analyzing chemical residues in the produced crops. One significant deficiency was compensated by the establishment of SoilChem Laboratory – meeting the conditions set forth by directives of the European Union –, due to the lack of environmental laboratories in the region.

Keywords:

soil and water analyzing laboratory, agriculture, environmentally aware,
food safety and technology network

1. INTRODUCTION

With the help of the Baross Gábor Program, conducted by the Homokkert Small-regional Integration Public Company consortium a research and development network and a food safety and food technological subcenter has been set up in the South Great Plain region in Hungary. It is structured around up-to-date technological and metrological solutions and results cooperation of scientific institutions, researcher non-profit organizations and the entrepreneur sector.

The micronetwork and the soil- and water analysis laboratory – coordinated by the Homokkert Public Company – provides agro-innovative services for the cooperatives and partner organizations (DATÉSZ Rt., Mórakert Cooperative). By doing so it improves the local products' competitiveness and the standard of nutrition and quality assurance.

2. THE IMPORTANCE OF AGRICULTURE IN THE REGION

45,000 people live in the area of Mórahalom, which is considered the center of the Homokhát Small-region. Most of the people work in agriculture, thus their living is exposed to the competitiveness of the vegetable and fruit grown by them. Agriculture uses 72% of the small-region's land. The rate of forests is high, resulted by the afforestation in the beginning of the last century. The rate of lawns is also high because of the previously existing vast meadows and mowing fields. However vegetable growing is typical in arable farming and in the garden cultivation branches and its economical importance is unquestionable, it occupies relatively small area from the region's land. The volume of land used for pomology and vineyards shows the characteristics of sand farming. Non-cultivated lands and waste lands are the signs of uncertainty of farming and marketing and the disarrays about the ownership of the tenures (Figure 1).

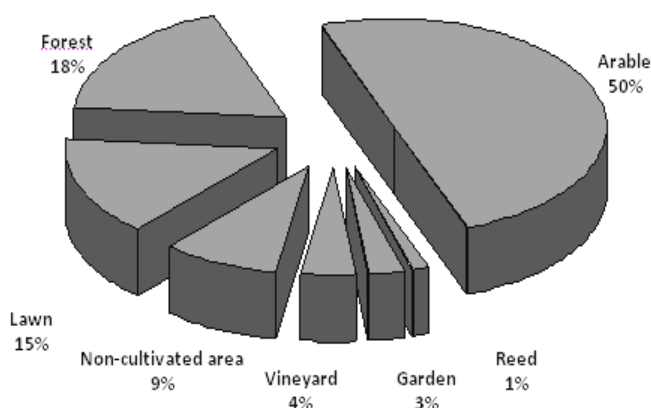


Figure 1. Distribution of cultivation branches of the small-region's area

The integrators, the cooperatives and other significant economic operators have to make sure the compliance with the market requirements, which means producing clear, healthy and high quality products. The most significant such integrator is Mórakert Cooperative founded in 1995 and declared as the first fruit and vegetable producer realizer organization by the Ministry of Agriculture and Rural Development in 2002. Its turnover and number of members has increased significantly in the last 10 years (Figure 2).

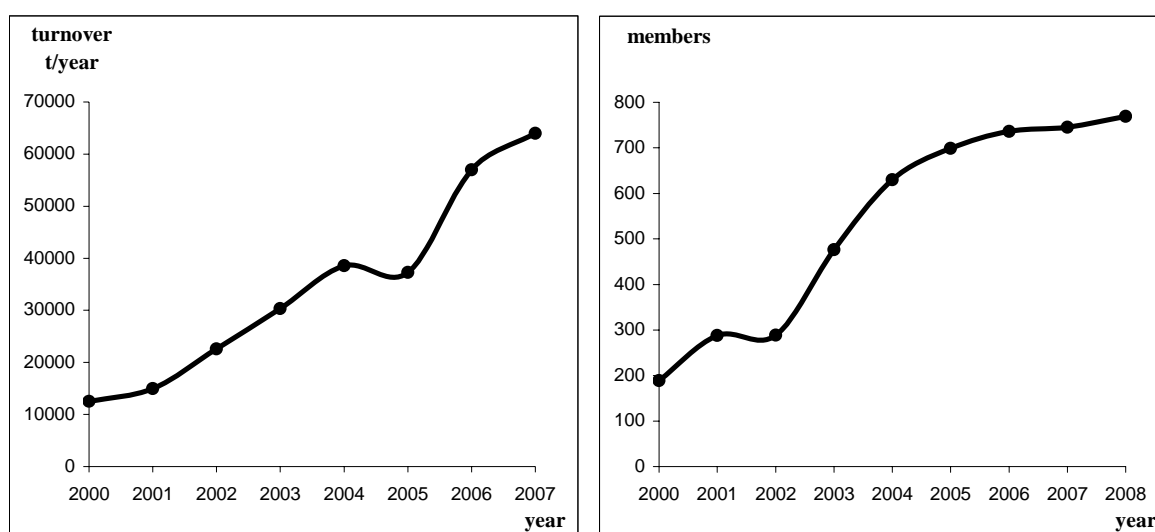


Figure 2. Growth of turnover and number of members of Mórakert Cooperative

3. HOMOKKERT PUBLIC COMPANY

The Hommokkert Small-regional Integration Public Company was corporated in 2000 by 9 agrarian cooperatives and the local authority of Mórahalom. The company was comprising producer and marketing cooperatives until the conversion in 2004 when the main profile of the company changed and two stratalgical directions were developed in connection with the agricultural priorities. These focus on the improvement of the living and income conditions of the rural population.

International connections

The Homokkert Public Company cultivates good relations with international partners. Seeking the possibility of cooperation with neighboring countries and participating in common projects are important parts of the company's activity. A recent collaboration was the establishment of a Borderland Commercial Center with Topolya and Temerin, two towns in Vojvodina, within the framework of an inter-regional project in 2008. The primary aim of this center is helping the cross-border trade of the agricultural products in the region.

Profiles of the Homokkert Public Company

On the one hand the main profile of the Company is encouraging alternative income activities – the so-called Renewable Energy Information Center was built in support of this objective – and on the other hand the research and development, innovation and innovation intermediation services. The Regional Food Safety and Technological Micronetwork needs to be highlighted here, which was set up in the framework of the Baross Program. The Network was evolved by the partnership of the Homokkert Public Company and Mórakert Cooperative

in Mórahalom, the DABIC Public Company in Szentes and the College of Kecskemét (Figure 3). Its goal is to establish an accredited institute complying with the international standards and placed near big producer-realizer cooperatives (e.g. Mórakert Cooperative).



Figure 3. Centers of the Regional Food Safety and Technological Micronetwork

Aims of regional food safety and technological micronetwork

- a) establishing a regional food safety and technological subcenter with the utilization of results and experiences of the regional center and network maintained by DABIC Public Utility Company
- b) founding an agrarian research workshop with the collaboration of acknowledged researcher-teachers with scientific degree and local experts, and developing an academic practicing section in connection with garden cultures and the safety of horticultural products
- c) establishing an experimental soil and water analyzing laboratory and the publication of results
- d) achieving experimental developments in relation with product innovation and changing production structure in vegetable, fruit and ornamental plant growing
- e) starting continuous horticultural research and development activity based on regional demands
- f) evolving a research and development and innovation micronetwork – with thousands of members - considering the specifics of producer-realizer cooperatives (TÉSZ) and the conditions of local product structure
- g) establishing a consultant network and educational activity
- h) experimental developing of analytical methods, e.g. for fast determination of chemical residues
- i) founding an agrarian research workshop that conduces to the production of high added-value or new products (bioproducts, functional foods) with developing growing methods and technologies

4. REASONABILITY OF MICRONETWORK

Directives of the EU – Food safety

Establishing and maintaining the Regional Food Safety and Technological Micronetwork is reasoned by directives and regulations of the EU. In hygienic overseeing of food producing, the European Union put emphasis on supervision of producing environment instead of the former final product checking in the last years. Therefore application of new analytical methods is required. SoilChem Laboratory – part of Regional Food Safety and Technological Micronetwork – wishes to keep pace with this continuous vocational improvement. Developing analytical procedures to support the development of new technologies – that result healthy and safe food – is one of SoilChem Laboratory’s primary goals. Nowadays food safety is number one priority of agrarian economy: organizations in agriculture and food industry must correspond to the higher and higher requirements of food safety and environmental protection, and must meet the consumers’ increasing demands.

Considering food safety regulation of the European Union, configuring quality insurance systems and helping producing activity at agrarian small and medium enterprises became indispensably necessary by now. In the interest of competitiveness of these enterprises preventive self-checking food safety systems must function effectively „from field to table”, ensuring the transparency of food chain. Successful food politic demands the absolute traceability of crops, food and their components. This enables the enterprises to

withdraw hazardous forage or food from the market in case of consumers' health is endangered. Healthy and safe food can only be ensured by continuous monitoring of critical points of the producing process and by running quality insurance systems. It is reasonable to establish and upkeep accredited food safety and technological centers and subcenters, placed near farmers in the interest of quantitative and qualitative determinations of health-damaging chemical and microbiological compounds.

Functions of centers:

Instrumental tests are indispensable to obtain knowledge of environmental factors and their impacts. Thus we can collect data that help us to intervene in the process of cultivation. Precision nutrition replenishment can be attained only in possession of the knowledge on the soil's current nutrition level. Therefore soil analysis is necessary both before and during every single cultivation process. More detailed information is needed of soil and irrigation water in case of horticultural crops (nutrient rate and quantity, harmful elements).

- a) monitoring chemical residues (pesticides, pharmaceuticals etc.) of crops and food
- b) detection of metal pollutants (lead, cadmium, mercury, arsenic, aluminium, copper, zinc, nickel) in food of plant and animal origin
- c) determination of nitrate in vegetables susceptible for nitrate accumulation
- d) complete analysis of soil and water
- e) microbiological monitoring to increase the hygiene of food processing technologies
- f) forage-safety monitoring
- g) issue accredited certificates

Economic advantages

The building up of the Micronetwork is appropriate concerning its economic advantages as well. The current international and domestic consumer habits seem to prefer products with known origin; customers appreciate the value derived from the specific circumstances of the production. Thus the quality advantages in the production lead to market advantages. With the characterization of agricultural and food industrial products grown on excellent soil, using adequate technology and defining the relating quality features and with the conscious perpetuation of these benefits these products can obtain market advantages.

5. CONCLUSIONS

The whole sector and region profits from the database of materials endangering food safety, building up and operation of preventive indication systems, meeting the requirements of identification and traceability, and applying new, conventional sampling methods. The Micronetwork's indirect economic effects can be measured in the improvement of competitiveness of the analyzed products, the prevention of the damages caused by loss of consumer trust, and the recognition of the network's trademark.

The operation of SoilChem Laboratory as a service provider, accredited institute makes the non-profit investment self-supporting in the future.

ACKNOWLEDGEMENTS

This work was supported by the Gábor Baross Program (BAROSS-3-2007-0009; OMF-01162/2007).



ADSORPTION OF ARSENIC COMPONENTS ON LAYERED DOUBLE HYDROXIDES AND MIXED OXIDES FOR WATER PURIFICATION

Tamás BUJDOSÓ¹, Ágnes PATZKÓ¹, Zoltán GALBÁCS², István LICSKÓ³, Imre DÉKÁNY¹

¹Department of Colloid Chemistry, University of Szeged, Szeged, HUNGARY

²Department of Inorganic and Analytical Chemistry, University of Szeged, Szeged, HUNGARY

³Department of Sanitary and Environmental Engineering, Budapest University of Technology and Economics, Budapest, HUNGARY

Abstract

Aim of this research was the removal of toxic and carcinogenic arsenate (AsO_4^{3-}) ions from drinking water with different metals (Mg, Mn, Al, Fe) content layered double hydroxides (LDH). The efficiency of the MgAl LDHs in the arsenic removal is increased with increasing nitrate content in LDH. The basal spacing of LDH was decreasing with 0.085 nm after ion-exchange. The calcinated form of each adsorbent resulted less arsenic removal, but less dissolution of metal from the oxide compared to the uncalcinated LDH. Increasing the manganese content in the MnFe LDH resulted in enhanced arsenic removal efficiency.

Keywords:

arsenic removal, drinking water, layered double hydroxide, adsorption, calcination

Introduction

Arsenic is a human genotoxin and chronic exposure is associated with development of cancers, including skin cancer [1]. The inorganic arsenic forms are metabolically inhibitors. Arsenate (As^{5+}) displaces the phosphate ion from the energy source ATP molecule, arsenite (As^{3+}) bonds with sulfhydryl group of the proteins (e.g. glutathione) and it inhibit their function. By United States Environmental Protection Agency (USEPA) 0.3 $\mu\text{g}/\text{kg}/\text{day}$ sanitary threshold of arsenic was accepted on the basic of statistics data. The European and World Health Organization (WHO) limit of arsenic content of drinking water is 10 $\mu\text{g}/\text{L}$. The arsenic accumulate in some groundwater and mineral by natural process [2, 3, 4, 5]. The arsenic atom displaces silicium, iron and aluminium atoms in the crystal lattice and this fact causes the high arsenic content of minerals. In the Pannonian basin the arsenic accumulate in the Pleistocene sediments by the rivers and the subsurface flows [6]. This arsenic content resolving into the groundwater from the 100-300 m deep strata. In our days the arsenic contamination in the groundwater is serious problem all over the world [7, 8]. An estimated 57 million people may be drinking high arsenic content water in Bangladesh and West Bengal, India. The strong antropogenic effect (e.g. mining, agriculture) is increasing the arsenic content of surface water, groundwater and soil [9]. The pH of groundwaters is between 6.5-9.5, the non-dissociated (H_3AsO_3) and monovalent anionic (H_2AsO_3^-) natural forms of arsenite are and arsenate exits in anionic forms ($\text{H}_2\text{AsO}_4^{1-}$, HAsO_4^{2-}) in this mildly alkaline range [10]. The arsenic forms and the geochemical components of groundwater determinate the applicable water treatment technology. In Hungary the removal of arsenic from drinking water with iron (III)-hydroxide is one of the current methods. The average efficiency is 60-80 % that can increase up to 95 % with optimized parameters. Granulated iron hydroxide (GEH) column is applied in numerous water plants. Goethite (FeOOH) and iron hydroxide are the component of GEH column. Arsenic removal efficiency of natural or synthetic iron oxides and hydroxides are examined in number of publications [11, 12, 13, 14]. T. Tuutijärvi et al. investigated the arsenate adsorption capacity of different size maghemite nanoparticles in a wide pH range [15]. Large advantage of these superparamagnetic is that the nanoparticles can be easily removed with magnetic field from treated water. Zero-valent iron particle removes arsenate and arsenite with high efficiency in natural groundwaters by adsorption, surface precipitation, and co-precipitation with various corrosion products [16, 17, 18]. Membrane processes (nanofiltration) are suited for arsenate release,

but are not efficient by the arsenite content groundwaters [19, 20]. The arsenic removal is enhanced by the hybrid membrane treatments [21, 22]. The layered double hydroxides (LDH) are one group of layered structured minerals in the nature. The sheets of the layered double hydroxide are formed from divalent metal ions (M^{2+} : Mg^{2+} , Ca^{2+} , Mn^{2+} , Co^{2+}) and trivalent metals ions (M^{3+} : Al^{3+} , Fe^{3+}) and exchangeable anions (A^{n-} : CO_3^{2-} , SO_4^{2-} , NO_3^- , Cl^-) compensate the positive surface charge between the layers ($[M_{1-x}^{2+}M_x^{3+}(OH)_2]A^{n-}_{x/n} \cdot yH_2O$). LDHs are applied as adsorber [23], catalyst [24], support in medicine [25], thin film component [26]. The positively surface charged LDH is suited for adsorb the negatively charged arsenic ion forms [27, 28, 29].

Materials

Magnesium nitrate hexahydrate ($Mg(NO_3)_2 \cdot 6H_2O$, puriss., Fluka), aluminium nitrate nonahydrate ($Al(NO_3)_3 \cdot 9H_2O$, puriss.), iron (III) chloride hexahydrate ($FeCl_3 \cdot 6H_2O$, analytical grade, Reanal Hungary), manganese sulphate hydrate ($Mn(SO_4) \cdot H_2O$, analytical grade), sodium hydroxide (NaOH, analytical grade), and sodium nitrate ($NaNO_3$, puriss.) were used to prepare layered double hydroxide. Potassium iodide (KI, puriss.), ascorbic acid ($C_6H_8O_6$ analytical grade), pyridine (C_5H_5N , analytical grade), potassium carbonate (K_2CO_3 , puriss., MOLAR Hungary), and sodium borohydride ($NaBH_4$, purum), silver diethyldithiocarbamate, Ag-DDTC ($C_5H_{10}AgNS_2$, puriss., Fluka) were used for arsenic(V) determination. Arsenic removal measurements employed the natural arsenic content groundwater and aqueous solution of disodium hydrogenarsenate heptahydrate ($AsHNa_2O_4 \cdot 7H_2O$, puriss., Fluka). The model groundwater originates from Gyula, town of Békés Country, in Hungary (Table 1).

Table 1 The chemical analysis of groundwater from Gyula

	Groundwater analysis	
	07. 2005.	05. 2006.
pH	8.33	8.69
General hardness, °dH	2.0	-
General hardness ^a	-	17.0 CaO
Conductivity, µS	681	528
Sodium ^a	100	-
Potassium ^a	1.0	-
Calcium ^a	10.0	9.2
Magnesium ^a	2.0	1.6
Chloride ^a	27.7	-
Hydrocarbonate ^a	360	-
Sulfate ^a	7.7	-
Arsenic^a	0.105	0.100
Ammonium ^a	-	0.60
Nitrite ^a	-	<0.01
Nitrate ^a	-	<0.07
Iron (II) ^a	-	0.043
Manganese (II) ^a	-	0.010
Boron ^a	-	0.38
Total Phosphor ^a	-	0.56
Alkalinity ^a	-	6.4
Dry matter ^a	396.6	-
COI	5.6	3.6

^a concentration in mg/L

Methods

Arsenic content was determined by silver diethyldithiocarbamate (Ag-DDTC) spectrophotometric methods. Reduction of As(V) by potassium iodide produced arsenic hydride (AsH_3), which was transferred to the pyridine solution of Ag-DDTC by the generated carbon dioxide. The reaction of AsH_3 and Ag-DDTC led to the formation of a colourful compound, whose absorbance was determined in an UVICON UV-VIS spectrophotometer ($\lambda_{max}=540$ nm). XRD experiments were carried out in a Philips X-ray diffractometer (PW 1930 generator, PW 1820 goniometer) with $CuK\text{-}\alpha$ radiation ($\lambda = 0.15418$ nm), 40 kV, 35 mA. Basal spacing was calculated from the reflection angle using the Bragg equation. The amounts of Mg^{2+} and Al^{3+} ions constituting the octahedral layers of double hydroxides were determined in a Jobin Yvon 24 sequential Inductively Coupled Plasma-Atomic Emission spectrometer. For nitrate anion determination, nitrate (NO_3^-) ions were converted to yellow nitrobenzene to be determined by photometry [30]. Carbonate (CO_3^{2-}) anions were determined by volumetric in the form of carbon dioxide. The amount of carbon dioxide was calculated by the gas law from the volume of the gas generated within the closed system [31].

Synthesis of layered double hydroxides and oxides

The salt of divalent ion (Mg^{2+} or Mn^{2+}) and trivalent ion (Al^{3+} or Fe^{3+}) were dissolved in 30 mL water at a $M^{2+}:M^{3+}$ molar ratio of 2:1. The MnFe LDH was synthesized at 1:1 and 0.5:1 molar ratios. 25 g of sodium hydroxide and 20 g of sodium nitrate were also dissolved in 170 mL water. Under vigorous stirring, alkaline solution was added dropwise to divalent and trivalent ion content solution in 3 min. The slurry was stirred at 25 °C for 20 minutes. The sediment was centrifuged, washed once with distilled water and centrifuged again; the product was then dried at 65 °C. The pH of the MgAl-LDH dispersion was adjusted to 9.1, 9.6 and 13.1 using 0.1 M NaOH and 0.1 M HNO_3 . One portion of LDHs was calcinated in air atmosphere at 500 °C during 10 hours.

Arsenic removal experiments in column

We used both open ended glass tube (250 mm long and 22 mm diameter). The similar amount of adsorbent was top of the filter bad (fibreglass, 5.0 g ion-free sand, 5.0 g quartz with 270 mm diameter). The treated groundwater circulated with 33-42 mL /min flow speed by peristaltic pump. 4.0 litre of groundwater was in the closed system and the residual arsenic concentration was determined every third hours. The treated groundwater was exchanged to fresh water then the arsenic concentration achieved the limit. The measured arsenic concentration stop indicated that the arsenic removal column saturated.

Results and discussion

In many places from Hungary arsenic content exceeds the health limit in drinking water. The arsenic content of water produced in commercially available sodas is illustrated in **Fig. 1**. In more than half of sodas from the Dél-Alföld arsenic content are above 10 µg/L, and in one of the samples is 10 times of the limit. In Hungary all settlements should be 10 µg/L of the arsenic content in drinking water till 2009.

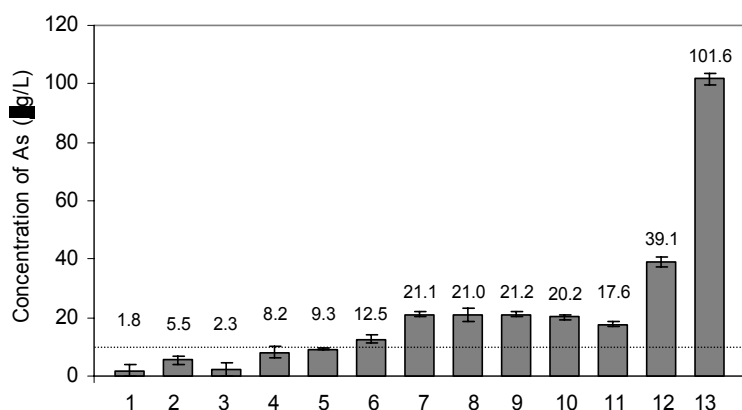


Figure 1. Arsenic content of different commercial sodas from Hungary

The 2:1 MgAl-LDH was investigated at 0.1 and 150 mg/L arsenic initial concentration in distilled water. The As(V)-containing dispersed LDH particles were dried at room temperature after adsorption and studied by X-ray diffraction in an air-dry state (**Fig. 2**). When the amount of adsorbed As(V) increased, the basal spacing gradually decreases with 0.085 nm and this clearly indicates the ion exchange taking place between the LDH layers. The reason for the decrease in basal spacing with increasing arsenate content is that an increasing number of nitrate anions are exchanged in the interlamellar space and the incorporating As(V) species also displace water molecules.

Different amount of 60 °C dried MgAl-, MnAl-, and MnFe-LDHs and the calcined adsorbents were added to the groundwater from Gyula. The groundwater was left in air atmosphere five days before the arsenic removal experiments in order to oxidise the total arsenite content to arsenate form. In case of the 2:1 MgAl-LDH at pH 13.1 the sample obtained nitrate/ carbonate ratio of 0.1, while the pH was 9.6 or 9.1, these values show 0.8 or 1.8. The molar ratio of Mg and Al ions constituting the octahedral layers was nearly 2:1 in the samples and could not influence the ion exchange of arsenate. The MgAl molar ratios are 1.91, 2.06 and 2.13 with increasing nitrate/ carbonate molar ratio. Effect of nitrate/ carbonate molar ratio between the layers was investigated by the 2:1 MgAl-LDH. The arsenic removal efficiency in percentage calculated by the (2) equation where c_0 and c_e are the initial and equilibrium arsenic concentrations.

$$As\ removal\ (\%) = [(c_0 - c_e) / c_0] 100 \quad (2)$$

In each of a series of 100 ml aliquots of arsenic content solution and 0.01-0.1 g of the adsorbent was suspended; after 5 min of intensive stirring, the adsorbent was removed by filtration. The equilibrium concentration of arsenic in the filtrate was determined. The specific excess adsorption of arsenic ($n^{\sigma(v)}$) was calculated by the (1) equation where V is the total amount of water, c_0 and c_e are the initial and equilibrium concentrations, of arsenic respectively, and m is the mass of the adsorbent.

$$n^{\sigma(v)} = V(c_0 - c_e) / m \quad (1)$$

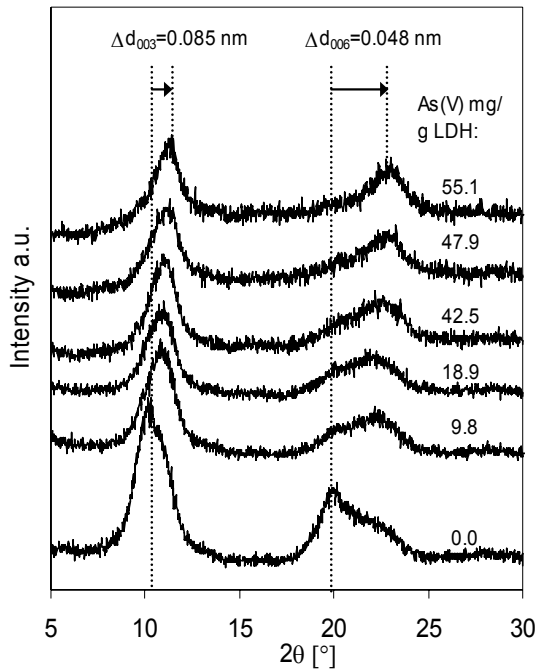


Figure 2. XRD pattern of adsorbed arsenic containing 2:1 MgAl-LDH

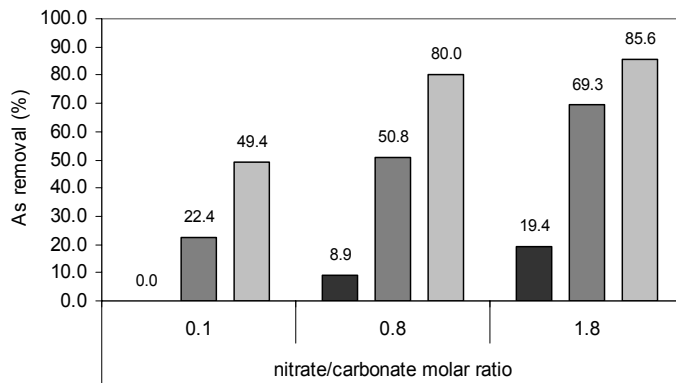


Figure 3. Arsenic removal efficiency of 2:1 MgAl-LDHs at different nitrate/carbonate molar ratio in the groundwater (0.1 ■, 0.5 ■, 1.0 ■, g LDH /L)

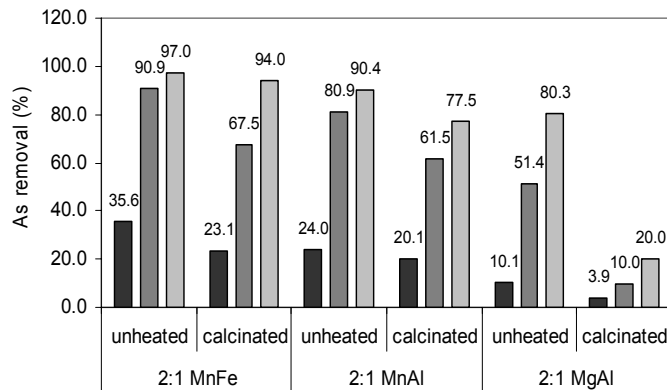


Figure 4. Arsenic removal efficiency of several type of 2:1 LDHs and oxides in the groundwater (0.1 ■, 0.5 ■, 1.0 ■, g LDH /L)

The arsenic adsorption capacity is increasing with increasing nitrate content of LDH (Fig. 3). At the lowest 0.1 NO₃⁻/CO₃²⁻ ratio the adsorption capacity is less than 1.8 ionic ratio, because carbonate may be irreversibly bound. The explanation is that greater atmospheric carbon dioxide is dissolved during the synthesis of LDH at higher pH. When the type of metal ions at 2:1 molar ratio LDH sheets were changed than different specific arsenic removal efficiencies were obtained in the treated water (Fig. 4). The results show that the 2:1 composition MnAl-LDH is adsorbed 1.5 times more arsenic amount, than the MgAl-LDH at 0.5 g/L adsorbent concentration. The manganese content LDH was bound twice as much arsenate than the magnesium content LDH at larger amount of adsorbent (0.5 and 1.0 g/L). The most successful MnFe-LDH reduced the arsenic content below the limit value in the treated water with 0.5 g/L amount of adsorbent. Calcinations of the various metal ion containing LDHs decreased the efficiency of arsenic removal with less degree than the unheated adsorbent, on contrary to the literature [32, 33]. The adsorbed arsenic content decreases to one fourth through calcination at 1.0 g/L MgAl content adsorbent. This difference decreases between the unheated and calcinated forms of MnAl and MnFe adsorbents. In case of 1.0 g/L of MnFe oxide 13 times more arsenic amount was removed from groundwater compared to that of MgAl oxide. One of the aims was the lower industrial cost; therefore LDHs were synthesized not only in distilled water, but in drinking water. The 2:1 MnAl-LDH adsorbent produced in drinking water removed the less on average 25% of arsenic from the treated water than in distilled water produced form (Fig. 5). In the drinking water synthesized sample can contain other components (e.g. calcium, magnesium) from the drinking water so has less efficiency than the distilled water prepared LDHs. The most arsenate adsorbing MnFe-LDH was investigated in the groundwater, henceforward. The molar ratios of manganese and iron ions were 0.5 and 1.0 during the preparations of LDHs. The different manganese containing dried powder sample was dosed to the fresh groundwater (> 1 day) and the 5 days old groundwater.

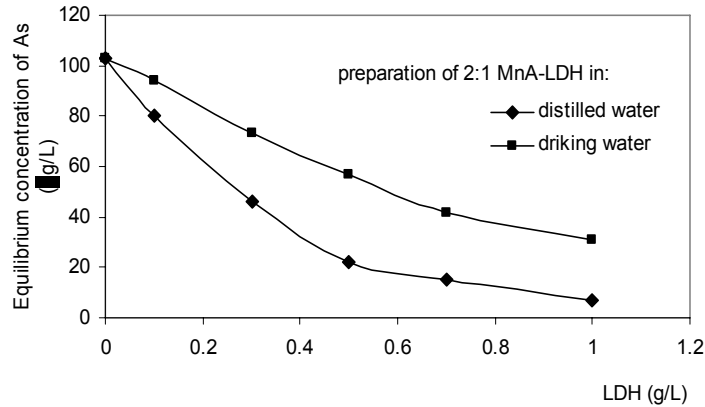


Figure 5. Arsenic conc. in the groundwater after arsenic removal of 2:1 MnAl-LDHs

The **Fig. 6** and **7** show that the arsenic content was reduced in the treated water by increasing the manganese content in the calcinated adsorbent. The MnFe-LDHs adsorbed less arsenic species in the fresh groundwater through both the arsenite (As^{3+}) and arsenate (As^{5+}) content. The arsenite can be removed more efficiently with MnFe oxides than the arsenate. It is noted that the calcinated samples remove less arsenate than the LDHs. There is not such a clear relationship between manganese content of adsorbent and arsenic removal efficiency of the unheated samples. Redissolution of manganese was calculated by the (3) equation where c is the manganese concentrations in the groundwater after the treatment and c_{max} is the maximum manganese concentration of samples.

$$Mn \text{ redissolution } (\%) = (c / c_{max}) 100 \quad (3)$$

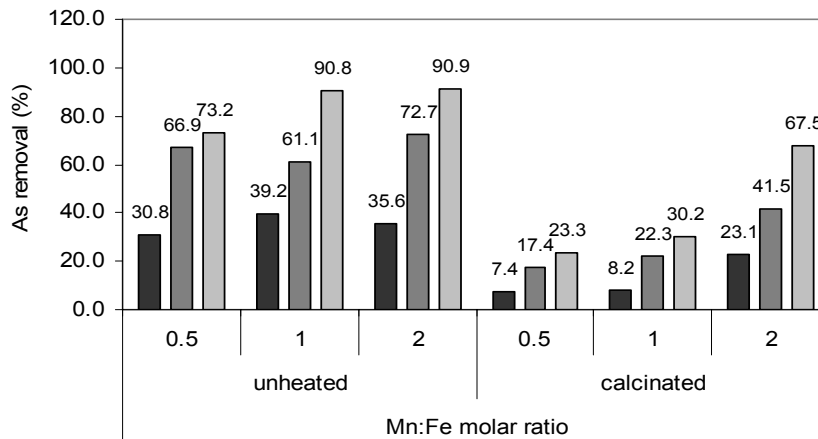


Figure 6. Arsenic removal efficiency of several molar ratio of MnFe LDHs and oxides in the groundwater (0.10 ■, 0.25 ■, 0.50 ■, g LDH /L)

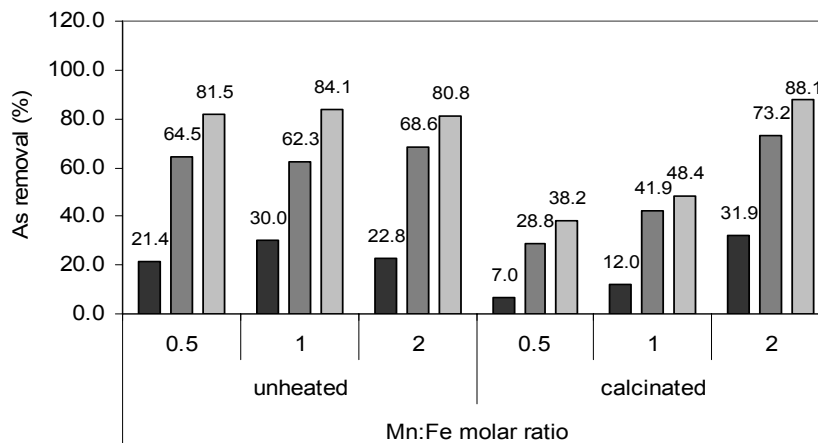


Figure 7. Arsenic removal efficiency of several molar ratio of MnFe LDHs and oxides in the fresh groundwater (0.10 ■, 0.25 ■, 0.50 ■, g LDH /L)

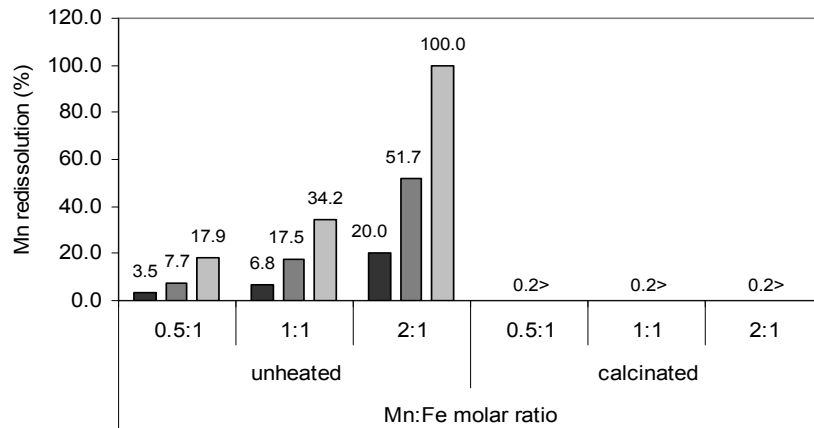


Figure 8. Redissolution of manganese from several molar ratio of MnFe LDHs and oxides after arsenic removal (0.10 ■, 0.25 ■, 0.50 ■, g LDH /L)

Redissolution of manganese from the unheated LDHs was increased in proportion to the increase of the solid at the same manganese-iron ratio (**Fig. 8**). The molar ratio of the manganese-iron was resulted in a greater degree of redissolution of manganese in the treated water at a given amount of investigated adsorbent. Manganese migration is negligible in the arsenic content calcined samples. Therefore, the health-damage of manganese migration could be abolished by the calcination.

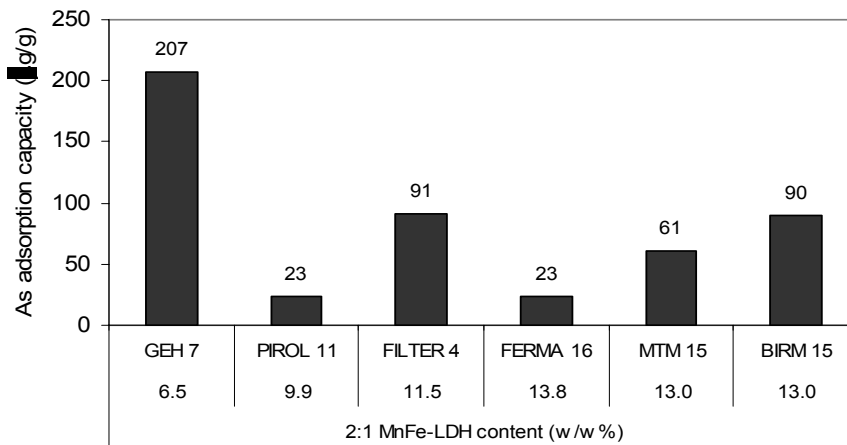


Figure 9. Arsenic adsorption capacity of several bearers at similar 2:1 MnFe-LDH content

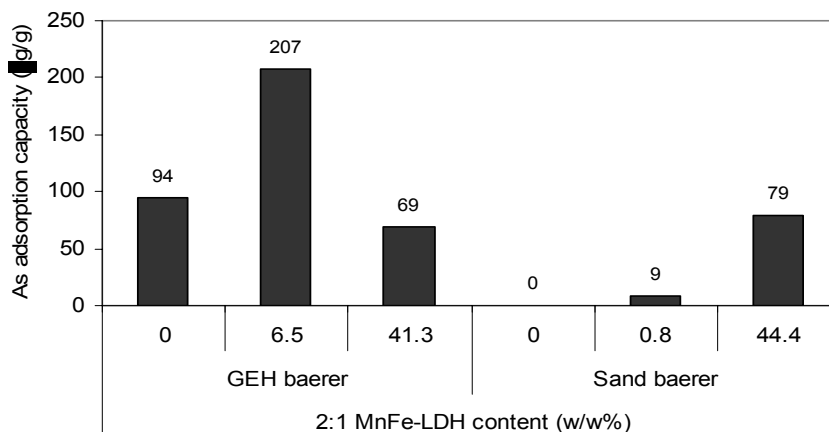


Figure 10. Arsenic adsorption capacity of GEH and sand bearers at different 2:1 MnFe-LDH content

The 2:1 MnFe-LDH precipitated onto the surface of different solid bearer. We investigated the effect of seven different bearers on the arsenic removal of LDH. The MnFe-LDH content bearers were loaded in the glass column. The groundwater was circulated, thus the measured arsenic concentration of the treated water increased below the health limit. In the similar LDH content bearer the GEH

adsorbed the most amount arsenate (207 mg/g) and half of this amount was adsorbed by FILTER 4 and BIRM 15 bearer (**Fig. 9**). The MTM 15 bearer adsorbed 61 mg arsenic/g from the groundwater. The PIROL 11 and FERMA 16 are the least arsenic removal columns. The GEH without LDH adsorbed 94 mg/g and 41.3 w/w% LDH 69 mg arsenic/g, respectively (**Fig. 10**). Larger amount of surface LDH inhibited the efficiency, because the LDH particles entirely cover the surface of larger size GEH particles and fill the pores of the bearer. The arsenic removal of indifferent sand bearer was also investigated. The adsorption of arsenate enhanced with increasing MnFe-LDH on the indifferent sand bearer. The 0.8 w/w% LDH content sand bearer column was regenerated with 100 mL of 5 mol/L concentration calcium chloride solution. The 0.2 w/w% of adsorbed arsenic content left for the column after six hours circulation. The arsenic saturated FERMA bearer was tried to regenerate with 1 mol/L concentration sodium chloride solution. The removal of arsenic from the column didn't exceed the 1.0 w/w% in this case. The 6.5 w/w% LDH content GEH was regenerated by 1.0 L of 1.0 mol/L sodium hydroxide. Half of arsenic content of column can be removed after one hour of treatment and further 5-10 % in the next hour.

Conclusion

Our aims were efficient arsenate removal and production of a cheap adsorbent for industrial application as the syntheses of LDHs were carried out in air atmosphere. When the LDH is synthesized at low pH (pH ~9) value in air atmosphere that little carbonate content and better arsenic adsorber the product will be. The MnFe-LDH at different metal content LDHs adsorbs the most arsenate from the groundwater at same metal molar ratio in the layers. The calcination of MnFe-LDHs decreases the arsenate removal but the binding of arsenite enhance and it dissolves the resolution of manganese from the solid phase. The type of bearer influences the arsenic removal at the column experiments. The best arsenate adsorbent GEH has optimal LDH content by the arsenic release. Sodium hydroxide can be used to regenerate of the LDH content columns.

Acknowledgment

This research was supported by the Economic Competitiveness Operational Programme “Development of complex technology for water purification to ensure water with appropriate quality” (GVOP-3.1.1.-2004-05-0186/3.0).

REFERENCES

- [1.] Ghazalla Benhusein, Elaine Mutch, Faith M. Williams: Effect of arsenic on DNA damage, glutathione content, apoptosis and necrosis in HaCat cells. *Toxicology*, 104–119, 231, 2007.
- [2.] Stephen C. Peters: Arsenic in groundwaters in the Northern Appalachian Mountain belt: A review of patterns and processes. *Journal of Contaminant Hydrology*, 8–21, 99, 2008.
- [3.] P.L. Smedley, H.B. Nicolli, D.M.J. Macdonald, A.J. Barros, J.O. Tullio: Hydrogeochemistry of arsenic and other inorganic constituents in groundwaters from La Pampa, Argentina. *Applied Geochemistry*, 259–284, 17, 2002.
- [4.] Matthew L. Polizzotto, Charles F. Harvey, Guangchao Li, Borhan Badruzzman, Ashraf Ali, Matthew Newville, Steven Sutton, Scott Fendorf: Solid-phases and desorption processes of arsenic within Bangladesh sediments. *Chemical Geology*, 97–111, 228, 2006.
- [5.] Xiu-Ping Yan, Robert Kerrich and M. Jim Hendry: Distribution of arsenic(III), arsenic(V) and total inorganic arsenic in porewaters from a thick till and clay-rich aquitard sequence, Saskatchewan, Canada. *Geochimica et Cosmochimica Acta*, 2637–2648, 62, 2000.
- [6.] Irén Varsányi, Lajos Ó. Kovács: Arsenic, iron and organic matter in sediments and groundwater in the Pannonian Basin, Hungary. *Applied Geochemistry*, 949–963, 2, 2006.
- [7.] Franco Frau, Carla Ardaù, Luca Fanfani: Environmental geochemistry and mineralogy of lead at the old mine area of Baccu Locci (south-east Sardinia, Italy). *Journal of Geochemical Exploration*, 105–115, 100, 2009.
- [8.] Helen A.L. Rowland, Andrew G. Gault, Paul Lythgoe, David A. Polya: Geochemistry of aquifer sediments and arsenic-rich groundwaters from Kandal Province, Cambodia. *Applied Geochemistry*, 3029–3046, 23, 2008.
- [9.] A. Dangić: Arsenic in surface- and groundwater in central parts of the Balkan Peninsula (SE Europe). *Trace Metals and other Contaminants in the Environment*, 127–156, 9, 2007.
- [10.] [10] P.L. Smedley, D.G. Kinniburgh: A review of the source, behaviour and distribution of arsenic in natural waters. *Applied Geochemistry*, 517–568, 17, 2002.
- [11.] Javier Giménez, María Martínez, Joan de Pablo, Miquel Rovira, Lara Duro: Arsenic sorption onto natural hematite, magnetite, and goethite. *Journal of Hazardous Materials*, 575–580, 14, 2007.

- [12.] O.K. Hartzog, V.A. Loganathan, S.R. Kanel, G.P. Jeppu, M.O. Barnett: Normalization, comparison, and scaling of adsorption data: Arsenate and goethite. *Journal of Colloid and Interface Science*, 6–13, 333, 2009.
- [13.] P. Lakshminathiraj, B.R.V. Narasimhan, S. Prabhakar, G. Bhaskar Raju: Adsorption of arsenate on synthetic goethite from aqueous solutions. *Journal of Hazardous Materials*, B136, 281–287, 2006
- [14.] Ilwon Ko, Allen P. Davis, Ju-Yong Kim, Kyoung-Woong Kim: Effect of contact order on the adsorption of inorganic arsenic species onto hematite in the presence of humic acid. *Journal of Hazardous Materials*, 53–60, 141, 2007.
- [15.] T. Tuutijärvi, et al., As(V) adsorption on maghemite nanoparticles, *J. Hazard. Mater.*, 2009.
- [16.] Konstantina Tyrovolou, Nikolaos P. Nikolaidis: Arsenic mobility and stabilization in topsoils. *Water research*, 1589 – 1596, 43, 2009.
- [17.] Pinhua Rao, Mark S.H. Mak, Tongzhou Liu, Keith C.K. Lai, Irene M.C. Lo: Effects of humic acid on arsenic(V) removal by zero-valent iron from groundwater with special references to corrosion products analyses. *Chemosphere*, 156–162, 75, 2009.
- [18.] Sushil Raj kanel, Bruce Manning, Laurent Charlet, and Heechul Choi: Removal of Arsenic from Groundwater by Nanoscale Zero-Valent Iron. *Environ. Sci. Technol.*, 1291–1298, 39, 2005.
- [19.] E. Fogarassy, I. Galambos, E. Bekassy-Molnar, Gy. Vatai: Treatment of high arsenic content wastewater by membrane filtration. *Desalination*, 270–273, 240, 2009.
- [20.] Shengji Xia, Bingzhi Dong, Qiaoli Zhang, Bin Xu, Naiyun Gao, Christel Causseranda: Study of arsenic removal by nanofiltration and its application in China. *Desalination*, 374–379, 204, 2007.
- [21.] F. Beolchini, F. Pagnanelli, I. De Michelis, F. Vegliò: Treatment of concentrated arsenic (V) solutions by micellar enhanced ultrafiltration with high molecular weight cut-off membrane. *Journal of Hazardous Materials*, 116–1211, 48, 2007.
- [22.] V.T. Nguyen, S. Vigneswaran, H.H. Ngo, H.K. Shon, J. Kandasamy: Effect of contact order on the adsorption of inorganic arsenic species onto hematite in the presence of humic acid. *Journal of Hazardous Materials*, 53–60, 141, 2007.
- [23.] Mohamed Bouraada, F. Belhafaoui, M.S. Ouali, Louis-Charles de Ménorval: Sorption study of an acid dye from an aqueous solution on modified Mg–Al layered double hydroxides. *Journal of Hazardous Materials*, 463–467, 163, 2009.
- [24.] A. Patzkó, R. Kun, V. Hornok, I. Dékány, T. Engelhardt, N. Schall: ZnAl-layer double hydroxides as photocatalysts for oxidation of phenol in aqueous solution. *Colloids and Surfaces A: Physicochem. Eng. Aspects*, 64–72, 265, 2005.
- [25.] Jin-Ho Choy, Soo-Jin Choi, Jae-Min Oh, Taeun Park: Clay minerals and layered double hydroxides for novel biological applications. *Applied Clay Science*, 122–132, 36, 2007.
- [26.] Hornok, V., Erdőhelyi, A., Dékány, I.: Preparation of ultrathin membranes by layer-by-layer deposition of layered double hydroxide (LDH) and polystyrene sulfonate (PSS). *Colloid Polym. Sci.*, 1050–1055, 283, 2005.
- [27.] Antonio Violante, Marianna Pucci, Vincenza Cozzolino, Jun Zhu, Massimo Pigna: Sorption/desorption of arsenate on/from Mg–Al layered double hydroxides: Influence of phosphate. *Journal of Colloid and Interface Science*, 333, 63–70, 2009.
- [28.] G.P. Gillman: A simple technology for arsenic removal from drinking water using hydrotalcite. *Science of the Total Environment*, 926–931, 366, 2006.
- [29.] Shan-Li Wang, Cheng Hua Liu, Ming Kuang Wang, Ya Hui Chuang, Po Neng Chiang: Arsenate adsorption by Mg/Al–NO₃ layered double hydroxides with varying the Mg/Al ratio. *Applied Clay Science*, 79–85, 43, 2009.
- [30.] Monteiro, M.I.C., Ferreira, F.N., Oliveira, N.M.M., Ávila, A.K.: Simplified version of the sodium salicylate method for analysis of nitrate in drinking waters. *Analytica Chimica Acta*, 125–129, 477, 2003.
- [31.] Bedenbaugh, J.H., Bedenbaugh, A.O., and Heard, T.S.: Substitution of volumetric for gravimetric methods and other improvements in a new molar volume-molar mass experiment. *Journal of Chemical Education*, 679–680, 66, 1989.
- [32.] Li Yang, Zoya Shahrivari, Paul K. T. Liu, Muhammad Sahimi, and Theodore T. Tsotsis: Removal of Trace Levels of Arsenic and Selenium from Aqueous Solutions by Calcined and Uncalcined Layered Double Hydroxides (LDH). *Ind. Eng. Chem. Res.*, 6804–6815, 44, 2005.
- [33.] N.K. Lazaridis, A. Hourzemanoglou, K.A. Matis: Flotation of metal-loaded clay anion exchangers. Part II: the case of arsenates. *Chemosphere*, 319–324, 47, 2002.



OXIDATIVE TREATMENT OF PHENOLIC WASTEWATERS: DETERMINATION OF THE EFFICIENCY OF FE-CONTAINING CATALYST

Adrienn BANGÓ, János HALÁSZ

University of Szeged, Faculty of Science and Informatics,
Department of Applied and Environmental Chemistry, HUNGARY

ABSTRACT

Phenol and substituted phenols are toxic organic pollutants commonly present in industrial water streams, especially in wastewater of chemical and pharmaceutical industries. However, the phenolic compounds in water can be natural origin, especially some Hungarian thermal water contains these materials. The effective removal of these toxic pollutants from wastewater is an important task of the environmental technology.

The treatment of phenol in aqueous solutions has been generally carried out by oxidation of molecular oxygen from the air, at elevated pressure in the presence of catalysts (CWAO: catalytic wet air oxidation). However, the development of CWAO technique is a continuous work to find the proper reaction conditions (oxidant, catalyst, etc.). Our task has been to study the applicability of iron containing materials with different structure in the oxidative treatment of phenolic wastewaters.

The catalyst samples (Fe-ZSM₅ zeolite, Fe-MCM₄₁ mesoporous silicate, Fe,Mg,Al-mixed oxide and supported Fe₂O₃) either were synthesized in our laboratory, or natural materials were used after thermal pretreatment (bauxite ore and red mud). XRD and BET adsorption methods were used for characterization of the catalysts. A recirculating bubble reactor was utilized to perform the oxidation of phenol in different origin waters. The reaction was followed by the determination of chemical oxygen demand (COD).

All the catalyst samples tested have reasonable activity in the air oxidation at ambient temperature, however, the efficiency can be improved by using of ozone. The obtained results proved the enforceability of the cheap mineral catalysts besides the expensive synthetic ones.

Keywords:

phenol, catalytic wet air oxidation, Fe-MCM-41, Fe-hydrotalcite, red mud

1. INTRODUCTION

Increasing interest for the environment is making it necessary to develop effective techniques to treat industrial waste waters containing compounds that are toxic to aquatic life. Phenol and substituted phenols are of particular interest because these toxic organic pollutants commonly present in industrial water streams, especially in wastewater of chemical and pharmaceutical industries. Moreover, phenol and its derivatives are powerful bactericide which prevents them from being treated in classical sewage processing plants even at concentrations as low as 50 mg/l [1]. Thus, phenolic aqueous effluents must be specially decontaminated before being biologically treatment. The effective removal of these pollutants from wastewater is a problem with great practical importance and interest.

In the present years, the treatment of phenol in aqueous solutions has been generally carried out by oxidation of molecular oxygen from the air at elevated pressure [2]. These are the so called "wet air oxidation: WAO" processes. The rate and efficiency of oxidation can be enhanced by the increasing of temperature and by the optimization of pH, however, the solubility of oxygen decreases at higher temperatures. The prosperous solution is decreasing of temperature, however, it could be achieved by application of catalyst. Nowadays, the investigation and development of catalysts, which would have high activity for oxidation of phenols and related compounds in aqueous solutions under mild conditions, are the objective of many studies in the wastewater treatment [3,4].

One of the most promising catalyst family for phenol oxidation is the transition metal containing micro and mesoporous materials [5-7].

The hydrotalcite type materials are layered double hydroxides (LDH) and their structures is very similar to that of the brucite $[Mg(OH)_2]$. For LDH-s an isomorphous substitution of Mg^{2+} by a trivalent element (generally aluminum) occurs in the brucite-like network and this replacing generates a positive charge in the brucite layer. The positively charged Mg-Al double hydroxide sheets are charge balanced by anions residing in the interlayer sections. During the synthesis of LDH both of magnesium and aluminum can be changed many bivalent or trivalent cations respectively resulted in materials with different character. LDH and LDH originated materials have many practical applications such as catalysts, adsorbents, anion-exchangers, stabilizers, etc. because of their relatively high surface area, basic properties, high metal dispersion and stability [8].

The MCM-41 material is a well-known member of the recently discovered mesoporous molecular sieves M41S family which possesses a regular hexagonal array of uniform pore openings with a broad spectrum of pore diameters between 1.5 and 10 nm [9].

As oxidation catalyst the $Fe^{2+} \leftrightarrow Fe^{3+}$ system is well-known in the Fenton type reactions in which H_2O_2 is the oxidation agent [10].

Recently, development of catalysts based on waste materials is an issue of great interest, because of two environmental objectives could be achieved simultaneously: (i) reuse the waste materials and (ii) the saving of raw materials, such as catalyst precursors [11]. After a proper pretreatment as possible waste material the „red mud” can be considered as hydrodechlorination catalyst. The red mud is a by-product in the manufacture of alumina using Bayer-process that contains mainly oxides of iron, aluminum, titanium, silicon, calcium and sodium. In Hungary the annual red mud production is over one million tons in the last decades. The environmental danger of red mud originates from the high alkalinity, and from the very fine-graining. The mixed oxide from red mud could be possible alternative of commercial scale catalysts implied for hydrodechlorination reactions [12].

In this paper we present the study on the preparation and application in air and ozone oxidation of phenol over Fe-containing synthesized (hydrotalcite, MCM-41) or natural origin catalysts (red mud and bauxite after heat treatment) at ambient temperature working on atmospheric pressure.

2. EXPERIMENTAL SECTION

Catalysts

The Al/Fe-mixed oxide was synthesized by coprecipitation from aluminum nitrate and iron nitrate solutions followed by calcination at 500 °C for four hours, and the alumina supported iron oxide was prepared by impregnating $\gamma-Al_2O_3$ with iron nitrate solution followed by heat treatment at 500 °C.

The Fe/Al/Mg-hydrotalcite ($M^{II}/M^{III} = 2$, and M^{III} : 0.9 Al and 0.1 Fe) was prepared by coprecipitation at constant pH = 10 ± 0.2 of an aqueous solution of $Mg(NO_3)_2$, $Al(NO_3)_3$ and $Fe(NO_3)_3$ with a solution of NaOH and Na_2CO_3 .

The Fe-ZSM-5 zeolite catalyst was prepared by solid state ion-exchange starting from the synthesized H-ZSM-5 and $FeCl_3 \cdot 5 H_2O$.

The Fe-MCM-41 specimen was prepared from sodium silicate, CTMA-Br and $Fe(NO_3)_3$ solution at pH 12. The crystallization was carried out at 373 K for 2 days followed by calcination at 823 K for six hours.

The *red mud* utilized for catalyst preparation was the original waste from the Ajka Aluminum Industry of Hungary. The wet *red mud* was filtered, dried at 100 °C followed by calcination at 500 °C for four hours. The average composition of the Hungarian *red mud* is displayed in Table 1.

Table 1: The average composition of Hungarian *red mud*

Al_2O_3	16-18 wt%	CaO	0,5-3,5 wt%
Fe_2O_3	33-48 wt%	V_2O_5	0,2-0,3 wt%
SiO_2	9-15 wt%	P_2O_5	0,5-1 wt%
TiO_2	4-6 wt%	CO_2	2-3 wt%
Na_2O	8-12 wt%	S	0.15-0.30 wt%
MgO	0.3-1 wt%	F	0.10-0.15 wt%

All the catalyst samples were heat treated at 400 °C for two hours before the use in the oxidation reaction. The catalyst samples were characterized by XRD, N_2 adsorption IR-spectroscopy and TEM.

Methods

The oxidation of phenol was carried out in a recirculating laboratory bubble column reactor (Fig. 1).

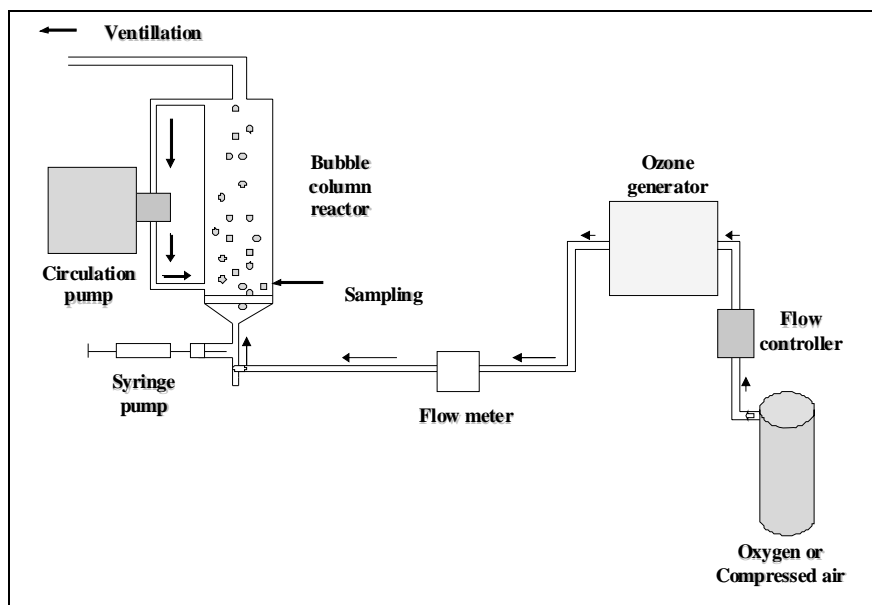


Figure 1: The experimental setup for oxidative treatment of phenol containing waters

In the bubble column reactor air at atmospheric pressure or ozone containing air (also at the same pressure) was used as flowing gas phase. The rate of the gas flow was constant: 50 dm³/h, and the reaction was carried out at ambient temperature.

The reaction was followed by the determination of Chemical Oxygen Demand (COD) using the operative Hungarian Standard, No: MSZ 448-20.

3. RESULTS AND DISCUSSIONS

Characterization of the catalysts

The X-ray diffractograms of the hydrotalcite and the hydrotalcite origin Fe-Mg-Al mixed oxide, Fe-ZSM-5 and Fe-MCM-41 samples prove the expected crystallinity, while the XRD data of bauxite and red mud are very complicated correspond to the complex structure of these materials.

The BET surface areas and pore diameters could be calculated by the evaluation of N₂ adsorption isotherms, the data are presented in Table 2. The Fe content of the catalysts were determined by X-ray fluorescence method.

Table 2: Characteristics of the catalysts

Catalyst sample	Average pore diameter (Å)	Character of the pore	BET surface area (m ² /g)	Fe content (w/w%)
Fe/Al/Mg-mixed oxide	180	wide	135	1.0
FeZSM-5	5.5	narrow	335	4.13
Fe-MCM-41	36	wide	964	1.5
Fe ₂ O ₃ /Al ₂ O ₃	-	wide	103	2.5
Bauxite, calcined	-	none	2.5	14.0
red mud, calcined	-	none	37	35.0

Oxidation measurements

In the first stage the catalysts were tested in a well determined reaction, namely in the oxidation of phenol solution in distilled water (concentration: 2000 mg/L), at ambient temperature, where the pH of the solution was 4.6. The reactions were run for four hours, with sampling and COD determination hourly. As oxidant air or ozone was applied, the latter was produced using an *OZOMATIC Modular* type ozone equipment. The data can be seen on Figure 1, lines A and B.

Considering the data it could be established, that using air the oxidation efficiency is low (under 5 %), and by charge of ozone the activity could be increased significantly, but the extent is also low.

To regard the catalyst it could be appointed that the efficiency of the cheap, iron oxide base materials near to activity of the synthetic samples, nevertheless their surface area is significantly less.

In the next measurements the solutions were stabilized using a phosphate-borax buffer solution of pH 6.8, and the reactions were run similarly as earlier. The results obtained can be seen in Figure 1, lines C and D.

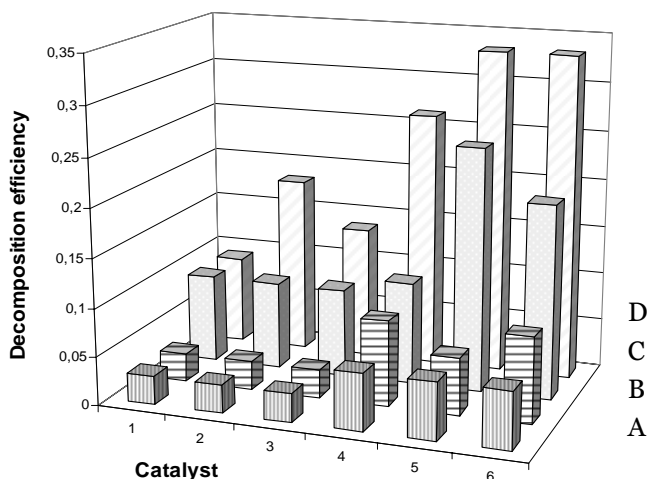


Figure 2: Catalytic oxidation of phenol in water with: a) air, B) ozone, C) air by buffering, d) ozone by buffering; Catalysts: 1. red mud, 2. Fe₂O₃/Al₂O₃, 3. bauxite, 4. Fe-ZSM-5, 5. Fe-hydrotaalcite, 6. Fe-MCM-41

To summarize the results obtained for synthetic waste water: the demolition of phenol could be achieved with relatively high efficiency. Choosing the optimal pH, the oxidation by ozone is proper, first of all in the presence of the synthetic, porous catalysts. Nevertheless, the activity of the natural origin catalysts with iron oxide content are less, these achievements are enough high to the demolition of the organic pollutants.

In the initial stage the oxidation was fast, however, after four hours a saturation could be observed. This behavior can be explained by the formation of stable intermediates which oxidation is hindered. The identification of these compounds, as well as the determination of the mechanism of the oxidation is an another task.

4. CWAO treatment of phenolic thermal water

Additional studies were carried out with used (cooled) thermal water from Szentes (southeast Hungary). The pH of this water 8.6 and its COD is 90 mg/dm³. The investigations were emphasized to utilize the natural origin catalysts, while for treatment of large amount of water – considering the economical conditions – the application of these materials possesses fundamental importance.

The results obtained can be seen on Fig. 3 and 4. In the reaction by air (Fig. 3) the tendency of efficiency curves is close to saturation for two hours, which indicate the formation of stable intermediates. These compounds could react with the radicals or could inhibit the active centers of the catalyst. To determine of these intermediates or steps is important for the clarifying the mechanism of the reaction, moreover for the optimization of the reaction conditions as well.

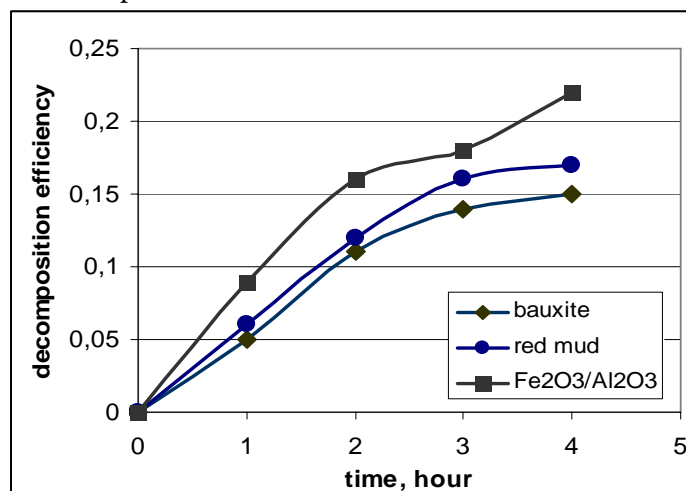


Figure 3: Oxidative treatment of used thermal water (COD: 90 mg/dm³) in the presence of iron oxide base catalysts, oxidative agent: air

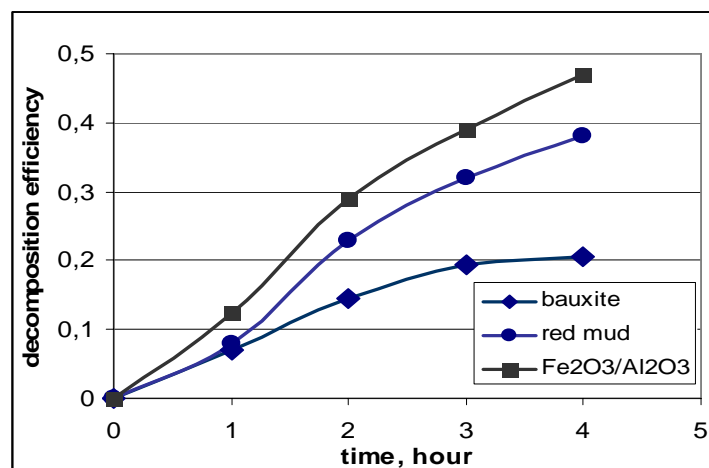


Figure 4: Oxidative treatment of used thermal water (COD: 90 mg/dm³) in the presence of iron oxide base catalysts, oxidative agent: ozone

Using ozone as oxidative agent, the decomposition efficiency increased in a large extent, and the saturation character could be observed only in the case of bauxite. Theoretically, this method is proper for removing of organic pollution in industrial scale. Considering the economical aspects, however, the utilization of ozone is too expensive for the treatment of the high amount of thermal water. Therefore, the development of catalytic air oxidation is the important task.

5. CONCLUSIONS

The mesoporous Fe-MCM-41, Fe/Al/Mg-mixed oxide and the microporous Fe-ZSM-5 zeolite are promising catalysts for the treatment of toxic wastewater containing phenol or other poisonous organic materials. Highest activity could be produced in the presence of Fe-MCM-41.

Considering the technological aspects the application of Fe-MCM41 would be prosperous because of the higher specific activity, however, from the economic point of view the application of the much less expensive natural catalysts (red mud or bauxite) could be suggested.

REFERENCES

- [1] Pintar, A., Levec, J., *Catalytic oxidation of organics in aqueous solutions I. – Kinetics of phenol oxidation*, J.f Catal., 135, 345-357 (1992).
- [2] Mishra, V.S., Mahjani, V.V. and Joshi, J.B., *Wet air oxidation*, Ind. Eng. Chem. Res., 34, 2-48 (1995).
- [3] Luck, F., *Wet air oxidation: past, present and future*, Catal. Today 53, 81-91 (1999).
- [4] Lin, S.S., Chen, C.L., Chang, D.J. and Chen, C.C., *Catalytic wet air oxidation of phenol by various CeO₂ catalysts*, Water Res., 36, 3009-3014 (2002).
- [5] Alejandre, A., Medina, F., Rodriguez, X., Salagre, P., Cesteros, Y. and Sueiras, J.E., *Cu/Ni/Al layered double hydroxides as precursors of catalysts for the wet air oxidation of phenol aqueous solutions*, Appl. Catal. B: Environmental, 30, 195-207 (2001).
- [6] Chen, H., Sayari, A., Adnot, A. and Laraci, F., *Composition-activity effects of Mn-Ce-O composites on phenol catalytic wet oxidation*, Appl. Catal. B: Environmental, 32, 195-204 (2001).
- [7] Wu, Q., Hu, X., Yue, P.L., Zhao, X.S. and Lu, G.Q., *Copper/MCM-41 as catalyst for the wet oxidation of phenol*, Appl. Catal. B: Environmental, 32, 151-156 (2001).
- [8] Cavani, F., Trifiro, F. and Vaccari, A., *Hydrotalcite-type anionic clays: Preparation, properties and applications*, Catal. Today, 1, 173-301 (1991).
- [9] Selvam, P., Bhatia, S.K. and Sonwane, C.G., *Recent advances in processing and characterization of periodic mesoporous MCM-41 silicate molecular sieves*, Ind. Eng. Chem. Res., 40, 3237-3261 (2001).
- [10] Neyens, E., Baeyens, J., *A review of classic Fenton's peroxidation as an advanced oxidation technique*, J. Hazard. Mater., 98, 33-50 (2003).
- [11] Sussil, S., Batra, V.S., *Catalytic applications of red mud, an aluminium industry waste: A review*, Appl. Catal. B: Environmental, 81, 64-77 (2008).
- [12] Halász, J., Hodos, M., Hannus, I., Tasi, G. and Kiricsi, I., *Catalytic detoxification of C₂-chlorohydrocarbons over iron containing oxide and zeolite catalysts*, Colloids and Surfaces A: Physicochem. Eng. Aspects, 265, 171-177 (2005).



THERMODYNAMIC STUDY OF A SYMMETRICAL DISAZO DIRECT DYE DERIVED FROM 4,4'-DIAMINO-BENZANILIDE ON MERCERIZED COTTON

SIMU Georgeta Maria, FUNAR-TIMOFEI Simona, BALȘ Gianina

Institute of Chemistry Timișoara, Romanian Academy,
B-dul Mihai Viteazul 24, 300223 Timișoara, ROMANIA

ABSTRACT:

The sorption isotherms of a symmetrical disazo direct dye with symmetrical structure on a mercerized cotton were determined at 60°, 86° and 96°C. In order to find out the best sorption model of the considered dyes, a theoretical study was also performed. The experimental data obtained from the dyeing process was fitted by non-linear and linear regression analysis to the classical Freundlich, Langmuir and Nernst isotherms. Better statistical results were obtained in the case of the Freundlich sorption model.

KEY WORDS:

Direct dyes, dyeing theory, adsorption isotherms, Nernst model, Freundlich model, Langmuir model

1. INTRODUCTION

The textile dyeing equilibrium of the direct dyes on cellulose fibres presents a great interest, but a general model which could offer complete explanations of the dye-cellulose fibre sorption was not reported yet [1-4].

The dye adsorption at equilibrium represents the maximum possible sorption from the dyebath, under certain conditions. From the final dye equilibrium concentrations, sorption isotherms are obtained, most of them corresponding to the Freundlich and Langmuir equations [1].

In the Freundlich model (equation 1) the dye is considered as being contained in an internal phase of volume V of the fibre [1].

$$[C]_f = K_F \cdot [C]_s^x \quad (1)$$

where:

$[C]_f$ represents the dye concentration in the fibre at equilibrium, in mol/kg dry fibre, and

$[C]_s$ represents the dye concentration in solution at equilibrium, in mol/L;

K_F is the equilibrium constant, and x is a sub-unitary power.

The Nernst adsorption isotherms (equation 2) are considered as a limit case of Freundlich and Langmuir adsorption isotherms [5].

$$[C]_f = K_P \cdot [C]_s \quad (2)$$

The Langmuir isotherm (equation 3) has been obtained from kinetics considerations [4]. The basic assumption is related to the idea that the dye adsorption takes place on independent fixed sites, in monomolecular layer and all the adsorption positions are equivalent energetically.

$$\frac{1}{[C]_f} = \frac{1}{S_f \cdot [C]_s} \cdot K_L + \frac{1}{S_f} \quad (3)$$

where S_f is the saturation value in mols/kg fibre and K_L is the equilibrium constant.

Some authors reported that the Langmuir model offers a better interpretation of the direct dye cellulose sorption than the Freundlich one [2-3, 6-9].

In this present work, an experimental and theoretical study of the sorption of one disazo direct dye with symmetrical structure on a cellulosic substrate was performed. The aim of this study was to establish the best sorption model of the considered dye. For this purpose, the equilibrium sorption data of the studied dye were fitted by non-linear regression analysis to the Nernst, Freundlich and Langmuir sorption models.

2. THE STUDY

General

All the chemicals were purchased from Merck Co, Aldrich Chemical Co and Reactivul București.

The dye used in this study was a disazo direct dye derived from 4,4'-diaminobenzanilide. The coupling component was resorcinol. The dye was synthesized, purified by several recrystallizations from distilled water and characterized by means of electronic spectra (VIS) and mass spectroscopy (MS-FAB) and its homogeneity was determined by thin layer chromatography (TLC).

Electronic spectra were recorded on a Cecil CE 7200 spectrophotometer. Mass spectra were recorded on a Nermag R 10-10 spectrometer, from nitrobenzylalcohol and glycerol as matrix. The TLC data were taken from silica gel plates (Merck 60F-25) and *i*-propanol/methylethylketone/ NH_4OH 25%=4:3:3 (v:v:v) as eluting system.

In the experimental study of the dye sorption on a cellulosic substrate, samples of mercerized cotton (100 %) were used. The samples were soaked in a bath with a liquor ratio of 20:1 at 80°C for 60 minutes, rinsed with distilled water and air - dried.

Procedures

Synthesis of resorcinol ← 4, 4'-diaminobenzanilide → resorcinol

A suspension of 11.5 g 4,4'-diaminobenzanilide (0.05 mol), 70 ml water, 26 ml (0.27 mol) 35% HCl and 50 g ice was bis-diazotised by the direct method [10].

11.4 g (0.1 mol) of resorcinol were dissolved in a solution containing 0.5 g sodium acetate in 90 mL water. The solution was cooled to 5°C and was added dropwise to the solution of bis-diazonium salt obtained above, in a 45 minutes period. The temperature of the reaction mixture was kept around 5°C and the pH of the reaction was maintained around 8.5 by addition of 0.5 mol/L Na_2CO_3 aqueous solution. The mixture was stirred for three hours at 5-10°C. The dye was precipitated by salting out with sodium chloride and was separated by vacuum filtration. The yellow disazo dye was obtained in 88% yield.

Samples of the synthesized dye, free of sodium chloride were obtained by dyeing cotton fabric in boiling solutions containing 5 g of dye in 250 mL water. After rinsing the dyed fabrics, the dye was extracted using solutions of 50-60% aqueous pyridine. The extracts were then evaporated, giving a dye free of salts.

Dyeing system and measurements

The dyeing processes were carried out in round flasks, equipped with a stirrer, a condenser and a thermometer. The dyeings were made at three temperatures, namely 60°, 86° and 96°C ($\pm 1^\circ\text{C}$). The cotton samples weight in every case was near 70 mg (± 0.1 mg). The liquor ratio was 150:1. The initial dyebath concentrations of the studied dye varied from 0.15 g/L to 5 g/L. Sodium chloride concentrations in the dyebath were in every case $6.84 \cdot 10^{-2}$ mol/L.

The time necessary for reaching equilibrium for each dye and each dyeing temperature was evaluated in a series of preliminary experiments.

The dyed cotton samples were removed from the hot dyebath and rinsed for about 30 seconds in ice water to remove the adhering dye liquor. The dye was extracted from the dyed samples with 25% aqueous pyridine at 80°C. The molar extinction coefficients were determined at one wavelength from the Lambert-Beer law.

The dye concentrations in the dyebath as well as the extracted dye from the substrate were recorded spectrophotometrically, using a Specord M40 UV-VIS spectrophotometer. Other details on the dyeing system can be found in references [6-9].

In order to find out the model which describes best the sorption of the studied dyes on mercerized cotton, the experimental data thus obtained were fitted to the classical Nernst, Freundlich and Langmuir sorption models by nonlinear regression analysis. For this purpose, the STATISTICA software [11] was used.

The standard deviation (expressed in [%]) of the experimental values obtained for the concentration of the dye on the substrate (C_f) from the calculated ones) was calculated according to equation (4).

$$SS = \left[\frac{1}{N} \sum_{i=1}^N \left(\frac{C_{fi \text{ exp}} - C_{fi \text{ calc}}}{C_{fi \text{ calc}}} \times 100 \right)^2 \right]^{\frac{1}{2}} \quad (4)$$

where the suffixes "exp" and "calc" refer to experimental and calculated values, respectively; suffix "i" refers to the number of sorption data.

Figure 1 presents the Freundlich dye adsorption isotherm at 60°, 86° and 96°.

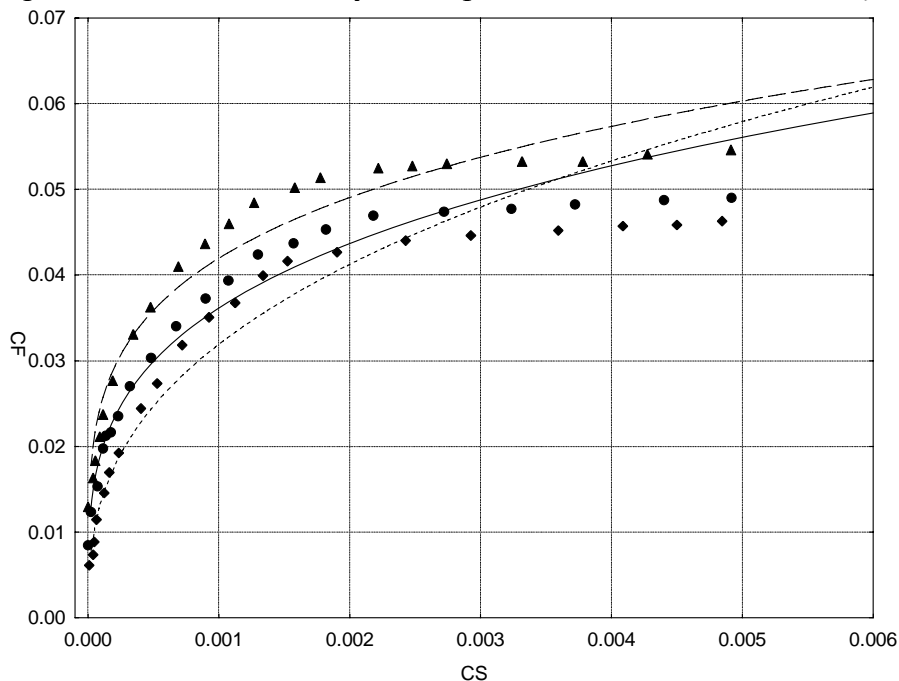
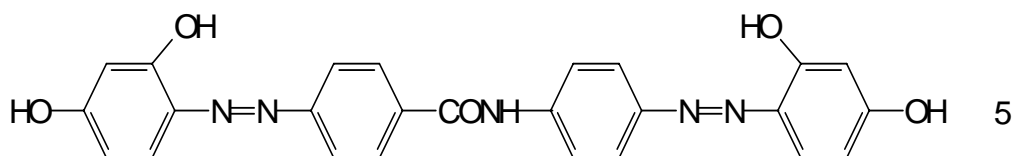


Figure 1. Freundlich adsorption isotherm at 60° (▲ points and large interrupted fitting line), 86° (● points and continuous fitting line) and 96° (◆ points and small interrupted fitting line)

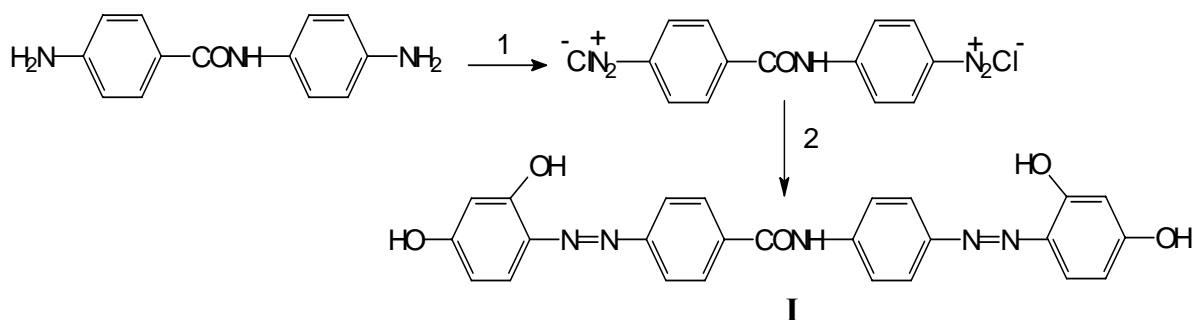
3. DISCUSSIONS

In the present study, the sorption isotherms of a symmetrical disazo direct dye on mercerized cotton were determined at 60°, 86° and 96°C. The studied dye (I) contains 4,4'-diaminobenzanilide as diazo component and resorcinol as coupling component.



Dye I

The dye was prepared in a two steps procedure, as shown in Scheme 1.



Scheme 1

1. NaNO₂, HCl, 0°C, 1 hour, 2. Resorcinol, 1:2 molar ratio, pH = 8.5-9, 5-12°C, 3 hours.

The bis-diazotization of 4, 4'-diaminobenzanilide was carried out by the direct method, in aqueous HCl solutions.

The coupling step was conducted at a pH value of 8.5-9, and with a 2-3% excess of coupling component. The progress of the coupling reaction was monitored by the usual way (drop reaction) and by thin layer chromatography (TLC), when the formation of dye **I** was examined. Dye **I** was obtained with overall high yields and was characterized by means of VIS spectra and negative (-) FAB – MS spectroscopy. Dye homogeneity was examined by TLC. The chromatographic mobility (R_f) of dye **I** was found equal to 0.76. The VIS spectrum was examined in the region of 350 to 800 nm. The spectra contain one maxim of absorption at about $\lambda_{max} = 435$ nm ($\epsilon_{1\text{cm}}^{1\text{g/L}} = 52$) in 0.1 mol/L aqueous NaOH solution. The molecular peak [MS(FAB-1)] was found at 468.45 m/z.

The disazo dye **I** was further used in the experimental study of the dye sorption on mercerized cotton, as shown in Experimental section. Dyeings were carried out until equilibrium was reached, at three different temperatures and in presence of sodium chloride. The experimental equilibrium dye concentrations in fibre $[C]_f$ and in solution $[C]_s$ were fitted to equations (1) and (2) by nonlinear regression analysis and to equation (3) by linear regression analysis, in order to provide the best model of sorption of the studied dye on cotton.

The values of the thermodynamic parameters K_F , K_L respectively S_f have been evaluated by means of nonlinear least squares fit of experimental sorption data to respective equations (1, 2), respectively by linear regression fit of experimental sorption data to equation (3) for K_P . The multiple regression coefficient (R) and the standard deviation (SS) calculated by equation (4) were used as statistical criterions in the regression analysis.

The thermodynamic data and the statistical results obtained for the studied dyes are presented in tables 1, 2 and 3.

TABLE 1
 Thermodynamic data and statistical results of the sorption on mercerized cotton
 of dye I according to equation $[C]_f = K_F \cdot [C]_s^x$ (Freundlich model)*

T [°C]	K_F [L/g]	x	R	SS [%]
96	0.411	0.37	0.949	11.59
86	0.238	0.27	0.979	6.6
60	0.199	0.23	0.977	9.3

* K_F represents the Freundlich partition constant; x- the subunitary power;
 R- the multiple regression coefficient and SS-the standard deviation.

TABLE 2
 Thermodynamic data and statistical results of the sorption on mercerized cotton
 of dye I according to equation $\frac{1}{[C]_f} = \frac{1}{S_f \cdot [C]_s} \cdot K_L + \frac{1}{S_f}$ (Langmuir model)*

T [°C]	S _i [mol/kg]	K _L [L/mol]	R	SS
96	0.041	10050.96	0.920	24.63
86	0.041	50252.52	0.703	27.62
60	0.046	125002.3	0.579	27.39

*S_i represents the saturation value; K_L - Langmuir partition constant;
 R –the multiple regression coefficient and SS-the standard deviation

TABLE 3
 Thermodynamic data and statistical results of the sorption on mercerized cotton
 of dye I according to equation $[C]_f = K_P \cdot [C]_s$ (Nernst sorption model)*

T [°C]	K _P 10 ⁻² [L/mol]	R	SS
96	13.63	0.883	10.49
86	15.09	0.864	32.09
60	17.19	0.866	62.84

* K_P - Nernst partition constant;
 R- the multiple regression coefficient and SS-the standard deviation.

Comparing the obtained data presented in Tables 1, 2 and 3 it could be seen that for the studied dye, overall high values of R respectively low standard deviation (SS) values were obtained for the Freundlich sorption model as compared to the classical Nernst and Langmuir models.

4. CONCLUSIONS

The equilibrium sorption isotherms of a symmetrical disazo direct dye on cotton were determined at three temperatures and one sodium chloride concentration.

Experimental data were fitted to the standard known adsorption isotherms of Nernst, Freundlich, and Langmuir by nonlinear regression. The results indicated best statistical values in the case of the Freundlich sorption model.

ACKNOWLEDGEMENTS

This work was supported by the Grant contract 71 GR of the MEC (Romania)

REFERENCES

- [1] Vickerstaff T., The Physical Chemistry of Dyeing, Imperial Chemical Industries Limited: London, **1954**.
- [2] Porter J. J., Perkins W. S., A Study Of The Thermodynamics Of Sorption Of Three Direct Dyes On Cellophane Film, *Textile Res J*, **40**, 81-87, **1970**.
- [3] Bairathi A., Dyeing Sorption Isotherms Of Three Direct Dyes And Their Mixtures On Purified Cotton, *Textile Chem. Color.*, **25**, 41-46, **1993**.
- [4] Peters R.H., Textile Chemistry. The Physical Chemistry of Dyeing, Elsevier Amsterdam, Vol. III, **1975**.
- [5] Rys P., Zollinger H., Fundamentals of the Chemistry and Application of Dyes, Wiley-Interscience: London-New York-Sydney and Toronto, **1972**.
- [6] Simu G., Funar-Timofei S., Hora S., Schmidt W. E., Kurunczi L., Şişu E., Morin N., Coloranti Directi Derivati ai 4,4'-Diaminobenzanilidei. I. Sinteza si Studiul Izotermelor de Adsorbție pe Bumbac ale unui Colorant Disazoic Direct cu Structura Asimetrici, *Rev Chim (Bucharest)*, **53**, 826-829, **2002**.

- [7] Simu G., Funar-Timofei S., Hora S., Kurunczi L., Experimental and Theoretical Study of the Adsorption of a Trisazo Direct Dye Derived from 4,4'-Diaminobenzanilide on a Cellulose Substrate, *Molec Cryst Liq Cryst*, **416**, 97-104, **2004**.
- [8] Simu G., Funar-Timofei S., Kurunczi L., Schmidt W., A Thermodynamic Study of the Sorption of an Asymmetric Disazo Direct Dye on Mercerized Cotton, *Rev Roum Chim*, **49(3-4)**, 345-349, **2004**.
- [9] Simu G., Funar-Timofei S., Kurunczi L., Hora S., Schmidt W., Grad M., Synthesis and Study of Adsorption Isotherms of a Trisazo Direct Dye on Cotton Fibre, *Cellulose Chem Technol*, **38 (5-6)**, 409-416, **2004**.
- [10] Simu G. M., Chicu S. A., Morin N., Schmidt W., Sisu E., Direct Dyes Derived from 4,4'-Diaminobenzanilide. Synthesis, Characterization and Toxicity Evaluation of a disazo symmetric direct dye, *Turk J Chem*, **28**, 579-585, **2004**.
- [11] STATISTICA 7.1, StatSoft Inc, Tulsa, OK, USA



INCLUSION COMPLEXES WITH A SYMMETRICAL DISAZO DYE WITH α - AND β -CYCLODEXTRINS

BALȘ Gianina, SIMU Georgeta Maria

Institute of Chemistry Timișoara of Romanian Academy, Timișoara, ROMANIA

ABSTRACT:

The results for the synthesis of a disazo dye with symmetrical structure derived from 4, 4'-diaminobenzanilide and its inclusion complexes (IC) with α - and β -cyclodextrins is reported. The free azo dye was prepared by the bis-diazotisation of 4,4'-diaminobenzanilide and the coupling reaction of the obtained bis-diazonium salt with alkaline solutions of the salicylic acid. The free azo dye and its inclusion complexes with α - and β - cyclodextrins were purified by gravity and flash column chromatography. Further, UV-VIS, FTIR and thin-layer chromatography (TLC) studies of the synthesized compounds were performed.

KEYWORDS:

Azo dye, Cyclodextrins, Inclusion complexes

1. INTRODUCTION

Cyclodextrins (CD) are macrocyclic compounds built from glucopyranose units linked by α -(1,4)-glycosidic bonds. CD can be obtained by enzymatic degradation of starch; in this process compounds with 6-12 glucopyranose units per ring are produced. Depending on the enzyme and the way in which the reaction is controlled, the main product is α , β or γ -cyclodextrin (6, 7 and 8 glucopyranose units, respectively).

Cyclodextrins can form inclusion complexes with a large number of organic molecules, a property that enables them to be used in a variety of different textile applications [1]. Through the incorporation, the physical and chemical proprieties of the "guest" compounds are changing. Their toxicity is lower, and they became biodegradable [2].

Azo dyes represent a major group of all the synthetic dyes and have extensive applications in textile industry, paper industry, additives, food, cosmetics and pharmaceutical industry [3]. The encapsulation of the disazo dye with cyclodextrins is a procedure that has been investigated as a method of controlling their stability, solubility and aggregation. It was found that rotaxane structure offers the protection of the dye which is encapsulated inside the cavity of the cyclodextrin, without forming covalent bonds [4].

In this work, the synthesis of a disazo dye and its inclusion complexes in α - and β -cyclodextrins is presented.

2. THE STUDY

The chemicals used in this study were of analytical grade and were obtained from Merck Co., Aldrich and Chimopar Bucharest. 4,4'-diaminobenzanilide was synthesized according to reference [5].

The thin layer chromatographic (TLC) data were taken from silica gel plates (Merck 60F-254) using isopropanol: methyl-ethyl-ketone: ammonia 25% = 4:3:3 as eluting system for the free azo dyes, respectively buthanol-ethanol-water = 4:3:5 as eluting system for their inclusion complexes.

For the gravity and flash column chromatography we used silica gel (Merck) as stationary phase and buthanol-piridine-water = 3:3:3 and buthanol-ethanol-water = 4:3:5 as eluting systems.

The FTIR spectroscopy was recorded on JASCO FT/IR -4200 from KBr pellets.

The UV-VIS spectra were recorded on a Cecil CE-7200 spectrophotometer from 1 mol/L NaOH aqueous solutions for the free disazo dyes, and from aqueous solutions in the case of the inclusion complexes.

General mode of synthesis of the azo dye AS

0.06 g 4,4'-diaminobenzanilide (0.26 mmol) was bis-diazotised using the direct method of diazotization, in mineral acid solution, with sodium nitrite. The reaction was maintained at 0±5 °C for 1 hour and the pH in the range of 0.5±1 [8]. The bis-diazonium salt thus obtained was coupled in a 1:2 molar ratio with alkaline solutions of the salicylic acid (dye AS). The pH of the reaction mixtures was maintained in the range of 8.5±9 by periodic addition of Na₂CO₃. The obtained dye was separated by filtration and was purified by gravity and flash column chromatography.

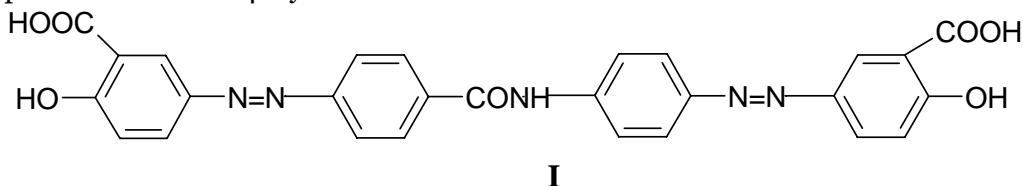
General mode of synthesis of the azo dyes/cyclodextrins complexes

0.06 g 4,4'-diaminobenzanilide (0.26 mmol) was bis-diazotised by the direct method. To the bis-diazonium salt thus obtained, aqueous solutions of the corresponding cyclodextrins (α , and respectively β) were added dropwise. The reaction mixture was maintained under vigorous stirring at 0±5 °C for 30 minutes. The encapsulated bis-diazonium salt was subjected to the coupling reaction with alkaline solutions of salicylic acid in the case of the β -cyclodextrin. In the case of the synthesis of the α -cyclodextrin complex, the alkaline solution of salicylic acid was added to the encapsulated bis-diazonium salt. The coupling reaction was monitored by the conventional method and by TLC. The reaction mixture was maintained under stirring at 7.5±8 pH, at 20 °C for 2 hours. The final products were separated by centrifugation and the rotaxane complexes were isolated by evaporation from the supernatant.

The synthesized dyes and their inclusion complexes were purified by gravity and flash column chromatography and were characterized by thin-layer chromatography (TLC), FTIR and UV-VIS spectroscopy.

3. DISCUSSIONS

The first step of this work was to prepare the disazo dye with structure (I), and further its complexes with α - and β -cyclodextrins.



From previous work [6], it was noticed that the bis-diazotization of 4,4'-diaminobenzanilide occurred with better yields when the direct method of bis-diazotisation is used. The temperature was maintained in the range of 0±5°C and the pH of the mixture around 1. In the coupling step, 3 % excess of coupling component was used. In order to avoid the formation of undesirable by-products, the bis-diazonium salt was quickly added to the alkaline solution of the coupling components and the pH was maintained and adjusted in the range of 8±9 by periodic addition of Na₂CO₃.

For the preparation of the inclusion complexes of the model dye (I) with α - and β -cyclodextrins, a simple procedure using the hydrophobic effect to direct rotaxane formation was developed. According to this procedure, 4, 4'-diaminobenzanilide was bis-diazotized by the direct method, and to the bis-diazonium salt thus obtained, an aqueous solution of α - and then β -cyclodextrin was added. The symmetric coupling reaction of the encapsulated bis-diazonium salt with alkaline solution of the coupling component (salicylic acid), in the case of the α -cyclodextrin, was obtained by 2 methods: firstly, the encapsulated bis-diazonium salt was added to the alkaline solution of the coupling component (SA) as described in reference [7]. Secondly, the alkaline solution of the coupling component is added to the encapsulated bis-diazonium salt. In the case of the β -cyclodextrin the encapsulated bis-diazonium salt was

subjected to the coupling reaction with alkaline solutions of salicylic acid. Further, the coupling reaction of the encapsulated bis-diazonium salt with salicylic acid was carried-out.

It was noticed that when the bis-diazonium salt is added to the alkaline solution in the presence of α -, respectively β -cyclodextrin, the solution immediately turns yellow. Thin layer chromatography reveals the formation of the rotaxane, respectively the non-rotaxanated dye, which is rather insoluble in water and can be separated from the rotaxane by centrifugation.

The progress of the coupling reaction was monitored by the usual way (drop reaction with an alkaline solution of 1-amino-8-hydroxy-3,5-naphthalene disulphonic acid and with the diazonium salt of p-nitroaniline) and by TLC.

The synthesized dyes and their inclusion complexes were purified by gravity and flash column chromatography, and were characterized by thin-layer chromatography (TLC), FTIR and UV-VIS spectroscopy. The results are shown in Table 1 and Figure 1.

Table 1.

Yields of reaction, chromatographic mobilities R_f , and spectrophotometric properties of the disazo dye I, non-encapsulated dye and rotaxane complexes.

Dye and dye_CD	η [%]	R_f^*	λ_{max}^{**} [nm]	$lg\epsilon$
AS	82	0.88	441	1.8
AS_ α -CD	13	0.65	269	2.3
AS_ β -CD	23	0.68	355	1.9

*Silicagel plates, iso-propanol:methy-ethyl-ketone:ammonia 25% = 4:3:3 as eluent of the synthesized dyes, respectively eluent: buthanol: ethanol: H₂O = 4: 3: 5 of the rotaxane complexes.

** λ_{max} – wavelenght of maxim absorbance, from dye solution in 1 mol/L NaOH, respectively aqueous solutions in the case of the inclusion complexes, CECIL 7200 spectrophotometer.

The FTIR study: KBr pellets, for the disazo dye and inclusion complexes are showed a difference among the initial α - and β -cyclodextrins, free disazo dye and its complexes. IR: for α -CD was found: OH, 3403 cm⁻¹; CH₂, 2925 cm⁻¹; CH, 1337 cm⁻¹; COC, 1079 cm⁻¹; for β -CD: OH, 3383 cm⁻¹; CH₂, 2927 cm⁻¹; CH, 1337 cm⁻¹; COC, 1079 cm⁻¹; for dye SA: OH, 3377 cm⁻¹; CH, 1590 cm⁻¹; CO, 1635 cm⁻¹; for SA/ α -CD complex: OH, NH, 3438 cm⁻¹; CONH, 2241 cm⁻¹; N=N, 1414 cm⁻¹; CO, 1641 cm⁻¹; CH, 1561 cm⁻¹; COC, 1021 cm⁻¹; and for SA/ β -CD complex: OH, NH, 3425 cm⁻¹; CONH, 2241 cm⁻¹; N=N, 1415 cm⁻¹; CO, 1638 cm⁻¹; CH, 1576 cm⁻¹; COC, 1030 cm⁻¹.

In Figure 1 the UV-VIS spectra for the disazo dye, cyclodextrins and inclusion complexes are shown. The absorption spectra in the 200÷700 nm region of the disazo dye and cyclodextrins were comparated with inclusion complexes, and differences in the spectra were observed. It was noticed that both obtained inclusion complexes show a hipschromic shift of their absorptions maxima in comparison to the free azo dye (SA).

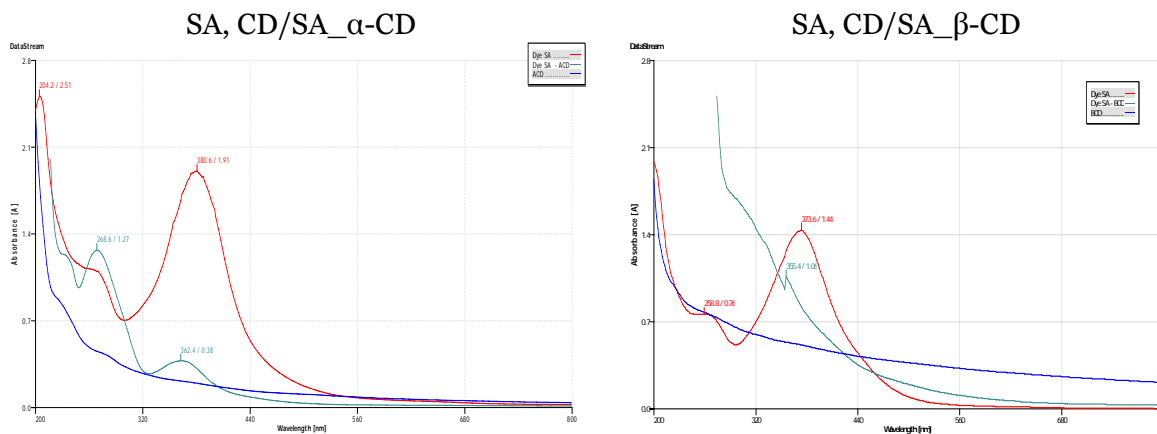


Figure 1. The UV-VIS spectra for the diazo dye, ciclodextrins and inclusion complexes

4. CONCLUSIONS

Two inclusion complexes of a symmetrical disazodye with α - and β -cyclodextrin have been obtained and characterized by UV-Vis spectra, FTIR and Thin Layer Chromatography.

The direct route to a rotaxane encapsulated azo dye will facilitate investigations into consequences of chromophore encapsulation.

REFERENCES

- [1] Bojana Von_cina, Vera Vivod, Darja Jausˇovec, β -Cyclodextrin as retarding reagent in polyacrylonitrile dyeing, *Dyes and Pigments*, **74**, 642-646, 2007.
- [2] Wenz G., Cyclodextrins as Building Blocks for Supramolecular Structures and Functional Units, *Angew. Chem. Int. ed. Engl.*, **33**, 803-822, 1994.
- [3] Aydan Yilmaz, Elif Yilmaz, Mustafa Yilmaz, Richard A. Bartsch, Removal of azo dyes from aqueous solutions using calix[4]arene and β -cyclodextrin, *Dyes and Pigments*, **74**, 54-59, 2007.
- [4] Anderson S., Claridge T.D.W., Anderson H. L., Azo-Dye Rotaxanes. *Angew. Chem. Int. ed. Engl.*, **12**, 36, 1997.
- [5] Simu G. M., Chicu A., Morin N., Schmidt W., Sisu E., Direct Dyes Derived from 4,4'-Diaminobenzanilide. Synthesis, Characterization and Toxicity Evaluation of a disazo symmetric direct dye. *Turkish Journal of Chemistry*, **28**, 1-7, 2004.
- [6] Simu G., Funar-Timofei S., Hora S., Schmidt W., Kurunczi L., Sisu E., Morin N., Coloranti Directi Derivati ai 4,4'-Diaminobenzanilidei. I. Sinteza si Studiul Izotermelor de Adsorbție pe Bumbac ale unui Colorant Disazoic Direct cu Structura Asimetrici, *Revista de Chimie – Bucharest.*, **53**, 826- 829, 2002.
- [7] Agrigoroaie G., Simu G. M., Pașka O., UV-VIS and TLC study of some direct azo dyes and their inclusion complexes with α - and β -cyclodextrin, *Proceedings of The 15th Symposium on analytical and environmental problems*, Szeged, Ungaria, 238-241, 2008.

OPTICAL STUDY OF STEEL SURFACES AFTER THERMOCHEMICAL TREATMENT

Simion JITIAN

Faculty of Engineering, Hunedoara

Abstract:

In this paper we introduced the ellipsometrical measurements of steel OLC-45 after thermochemical treatment. We obtained the optical constants and the film thickness of nitrated case formed on the steel surface after thermochemical treatment. This nitrated case and the metallic substrate have different mechanical properties because of the metallic nitride formed.

The correlation between the optical properties and the mechanical properties of metallic surfaces allow to correctly decide upon the optimal thermochemical treatment settings for a certain type of steel.

Keywords:

ellipsometry, optical constants, thermochemical treatment, nitriding steel

1. INTRODUCTION

The thermochemical treatment of the metallic surface forms films with special properties, which differ from those of the metal.

Ellipsometry is an optical study of metal surfaces of a special smoothness. It allows us to obtain the optical properties of the solid surfaces and of the surface films formed on the solid surfaces from a change in the state of light polarization that is reflected on the surface [1,3,6].

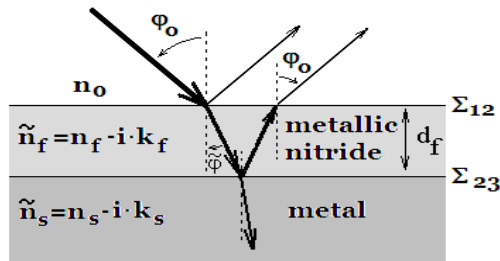


Figure 1. Light reflection on a metal covered by an optically absorbent film

Figure 1 presents the model of the metal surface coated with a film formed by the superficial thermochemical treatment, which reflects a monochromatic radiation.

The fundamental ellipsometry equation links the measurable angles Δ and Ψ to the optical constants of the substrate \bar{n}_s, \bar{k}_s , the superficial film thickness d_f and the optical constants of the superficial film \bar{n}_f, \bar{k}_f :

$$\text{tg}\Psi e^{i\Delta} = f(n_o, \varphi_o, \lambda, \bar{n}_f, \bar{k}_f, d_f, \bar{n}_s, \bar{k}_s) \quad (1)$$

In order to know the optical properties of the film formed on the surface after thermochemical treatment it is necessary to know the optical constants \bar{n}_s and \bar{k}_s of the substrate [1,6].

They are determined by a measurement of the angles $\bar{\Delta}_o$ and $\bar{\Psi}_o$, for the metal, before the thermochemical treatment. The optical constants of the substrate are obtained by solving the equation:

$$\text{tg}\bar{\Psi}_o e^{i\bar{\Delta}_o} = f(n_o, \varphi_o, \lambda, \bar{n}_s, \bar{k}_s) \quad (2)$$

The films formed on the surface of steel are optically absorbent so that both the thickness d_f and the optical constants \bar{n}_f and \bar{k}_f must be determined.

If the superficial film with complex refractive index $\tilde{n}_f = \bar{n}_f - i \cdot \bar{k}_f$ is optically absorbent, the relationship described by (1) does not allow the determination of three

unknown: d_f , \bar{n}_f and \bar{k}_f by a single pair of Δ and Ψ parameters, measured at a single angle of incidence.

The graphical methods are commonly used to determine the three sizes d_f , \bar{n}_f and \bar{k}_f by means of the ellipsometric measurements:

- ✚ at two or more different incidence angles;
- ✚ at two or more wavelengths;
- ✚ for two or more incidence media with different refractive indices [1,2,6].

Reference literature presents in detail the technique for processing the data resulting from experimental measurements [1,4,6].

If the optically absorbent superficial film thickness is greater than a minimum value d_m , then radiation is absorbed in the superficial film and does not reach the Σ_{23} interface. In this case angles Δ and Ψ do not depend on the film thickness. They remain constant as can be observed in Figure 2. From Δ_f and Ψ_f we obtained the optical constants of the superficial film as bulk material. The minimum film thickness from which Ψ and Δ remain constant depends on the optical constants of the superficial film.

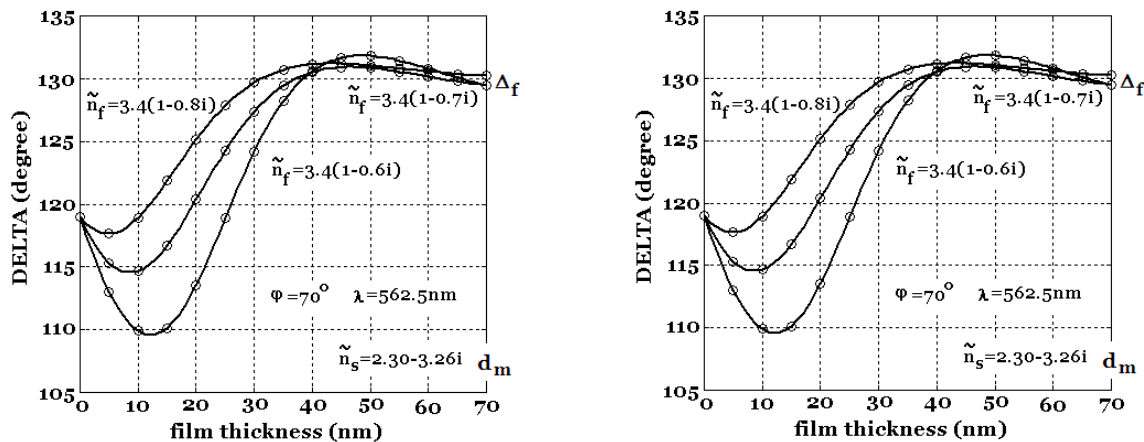


Figure 2 Δ and Ψ angles versus the thickness of an optically absorbent film formed on the metallic surface.

The ellipsometry relationship expressed by (1) no longer allows the determination of the thickness d_f of the superficial film. From the relationship:

$$\operatorname{tg} \bar{\Psi}_f e^{i\bar{\Delta}_f} = f(n_o, \varphi_o, \lambda, \bar{n}_f, \bar{k}_f) \quad (3)$$

we can only determine the optical constants \bar{n}_f and \bar{k}_f based on the ellipsometrical angles at one angle of incidence.

In relation (1) it is assumed that the superficial film has an arbitrarily chosen value, but greater than d_m .

2. EXPERIMENTS

The surface of steel samples OLC-45, was polished and then burnish extra-brightly with aluminum oxide burnishing powder. Before the ellipsometrical measurements for the determination of the optical constants, the metal surface of the freshly polished samples was washed in a jet of distilled water to remove impurities and then it was washed with absolute ethanol.

The thermochemical treatment of steel samples was performed in an ion-nitriding furnace for 8 hours. The samples were then washed by the method described above, before the ellipsometrical measurements of the film that was formed.

The ellipsometrical angles Δ and Ψ through which we determined the optical constants of the surfaces were measured by means of a photoelectric ellipsometer in PCSA assembly (polarized, compensatory, surface, analyzer) with an accuracy of 0.1° .

The calculations were made with the help of our own computer program based on the calculation developed by McCrackin [6].

3. RESULTS AND DISCUSSION

There were two methods used for determining the thickness and the optical constants of the surface films.

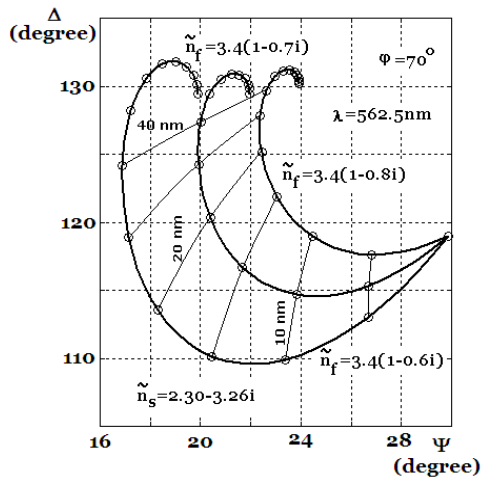


Fig. 2 The theoretical curves $\Delta=f(\Psi)$ for superficial optical absorbent film.

measurements for metal covered with the surface film, at two different incidence angles: 60 ° and 70 ° [5].

$$\operatorname{tg}\Psi_1 e^{i\Delta_1} = f(n_o, \varphi_{o1}, \lambda, \bar{n}_f, \bar{k}_f, d_f, \bar{n}_s, \bar{k}_s) \quad (4)$$

$$\operatorname{tg}\Psi_2 e^{i\Delta_2} = f(n_o, \varphi_{o2}, \lambda, \bar{n}_f, \bar{k}_f, d_f, \bar{n}_s, \bar{k}_s) \quad (5)$$

The results of the measurements, the optical constants and the superficial film thickness are shown in Table 1.

For nitride layers whose thickness is larger than 100 nm the ellipsometrical measurement determines only the optical constants of the layer, by means of equation (3).

Table 1. The ellipsometrical angles measured and the optical characteristics of the metal and of the superficial film obtained by ion-nitriding of OLC-45 steel

Sample	Metallic substrate					Nitriding steel					
	φ_o	Δ	Ψ	\bar{n}_s	\bar{k}_s	φ_o	Δ	Ψ	\bar{n}_f	\bar{k}_f	d_f
-	deg.	deg.	deg.	-	-	deg.	deg.	deg.	-	-	nm
1	70	118,45	29,35	2,32	3,18	60	152,07	28,72	3,46	2,46	22
						70	124,92	20,35			
2	70	119,01	29,85	2,30	3,26	60	147,39	28,72	3,4	2,48	15
						70	118,42	22,06			

4. CONCLUSIONS

The determination of the optical constants and the surface film thickness require at least two ellipsometrical measurements at different incidence angles or wavelength or by using different incidence media with different refractive indices.

The optical characteristics of optical absorbent films can be obtained by rather laborious graphical methods.

If the superficial films have the thicknesses greater than 0.1 μm , it is not possible to determine the thickness by the ellipsometrical method. The optical constants determined from the Δ and Ψ ellipsometrical angles correspond to the bulk metallic nitride.

The correlation between the optical properties of films formed after thermo chemical treatment and the mechanical properties of the metals allow an optimal treatment to be applied to particular steel.

REFERENCES

- [1] Azzam, R.M.A. și Bashara, N.M., „*Ellipsometry and Polarized Light*”, North-Holland Publ. Comp., Amsterdam-New-York-Oxford, 1977
- [2] Jitian, S., *Analele Univ. E. Murgu Reșița*, 1996, p.161
- [3] Jitian S., *Stud. Univ. Babes-Bolyai. Chem.*, **XXXI**(2), 1986, p.69
- [4] Mc. Crackin, F.L., „*A Fortran Program for Analysis of Ellipsometer Measurement*”, Natl. Bur. Std., Technical Note 479, Washington, 1969
- [5] Mieluch, J., *Polish Journal of Chemistry*, **52**, 1978, p. 151
- [6] Moisil, D. și Moisil, G., „*Teoria și practica elipsometriei*”, Ed. Tehnică, București, 1973



DETERMINATION OF THE ROUGHNESS LEVELLING DEPTH FOR METALLIC SURFACES BY OPTICAL MEASUREMENTS BASED ON THE LIGHT REFLEXION

Simion JITIAN

Faculty of Engineering Hunedoara, ROMANIA

Abstract:

The used optical method is based on the roughness metallic surface model, which supposed one superficial inhomogeneous film. This is considered a mixture of the basic metal and the air. For this film, the thickness, the amount of the metal per unit area of the surface and the weight fraction of the metal in the film are determined by the ellipsometric method. These values for Cu, Ni and steel allow the determination of the roughness leveling depth.

Key words:

ellipsometry, roughness, superficial film

1. INTRODUCTION

As a result of mechanical processing of metallic surface arise rupture of the crystal lattice and the formation of a transitional layer composed of amorphous crystalline areas of metal and impurities from the processing method [1,3].

Impurities existing on the rough surface can be removed by washing the area with various solvents, and transition layer will have properties intermediate two adjacent medium.

As well it should polish, metal surface has a roughness that can be characterized by mean deviation of the roughness to the median line:

$$R_a = \frac{1}{\ell} \int_0^{\ell} |y - m| \cdot dx \quad (1)$$

Median line taken as a reference is characterized by roughness leveling depth R_p taken to the outside line of profile or to the inside line of it:

$$R_p = \frac{1}{\ell} \int_0^{\ell} y \cdot dx \quad (2)$$

y is coordinate of a point of the profile diagram to the inside line, $m=R_p$ coordinate of the average line to the inside line and ℓ is the measured length [4].

In the case of the minute surface, use of mechanical feeler is limited by the size of pick-up.

Ellipsometric method, based on variation of the polarization of light when reflected on the surface between two media, can be used to characterize roughness of metal surfaces [2]. By this method can determine the thickness and optical properties of superficial films on metal surfaces with an accuracy of the order hundredth of nanometer.

The method used is based on a model of the rough metallic surface as in Figure 1. Rough surface may be resembled with a superficial film made from a mixture of metal (with the index of refraction \tilde{n} and density ρ) and the immersion medium (with the index of refraction n_o and density ρ_o), as in Figure 1.

Refraction index n_f and thickness d_f of the film can be determined by ellipsometric readings based on the optical model of the superficial intermediate film, shown in Figure 1,

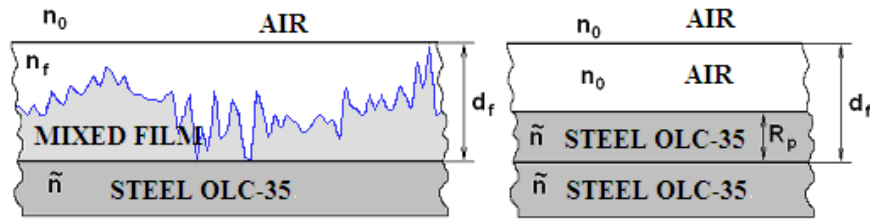


Figure 1. Model of rough surface resembled with a transition layer

The weight fraction of the metal in the film:

$$f = \frac{r_f - r_0}{\tilde{r} - r_0} \quad (3)$$

and the amount of the metal per unit area of the surface:

$$m_f = \rho_f \cdot d_f \cdot f \quad (4)$$

on determine from these optical values.

In this relationship ρ_f represents film density calculated with the phrase:

$$\rho_f = \frac{1}{\frac{f}{\rho} + \frac{1-f}{\rho_0}} \quad (5)$$

r_0 , \tilde{r} and r_f are the specific refractions of immersion environment (air), metal, and the superficial film:

$$r_0 = \frac{n_0^2 - 1}{n_0^2 + 2} \cdot \frac{1}{\rho_0} ; \quad \tilde{r} = \frac{\tilde{n}^2 - 1}{\tilde{n}^2 + 2} \cdot \frac{1}{\rho} ; \quad r_f = \frac{n_f^2 - 1}{n_f^2 + 2} \cdot \frac{1}{\rho_f} \quad (6)$$

Model shown in Figure 1 shows that the product between density of metal ρ and roughness leveling depth R_p is equal to the amount of metal per unit area of the film:

$$m_f = \rho \cdot R_p \quad (7)$$

2. EXPERIMENTAL PART

Measurements of the roughness of metal surfaces of copper, nickel and steel OLC-35 were carried out.

Samples of metallic copper, nickel and steel OLC-35 were cut to size 45x22x5 (mm), then were polished with glass paper grain size 12. Samples were burnish extra-bright before measurements with abrasive metallographic paper to grain M14, then with the burnishing powder of aluminum oxide "Presi 2" Italy. The samples were washed with absolute ethanol.

Metallic surface roughness was measured with a profilograph "Profilograf-201". For accounting of roughness we used the M system, which uses the median line of profile for the baseline [6]. Calculated physical and statistical parameters for the effective profiles were: the roughness leveling depth R_p and average deviation of roughness R_a reported to the median line.

Ellipsometric measurements were made with a photoelectric ellipsometer IFTAR (PCSA assembly) using monochromatic light with wavelength $\lambda = 546.1$ nm, at the angle of incidence $\varphi_0 = 70^\circ$.

3. Results and Discussion

In Figure 2 shows, for example, profile diagram recorded for the surface of a sample of nickel.

Table 1 are given values of R_p and R_a for metal surfaces studied, calculated from profile diagram recorded. The calculations were made using a computer one's own program in Matlab language.

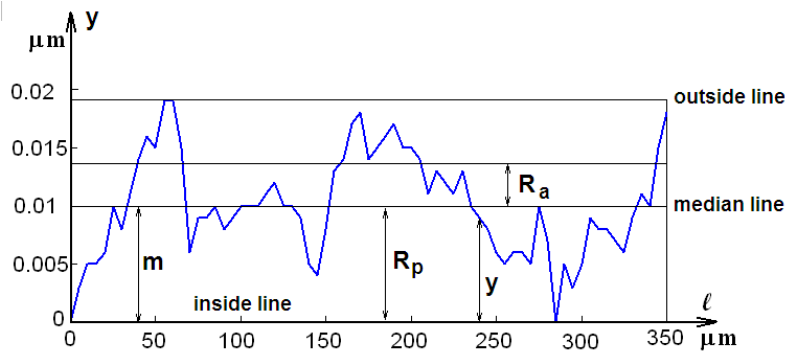


Figure 2. Profile diagram for nickel

Table 1

Metal	l	R_p	R_a
-	μm	μm	μm
Copper	60	0.026	0.022
Nickel	350	0.010	0.004
Steel OLC-35	60	0.010	0.004

Ellipsometric measurements and optical values calculated for rough superficial film, based on optical model shown in Figure 1, are presented in Table 2. To calculate optical values for superficial film were used optical constants of metal, and ellipsometric quantities measured at incidence angle $\varphi_0 = 70^\circ$ and wavelength $\lambda = 546.1 \text{ nm}$.

All calculations were performed using a software own, based on the McCrackin program for processing ellipsometric measurements [5].

Table 2

Metal	optical constants of metal		ρ	Δ	Ψ	d_f	n_f
	n	k					
-	-	-	g/cm^3	grd.	grd.	nm	-
Copper	0.82	2.21	8.93	74.47	35.51	345,6	0.98
Nickel	1.79	3.30	8.90	97.56	35.37	23.4	1.25
Steel OLC-35	2.54	3.42	7.86	98.44	32.03	11.5	2.12

Were calculated the weight fraction of the metal in the film f and the amount of the metal per unit area of the surface m_f , according to the relations (3) and (4), using the optical values n_f and d_f calculated for rough superficial film.

Levelling depth of roughness R_p , shown in Table 3, was calculated according to the relationship (7).

Table 3

Metal	d_f	f	m_f	ρ	R_p^{optic}	$R_p^{mechanic}$
	nm	-	mg/cm^2	g/cm^3	μm	μm
Copper	34,6	0.50	0.0031	8.93	0.035	0.026
Nickel	23.4	0.84	0.0077	8.90	0.009	0.010
Steel OLC-35	11.5	0.97	0.0076	7.86	0.010	0.010

It notes that in general there is a pretty good correlation between the leveling depths of roughness, optically determined (by ellipsometric measuring) R_p^{optic} and the same, mechanically determined (with profilograph) $R_p^{mechanic}$. Differences that may arise due to the fact that the base length of profil graph is of the order tenth of a millimeter while the optical surface of the metallic sample examined has an area with radius of about 2mm. Differences may occur because of errors due to limitations imposed by the size of profilograph pick-up.

4. CONCLUSIONS

For characterization of micro-roughness of metal surfaces ellipsometric method, based on modifying of the polarization of light reflected from the solid surfaces, is used. This method has an accuracy of the order tenth of a nanometer can provide information about the structures of various films on solid or liquid surfaces. The method does not require direct contact with the measured area and requires approximately 20 minutes measuring time.

Although a simple ellipsometric measurement not allow determination of roughness (expressed by the mean deviation of the roughness R_a to the median line taken as reference), it provides very valuable information about areas in terms of roughness. Levelling depth of roughness R_p determined by the optical measurement can be used later as middle reference line for calculating the roughness.

Ellipsometric measurements at several angles of incidence, or to different states of polarization of radiation, may provide additional information that can be used to characterize the roughness of surfaces.

Ellipsometric method can be used only for highly polished solid surfaces, reflecting specular light.

REFERENCES

- [1] Adamson A.W., „Physical Chemistry of Surfaces”, J. Wiley & Sons Inc., New-York, 1967
- [2] Azzam R.M.A. și Bashara N.M., „Ellipsometry and Polarized Light”, Elsevier Science., Amsterdam, 1987
- [3] Beckman K.H. și Harrick N.J., „Proceedings of Symposium on Optical Properties of Dielectric Film”, Murray Hill, New Jersey, 1968, p.123
- [4] Dodoc P., Metrologie generală, EDP, București, 1979
- [5] McCrackin F.L. „A Fortran Program for Analysis of Ellipsometer Measurements”, Natl. Bur. Std. USA, Technical Note 479, Washington, 1969.
- [6] SR ISO 468:1997 Rugozitatea suprafețelor. Terminologie. Măsurarea parametrilor de rugozitate a suprafeței



DETERMINATION OF OPTICAL CONSTANTS OF POLYMER FILMS THROUGH REFLECTION

Simion JITIAN

Faculty of Engineering Hunedoara, ROMANIA

Abstract:

The transmittance values measured in IR specular external reflection (RS) or internal reflection (ATR) spectra can be used to determine the optical constants of solid surfaces or dielectric films laid on solid substrates.

To obtain the optical constants of polystyrene films laid on steel we used Kramers-Kronig analysis. In this case, the optical constants are obtained from IR external reflection spectrum recorded at a single incidence angle. The transmittance measured and the phase shift angle obtained by Kramers-Kronig integral, are used in this case.

Using Kramers-Kronig analysis offers the advantage of processing a large volume of data.

Keywords:

Reflection-absorption, optical constants, IR spectra, Kramers-Kronig analysis, dispersion analysis

1. INTRODUCTION

The study of reflectance spectra of films deposited on solid surfaces allows the determination of thickness and optical constants of these: refractive index n and absorption index k .

In order to determine the optical constants of polymer films one can use the specular external reflectance spectra or the internal reflectance spectra. If the polymer film deposited on the metal is thick, it can be treated as a bulk material. The reflectance spectrum recorded is not influenced by the substrate.

The reflection and transmission of radiation on solid surfaces are expressed by the complex reflection coefficient $\tilde{r} = |\tilde{r}| \exp(i\theta)$ and the complex transmission coefficient $\tilde{t} = |\tilde{t}| \exp(i\theta)$. They depend on the complex refractive index of the film $\tilde{n} = n - ik$ and on the angle of incidence.

Reflectance, denoted by R represents the ratio of the reflected radiation intensity I_r and the incident radiation intensity I_0 and it is equal to the square complex reflection coefficient:

$$R = r^2 = |\tilde{r}|^2.$$

Transmittance, denoted by T represents the ratio of the transmitted radiation intensity I_t and the incident radiation intensity I_0 and is equal to the square complex transmission coefficient: $T = t^2 = |\tilde{t}|^2$.

For thick films (with thickness higher than $50 \mu\text{m}$), the optical constants are determined from the specular reflectance spectra (RS) or from the attenuated total reflectance spectra (ATR). You can use the reflectances R_1 and R_2 measured at two angles of incidence or the reflectance R at one angle of incidence and θ angle measured across the whole spectral domain [4,8,14]. This is possible by Kramers-Kronig analysis, using integral:

$$\theta(v_i) = \frac{v_i}{\pi} \int_0^{\infty} \frac{\ln R(v)}{v^2 - v_i^2} dv \quad (1)$$

From reflectance R and angle θ , the complex refractive index is determined, for normal incidence:

$$\tilde{n} = n - ik = \frac{(1 - R) - i \cdot 2\sqrt{R} \sin \theta}{1 + R - 2\sqrt{R} \cos \theta} \quad (2)$$

In case of specular reflection from the polymer thin films deposited on metals (with thickness less than 10 μm), the reflected radiation contains two components: one reflected from the air-film interface (I_r intensity) and one reflected by the film-metal interface (I_t intensity), after having crossed twice the polymer film, as shown in Figure 1.

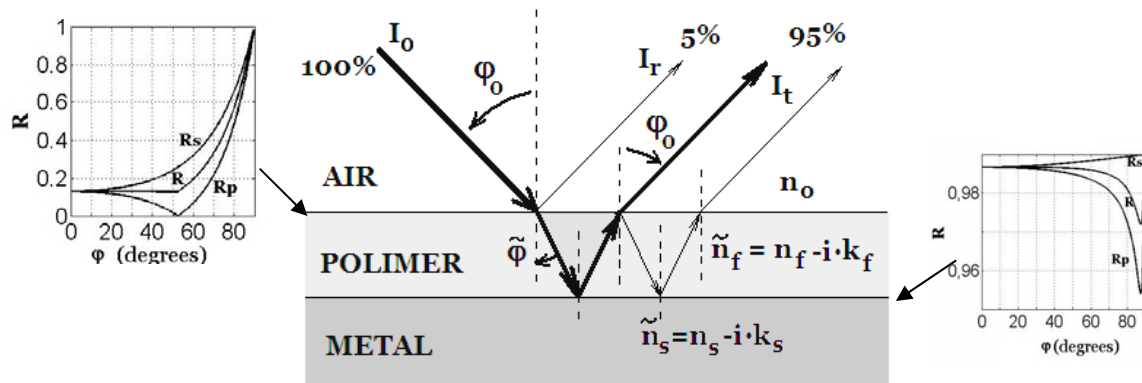


Figure 1. The specular reflection of radiation for thin films deposited on metals

The reflectance due to reflection at the air/film interface is about 5% since the refractive indices of polymers is less than 1.5 in the middle-IR spectral domain. The reflection at the polymer/metal interface is much higher and the reflectance is about 99%. The radiation reflected from the polymer/metal interface and crossing twice the polymer film is thus about 95% of the incident radiation intensity. It is almost 20 times more intense than the reflected beam to the air/polymer interface. For this reason, this spectrum is a reflection-absorption spectrum (or a transmittance spectrum). It is similar in terms of quality to the transmission spectrum of the polymer film.

This spectrum can be processed to obtain optical constants n and k [9].

It is necessary to know the transmittance $T(\nu)$ along the whole spectral domain and by means of the Kramers-Kronig relationship the θ angle is determined [12.13].

$$\theta(\nu) + 2m\pi = -\frac{\nu}{\pi} P \int_0^{\infty} \frac{\ln T(\nu')}{\nu'^2 - \nu^2} d\nu' + 2\pi\nu d \quad (3)$$

Transmittance T and θ angle are related to the complex refractive index by the relationship:

$$\sqrt{T} e^{i\theta} = \frac{4\tilde{n}}{(\tilde{n} + 1)^2 e^{-i\delta} - (\tilde{n} - 1)^2 e^{i\delta}} \quad (4)$$

where: $\delta = 2\pi\nu\tilde{n}d_f / c$ depends on the thickness d_f of the film [3].

Dispersion analysis is another way of obtaining the optical constants of thin films deposited on metal surfaces. This method can be more flexible than the Kramers-Kronig relations as it can be applied to a more complicated geometry.

Dispersion analysis is based on building an appropriate model for calculating the dielectric and optical properties of this model. The best known is the Drude-Lorentz damped harmonic oscillator model [11] for the complex dielectric function:

$$\varepsilon(\nu) = \varepsilon_{\infty} + \sum_j \frac{\nu_{pj}^2}{\nu_{oj}^2 - \nu^2 - i\gamma_j\nu} \quad (5)$$

It describes the optical response of a set of harmonic (damped) oscillators. Here ε_{∞} is the so-called "high-frequency dielectric constant", which represents the contribution of all oscillators at very high frequencies. Parameters ν_{pj} , ν_{oj} and γ_j are the "plasma" frequency, the transverse frequency (eigenfrequency) and the linewidth (scattering rate) respectively of

the j -th Lorentz oscillator. Reflectance R or transmittance T can be obtained from the theoretical model of the complex dielectric function. The spectra of these optical magnitudes are compared to those experimentally determined. The model parameters are continuously adjusted to fit the theoretical values with the experimental data measured. For the reflection-absorption spectra, the theoretical transmittance and the experimental transmittance are compared. When the differences between the theoretical and experimental spectra are minimal, the parameters fitting process is stopped.

Suppose, we have a set of N experimental data points $\{x_j, y_j, \sigma_j\}$ ($j = 1, \dots, N$), that we want to fit. Here, x_j is the data coordinate, y_j is the data value and σ_j is the data error bar. Next, we take a model, which calculates the model value $y = f(x, p_1, \dots, p_M)$ for a set of M internal parameters.

So-called Levenberg-Marquardt algorithm is used to minimize the amount

$$\chi^2 = \sum_j^N \left(\frac{y_j - f(x_j, p_1, \dots, p_M)}{\sigma_j} \right)^2 = \chi^2(p_1, \dots, p_M) \quad (5)$$

is used.

The fitting process stops when the stopping criterion is fulfilled [10].

In the case of the internal reflection at angles of incidence greater than the critical angle, the radiation is totally reflected on the surface film. The evanescent-wave penetrates into the superficial thin film. The depth of radiation penetration into the superficial film is given by the relationship:

$$d_p = \frac{\lambda}{2\pi \sqrt{n_o^2 \sin^2 \varphi_o - n_f^2}} \quad (5)$$

The depth of penetration is a measure of how far radiation penetrates into the sample in an ATR experiment, calculated as the depth at which the electric field of the evanescent wave has decreased to 37% of its original value.

Figure 2 presents the model of the internal reflection on thin films (with thickness d_f less than the depth of penetration d_p) deposited on metal mirrors.

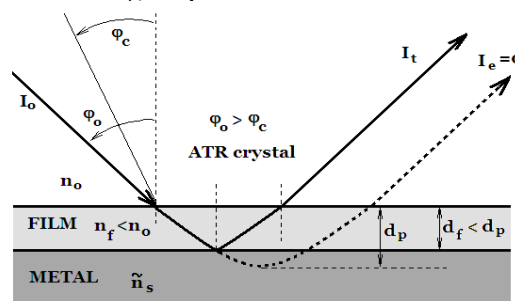


Figure 2. The attenuated total reflection from thin film deposited on metal surface

The radiation that penetrates through the polymer film as well as an evanescent wave, is reflected on the polymer/metal interface and it crosses the polymer film again. In this case, the internal reflectance spectra of thin films resemble more the transmission spectra and have a much different aspect, as compared to those recorded for thick films [4,6]. In the case of thin film, absorption bands are not displaced or distorted, if the incidence angle is close to the limit. The spectrum recorded is influenced by the nature of the substrate.

In order to determine the thickness of the surface films, one may use only the external reflectance spectra. For this, it is necessary that the film should have even thickness and that it should have values comparable to the wavelength of the radiation. Interference fringes may occur between the radiation reflected from the interface air/film and one that reflects the film/metal interface and crossing the film 2 times. The interference fringes are missing in case of internal reflection [4].

2. EXPERIMENTS

Thin films of polystyrene (PS) were obtained by depositing a solution of polymer dissolved in toluene on the surface of OLC-35 steel. Reducing the solvent evaporation rate allows us to obtain a film with an even thickness. The low concentration of polymer in the solvent allowed us to obtain thin films with thickness less than $1\mu\text{m}$. Then, the metal sample coated with polymer was heated to 500°C , in order to evaporate all traces of solvent. The metallic surfaces used as substrates were obtained by grinding and polishing.

IR reflectance spectra were recorded using the specular reflection device of the UR-20 spectrograph.

In order to obtain the optical constants of the polymer film, the reflection-absorption spectra were processed using the RefFIT software [10].

3. RESULTS AND DISCUSSION

The IR reflection-absorption spectra recorded at incidence angles of 20 and 55 degrees are shown in Figure 3. The diagram shows the spectral ranges $500\text{--}850\text{ cm}^{-1}$ and $2400\text{--}3360\text{ cm}^{-1}$, which contain absorption bands corresponding to the C-H stretching vibrations of aromatic nucleus [2].

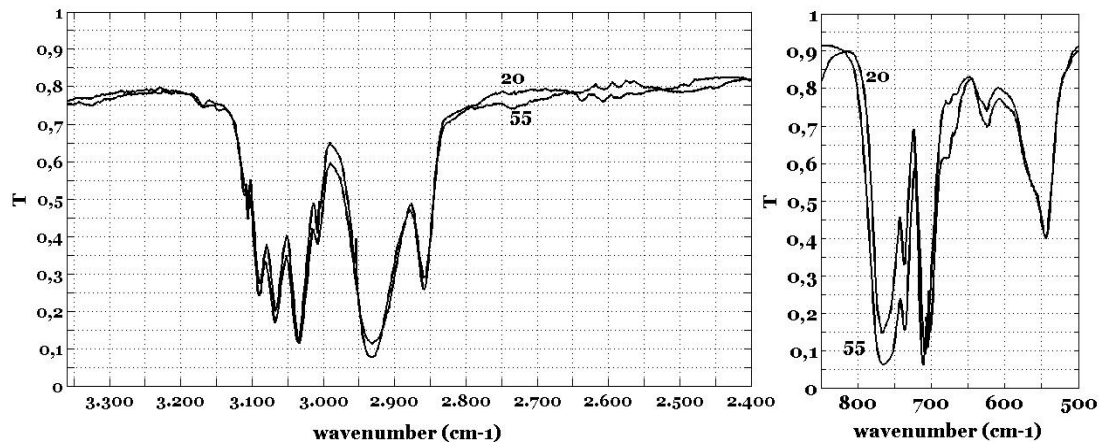


Figure 3. The reflection-absorption spectrum of polystyrene deposited on steel, recorded for 20 and 55 degrees angles of incidence

It is noted that changing the angle of incidence does not alter significantly the transmission spectrum of polystyrene. Reflectance R and transmittance T depend very little on the incidence angle, as can be observed in Figure 1.

Because the thickness of the superficial film is less than $1\mu\text{m}$, the interference fringes are not present in the recorded spectra. For the same reason the recorded spectrum is a reflection-absorption (transflection) one.

The spectrum obtained can be processed to obtain the optical constants n (refractive index) and k (absorption index).

In order to improve the accuracy of the dielectric function, both R-A spectra recorded at incidence angles of 20 and 55 degrees were simultaneously fit. We also used the refractive index of polystyrene $n_f = 1.57$ ellipsometrically determined for $\lambda = 562.5\text{ nm}$ [7] and the value $n_f = 1.5842$ for $\lambda = 633\text{ nm}$ [1].

The refractive index spectrum obtained by dispersion analysis of reflection-absorption spectrum for polystyrene deposited on steel is shown in Figure 4.

Absorption index k has a spectrum very similar to the absorption spectrum. The values of the absorption coefficient are low so that it can be concluded that polystyrene is almost transparent and in the IR range. In this spectrum the positions of the absorption bands do not show deviations from the positions of the absorption bands in the reflection-absorption spectrum. It can also be noticed that the intensity of absorption bands decreases at higher frequencies. The wavenumbers corresponding to the model used are about 5 cm^{-1} higher than those of literature [2].

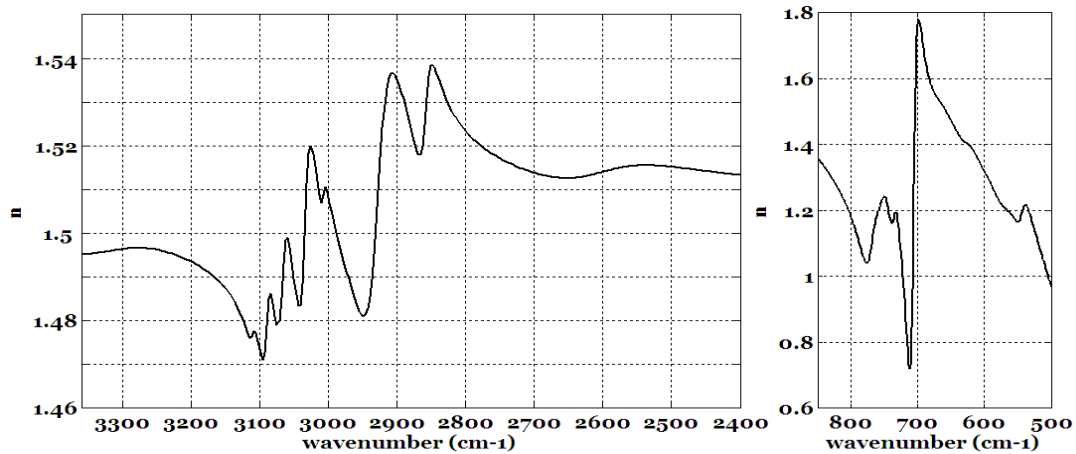


Figure 4. The refractive index spectrum for polystyrene deposited on steel

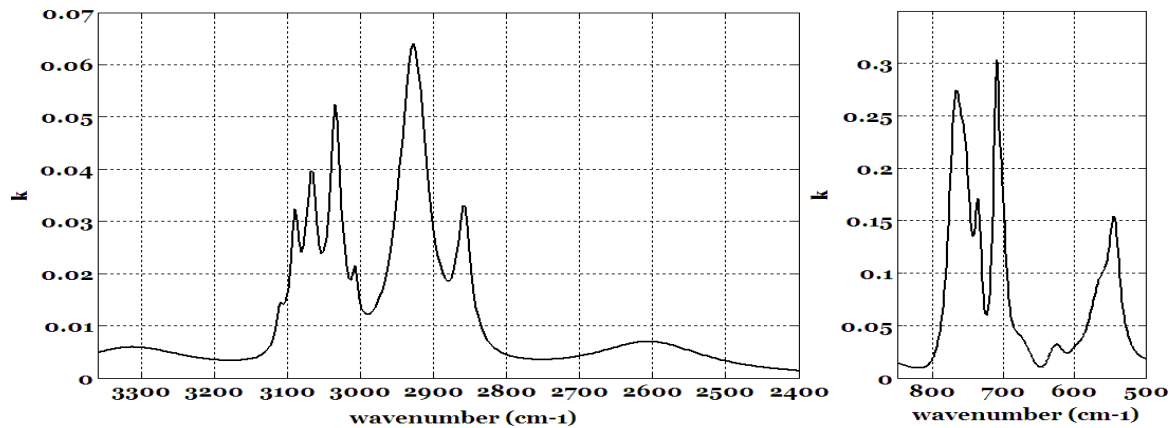


Figure 5. The absorption index (extinction coefficient k) spectrum for polystyrene deposited on steel

4. CONCLUSIONS

The IR reflectance spectra for thin films (with thickness less than $1\mu\text{m}$) are reflection-absorption spectra in which transmittance T is recorded. The reflection-absorption spectrum for polymer films is very similar in terms of quality to the transmission spectrum.

The dispersion analysis of the reflection-absorption spectra is more accurate and easier than the Kramers-Kronig analysis. Kramers-Kronig analysis is used mainly for superficial thick films or for bulk material.

Simultaneous fitting of several datasets of different types related to the superficial film leads to obtaining correct values for optical constants n and k .

The internal reflectance spectra for thin films, deposited on metals, with thickness less than the depth of penetration at angles of incidence greater than the critical angle are the reflection-absorption spectra and not the attenuated total reflectance spectra. They have the same look as the transmission spectra and can be used to determine the optical constants of the superficial film.

REFERENCES

- [1] Ay F., Kocabas A., Kocabas C., Aydinlia A. and Agan S., *Appl. Phys.*, 96(2), p.7147, 2004
- [2] Bădilescu S., Giurginca M., Toader M. and Tălpuș V., „Spectroscopia în infraroșu a polimerilor și auxiliarelor”, Ed. Tehnică, București, 1982;
- [3] Borondics F., Kamarás K., Nikolou M., Tanner D.B., Chen Z.H., and Rintzler A.G., *Physical Review B*, 74, p.045431, 2006;
- [4] Harrick N.J., „Internal Reflection Spectroscopy, Wiley, New York, 1967;
- [5] Jacob W., von Keudell A., and Schwarz-Selinger Th., *Braz. J. Phys.*, **30** (3), 2000;

- [6] Jitian S., Annals of the Faculty of Engineering Hunedoara, 3(5), p.140, 2001;
- [7] Jitian S. and Chifu E., Studia Univ. Babeş-Bolyai, Chemia, XXXI(2), p.69, 1986;
- [8] Kiyoshi Yamamoto, „Optical Theory Applied to Thin Films”, Ph. Thesis, Case Western Reserve University, 1994;
- [9] Koichi Nishikida, Etsuo Nishio and Robert W. Hannah, „Selected Applications of Modern FT-IR Techniques”, Kodansha Ltd, Tokyo, 1995;
- [10] Kuzmenko A.B., „Guide to Reffit: software to fit optical spectra”, 2004, available online at: <http://optics.unige.ch/alexey/reffit.html>;
- [11] Kuzmenko A.B., Review of Scientific Instruments, 76(8), pp. 083108.1-083108.9, 2005;
- [12] Nilsson P.-O., Applied Optics, 7(3), pp. 435-442, 1968;
- [13] Palmer K.F. and Williams M.Z., Applied Optics, 24(12), p.1788, 1985;
- [14] Vettergren V.I., Smirnova N.S. and Chmel A.E., Zhurnal Prikladnoi Spektroskopii, 22(2), p.352, 1975;



MATHEMATICAL MODEL FOR THE BLOOD FLOW IN CAPILLARY VESSELS

¹ Sonia PETRILA, ² Balazs ALBERT

¹ "Tiberiu Popoviciu" Informatics Highschool, Cluj-Napoca, ROMANIA

² University "Babes-Bolyai", Cluj-Napoca, ROMANIA

Abstract:

In this paper we develop an original model for the blood flow in capillaries. In the first approach the Stokes system is accepted for the blood flow in capillaries and the fluid is considered to be incompressible. The vessels' walls have a linear elastic and permeable behavior. For the second model a non-Newtonian, rheological model for the blood flow, with a non-constant viscosity coefficient, is used, the walls of the capillaries being linearly elastic, permeable and porous.

Key words:

blood flow in capillary vessels, Newtonian-model, rheological model, elastic permeable porous walls.

1. INTRODUCTION

The most important aspect of the blood flow in capillaries is to supply "with food" the living cells of the organs and to remove the byproducts from every cell. The capillary vessels are built so that molecules with different dimensions can penetrate through the tissues in the surroundings of the capillaries in both ways. Generally capillaries are considered as tubes with very thin and porous walls, through which the transport of certain substances are realized. The presence of these pores and the small diameter of the capillaries distinguish these types of vessels from the others. Due to this reduced diameter and the slow character of the flow we can neglect the non-stationary (pulsating) aspect connected to the rhythmical pumping of the blood by the heart. Furthermore we can neglect the inertial (convective) aspects connected to the viscosity of the blood. Moreover the permeable (porous) character of the capillaries is dominating the elasticity of the vessels' walls.

2. NEWTONIAN MODEL FOR THE BLOOD FLOW IN CAPILLARIES

The first model we propose accepts for the blood flow in thin vessels the Stokes system for incompressible fluids, taking into consideration that the Reynolds number is small. Implicitly it is accepted that the blood is homogenous, the viscosity is constant, the flow has a laminar character and there are no exterior field forces.

The vessels' walls have a linear elastic and permeable behavior and the fluid (substance) change through these walls, very small in volume, respects the Starling hypothesis [7]. This classical hypothesis, which was checked experimentally later by many researchers (Mauro [3], Meschia [4], etc.), maintains the fact that the mass debit through this kind of capillary wall is proportional with the pressure difference between the exterior and the interior of the capillary tube. Moreover, using the results of Beavers and Joseph [1], it is accepted the existence of a slip condition, along the permeable surface, which is "covered" by a porous media, an essential condition confirmed also experimentally.

For simplification we accept the axi-symmetric character of the flow, the axis of symmetry being Oz . Using the cylindrical coordinates (r, θ, z) , the motion domain will be, at every time t :

$$\Omega(t) \equiv \{(r, \theta, z) / r < R + \eta(z, t), \theta \in [0, 2\pi), z \in (0, L)\}, \quad (1)$$

where R and L are the (initial) radius and the length of the tube respectively, η is the elastic displacement of the wall $\Sigma(t) \equiv \{r = R + \eta(z, t), z \in (0, L)\}$ at the considered moment.

Noting by (u, v) the velocity components of the blood in the directions z and r respectively, by p the pressure while by μ the dynamic viscosity coefficient, the motion equations (Stokes) and the continuity equation becomes

$$\frac{\partial p}{\partial r} = \mu \left(\frac{\partial^2 v}{\partial r^2} + \frac{1}{r} \frac{\partial v}{\partial r} - \frac{v}{r^2} + \frac{\partial^2 v}{\partial z^2} \right) \quad (2)$$

$$\frac{\partial p}{\partial z} = \mu \left(\frac{\partial^2 u}{\partial r^2} + \frac{1}{r} \frac{\partial u}{\partial r} + \frac{\partial^2 u}{\partial z^2} \right) \quad (3)$$

and

$$\frac{1}{r} \frac{\partial}{\partial r} (rv) + \frac{\partial u}{\partial z} = 0 \quad (4)$$

For the boundary conditions, noting by \bar{p} the average of the pressure values given in the respective section, we get:

$$\frac{\partial u}{\partial r} = 0 \text{ and } v = 0, \text{ for } r = 0 \quad (5)$$

$$\frac{\partial u}{\partial r} = -\frac{\beta}{\sqrt{k}} u \text{ and } v = K(p - \nu), \text{ for } r = R + \eta \quad (6)$$

$$\bar{p}(r, z) = p_a, \text{ for } z = 0 \quad (7)$$

$$\bar{p}(r, z) = p_v, \text{ for } z = L. \quad (8)$$

Here $\frac{\partial u}{\partial r} = -\frac{\beta}{\sqrt{k}} u$ is the Beavers-Joseph slip condition, where β is the slip parameter,

while k is the specific permeability of the porous media, $v = K(p - \nu)$ is the consequence of the Starling law, where K is the constant permeability of the wall, while ν (built by the interstitial and osmotic pressure) is a given constant. Concerning to p_a and p_v they are the arterial and venous pressure, both supposed constants.

Referring to the elasticity of the capillary wall, accepting the linear elastic membrane model, the radial component of the stress can be expressed by the radial displacement η , such that:

$$T_r = \rho_m h \frac{\partial^2 \eta}{\partial t^2} + \frac{hE}{1 - \sigma^2} \frac{1}{R^2} \eta + p_{ref} \frac{\eta}{R}, \quad (9)$$

where h is the thickness of the membrane, E the Young modulus, σ the Poisson coefficient, ρ_m is the density of the capillary wall, while p_{ref} is the reference pressure in the “unperturbed” state, supposed to be constant (the above mentioned p is in fact $p - p_{ref}$).

It is obvious that on a this kind of elastic wall the kinematic condition for the continuity of the pressure, evaluated on the deformed interface $\Sigma(t)$, must be satisfied, namely

$$\frac{\partial \eta(z, t)}{\partial t} = v(R + \eta(z, t), z) \text{ and } u(R + \eta(z, t), z) = 0. \quad (10)$$

These conditions together with the previous Beavers-Joseph and Starling conditions lead to $\frac{\partial \eta}{\partial t} = K(p - \nu)$ and $\frac{\partial u}{\partial r} = 0$ for $r = R + \eta$ respectively.

Concerning the dynamic condition, it implies the continuity of the stress along the deformable interface (wall). As the constitutive law accepted in this case is that of the Newtonian fluid, we must have along $\Sigma(t)$

$$[(p - p_{ref})[\mathbf{T}] - 2\mu[\mathbf{D}]]\mathbf{n} \cdot \mathbf{e}_r = T_r, \quad (11)$$

which leads to

$$[(p - p_{ref})[\mathbf{T}] - 2\mu[\mathbf{D}]]\mathbf{n} \cdot \mathbf{e}_r \left(1 + \frac{\eta_r}{R}\right) \sqrt{1 + \left(\frac{\partial \eta}{\partial t}\right)^2} = T_r, \quad (12)$$

on $\Sigma(t)$, at any time t .

3. RHEOLOGICAL NON-NEWTONIAN MODEL

In the previous model the blood was investigated as a Newtonian fluid and the system of equations was the Stokes system. Now we accept for the blood a rheological non-Newtonian representation with a non-constant viscosity coefficient. All the other assumptions (non-stationary character, incompressibility, homogeneity, linear elasticity, porosity of the wall) are the same, like in the previous model. The Starling hypothesis and the Beavers-Joseph slip condition are also fulfilled.

We accept again the axi-symmetric character of the blood flow in the capillary tube, the axis of symmetry being Oz . Using the cylindrical coordinates (r, θ, z) , the motion domain will be, at every time t , $\Omega(t) \equiv \{(r, \theta, z) / r < R + \eta(z, t), \theta \in [0, 2\pi), z \in (0, L)\}$, where R , L , $\eta(z, t)$ and $\Sigma(t)$ have the same meaning as in the previous model.

In the meridian plane $\theta = const$ if u_z and u_r are the components of the velocity in z and r directions, if p is the pressure (evaluated to a reference pressure p_{ref}), then in the absence of the exterior forces, the mass conservation principle (continuity equation) can be written as

$$\frac{1}{r} \frac{\partial}{\partial r} (ru_r) + \frac{\partial u_z}{\partial z} = 0. \quad (13)$$

Concerning the flow equations they are obtained from the general Cauchy motion equations, where for the stress tensor we accept the following representation (rheological model for blood)

$$\mathbf{T} = -[p + \lambda \left(\frac{\partial K}{\partial \dot{\gamma}} \dot{\gamma} + \frac{\alpha}{\eta_p} K^2 \right)] \mathbf{I} + 2(\eta_s + \eta_{RBC}) \mathbf{D}, \quad (14)$$

where \mathbf{D} is the rate of strain tensor while \mathbf{I} the unity tensor, p the physical pressure, while η_{RBC} is given by (the Cross model):

$$\eta_{RBC} = \frac{\eta_0^*}{1 + (k\dot{\gamma})^{1-n}} \equiv \eta_p + \lambda K(\dot{\gamma}). \quad (15)$$

with $\dot{\gamma} = |4I_2|^{1/2}$, I_2 being the second invariant of the rate of strain tensor \mathbf{D} , η_s the plasma viscosity, η_p and η_0^* the viscosity coefficients of the blood, α the "relaxation time", k is a time constant for the shear thinning behavior, n the shear thinning index, λ the mobility parameter, while the function

$$K(\dot{\gamma}) = \frac{1}{\lambda} \left(\frac{\eta_0^*}{1 + (k\dot{\gamma})^{1-n}} - \eta_p \right), \text{ for } \lambda > 0 \quad (16)$$

is the so called normal function in the variable $\dot{\gamma}$, which measures the variation of deformation.

For sake of simplicity we denote

$$\eta(\dot{\gamma}) = \lambda K(\dot{\gamma}) + \eta_s + \eta_p \equiv \eta_s + \eta_{RBC},$$

$$L = -\frac{2\alpha\lambda}{\eta_p} \frac{\partial K}{\partial \dot{\gamma}} - \lambda \frac{\partial^2 K}{\partial \dot{\gamma}^2} \ddot{\gamma} \text{ and}$$

$$M = -\frac{k\eta_0^*(1-n)(k\dot{\gamma})^{-n}}{[1+(k\dot{\gamma})^{1-n}]^2}, \text{ so that, expressing the tensor } \mathbf{D} \text{ and the other operators}$$

($\frac{\partial}{\partial x_i} = \dots$ etc.) in cylindrical coordinates, we arrive to the following two equations of flow (in

u_z and $u_r, u_\theta = 0$)

$$\begin{aligned} \rho \left(\frac{\partial u_r}{\partial t} + u_r \frac{\partial u_r}{\partial r} + u_z \frac{\partial u_r}{\partial z} \right) = -\frac{\partial p}{\partial r} + \eta(\dot{\gamma}) \left(\frac{\partial^2 u_r}{\partial r^2} + \frac{1}{r} \frac{\partial u_r}{\partial r} + \frac{\partial^2 u_r}{\partial z^2} \right) + \\ + L \frac{\partial \dot{\gamma}}{\partial r} + M \left[-\frac{\partial \dot{\gamma}}{\partial r} + 2 \frac{\partial \dot{\gamma}}{\partial r} \frac{\partial u_r}{\partial r} + \frac{\partial \dot{\gamma}}{\partial z} \left(\frac{\partial u_r}{\partial z} + \frac{\partial u_z}{\partial r} \right) \right], \end{aligned} \quad (17)$$

$$\begin{aligned} \rho \left(\frac{\partial u_z}{\partial t} + u_r \frac{\partial u_z}{\partial r} + u_z \frac{\partial u_z}{\partial z} \right) = -\frac{\partial p}{\partial z} + \eta(\dot{\gamma}) \left(\frac{\partial^2 u_z}{\partial r^2} + \frac{1}{r} \frac{\partial u_z}{\partial r} + \frac{\partial^2 u_z}{\partial z^2} \right) + \\ + L \frac{\partial \dot{\gamma}}{\partial z} + M \left[-\frac{\partial \dot{\gamma}}{\partial z} + 2 \frac{\partial \dot{\gamma}}{\partial z} \frac{\partial u_z}{\partial z} + \frac{\partial \dot{\gamma}}{\partial r} \left(\frac{\partial u_r}{\partial z} + \frac{\partial u_z}{\partial r} \right) \right]. \end{aligned} \quad (18)$$

These evolution systems are completed by the boundary conditions which express both the presence of a pressure gradient along the Oz axis (in accord with the rhythmical pumping of the blood in vessels) and the elastic character of the permeable, porous wall, more precisely

$$\frac{\partial u_z}{\partial r} = 0 \text{ and } u_r = 0 \text{ for } r = 0, \quad (19)$$

$$\frac{\partial u_z}{\partial r} = -\frac{\beta}{\sqrt{K}} u_z \text{ and } u_r = K(p - \nu) \text{ for } r = R + \eta(z, t), \quad (20)$$

(the first relation in (20) expresses the Beavers-Joseph slip condition with the slip parameter β while K is the specific permeability of the porous media, meantime $u_r = K(p - \nu)$ is the consequence of the Starling law, with K the constant permeability of the wall, ν , built by the interstitial and osmotic pressure, supposed to be fixed and a a given constant), while for the pressure we have

$$p = \frac{\cos(\omega t)}{a} + p_m \text{ for } z = 0, \text{ where } a > 0, \quad (21)$$

$$p = \frac{\cos(\omega t)}{a + L} + p_m \text{ for } z = L, \text{ where } a > 0, \quad (22)$$

where $p_m = \frac{\int_0^R f(r) dr}{R} \equiv f(\xi)$, f is a primitivable and derivable function according to r , with

a maximum for $r = 0$ and a minimum for $r = R + \eta$. It can be remarked that $p|_{z=0} > p|_{z=L}$ at any time of the motion $(0, T)$.

Observations: These boundary conditions on the “edges” $z = 0$ and $z = L$ of the capillary are in accord with the acceptance of a representation for the pressure of the type

$p = \frac{\cos(\omega t)}{a + z} + f(r)$, namely of a pressure gradient (in the cylindrical reference \vec{e}_z, \vec{e}_r) under

the form $\text{grad} p = -\frac{\cos(\omega t)}{(a + z)^2} \vec{e}_z + f'(r) \vec{e}_r$. If $f'(0) = 0$ and $f'(R + \eta(z, t)) = 0$ we have

$\text{grad}p|_{Oz} = -\frac{\cos(\omega t)}{(a+z)^2} = \text{grad}p|_{r=R+\eta(z,t)}$, in accord with the motion of the pressure in the interior of the capillary.

On the other hand accepting for the capillary wall the linear elastic membrane model, the radial component of the membrane's stress is expressed by the radial displacement η as follows

$$T_r = \rho_m h \frac{\partial^2 \eta}{\partial t^2} + \frac{hE}{1-\sigma^2} \frac{1}{R^2} \eta + p_{ref} \frac{\eta}{R}, \quad (23)$$

where h is the thickness of the membrane, E the Young modulus, σ the Poisson coefficient, ρ_m is the density of the capillary wall while p_{ref} is the reference pressure in the "unperturbed" state. It is evident that this stress must coincide with the stress generated by the blood on the same radial direction, namely $\vec{T} = \mathbf{T}\vec{n} \cdot \vec{e}_r = T_r$, which represents the relation for determining f (the pressure) or $\eta(z,t)$.

At the same time the kinetic condition must be satisfied on the elastic wall, $\frac{\partial \eta}{\partial t} = u_r(R + \eta(z,t), z)$ but also $u_z(R + \eta(z,t), z) = 0$, what leads to $\frac{\partial \eta}{\partial t} = K(p(z, r, t) - \nu)$ and $\frac{\partial u_z}{\partial r} = 0$ for $r = R + \eta$ respectively.

It can be remarked that the last relation, together with $u_z(R + \eta(z,t), z) = 0$, implies $u_z = 0$ in the whole a surrounding of the elastic wall while the conditions $\frac{\partial u_z}{\partial r} = 0$ and $u_r = 0$ for the axis $r = 0$ show that $\vec{u} = u_z \vec{e}_z$ depends only on z and t so that we have a pulsating flow along the axis Oz , which "calms down" on the elastic wall ($u_z = 0$) where the exterior imposed pressure will have a minimum. At the same time from $\frac{\partial \eta}{\partial t} = K(p(z, r, t) - \nu) \Big|_{r=R+\eta(z,t)}$ we obtain $\frac{\partial^2 \eta}{\partial t^2} = K \left(\frac{-\omega \sin(\omega t)}{a+z} \right) \Big|_{r=R+\eta(z,t)}$. This last evaluation for $\frac{\partial^2 \eta}{\partial t^2}$ permits us to make precise the condition on the capillary wall (linear elastic membrane), namely the expression of the "equilibrium" condition $\mathbf{T}\vec{n} \cdot \vec{e}_r = T_r$ in cylindrical coordinates. More precisely if we note by

$$P = [p + \lambda \left(\frac{\partial K}{\partial \dot{\gamma}} \ddot{\gamma} + \frac{\alpha}{\eta_p} K^2 \right)] \quad (24)$$

the equilibrium condition becomes

$$\begin{aligned}
 & -\frac{P}{\sqrt{1 + \left(\frac{\partial \eta}{\partial z}\right)^2}} + \frac{2\eta(\dot{\gamma})}{\sqrt{1 + \left(\frac{\partial \eta}{\partial z}\right)^2}} \frac{\partial u_r}{\partial r} - \frac{\frac{\partial \eta}{\partial z}}{\sqrt{1 + \left(\frac{\partial \eta}{\partial z}\right)^2}} \left(\frac{\partial u_r}{\partial z} + \frac{\partial u_z}{\partial r} \right) = \\
 & \rho_m h \left(-\frac{K\omega \sin(\omega t)}{a+z} \right) + \frac{hE}{1-\sigma^2} \frac{1}{R^2} \eta + p_{ref} \frac{\eta}{R},
 \end{aligned} \quad (25)$$

what provides an equation to determine the deformation of the capillary wall, namely $\eta(z,t)$, so that the whole set of unknowns of our problem can be determined.

4. CONCLUSIONS

In this paper we elaborated an original mathematical model for the blood flow in capillary vessels. First we presented a model where the blood was accepted as a Newtonian

fluid. In the second approach we extended the model to a more general rheological (non-Newtonian) blood behavior which stands closer to the realistic phenomena.

The previous model will be approached numerically in another paper where we will also consider a more general behavior for the blood.

REFERENCES

- [1] Beavers, G.S., Joseph, D.D.: Boundary conditions at a naturally permeable wall, *J. Fluid Mech.*, 30, 1967.
- [2] Landis, E.M., Pappenheimer, J.R.: *Handbook of Physiology*, ed. W.F. Hamilton and P. Dow (Am. Physiol. Soc., Washington, 2963), p. 961.
- [3] Mauro, A.: Nature of solvent transfer in Osmosis. *Science*, **126**, 252, 1957.
- [4] Meschia, G., Setnikar, I.: Experimental study of osmosis through a collodion membrane, *J. Gen. Physiol.*, **42**, 429, 1958.
- [5] Oka, S., Murata, T.: A theoretical study of the flow of blood in a capillary with permeable wall, *Jap. J. Appl Phys.*, 9, 1970.
- [6] Petrila, T., Trif, D.: *Basics of Fluid Mechanics and Introduction to Computational Fluid Dynamics*, Springer Science, New York, 2005.
- [7] Starling, E.M.: On the absorption of fluids from the convective tissue spaces, *J. Physiol.*, 19, 1896.



A THREE DIMENSIONAL AXI-SYMMETRIC MODEL FOR THE BLOOD FLOW IN THIN VESSELS

¹ Sonia PETRILA, ² Balazs ALBERT

¹ “Tiberiu Popoviciu” Informatics Highschool, Cluj-Napoca, ROMANIA

² University “Babes-Bolyai”, Cluj-Napoca, ROMANIA

Abstract:

In this paper, taking into consideration the rheological Cross model, we elaborate a three dimensional axi-symmetric numerical model for the blood flow in thin vessels with adequate algorithms. First we consider the vessel wall to be rigid than we take into account the elastic and porous behavior of this wall what leads to a more realistic approach of the problem.

Key words:

rheological Cross model, blood flow in thin vessels, elastic porous walls.

1. INTRODUCTION

In the proposed model, set up in this work, we accept for the blood flow a rheological non-Newtonian representation with a non-constant viscosity coefficient. The blood is considered to be a homogenous fluid, the flow has a laminar character and there are no exterior field forces. The walls of the vessels have a linear elastic, permeable and porous behavior. For the blood flow in the vessel we also accept an axial symmetry (Oz being the axis of symmetry). Using the cylindrical coordinates (r, θ, z) , the motion domain will be, at every time t , $\Omega(t) \equiv \{(r, \theta, z) / r < R + \mu(z, t), \theta \in [0, 2\pi), z \in (0, L)\}$, where R and L are the (initial) radius and the length of the tube(vessel) respectively, μ is the elastic displacement of the wall $\Sigma(t) \equiv \{r = R + \mu(z, t), z \in (0, L)\}$ at the considered moment.

2. NUMERICAL MODEL FOR THE BLOOD FLOW IN THIN VESSELS

This model is based on the rheological Cross model, where the viscosity coefficient for the blood is not constant and can be written as follows

$$\eta(\dot{\gamma}) = \eta_s + \frac{\eta_0^*}{1 + k\dot{\gamma}^{1-n}}, \quad (1)$$

where η_s is the plasma viscosity, $\dot{\gamma} = |4I_2|^{1/2}$, I_2 being the second invariant of the rate of strain tensor \mathbf{D} (\mathbf{D} is the rate of strain tensor), η_0^* the viscosity coefficient of the blood and k is a time constant for the shear thinning behavior.

In the absence of the exterior forces we can write for the continuity equation

$$\frac{1}{r} \frac{\partial}{\partial r} (ru_r) + \frac{\partial u_z}{\partial z} = 0, \quad (2)$$

where u_z and u_r are the components of the velocity in z and r directions respectively. For the flow equations we use the general Cauchy motion equations, where we accept for the stress tensor the following representation

$$\mathbf{T} = -[p + \lambda(\frac{\partial K}{\partial \dot{\gamma}} \dot{\gamma} + \frac{\alpha}{\eta_p} K^2)]\mathbf{I} + 2(\eta_s + \eta_{RBC})\mathbf{D}, \quad (3)$$

where where \mathbf{D} is the rate of strain tensor while \mathbf{I} is the unity tensor, p the physical pressure and η_{RBC} is given by the Cross model

$$\eta_{RBC} = \frac{\eta_0^*}{1 + (k\dot{\gamma})^{1-n}}, \quad (4)$$

with n the shear thinning index, α the mobility parameter, while the function

$$K(\dot{\gamma}) = \frac{1}{\lambda} \left(\frac{\eta_0^*}{1 + (k\dot{\gamma})^{1-n}} - \eta_p \right), \text{ for } \lambda > 0, \quad (5)$$

is the so called normal function of the variable $\dot{\gamma}$, which measures the variation of deformation.

Using the above mentioned Cross model, the continuity equation and the Cauchy motion equations, expressing the tensor \mathbf{D} and the other involved operators in cylindrical coordinates, we arrive to the following three dimensional axi-symmetric system

$$\frac{1}{r} \frac{\partial(ru)}{\partial r} + \frac{\partial v}{\partial z} = 0 \quad (6)$$

$$\rho \left(\frac{\partial u}{\partial t} + u \frac{\partial u}{\partial r} + v \frac{\partial u}{\partial z} \right) + \frac{\partial p}{\partial r} = \eta(\dot{\gamma}) \Delta' u +$$

$$+ L \frac{\partial \dot{\gamma}}{\partial r} + M \left[-\frac{\partial \dot{\gamma}}{\partial r} + 2 \frac{\partial \dot{\gamma}}{\partial r} \frac{\partial u}{\partial r} + \frac{\partial \dot{\gamma}}{\partial z} \left(\frac{\partial u}{\partial z} + \frac{\partial v}{\partial r} \right) \right] \quad (7)$$

$$\rho \left(\frac{\partial v}{\partial t} + u \frac{\partial v}{\partial r} + v \frac{\partial v}{\partial z} \right) + \frac{\partial p}{\partial z} = \eta(\dot{\gamma}) \Delta' v +$$

$$+ L \frac{\partial \dot{\gamma}}{\partial z} + M \left[-\frac{\partial \dot{\gamma}}{\partial z} + 2 \frac{\partial \dot{\gamma}}{\partial z} \frac{\partial v}{\partial z} + \frac{\partial \dot{\gamma}}{\partial r} \left(\frac{\partial u}{\partial z} + \frac{\partial v}{\partial r} \right) \right]. \quad (8)$$

where u is the radial velocity (in direction r), v the axial velocity (in direction z) and p is the pressure, while

$$\dot{\gamma} = \sqrt{2 \left(\frac{\partial u}{\partial r} \right)^2 + 2 \left(\frac{\partial v}{\partial z} \right)^2 + \left(\frac{\partial u}{\partial z} + \frac{\partial v}{\partial r} \right)^2 + 2 \left(\frac{u}{r} \right)^2}$$

$$L = -\frac{2\lambda\alpha}{\eta_p} K \frac{\partial K}{\partial \dot{\gamma}} - \lambda \frac{\partial^2 K}{\partial \dot{\gamma}^2} \dot{\gamma} \quad (9)$$

$$M = \lambda \frac{\partial K}{\partial \dot{\gamma}}, K(\dot{\gamma}) = \frac{1}{\lambda} \left(\frac{\eta_0^*}{1 + k\dot{\gamma}^{1-n}} - \eta_p \right)$$

These evolution systems are completed by the boundary conditions which express both the presence of a pressure gradient along the Oz axis (in accord with the rhythmical pumping of the blood in vessels) and the elastic character of the permeable, porous wall

$$\frac{\partial u_z}{\partial r} = 0 \text{ and } u_r = 0 \text{ for } r = 0, \quad (10)$$

$$\frac{\partial u_z}{\partial r} = -\frac{\beta}{\sqrt{K}} u_z \text{ and } u_r = K(p - \nu) \text{ for } r = R + \mu(z, t), \quad (11)$$

In the first relation of (11) the Beavers-Joseph slip condition is expressed with the slip parameter β while K is the specific permeability of the porous media, meantime $u_r = K(p - \nu)$ is the consequence of the Starling law, with K the constant permeability of the wall, ν is built by the interstitial and osmotic pressure, supposed to be fixed, and a is a given constant.

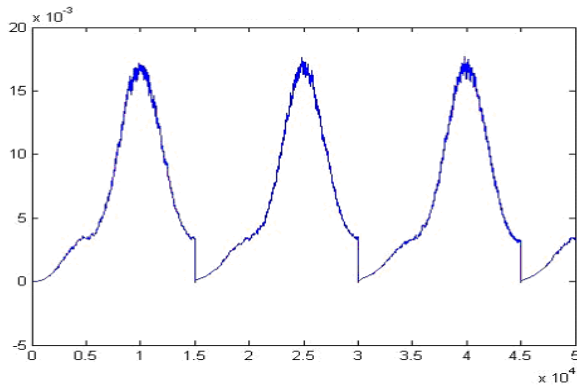


Figure 1. Evolution of the central axial velocity

We have calculated the case of the rigid wall and numerical tests have been effectuated for a vessel with radius 100μm. It was used the finite difference method (to simplify the program on a right angle domain), with separate nodes for u, v, p .

The evolution in time was made with the Adams-Basforth-Crank-Nicholson method with implicit part for the Laplacian and explicit part for the non-linear components. Thus, at every time step a huge linear system is to be solved but with a sparse matrix. It is necessary to work with small time step

($dt=0.0001$) for assuring the numerical stability. The algorithm presents some oscillations of the calculated solution but these don't disturb the stability. The work efficiency is acceptable (15000 time steps in about 2 hours). The attached figure 1 presents the evolution of the longitudinal velocity in the centre of the vessel for oscillating input and output pressure.

$$p_{in} = 10100 Pa * fact$$

$$p_{out} = 10000 Pa * fact$$

$$fact = \begin{cases} \sin \pi t, 0 < t < \frac{1}{2} \\ \frac{3}{2} - \frac{1}{2} \cos(2\pi(t - \frac{1}{2})), \frac{1}{2} < t < \frac{3}{2} \end{cases} \quad (12)$$

3. NUMERICAL MODEL FOR THE ELASTIC WALLS

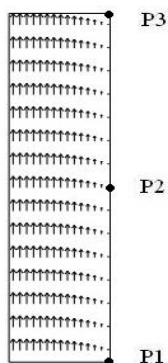


Figure 2. The velocity field at time $t=1$

One step further we use the presented mathematical model in the case when the elasticity and the porosity of the vessel wall are also considered. The data used for the numerical algorithms were achieved experimentally by C. Balan [1].

We have worked with a small vessel segment of radius $10^{-4}m$ and length of $4*10^{-4}m$. The blood parameters of the proposed model are: $\eta_s = 10^{-3} Pas$, $\eta_0^* = 1Pas$, $k = 100$, $n = 0.2$, $\lambda = 100$, $\alpha = 50$, the mass density is $1060kg/m^3$. We considered an oscillatory pressure $p_{in} = 10100 + 150 \cos(2\pi t) Pas$ on the input boundary ($z = 0$) and a constant pressure on the output boundary $p_{out} = 10000 Pa$. The permeability constant

is $K = 5*10^{-5}$ and the osmotic pressure is $\nu = 9900$. On the axis of symmetry we imposed the axial symmetry requirements and on the tube walls the Beavers-Joseph condition [2] and the permeability condition (Starling law [5]) $u_r = K(p - \nu)$.

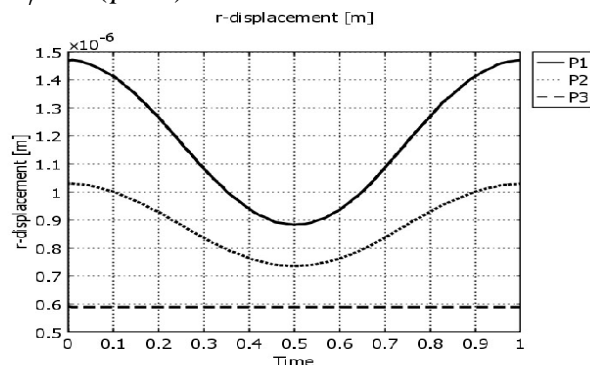


Figure 3. The r-displacement of the wall at points P1, P2 and P3

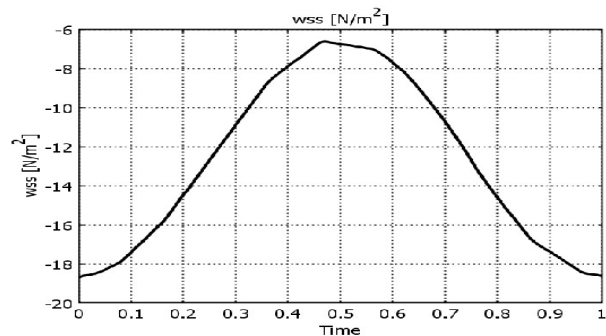


Figure 4. The WSS at point P2

On the attached figures some results of the numerical experiments are presented: on figure 2 the velocity field at the moment $t = 1$, on figure 3 the r-displacement (in the direction of the radius) of the wall at points P1, P2 and P3, on figure 4 the wall shear stress ($WSS = \eta(\frac{\partial u_r}{\partial z} + \frac{\partial u_z}{\partial r})$ evaluated at P2 is shown).

4. CONCLUSIONS

In this paper by considering a more general rheological model for the blood flow in thin vessels, with adequate numerical algorithms and solvers, we got some results for the longitudinal velocity in the case of the rigid vessel wall. Considering the elastic, porous behavior of the wall we obtained other results for the velocity field, for the r-displacement of the wall and for the wall shear stress (WSS).

In the future we will try to elaborate other numerical algorithms for reducing the calculation time and to eliminate completely the oscillating behavior. We also mention that this implemented rheological model can be easily set up, adjusting the parameters to obtain a better correspondence with the physical measurements.

The completed model can be applied for stenotic arteries, even in the 3-D case (axisymmetric).

REFERENCES

- [1] Balan, C.: Experimental and numerical investigations on the pure material instability of an Oldroyd's 3-constant model, *Continuum Mech. Thermodyn.*, 13, p. 399-414, 2001.
- [2] Beavers, G.S., Joseph, D.D.: Boundary conditions at a naturally permeable wall, *J. Fluid Mech.*, 30, 1967.
- [3] Petrița, T., Trif, D.: *Basics of Fluid Mechanics and Introduction to Computational Fluid Dynamics*, Springer Science, New York, 2005.
- [4] Pontrelli, G.: Blood flow through a circular pipe with an impulsive pressure gradient, *Math. Mod. & Meth. Appl.Sci.* 10(2), 187-202, 2000
- [5] Starling, E.M.: On the absorption of fluids from the convective tissue spaces, *J. Physiol.*, 19, 1896.



CONSIDERATIONS UPON THE C_R^2 TRUNCATED EXPONENTIAL DISTRIBUTION

Ştefan MAKSAY, Diana A. BISTRIAN

"Politehnica" University of Timisoara,
Faculty of Engineering Hunedoara, ROMANIA

Abstract

In this paper we generalize the one-dimensional exponential distribution, considering a continuous and twice differentiable extension of the truncated discontinuous probability density of exponential distribution.

Theoretical statements are in agreement with numerical analysis of data sets, calculations being performed in MathCAD package.



ON H-TRICHOTOMY IN BANACH SPACES

Codruta STOICA¹, Mihail MEGAN²

¹Department of Mathematics and Computer Science,
"Aurel Vlaicu" University of Arad, ROMANIA

²Department of Mathematics, West University of Timisoara, ROMANIA

Abstract

In this paper we emphasize the notion of skew-evolution semiflows, considered a generalization of semigroups, evolution operators and skew-product semiflows, which arise in the stability theory. We define and characterize a particular case of trichotomy, called the H -trichotomy, which is useful in describing the behaviors of the solution of evolution equations. We emphasize the fact that the trichotomy, introduced in finite dimensions in [1] and [5], is a natural generalization of dichotomy. A similar concept for stability was studied for evolution operators in [2]. This paper considers also other asymptotic properties, as exponential growth and decay, stability and instability.

Mathematics Subject Classification: 34D09

Keywords:

evolution equation, skew-evolution semiflow, H -trichotomy

1. INTRODUCTION

The concept of skew-evolution semiflows arises in the theory of evolution equations, which, as well as the theory of optimal control, is an important tool in describing processes derived from engineering or economics. The dynamical systems that study the real life phenomena are complex and the identification of appropriated mathematical models is difficult because in the case of systems described by partial differential equations the state space is often of infinite dimension. It is interesting to reconsider the definitions of asymptotic properties for differential equations by means of skew-evolution semiflows. In what follows, we will consider a more general case for asymptotic behaviors that not involves necessarily exponentials, but, instead, properly defined functions. Let us define the set Γ of all continuous functions $H: \mathbb{R}_+ \rightarrow \mathbb{R}_+^*$. We will denote by Θ the set of all functions $f: \mathbb{R}_+ \rightarrow \mathbb{R}_+$ with the property that there exists a constant $\mu \in \mathbb{R}$ such that $f(t) = e^{\mu t}$, $\forall t \geq 0$, with the subsets Θ_+ and Θ_- , for positive, respectively negative values of μ . By Ψ is denoted the set of continuous functions $h: \mathbb{R}_+ \rightarrow [1, \infty)$ defined such that, for all $H \in \Gamma$, there exist a function $f \in \Theta$ and a constant $k > 0$ with the properties

$$h(s) \leq kf(t-s)H(t), \quad \forall t, s \geq 0 \text{ and } h(2t)h(2s) \leq H(t+s), \quad \forall t, s \geq 0.$$

Remark 1.1. The set Ψ is not empty, as we can consider

$$h(t) = f(t) = e^{\nu t} \text{ and } H(t) = e^{2\nu t}, \quad \nu > 0, t \geq 0.$$

We will emphasize the notion of skew-evolution semiflows by means of evolution semiflows and evolution cocycles, as introduced by us in [4]. They naturally generalize notions as operators semigroups, evolution operators or skew-product semiflows. A skew-evolution semiflow depends on three variables, contrary to a skew-product semiflow, which depends only on two, and, hence, the study of asymptotic behaviors for skew-evolution semiflows in the nonuniform setting arises as natural, relative to the third variable. In this paper we will also consider the definitions and characterizations of some asymptotic properties, by means of the set of functions Θ , Γ and Ψ .

2. SKEW-EVOLUTION SEMIFLOWS

Let us consider (X, d) a metric space, V a real or complex Banach space, V^* its topological dual and $B(V)$ the family of linear V -valued bounded operators defined on V . The norm of vectors and operators is $\|\cdot\|$.

In what follows, we will denote $Y = X \times V$ and we will consider the set $T = \{(t, t_0) \in \mathbf{R} \mid t \geq t_0 \geq 0\}$. By I is designed the identity operator on V .

Definition 2.1. A mapping $\varphi: T \times X \rightarrow X$ with the properties:

- (s₁) $\varphi(t, t, x) = x, \forall (t, x) \in \mathbf{R}_+ \times X$;
 (s₂) $\varphi(t, s, \varphi(s, t_0, x)) = \varphi(t, t_0, x), \forall (t, s), (s, t_0) \in T, \forall x \in X$

is called *evolution semiflow* on X .

Definition 2.2. A mapping $\Phi: T \times X \rightarrow B(V)$ with the properties:

- (c₁) $\Phi(t, t, x) = I, \forall (t, x) \in \mathbf{R}_+ \times X$;
 (c₂) $\Phi(t, s, \varphi(s, t_0, x))\Phi(s, t_0, x) = \Phi(t, t_0, x), \forall (t, s), (s, t_0) \in T, \forall x \in X$

is called *evolution cocycle* over the evolution semiflow φ .

Definition 2.3. The mapping

$$C: T \times Y \rightarrow Y, C(t, s, x, v) = (\varphi(t, s, x), \Phi(t, s, x)v),$$

where φ is an evolution semiflow on X and the mapping Φ is an evolution cocycle over φ , is called *skew-evolution semiflow* on Y .

The next example emphasizes a skew-evolution semiflow generated by a system of differential equations.

Example 2.1. Let us consider the system of differential equations

$$\begin{cases} \dot{u} = (2t \sin t - 3)u \\ \dot{w} = (t \cos t + 2)w \\ \dot{z} = (2 - \cos t)z. \end{cases}$$

Let us define the spaces $X = \mathbf{R}_+$ and $V = \mathbf{R}^3$, which is endowed with the norm $\|v\| = |v_1| + |v_2| + |v_3|$, where $v = (v_1, v_2, v_3) \in V$.

The mapping

$$\varphi: T \times \mathbf{R}_+ \rightarrow \mathbf{R}_+, \varphi(t, s, x) = t - s + x$$

is an evolution semiflow on \mathbf{R}_+ .

The mapping

$$\Phi: T \times X \rightarrow B(V), \Phi(t, s, x)(v_1, v_2, v_3) = (U(t, s)v_1, W(t, s)v_2, Z(t, s)v_3),$$

where $U(t, s) = u(t)u^{-1}(s)$, $W(t, s) = w(t)w^{-1}(s)$, $Z(t, s) = z(t)z^{-1}(s)$, $\forall (t, s) \in T$ and $u(t)$, $w(t)$ and $z(t)$, where $t \in \mathbf{R}_+$, are the solutions of the given system of differential equations, is an evolution cocycle over the evolution semiflow φ on the metric space \mathbf{R}_+ . We obtain that $C = (\varphi, \Phi)$ is a skew-evolution.

The following asymptotic behaviors of skew-evolution semiflow are useful in characterizing the property of H -trichotomy, as well as their characterizations.

Definition 2.2. A skew-evolution semiflow $C = (\varphi, \Phi)$ is said to have *exponential growth* if there exists a nondecreasing function $g: \mathbf{R}_+ \rightarrow [1, \infty)$ with the property $\lim_{t \rightarrow \infty} g(t) = \infty$ such that:

$$\|\Phi(t, t_0, x)v\| \leq g(t-s)\|\Phi(s, t_0, x)v\|, \forall (t, s), (s, t_0) \in T, \forall (x, v) \in Y.$$

Proposition 2.1. A skew-evolution semiflow $C = (\varphi, \Phi)$ has exponential growth if and only if there exist some constants $M \geq 1$ and $\omega > 0$ such that:

$$\|\Phi(t, t_0, x)v\| \leq Me^{\omega(t-s)}\|\Phi(s, t_0, x)v\|, \forall (t, s), (s, t_0) \in T, \forall (x, v) \in Y.$$

Proof. Necessity. Let $t \geq s \geq t_0 \geq 0$ and n be the integer part of the real number $t - s$. We obtain successively

$$\begin{aligned} \|\Phi(t, t_0, x)v\| &\leq g(1)\|\Phi(t-1, t_0, x)v\| \leq \dots \leq [g(1)]^n\|\Phi(t-n, t_0, x)v\| \leq \\ &\leq Me^{n\omega}\|\Phi(s, t_0, x)v\| \leq Me^{\omega(t-s)}\|\Phi(s, t_0, x)v\|, \end{aligned}$$

for all $(t, s), (s, t_0) \in T$ and all $(x, v) \in Y$, where we have denoted $M = g(1) > 1$ and $\omega = \ln M > 0$.

Sufficiency. It is obtained immediately if we consider $g(u) = Me^{\omega u}$, $u \geq 0$. \square

Definition 2.3. A skew-evolution semiflow $C = (\varphi, \Phi)$ is said to be with *exponential decay* if there exists a nondecreasing function $g: \mathbf{R}_+ \rightarrow [1, \infty)$ with the property $\lim_{t \rightarrow \infty} g(t) = \infty$ such that:

$$\|\Phi(s, t_0, x)v\| \leq g(t-s)\|\Phi(t, t_0, x)v\|, \quad \forall (t, s), (s, t_0) \in T, \quad \forall (x, v) \in Y.$$

Proposition 2.2. A skew-evolution semiflow $C = (\varphi, \Phi)$ has exponential decay if and only if there exist some constants $M \geq 1$ and $\omega > 0$ such that:

$$\|\Phi(s, t_0, x)v\| \leq Me^{\omega(t-s)}\|\Phi(t, t_0, x)v\|, \quad \forall (t, s), (s, t_0) \in T, \quad \forall (x, v) \in Y.$$

Proof. Necessity. Let $t \geq s \geq t_0 \geq 0$. There exists a natural number n such that. We have following relations

$$\begin{aligned} \|\Phi(s, t_0, x)v\| &\leq g(1)\|\Phi(s+1, t_0, x)v\| \leq \dots \leq [g(1)]^n \|\Phi(s+n, t_0, x)v\| \leq \\ &\leq Me^{n\omega} \|\Phi(t, t_0, x)v\| \leq Me^{\omega(t-s)} \|\Phi(t, t_0, x)v\|, \end{aligned}$$

for all $(t, s), (s, t_0) \in T$ and all $(x, v) \in Y$, where we have considered the constants $M = g(1) > 1$ and $\omega = \ln M > 0$.

Sufficiency. It follows immediately for $g(u) = Me^{\omega u}$, $u \geq 0$.

3. ON THE PROPERTY OF H-TRICHOTOMY

A general concept of exponential trichotomy is emphasized in this section.

Definition 3.1. A mapping $P: Y \rightarrow Y$ given by $P(x, v) = (x, P(x)v)$, where $P(x)$ is a projection on $Y_x = \{x\} \times V$ and $x \in X$, is called *projector* on Y .

Definition 3.2. A skew-evolution semiflow $C = (\varphi, \Phi)$ is said to be *H-trichotomic* if there exist some mappings $N_1, N_2, N_3: \mathbf{R}_+ \rightarrow \mathbf{R}_+^*$ and three projectors families $\{P_k\}_{k \in \{1,2,3\}}$ such that following conditions hold:

(t₁) for each projector P_k , $k \in \{1,2,3\}$, the relation

$$P(\varphi(t, s, x))\Phi(t, s, x) = \Phi(t, s, x)P(x)$$

holds for all $(t, s) \in T$ and all $x \in X$;

(t₂) for all $x \in X$, the projections $P_1(x)$, $P_2(x)$ and $P_3(x)$ satisfy the conditions

$$P_1(x) + P_2(x) + P_3(x) = I \text{ and } P_i(x)P_j(x) = 0, \text{ for all } i, j \in \{1,2,3\}, i \neq j;$$

(t₃) following inequalities

$$\begin{aligned} (t_3^1) \quad H(t)\|\Phi(t, t_0, x)P_1(x)v\| &\leq N_1(s)\|\Phi(s, t_0, x)P_1(x)v\|; \\ (t_3^2) \quad H(s)\|\Phi(s, t_0, x)P_2(x)v\| &\leq N_2(t)\|\Phi(t, t_0, x)P_2(x)v\|; \\ (t_3^3) \quad \|\Phi(t, t_0, x)P_3(x)v\| &\leq N_3(s)H(t)\|\Phi(s, t_0, x)P_3(x)v\| \text{ and} \\ &\|\Phi(s, t_0, x)P_3(x)v\| \leq N_3(t)H(s)\|\Phi(t, t_0, x)P_3(x)v\|, \end{aligned}$$

hold for all $(t, s), (s, t_0) \in T$, for all $(x, v) \in Y$ and all $H \in \Gamma$.

Remark 3.1. In the particular case $H(t) = e^{\nu t}$, $t \geq 0$, $\nu > 0$, the exponential trichotomy for skew-evolution semiflows, defined and characterized by us in [3] for evolution operators, is obtained in a nonuniform setting.

Remark 3.2. (i) A projector P on Y with property (t₁) is also called invariant relative to the skew-evolution semiflow $C = (\varphi, \Phi)$;

(ii) If three projectors families $\{P_k\}_{k \in \{1,2,3\}}$ satisfy relations (t₁) and (t₂) of Definition 3.2, they are usually said to be compatible with the skew-evolution semiflow C .

In what follows, we will denote a skew-evolution semiflow $C_k = (\varphi, \Phi_k)$, $k \in \{1,2,3\}$, where $\Phi_k(t, s, x)v = \Phi(t, s, x)P_k(x)v$, $(t, s) \in T$, $(x, v) \in Y$.

Example 3.1. Let us consider the skew-evolution semiflow given in Example 2.1.

We obtain for the evolution cocycle $\Phi: T \times X \rightarrow B(V)$ following relations

$$\begin{aligned} \Phi(t, s, x)(v_1, v_2, v_3) &= \\ &= (e^{2t \cos t - 2s \cos s - 2 \sin t + 2 \sin s - 3t + 3s} v_1, e^{t \sin t - s \sin t + \cos t - \cos s + 2t - 2s} v_2, e^{-\sin t + \sin s + 2t - 2s} v_3) \end{aligned}$$

Let us define the projectors $P_1(x, v) = (v_1, 0, 0)$, $P_2(x, v) = (0, v_2, 0)$ and $P_3(x, v) = (0, 0, v_3)$. As following relation holds

$$2t \cos t - 2s \cos s - 2 \sin t + 2 \sin s - 3t + 3s \leq -t + 5s + 4, \quad \forall (t, s) \in T,$$

we have that

$$H_1(t)\|\Phi(t, s, x)P_1(x)v\| \leq N_1(s)|v_1|, \quad \forall (t, s, x, v) \in T \times Y,$$

where we have denoted $H_1(t) = e^t$ and $N_1(s) = e^{5s+4}$.

According to the inequality

$$t \sin t - s \sin s + \cos t - \cos s + 2t - 2s \geq t - 3s - 2, \quad \forall (t, s) \in T,$$

it follows that

$$N_2(t) \|\Phi(t, s, x) P_2(x) v\| \geq H_2(s) |v_2|, \quad \forall (t, s, x, v) \in T \times Y,$$

where we have considered $H_2(s) = e^{-3s}$ and $N_2(t) = e^{-t+2}$.

Also, as

$$-\sin t + \sin s + 2t - 2s \leq 2t - s + 1, \quad \forall (t, s) \in T,$$

we have

$$\|\Phi(t, s, x) P_3(x) v\| \leq N_3(s) H_3(t) |v_3|, \quad \forall (t, s, x, v) \in T \times Y$$

and, as

$$-\sin t + \sin s + 2t - 2s \geq t - 2s - 1, \quad \forall (t, s) \in T,$$

we obtain

$$N_3(t) H_3(s) \|\Phi(t, s, x) P_3(x) v\| \geq |v_3|, \quad \forall (t, s, x, v) \in T \times Y,$$

where, in both cases, we have denoted $H_3(u) = e^{2u}$ and $N_3(u) = e^{-u+1}$.

As a remark, we can consider, without any loss of generality, the function denoted $H(t) = \min\{H_1(t), H_2(t), H_3(t)\}$, $t \geq 0$.

It follows that the skew-evolution semiflow $C = (\varphi, \Phi)$ is H -trichotomic.

The next main result of this paper can be considered as an integral characterization for the concept of H -trichotomy.

Theorem 3.1. *Let $H \in \Gamma$ and $h \in \Psi$. A skew-evolution semiflow $C = (\varphi, \Phi)$ is H -trichotomic if and only if there exist some mappings $M_1, M_2, M_3: \mathbb{R}_+ \rightarrow \mathbb{R}_+^*$, some functions $f_1, f_2 \in \Theta$ and three projectors families $\{P_k\}_{k \in \{1,2,3\}}$ compatible with C such that the skew-evolution semiflow C_1 has exponential growth and the skew-evolution semiflow C_2 has exponential decay and such that following conditions hold:*

$$(i) \frac{1}{H(t)} \int_{t_0}^t h(\tau) \|\Phi_1(t, \tau, x)^* v^*\| d\tau \leq M_1(t_0) \|P_1(x) v^*\|;$$

$$(ii) h(t_0) \int_{t_0}^t \frac{1}{H(\tau)} \|\Phi_2(\tau, t_0, x) v\| d\tau \leq M_2(t_0) \|\Phi_2(t, t_0, x) v\|;$$

$$(iii) \int_s^t f_1(\tau - s) \|\Phi_3(\tau, t_0, x) v\| d\tau \leq M_3(t_0) \|\Phi_3(s, t_0, x) v\|;$$

$$(iv) \int_s^t f_2(t - \tau) \|\Phi_3(\tau, t_0, x) v\| d\tau \leq M_3(t_0) \|\Phi_3(t, t_0, x) v\|,$$

for all $(t, s), (s, t_0) \in T$ and all $(x, v) \in Y$, $v^* \in V^*$ with $\|v^*\| \leq 1$.

Proof. *Necessity.* As the skew-evolution semiflow C is H -trichotomic, it implies that the relations (t₃) of Definition 3.2 hold.

(i) There exist a function $f \in \Theta_-$ and a constant $k > 0$ with the property

$h(s) \leq kf(t-s)H(t)$, $\forall t \geq s \geq 0$. Let us denote $f(t) = e^{-\nu t}$, $\nu > 0$. We obtain

$$\|\Phi_1(t, t_0, x) v\| \leq \frac{N_1(s)}{H(t)} \|\Phi_1(s, t_0, x) v\| \leq \overline{M}_1(s) e^{-\nu(t-s)} \|\Phi_1(s, t_0, x) v\|,$$

for all $(t, s), (s, t_0) \in T$ and for all $(x, v) \in Y$, where we have considered the function $\overline{M}_1: \mathbb{R}_+ \rightarrow \mathbb{R}_+^*$,

$$\overline{M}_1(u) = k \frac{N_1(u)}{h(u)}.$$

We obtain further

$$\frac{1}{H(t)} \int_{t_0}^t h(\tau) \|\Phi_1(t, \tau, x)^* v^*\| d\tau \leq k \int_{t_0}^t e^{-\nu(t-\tau)} \|\Phi_1(t, \tau, x)^* v^*\| d\tau \leq M_1(t_0) \|P_1(x) v^*\|,$$

where we have denoted $M_1(u) = kv^{-1}\overline{M}_1(u)$, $u \geq 0$.

(ii) There exist a function $f \in \Theta_-$ and a constant $k > 0$ with the property

$h(t_0) \leq kf(s-t_0)H(s)$, $\forall s \geq t_0 \geq 0$. Let us consider $f(t) = e^{-\nu t}$, $\nu > 0$. We have

$$\begin{aligned} \|\Phi_2(s, t_0, x)v\| &\leq \frac{N_2(t)}{H(s)} \|\Phi_2(t, t_0, x)v\| \leq k \frac{N_2(t)}{h(t_0)} e^{-\nu(s-t_0)} \|\Phi_2(t, t_0, x)v\| \leq \\ &\leq k \frac{N_2(t)}{h(t_0)} e^{\nu t} e^{-\nu(t-s)} e^{-\nu(2s-t_0)} \|\Phi_2(t, t_0, x)v\| \leq \overline{M}_2(t) e^{-\nu(t-s)} \|\Phi_2(t, t_0, x)v\|, \end{aligned}$$

for all $(t, s), (s, t_0) \in T$ and for all $(x, v) \in Y$, where we have denoted the function $\overline{M}_2: \mathbf{R}_+ \rightarrow \mathbf{R}_+$, $\overline{M}_2(u) = kN_2(u)e^{\nu u}$.

(iii) and (iv) are obtained by a similar argumentation, according to Proposition 2.1 and Proposition 2.2.

Sufficiency. (i) Let $t \geq t_0 + 1$ and $s \in [t_0, t_0 + 1]$. As $H \in \Gamma$ and $h \in \Psi$, there exists a constant $\alpha > 0$ such that $h(s) \leq e^{-\alpha(t-s)}H(t)$, for all $(t, s) \in T$. Then, as the skew-evolution semiflow C_1 has exponential growth, according to Proposition 2.1, there exist some constants $M \geq 1$ and $\omega > 0$ such that following relations hold

$$\begin{aligned} e^{-(\alpha+\omega)} \left\| \left\langle v^*, e^{\alpha(t-t_0)} \Phi_1(t, t_0, x)v \right\rangle \right\| &= e^{-(\alpha+\omega)} \int_{t_0}^{t_0+1} \left\| \left\langle \Phi_1(t, \tau, x)^* v^*, e^{\alpha(t-t_0)} \Phi_1(\tau, t_0, x)v \right\rangle \right\| d\tau \leq \\ &\leq \int_{t_0}^{t_0+1} e^{\alpha(t-\tau)} \left\| \Phi_1(t, \tau, \varphi(\tau, t_0, x))^* v^* \right\| e^{-\omega(\tau-t_0)} \|\Phi_1(\tau, t_0, x)v\| d\tau \leq \\ &\leq M \|v\| \int_{t_0}^t e^{\alpha(t-\tau)} \left\| \Phi_1(t, \tau, \varphi(\tau, t_0, x))^* v^* \right\| d\tau \leq MN_1(t_0) \|P_1(x)v\| \|P_1(x)v^*\|. \end{aligned}$$

By taking supremum relative to $\|v^*\| \leq 1$, we have

$$\|\Phi_1(t, t_0, x)v\| \leq M_1(t_0) e^{-\alpha(t-t_0)} \|P_1(x)v\|,$$

for all $t \geq t_0 + 1$ and all $(x, v) \in Y$, where $M_1(u) = MN(u)e^{\alpha+\omega}$, $u \geq 0$.

On the other hand, for $t \in [t_0, t_0 + 1]$ and $(x, v) \in Y$, we obtain

$$\|\Phi_1(t, t_0, x)v\| \leq Me^{\omega(t-t_0)} \|v\| \leq \widehat{M} e^{-\alpha(t-t_0)} \|v\|,$$

where we have denoted $\widehat{M} = Me^{\alpha+\omega}$. Hence, it follows that

$$\|\Phi_1(t, t_0, x)v\| \leq [M_1(t_0) + \widehat{M}] e^{-\alpha(t-t_0)} \|v\|,$$

for all $(t, t_0) \in T$ and for all $(x, v) \in Y$.

Further, if we consider

$$H(u) = f(u) \text{ and } N_1(u) = [M_1(u) + \widehat{M}]f(u),$$

where $f(u) = e^{\nu u} \in \Theta_+$ and $u \geq 0$, we obtain relation (3').

(ii) We have considered $H \in \Gamma$ and $h \in \Psi$, hence there exists a constant $\beta > 0$ such that $h(s) \leq e^{-\beta(t-s)}H(t)$, for all $(t, s) \in T$. As the skew-evolution semiflow C_2 has exponential growth, according to Definition 2.3, there exists a nondecreasing function $g: \mathbf{R}_+ \rightarrow [1, \infty)$ with the property $\lim_{t \rightarrow \infty} g(t) = \infty$ such that

$$\|\Phi_2(s, t_0, x)v\| \leq g(t-s) \|\Phi_2(t, t_0, x)v\|, \quad \forall (t, s), (s, t_0) \in T, \quad \forall (x, v) \in Y.$$

We will denote

$$K = \int_0^1 e^{-\beta\tau} g(\tau) d\tau.$$

We obtain successively following relations

$$\begin{aligned} K\|P_2(x)v\| &= \int_{t_0}^{t_0+1} e^{-\beta(\tau-t_0)} g(\tau-t_0) \|\Phi_2(t_0, t_0, x)v\| d\tau \leq \\ &\leq \int_{t_0}^{t_0+1} e^{-\beta(\tau-t_0)} \|\Phi_2(\tau, t_0, x)v\| d\tau \leq M_2(t) e^{\beta(t-t_0)} \|\Phi_2(t, t_0, x)v\|, \end{aligned}$$

for all $(t, t_0) \in T$ and for all $(x, v) \in Y$. According to Definition 2.2, this relation is equivalent with

$$\|\Phi_2(s, t_0, x)v\| \leq \frac{1}{K} M_2(t) e^{\beta(t-s)} \|\Phi_2(t, t_0, x)v\|,$$

for all $(t, s), (s, t_0) \in T$ and for all $(x, v) \in Y$.

If we take

$$H(u) = f(u) \text{ and } N_2(u) = M_2(u)f(u),$$

for $f(u) = e^{-\beta u} \in \Theta_-$ and $u \geq 0$, relation (2.3) is obtained.

(iii) and (iv) can similarly be proved.

4. CONCLUSIONS

In the last decades, a great progress concerning the study of asymptotic behaviors for evolution equations can be observed. The possibility of reducing the nonautonomous case in the study of evolutionary families or skew-product flows to the autonomous case of evolution semigroups on Banach spaces is considered an important way toward interesting applications. The study of the asymptotic behavior of linear skew-product semiflows has been used in the theory of evolution equations in infinite dimensional spaces. The approach from the point of view of asymptotic properties for the evolution semigroup associated to the linear skew-product semiflows was essential. Instead, in our study we have considered more general characterizations for the asymptotic properties of the solutions of evolution equations, described by means of skew-evolution semiflows, which generalize the above notions. Also, the approach was not restrained by considering in the definitions exponentials. As a remark, in Definition 3.2 we have the definitions for H -stability, H -instability, H -growth and H -decay, characterized, respectively, by Theorem 3.1, which extends toward applications in engineering and economics the study of evolution equations.

Acknowledgement. This work is financially supported by the Research Grant CNCSIS PN II ID 1080 of the Romanian Ministry of Education, Research and Innovation.

REFERENCES

- [1] S. Elaydi, O. Hajek, *Exponential trichotomy of differential systems*, J. Math. Anal. Appl., **129** (1988) 362-374.
- [2] M. Megan, *On H-stability of evolution operators*, Preprint Series in Mathematics, West University of Timisoara, **66** (1995) 1-7.
- [3] M. Megan, C. Stoica, *On uniform exponential trichotomy of evolution operators in Banach spaces*, Integral Equations Operator Theory, **60**, No. 4 (2008) 499-506.
- [4] M. Megan, C. Stoica, *Exponential instability of skew-evolution semiflows in Banach spaces*, Studia Univ. Babeş-Bolyai Math., **LIII**, No. 1 (2008) 17-24.
- [5] R.J. Sacker, G.R. Sell, *Existence of dichotomies and invariant splittings for linear differential systems III*, J. Differential Equations, **22** (1976) 497-522.



ASYMPTOTIC BEHAVIORS OF STOCHASTIC EVOLUTION COCYCLE

Diana STOICA

"Politehnica" University of Timisoara, Faculty of Engineering of Hunedoara, ROMANIA

Abstract:

The paper presents the properties of exponential stability for stochastic evolution semiflow and stochastic evolution cocycles. Some characterizations which generalize classic results are also provided.

Keywords:

Stochastic evolution semiflow, stochastic evolution cocycles, exponential stability

1. INTRODUCTION

The problem of existence of stochastic semiflows for semilinear stochastic evolution equation is a non-trivial one, mainly due to the well-established fact that finite-dimensional methods for constructing (even continuous) stochastic flow break down in the infinite dimensional setting of semilinear stochastic evolution equations (cf. [3], [7], [8]). For linear stochastic evolution equation with finite-dimensional noise, a stochastic semiflow (i.e. random evolution operator) was obtained in [1].

In [5], is prove the existence of perfect differentiable cocycles generated by mild solutions of a large class of semilinear stochastic evolution equations (sees) and stochastic partial differential equations (spdes).

In this article we consider the stochastic evolution cocycle over a stochastic evolution semiflow, and present the proprieties of exponential stability.

We considered (X, d) metric space and denote V and U real Hilbert spaces. Let $B(V)$ be a Banach space of all linear and bounded maps $A: V \rightarrow V$. We denote the sets $T = \{(t, t_0) \in \mathbb{R}^2, t \geq t_0 \geq 0\}$ and $Y = X \times V$. The mapping $P: Y \rightarrow Y$ given by $P(x, v) = (x, P(x)v)$, $\forall (x, v) \in Y$ is an projector on Y , where $P(x)$ is a projection on $Y_x = \{x\} \times V$, $x \in X$. Let $B(X)$ denote its Borel σ -algebra.

Assume $(\Omega, \mathcal{F}, \mathbf{P})$ is a complete probability space with a normal filter $\{\mathcal{F}_t\}_{t \geq 0}$, i.e. \mathcal{F}_0 contains the null sets in \mathcal{F} and $\mathcal{F}_t = \bigcap_{s > t} \mathcal{F}_s$, for all $t \geq 0$, and let us consider a real valued $\{\mathcal{F}_t\}$ -Wiener process $\{W(t)\}$, $t \geq 0$.

Definition 1. A stochastic process $W(t): (\Omega, \mathcal{F}, \mathbf{P}) \rightarrow U$ is a Wiener process if and only if $W(t) = \sum_{i=1}^{\infty} \beta_i(t) e_i$ where $\beta_i(t)$ are real Wiener process, independents, which are the mean $E(\beta_i(t)^2) = \lambda_i t$, where $\sum_{i=1}^{\infty} \lambda_i < \infty$, $\{e_i\}, i = 1, 2, \dots$ is an orthonormal system of vectors from U .

Definition 2. Let be X a Banach space. A stochastic evolution semiflow on X is a random field $\varphi: T \times X \times \Omega \rightarrow X$ satisfying the following proprieties:

- (1) $\varphi(t, t, x, \omega) = x$, for all (t, x) from $T \times X$ and $\omega \in \Omega$;
- (2) $\varphi(t, s, \varphi(s, t_0, x, \omega), \omega) = \varphi(t, t_0, x, \omega)$, $\forall (t, s), (s, t_0) \in T, \forall x \in X$, and $\omega \in \Omega$.

Definition 3. A stochastic evolution cocycles on V , over an stochastic evolution semiflow $\varphi : T \times X \times \Omega \rightarrow X$, is a random field $\Phi : T \times X \times \Omega \rightarrow B(V)$, with the following proprieties:

- (1) $\Phi(t, t, x, \omega) = I, \forall (t, x) \in \mathbb{R}_+ \times X$, and $\omega \in \Omega$,
 (2) $\Phi(t, s, \varphi(s, t_0, x, \omega), \omega) \Phi(s, t_0, x, \omega) = \Phi(t, t_0, x, \omega), \forall (t, s), (s, t_0) \in T, \forall x \in X$, and $\omega \in \Omega$.

Definition 4. An stochastic evolution cocycles Φ has uniformly exponential growth if exist the constants $M \geq 1, \lambda > 0$ such that

$$E \|\Phi(t, s, x, \omega)\|^2 \leq M e^{\lambda(t-s)}, \forall (t, s) \in T, \forall x \in X \text{ and } \omega \in \Omega. \quad (1)$$

Definition 5. The stochastic evolution cocycles Φ is called strongly measurable if for every $(s, x, \omega, v) \in T \times X \times \Omega \times V$ the mapping $t \rightarrow \|\Phi(t, s, x, \omega)v\|$ is measurable on $[s, \infty)$.

Definition 6. The mapping, $C : T \times X \times V \times \Omega \rightarrow X \times V$, definite by

$$C(t, s, x, v, \omega) = (\varphi(t, s, x, \omega), \Phi(t, s, x, \omega)v), \quad (2)$$

where Φ is a stochastic evolution cocycles over an stochastic evolution semiflow φ , is called stochastic skew-evolution semiflow on Y .

2. UNIFORMLY EXPONENTIALLY STABILITY

Let be $F : [0, T] \times \Omega \rightarrow H$ an stochastic process, then $E(F) = \int_{\Omega} F(\Omega) dP(\omega)$ represent the mean of stochastic process F , where P is the probability measure. If $F \in C([0, T], L^2(\Omega, H))$ then

$$\int_0^T E \|F(t)\|^2 dt = E \int_0^T \|F(t)\|^2 dt. \quad (3)$$

For an process Wiener $W(t)$ in rapport with the filter $\{F_t\}$ we have

$$E \left\| \int_0^T F(t) dw(t) \right\|^2 = E \int_0^T \|F(t)\|^2 dt. \quad (4)$$

Definition 7. The stochastic evolution cocycles Φ is said to be uniformly exponentially stable if for some positive constants $N \geq 1, \nu > 0$ one has

$$E \|\Phi(t, t_0, x, \omega)v\|^2 \leq N e^{-\nu(t-t_0)} E \|\Phi(s, t_0, x, \omega)v\|^2, \quad (5)$$

for all $(t, s), (s, t_0) \in T, (x, v) \in X \times V$, and $\omega \in \Omega$.

Lemma 8. The stochastic skew-evolution semiflow $C=(\varphi, \Phi)$, is uniformly exponentially stable if and only if a no decreasing function $f : [0, \infty) \rightarrow [1, \infty)$, with property $\lim_{t \rightarrow \infty} f(t) = \infty$, such that we have the relation:

$$f(t-s) E \|\Phi(t, t_0, x, \omega)v\|^2 \leq E \|\Phi(s, t_0, x, \omega)v\|^2, \quad (6)$$

for all $(t, s), (s, t_0) \in T, (x, v) \in X \times V$, and for all $\omega \in \Omega$.

Proof. Necessity. If $C=(\varphi, \Phi)$, is uniformly exponentially stable, result from Definition 7 that for $f(t) = N^{-1}e^{\nu t}$.

Sufficiency. Let be $t \geq s \geq t_0 \geq 0$ and we denote $t - s = [n]$. Let $N = f(1) > 1$ and $\nu = \ln N$. That result:

$$\begin{aligned} E \|\Phi(s, t_0, x, \omega)v\|^2 &\geq f(1) E \|\Phi(s+1, t_0, x, \omega)v\|^2 \geq \dots \geq N^n E \|\Phi(s+n, t_0, x, \omega)v\|^2 \geq \\ &\geq N^{n+1} E \|\Phi(t, t_0, x, \omega)v\|^2 \geq N e^{\nu n} E \|\Phi(t, t_0, x, \omega)v\|^2 \geq N e^{\nu(t-s)} E \|\Phi(t, t_0, x, \omega)v\|^2 \end{aligned}$$

and so

$$E \|\Phi(s, t_0, x, \omega)v\|^2 \geq N e^{\nu(t-s)} E \|\Phi(t, t_0, x, \omega)v\|^2,$$

for all $(t, s), (s, t_0) \in T, (x, v) \in X \times V$, and for all $\omega \in \Omega$.

Thus the stochastic skew-evolution semiflow $C=(\varphi, \Phi)$, is uniformly exponentially stable.†

Theorem 9. Let be $C=(\varphi, \Phi)$, an skew-product semiflow with uniformly exponential growth, and is strong measurable. Then C is uniformly exponentially stable if and only if $\exists M \geq 0$ a constant, such that:

$$\int_t^\infty E \|\Phi(s, t_0, x, \omega)v\|^2 ds \leq ME \|\Phi(t, t_0, x, \omega)v\|^2, \quad (7)$$

for all $(t, t_0) \in T$, $(x, v) \in X \times V$, and for all $\omega \in \Omega$.

Proof. Necessity. Let be an stochastic skew-evolution semiflow $C=(\varphi, \Phi)$, uniformly exponentially stable. Then, for $N \geq 1, \nu > 0$ we have from Definition 7, that

$$E \|\Phi(s, t_0, x, \omega)v\|^2 \leq Ne^{-\nu(s-t)} E \|\Phi(t, t_0, x, \omega)v\|^2, \quad (8)$$

for all $(s, t), (t, t_0) \in T$, $(x, v) \in X \times V$, and for all $\omega \in \Omega$. Then from integration of this inequality result:

$$\int_t^\infty E \|\Phi(s, t_0, x, \omega)v\|^2 ds \leq NE \|\Phi(t, t_0, x, \omega)v\|^2 \int_t^\infty e^{-\nu(t-s)} ds \leq ME \|\Phi(t, t_0, x, \omega)v\|^2,$$

for all $(t, t_0) \in T$, $(x, v) \in X \times V$, and $\omega \in \Omega$, where $M = N\nu^{-1}$.

Sufficiency. For $t \geq t_0 + 1$, and ω from Definition 4 we have

$$\begin{aligned} \frac{1 - e^{-\omega}}{\omega} E \|\Phi(t, t_0, x, \omega)v\|^2 &\leq \int_{t_0}^t e^{-\omega(t-s)} E \left\| \langle v^*, \Phi(t, s, \varphi(s, t_0, x, \omega))\Phi(s, t_0, x, \omega)v \rangle \right\|^2 ds \leq \\ &\leq M' \|v^*\| \int_{t_0}^t E \|\Phi(s, t_0, x, \omega)v\|^2 ds \leq M'M \|v\| \|v^*\|, \end{aligned}$$

for all $(t, t_0) \in T$, $(x, v) \in X \times V$, and $\omega \in \Omega$. So we have the relation

$$E \|\Phi(t, t_0, x, \omega)v\| \leq K \|v\|, \quad \forall (t, t_0, x, v, \omega) \in T \times Y \times \Omega,$$

where $K = M'(e^\omega + M/c)$, $c = (1 - e^{-\omega})/\omega$.

Thus result that

$$\begin{aligned} (t - t_0) E \|\Phi(t, t_0, x, \omega)v\|^2 &= \int_{t_0}^t E \|\Phi(t, t_0, x, \omega)v\|^2 ds = \\ &= \int_{t_0}^t E \|\Phi(t, s, \varphi(s, t_0, x, \omega))\Phi(s, t_0, x, \omega)v\|^2 ds \leq \\ &\leq K \int_{t_0}^t E \|\Phi(s, t_0, x, \omega)v\|^2 ds \leq KM \|v\|. \end{aligned}$$

In conclusion we obtain the relation

$$(t - t_0 + 1) E \|\Phi(t, t_0, x, \omega)v\|^2 \leq K(M + 1) \|v\|,$$

for all $(t, t_0) \in T$, $(x, v) \in X \times V$, and $\omega \in \Omega$.

Thus for function $f : [0, \infty) \rightarrow [1, \infty)$, with property $\lim_{t \rightarrow \infty} f(t) = \infty$, definite by

$$f(t) = \frac{t + 1}{K(M + 1)},$$

Result from Lemma 8, that C is uniformly exponentially stable.†

REFERENCES

- [1] A. Bensoussan, F. Flandoli, Stochastic inertial manifold, *Stochastic Rep.* 53 (1995), no. 1-2, 13–39.
- [2] S.N. Chow, H. Leiva, Two definitions of exponential dichotomy for skew-product semiflow in Banach spaces, *Proc. Amer. Math. Soc.* 124 (1996), 1071–1081.
- [3] F. Flandoli, Stochastic flows for non-linear second-order parabolic SPDE, *Ann. Probab.* 24 (1996), no. 2, 547–558.
- [4] M. Megan, A. L. Sasu, and B. Sasu, On uniform exponential stability of linear skew-product semiflows in Banach spaces, *Bulletin of the Belgian Mathematical Society - Simon Stevin*, 9 (2002) 143–154.
- [5] M. Megan, C. Stoica, On Uniform Exponential Trichotomy of Evolution Operators in Banach Spaces, *Integral Equations and Operator Theory*, 60 (2008) 499–506.
- [6] S. E. A. Mohammed, T. Zhang, H. Zhao, The stable manifold theorem for semilinear stochastic evolution equations and stochastic partial differential equations, Arxiv preprint math.PR/0503320, 2005 - arxiv.org.
- [7] G. Da Prato, J. Zabczyk, *Stochastic Equations in infinite dimensions*, University Press, Cambridge, 1992.
- [8] Skorohod, A.V., *Random linear operators*, Riedel, 1984.
- [9] C. Stoica, M. Megan, Discrete Asymptotic Behaviors for Skew-Evolution Semiflows on Banach Spaces, arXiv: 0808.0378v2 [math.CA].
- [10] V.M. Ungureanu, Representations of mild solutions of time-varying linear stochastic equations and the exponential stability of periodic systems, *Electronic Journal of Qualitative Theory of Differential Equations* 4 (2004), 1–22.



SOME DISADVANTAGES OF STANDARD BUCKLING ANALYSIS COMPARING TO INCREMENTAL GEOMETRIC NONLINEAR ANALYSIS

Ivana MATIJEVIĆ¹, Dušan KOVAČEVIĆ²

^{1,2}University of Novi Sad, Faculty of Technical Sciences
Trg Dositeja Obradovica 6, 21000 Novi Sad, SERBIA

Abstract:

Modeling of real behavior of structural systems requires complex assumptions, which have, as consequences, nonlinear stress-strain state. One of the causes of nonlinear behavior is geometric nonlinearity.

Determining of critical load parameter by standard bifurcation buckling solution is appropriate for solving stability problems if the longitudinal and lateral load ratio is small. In case that structure has large displacements, it is necessary to use incremental-iterative solution. The main advantage of this concept is possibility to verify changes in: loads, mechanical-reological properties of material, geometry of structural system, and modeling effect of those changes on structural behavior.

Keywords:

finite element method, geometric nonlinearity, buckling analysis

1. INTRODUCTION

A FEM linear model in some cases of numerical analysis of structural systems is not appropriate. Assumptions in linear analysis are simple and results may vary of close solution. Using simple FEM models, it is possible to achieve efficiency of analyses and calculations, but without adequate accuracy. Also, bearing capacity, adaptability and durability of structural system can be endangering.

For modelling of real behaviour of structural system nonlinear stress-strain relation should be taken into consideration. The nonlinear analysis is more complex than linear analysis because:

- + during the load process deformations are not proportional,
- + after the effect of load, model does not have original form,
- + for finite values of displacements, deformations and stresses principle of superposition can not be applied and
- + the stiffness matrix and load vector of loading can not be fully formed due to the fact that they depending on the final solution.

One of the causes of nonlinear behaviour is geometric nonlinearity, where relation between strains and displacement is nonlinear, but material has linear elastic properties.

Geometric nonlinearity arises when deformations and/or displacements are large enough to significantly change geometry and position of the system. As a consequence of large deformation and/or displacement, relation deformation-displacement and equilibrium are nonlinear. Reaching the limit state in the geometric nonlinearity is loss of stability of structural system.

Problems of geometric nonlinearity can be classified as continual nonlinearity (smooth nonlinearities). The characteristic examples of smooth nonlinearity are nonlinear behavior due to large displacements and/or deformations, elasto-plastic material properties, reological

properties of material, etc. Continual "smooth" functions are used for approximation of continual nonlinearity.

Figure 1 show examples of large deformations and large displacements. For large deformations, changes in shape are significant and for large displacements, changes in translational and/or rotational position are significant. Procedures for solving such problems are numerous and implemented in the general computer FEM software.

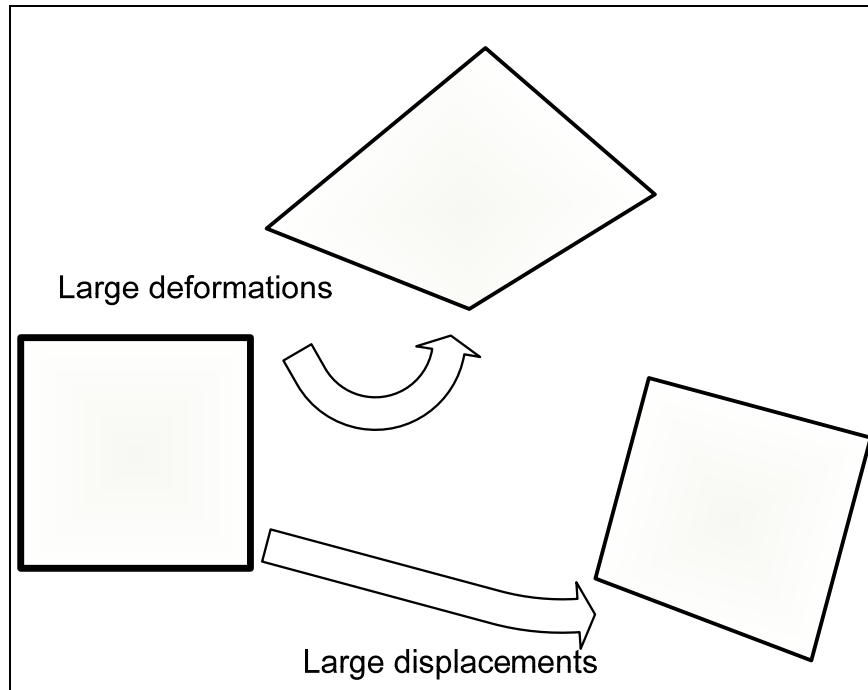


Figure 1. Examples of geometric nonlinearity: large displacements and large deformations

2. FEM MODELING OF GEOMETRIC NONLINEAR BEHAVIOR

For analyzing of geometric nonlinear phenomenon follow theories can be applied:

- + general geometric nonlinear theory,
- + geometric nonlinear theory in strict sense (second-order theory),
- + "linearized" second-order theory and
- + so-called "P- Δ " methods.

The greatest accuracy of numerical solution can be achieved using general nonlinear theory and the lowest accuracy is obtained by applying "P- Δ " methods.

Geometric nonlinear theory in strict sense assumed linear relations between displacements and deformations on deformed model of structures. This model is simple and because of quality approximation it can be used in modeling most of structural problems.

According to "linearized" second-order theory equilibrium equations are linear. The widest application of this theory is in analyzing of so-called "bifurcational stability" of construction although in some cases solution is not adequate. The main disadvantage of this theory is analyzing of undeformed structure, what is particularly significant in problems of stability of structural systems with large displacements.

The main problem in geometric nonlinear analysis is testing stability of structural system, i.e. determining of critical load. The critical load depends on the system topology (Figure 2), which may occur following cases:

- + due to increasing of load, stiffness of system increases,
- + after decreasing, stiffness of system is increasing, but it can be a point where buckling may occur and
- + loss of stability is realized by suddenly transition to a new equilibrium branch ("snap-trough" effect).

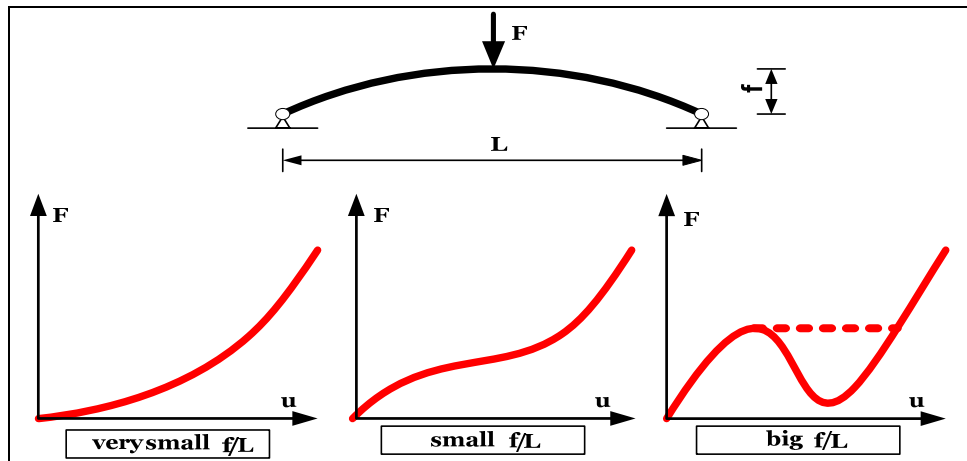


Figure 2. Topology of system and geometric nonlinear behavior

Determining of critical load parameter by standard bifurcation buckling solution is appropriate for solving stability problems if the longitudinal and lateral load ratio is small. In case that structure has large displacements, it is necessary to use incremental-iterative solution.

2.1. Linear buckling analysis

Verification of stability in geometric nonlinear analysis is determining of critical load for which the tangent stiffness matrix of FEM model becomes singular. The critical load is obtained by solving homogeneous problem according to "linearized" second-order theory:

$$([K_0] + \lambda[K_G]) = 0 \quad (1)$$

where:

$[K_0]$ – linear stiffness matrix,

$[K_G]$ – geometric stiffness matrix and

λ - factor of critical load.

Linear buckling analysis uses K_0 and K_G based on the undeformed geometry of the structure, which is the main disadvantage of this theory. Because most buckling problems are nonlinear, the buckling analysis should be based on the tangent stiffness and incremental methods.

2.2. Incremental geometric nonlinear analysis

One of the methods for solving nonlinear problems is incremental methods. They use the tangent stiffness, which for single degree of freedom problem is the slope of the load versus displacement, $k_t = dF/du$. Tangent stiffness matrix is obtained as the sum of linear and geometric stiffness matrix of FEM model. Incremental methods are based on the approximation of total load on a range of smaller part – increments. The incremental loads are added successively and in each increment they are linear. The solution of nonlinear problem is obtained as sum of all linear incremental solutions. Better quality of approximations can be achieved using a number of increments, but numerical efficiency can be reduced.

In general case, nonlinear problem can be presented as:

$$[K_t]\{\Delta u\} + \lambda\{F\} = 0 \quad (2)$$

$$\{P\} + \lambda\{F\} = 0 \quad (3)$$

where:

$\{P\}$ – vector of generalized forces of FEM model and

$\{F\}$ – vector of load.

Incremental vector of displacements is obtained:

$$\{\Delta u\}_i = [K_t]^{-1} \Delta \lambda_i \{F\} \quad (4)$$

where:

$$\{\Delta u\}_i = \{u\}_{i+1} - \{u\}_i \quad (5)$$

$$\{\Delta F\}_i = \{F\}_{i+1} - \{F\}_i \quad (6)$$

$$\Delta \lambda_i = \lambda_{i+1} - \lambda_i \quad (7)$$

The tangent matrix is formulated for the beginning of increment, and for the first increment is used linear matrix stiffness.

The incremental solution error is appearing because of linearization in each increment and it can be corrected by applying of some iterative procedures. The main advantages of incremental concept are step-by-step procedure which corresponds to the basic principles of FEM and possibility to verify changes in: loads, mechanical-reological properties of material, geometry of structural system, and modeling effect of those changes on structural behavior.

3. NUMERICAL EXAMPLES

As an illustration of previous consideration several numerical tests will be given. All examples are based on geometric nonlinear theory and "linearized" second-order theory. Figure 3 show FEM model of cantilever with rotation of fixed support.

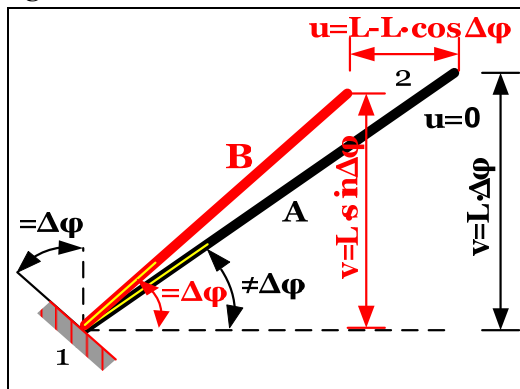


Figure 3. FEM model of cantilever - "linearized" second-order theory (A) and geometric nonlinear theory (B)

For $\Delta\phi = +45^\circ$ node 2 has displacements and according to "linearized" second-order theory it is: " $v=L\Delta\phi$ " and " $u=0$ ". According to incremental solution the high solution accuracy is achieved: " $v=L\sin\Delta\phi$ " and " $u=L-(\cos\Delta\phi-1)$ ".

In the next numerical test (Figure 4) shallow arch is analyzed. For iterative correction of incremental solution three methods were analyzed: Newton-Raphson iteration (NR), modified Newton-Raphson iteration (MNR) and method of initial stiffness (MIS). The results are shown in Table 1.

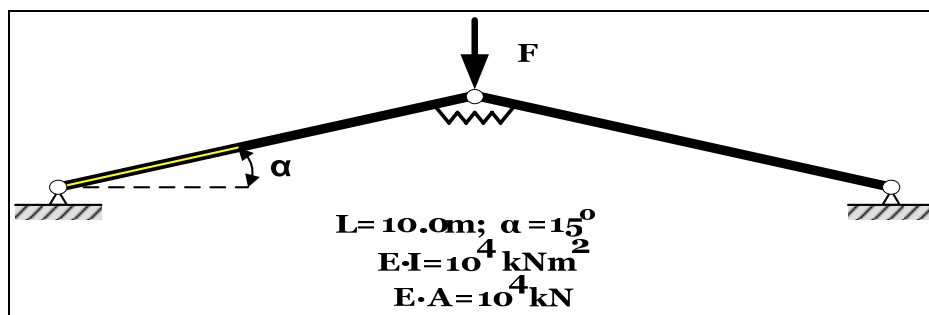


Figure 4. Geometric nonlinear behaviour of shallow arch

Table 1. Load F for different methods of analysis

Load F (kN)	20		60		Fcr (kN)	
Fixed support ratio (%)	100	0	100	0	100	0
Linear theory	10.53	14.93	31.59	44.78	/	/
"Linearized" second-order theory	10.88	15.78	34.96	53.41	587.2	346.8
MIS	10.98	16.33	36.45	67.61	149.3	69.12
MNR	10.98	16.33	36.44	67.61	149.2	69.10
NR	10.98	16.33	36.44	67.65	149.2	69.10
Exact solution	10.99	16.35	36.55	68.60	149.1	69.09

The differences in solution (up to 25%) occur because of changes of tangent stiffness matrix due to correction of geometry system. Incremental-iterative solution with 20 increments provides greater accuracy than "linearized" second-order theory. Advantages of incremental solution occur when the ratio of critical load and applied load is high. Critical load is 69.09kN for fixed support ratio of 0% and 149.1kN for ratio of 100%. According to "linearized" second-order theory $F_{cr}=346.75\text{kN}$ for 0% and $F_{cr}=587.2\text{kN}$ for 100% ratio, which is too high error.

Third numerical test illustrate disadvantage of "linearized" second-order theory. Figure 5 show FEM model of frame with rigid and hinge interface condition between beam and column. The beam has 2I240 and column has I240 cross section. The material is assumed to remain linear elastic at all times, with $E=210\text{GPa}$. It will be analyzed critical load of a FEM model for "linearized" second-order theory (*) and for geometric nonlinear theory (**).

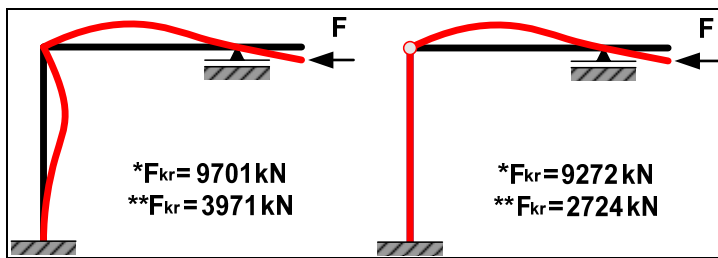


Figure 5. Numerical test for critical load of FEM model

The results of stability analysis of FEM models shows a difference in the buckling forms, as well as the value of critical force ($\Delta=244\%$ for FEM model with rigid interface conditions and $\Delta^{**}=340\%$ for FEM model with hinge interface condition).

Next numerical test, Figure 6, show FEM model of frame structure loaded by two vertical forces. On response diagram "load-displacement", Figure 7, load parameter $L_{dp}=1$ is the value of critical load when the structure, after hardening, loses stability. Response diagram illustrate linear relation between load and displacement up to $\sim P_{cr}/2$, which indicates an error if linear model is applied.

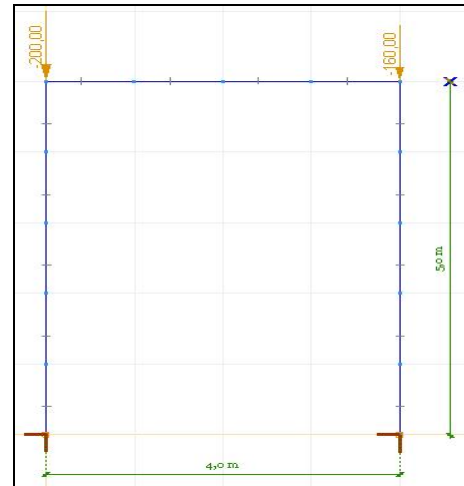


Figure 6. FEM model of frame structure

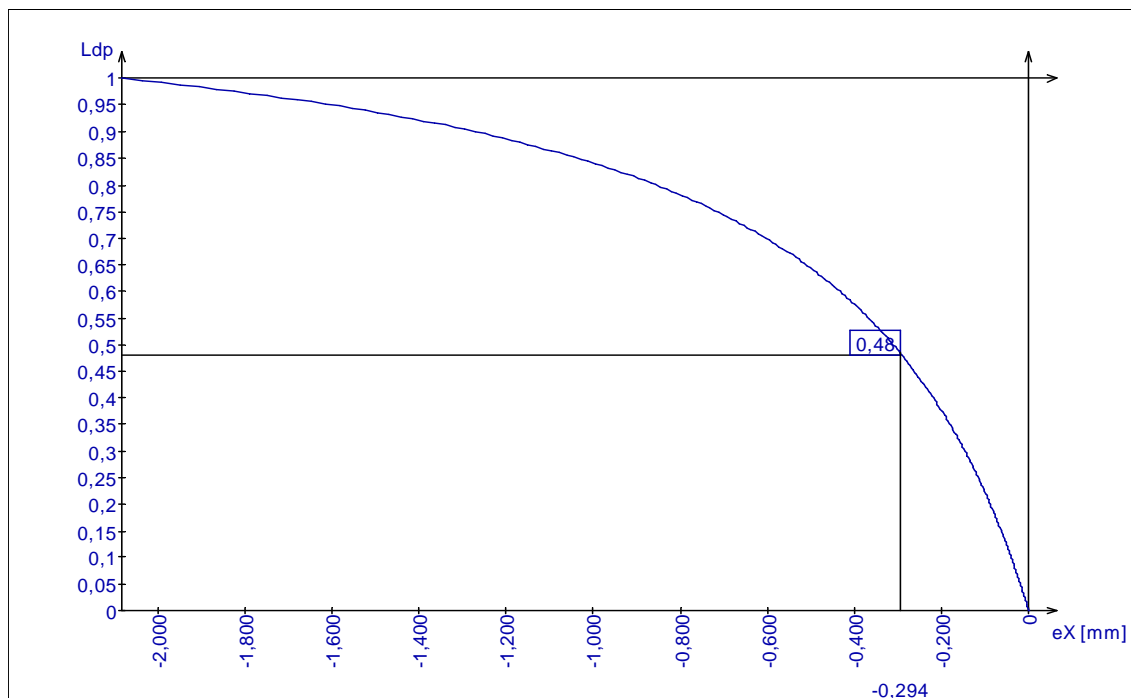


Figure 7. FEM model and response diagram of frame structure

4. CONCLUSIONS

In this paper geometric nonlinearity problems were analyzed. Determining of critical load and stability verification of the structure through the different concepts were presented. For adequate FEM numerical analysis of structural system advantages and disadvantages of implemented mathematical models must be emphasized, because the results can be different.

This paper emphasized advantages of incremental-iterative concept comparing to standard buckling analysis. The main disadvantage of incremental concept for adequate approximation is determining the size and number of increments. Difficulties to determine the solution exactly without analytical or experimental solutions is also disadvantage of incremental concept.

REFERENCES

- [1] K.J. Bathe: *Finite Element Procedures in Engineering Analysis*, Prentice-Hall Inc., New Jersey, 1982.
- [2] R.D. Cook: *Finite Element Modeling for Stress Analysis*, John Wiley & Sons, Inc., 1995.
- [3] D. Kovačević: *FEM Modeling in Structural Analysis* (in Serbian), Građevinska knjiga, Belgrade, 2006.
- [4] J.S. Przemieniecki: *Theory of Matrix Structural Analysis*, McGraw-Hill, New York, 1968.
- [5] *AxisVM® 9 Structural Analysis Software - User Manual*, InterCAD, Budapest, 2008.



SOME GENERALISATION OF THE BARTLE, DUNFORD AND SCHWARTZ INTEGRABILITY MODEL

Octavian LIPOVAN

“Politehnica” University of Timisoara,
Department of Mathematics, ROMANIA

ABSTRACT

In [4] the author introduces the notion of pseudosubmeasure as generalization of the submeasure concept [2], and studies some proprieties of the pseudosubmeasure functions with values in a pseudometric space.

The purpose of this paper is to develop an integration theory for these functions, with respect to a semigroup valued measure, using families of pseudosubmeasure and the associated topological rings.

AMS Subject Classification Code (2000):28A20, 28B15

1. PRELIMINARIES

The notions and the notations used here follow the paper [4].

Let D be an ordered set with the smallest element d_0 . On this set we define a mapping:

$(d_1, d_2) \rightarrow d_1 + d_2$ with the following properties:

$$(P1) \quad d_0 + d = d + d_0; \forall d \in D$$

$$(P2) \quad d_1 + d_2 = d_2 + d_1; \forall d_1, d_2 \in D$$

$$(P3) \quad d_1 \leq d_2 \Rightarrow d + d_1 \leq d + d_2; \forall d \in D$$

There exists a subset $D_1 \subseteq D$ left directed such that

$$(P4) \quad \forall d \in D_1, \exists d_1 \in D \text{ so that } d_1 + d_1 \leq d.$$

Definition 1.1. A pseudometric on a set X is a D -valued function $p : X \times X \rightarrow D$ so that:

$$(i) \quad p(x, y) = d_0 \Leftrightarrow x = y$$

$$(ii) \quad p(x, y) = p(y, x), x, y, z \in X$$

$$(iii) \quad p(x, y) \leq p(x, z) + p(z, y); x, y, z \in X.$$

A set X together with a pseudometric ρ is called a pseudometric space and is denoted by (X, ρ, D) .

Remark 1.2. Every uniform space (X, \mathcal{U}) is pseudosemimetrizable, [4].

Let S be a ring (or algebra) of subsets of fixed set S .

Definition 1.3. A pseudosubmeasure on a ring $S \subset \mathcal{P}(S)$ is a mapping $\gamma : S \rightarrow D$ such that:

- (S₁) $\gamma(\emptyset) = d_0$
- (S₂) $E \subseteq F \Rightarrow \gamma(E) \leq \gamma(F), E, F \in S$
- (S₃) $\gamma(E \cup F) \leq \gamma(E) + \gamma(F), E, F \in S$

If γ has the property that $\gamma(A) = d_0 \Rightarrow A = \emptyset$, then mapping $p : S \times S \rightarrow D$; $\rho(A, B) = \rho(A \Delta B)$ is a pseudometric on S invariant to translation Δ (symmetric difference).

Let $\Gamma = \{\gamma_i : S \rightarrow D\}_{i \in I}$ be a family of pseudosubmeasure on $S \subset P(S)$ and consider the family $\Omega_\Gamma = \{v_{K,d} : K = \text{finite} \subseteq I, d \in D_1\}$, where $v_{K,d} = (A \in S : \gamma_i(A) \leq d, i \in K)$.

Then there exist a FN-topology $\tau(\Gamma)$ on S so that $\mathcal{S}(\Gamma) = (S, \Delta, \cap, \tau(\Gamma))$ is a topological ring. Let (X, ρ, D) be a pseudometric space.

By generalizing the model established in [3], we introduce an uniform structure on X^S in the following way: To every $K = \text{finite} \subseteq I, d \in D$, we associate the set:

$$\mathcal{W}_k(D) = \{(f, g) \in X^S \times X^S ; \gamma_i\{s \in S ; \rho(f(s), g(s)) \geq d\} < d, i \in K\}$$

Then, the family $\{W_k(d); d \in D_1, K = \text{finite} \subseteq I\}$ forms a base for an uniform structure \mathcal{U}_Γ on X^S . We denote $X^S(\Gamma) = (X^S, \mathcal{U}_\Gamma)$. The map $f \in X^S$ is a S -step function if there exists $x_i \in X, E_i \in S, i = 1, 2, \dots, n, x_i \neq x_j, E_i \cap E_j = \emptyset, i \neq j, S = \bigcup_{i=1}^n E_i$ so that $\forall s \in E_i$ imply $f(s) = x_i, i = 1, 2, \dots, n$.

The space of S -step functions will be denoted by $\mathcal{E}(S, X)$.

Definition 1.4. The function $f \in X^S$ is Γ -pseudosubmeasurable if f belongs to the closure of $\mathcal{E}(S, X)$ in $X^S(\Gamma)$.

We denote by $\mathcal{M}[S, \Gamma, X]$ the set of these functions.

Definition 1.5. Let $\{f_a\}$ be a generalized sequence in $\mathcal{M}[S, \Gamma, X]$ and $f \in \mathcal{M}[S, \Gamma, X]$. If $f_a \rightarrow f$ in $X^S(\Gamma)$, then $\{f_a\}$ converges to f in Γ -pseudomeasures and we denote $f_a \xrightarrow{r} f$.

2. BASIC ASSUMPTIONS

Let S be a nonempty set, $\mathcal{S} \subset P(S)$ be an algebra of subsets of S and consider a family of pseudosubmeasures $\Gamma = \{\gamma_i : S \rightarrow D\}_{i \in I}$.

Let $(X_i, \rho_i, D^i), i = 1, 2, 3$ be three pseudometric abelian semigroups for which the addition is uniformly continuous with respect to the pseudometric ρ_i .

In the sequel we consider an additive set function $\mu : S \rightarrow X_2, \mu(\emptyset) = 0$, and we will choose a family of pseudosubmeasures as it will be specified.

The maps which are to be integrated with respect to μ will belong to X_1^S and the integral will take values in X_3 or its completion \hat{X}_3 .

Suppose that a separate continuous bilinear map exists $X_1 \times X_2 \rightarrow X_3; (x, y) \mapsto x \cdot y$ so that:

- i) $x \cdot 0 = 0 \cdot y = 0, (x \in X_1, y \in X_2)$
- ii) $(x_1 + x_2) \cdot (y_1 + y_2) = x_1 \cdot y_1 + x_1 \cdot y_2 + x_2 \cdot y_1 + x_2 \cdot y_2, (x_1, y_1 \in X_1, x_2, y_2 \in X_2).$

Finally we suppose that Γ_μ, μ and the above bilinear map are chosen so that the following continuity axioms are satisfied:

C1) For every $F \in \mathcal{S}$ and every $d' \in D_1^3$ there exists $d \in D_1^1$ with the following property: for any $n \in \mathbb{N}$, if $\rho_1(x_i, y_i) < d', i = 1, 2, \dots, n$ and $\{E_i\}$ is sequence of pairwise disjoint set from \mathcal{S}

then:
$$\rho_3\left(\sum_{i=1}^n x_i \mu(E_i \cap F), \sum_{i=1}^n y_i \mu(E_i \cap F)\right) < d.$$

C2) For any $x \in X_1, \lim_{\substack{E \rightarrow \emptyset \\ E \in \mathcal{S}}} x \mu(E) = 0.$

3. INTEGRABLE FUNCTIONS

Let $f \in \mathcal{E}(\mathcal{S}, X)$ be a \mathcal{S} -step function.

Definition 3.1. For $E \in \mathcal{S}$, the integral of f on E is by definition
$$\int_E f d\mu = \sum_{i=1}^n x_i \mu(E_i \cap E).$$

We denote by $\mathcal{E}(\mathcal{S}, \Gamma_\mu, X_1, X_3)$ the set of Γ_μ -integrable step functions.

Theorem 3.2. (i) Relatively to the operation $(f + g)(s) = f(s) + g(s)$, the space $\mathcal{E}(\mathcal{S}, \Gamma_\mu, X_1, X_3)$ is a subsemigroup of X_1^3 .

(ii) For $E \in \mathcal{S}$, the map $f \rightarrow \int_E f d\mu$ from $\mathcal{E}(\mathcal{S}, \Gamma_\mu, X_1, X_3)$ to X_3 is additive.

(iii) For $f \in \mathcal{E}(\mathcal{S}, \Gamma_\mu, X_1, X_3)$ the map $E \rightarrow v(E), v(E) = \int_E f d\mu, E \in \mathcal{S}$ is an additive function.

(iv) For $f \in \mathcal{E}(\mathcal{S}, \Gamma_\mu, X_1, X_3); \lim_{E \xrightarrow{\Gamma_\mu} 0} v(E) = \lim_{E \xrightarrow{\Gamma_\mu} 0} \int_E f d\mu = 0$

The proof follows from definition 3.1 and axioms C₁ and C₂. The extension of the integral from step functions to the arbitrary functions in X_1^S is based on the following result:

Lemma 3.3. Let $\{f_\alpha\}$ be a generalized sequence from $f \in \mathcal{E}(\mathcal{S}, \Gamma_\mu, X_1, X_3)$, which is

Cauchy in $X_1^S(\Gamma_\mu)$. For $\left\{ \int_E f_\alpha d\mu \right\}$ to be a Cauchy sequence in X_3 uniform with respect to E

$\in \mathcal{S}$ it is necessary and sufficient that:

a) For any neighbourhood V of 0 in X_3 there exists an index $\alpha_0, K = \text{finite} \subset I$ and $d \in D$,

so that: $\alpha \geq \alpha_0$ and $\gamma_i(E) < d, i \in K$ imply $\int_E f_\alpha d\mu \in V$

b) For any neighbourhood V of 0 in X_3 there exists an index α_0 and $F \in \mathcal{S}$ so that $\int_E f_\alpha d\mu \in V$ if $\alpha \geq \alpha_0$ and $E \in \mathcal{S}, E \subset S - F$.

Proof. Necessity. For any neighbourhood V of 0 in X_3 there exists a symmetric entourage W of the uniform structure from X_3 so that $W^2(0) \subseteq V$.

Let α_0 be so that $\left(\int_E f_\alpha d\mu, \int_E f_{\alpha_0} d\mu \right) \in W$ for any $E \in \mathcal{S}$ if $\alpha \geq \alpha_0$.

From Theorem 3.2., IV, it results that there exists $d \in D_1, K = \text{finite} \subset I$ so that we have: $\int_E f_{\alpha_0} d\mu \in W(0)$ if $\gamma_i(E) < d, i \in K$.

Therefore $\int_E f_\alpha d\mu \in V$ if $\alpha \geq \alpha_0$ and $\gamma_i(E) < d, i \in K$, that is the condition a).

The condition b) is obtained by taking $E = \{s \in S : f_{\alpha_0}(s) \neq 0\}$. We have $F \in \mathcal{S}$, and $\int_E f_{\alpha_0} d\mu = 0$ for all $E \in \mathcal{S}$ with $E \subset S - F$.

Sufficiency. Let W be a symmetric entourage for X_3 and let $\alpha_0, K = \text{finite} \subset I, d \in D_1$ and F be chosen depending on the neighbourhood $W(0)$ according to the conditions a) and b) simultaneously. For F and W , let entourage U from X_1 be chosen according to axiom C_1 .

We write: $F_{\alpha\alpha'} = \{s \in S : (f_\alpha(s), f_{\alpha'}(s)) \notin U\}, F_{\alpha\alpha'} \in \mathcal{S}$.

Since $\{f_\alpha$ is Cauchy in $X_1^S(\Gamma_\mu)$ there exists $\alpha_1 \geq \alpha_0$ so that $\gamma_i(F_{\alpha\alpha'}) < d, i \in K$ for $\alpha, \alpha' \geq \alpha_1$. For $E \in \mathcal{S}$ in the semigroup $X_3 \times X_3$, we can write:

$$\left(\int_E f_\alpha d\mu, \int_E f_{\alpha'} d\mu \right) = \left(\int_{E \cap F_{\alpha\alpha'}} f_\alpha d\mu, \int_{E \cap F_{\alpha\alpha'}} f_{\alpha'} d\mu \right) + \left(\int_{E \setminus (F_{\alpha\alpha'} \cup F)} f_\alpha d\mu, \int_{E \setminus (F_{\alpha\alpha'} \cup F)} f_{\alpha'} d\mu \right) +$$

$$\left(\int_{E \setminus (F_{\alpha\alpha'} \cap F)} f_\alpha d\mu, \int_{E \setminus (F_{\alpha\alpha'} \cap F)} f_{\alpha'} d\mu \right) \in W(0) \times W(0) + W(o) \times W(0) + W \subseteq W^2 + W^2 + W^2, \alpha, \alpha' \geq \alpha_1$$

Corollary 3.4. Let $\{f_\alpha\}$ and $\{g_\beta\}$ be two generalized sequences from $\mathcal{E}(S, \Gamma_\mu, X_1, X_3)$, convergent in $X_1^S(\Gamma_\mu)$ to the same function.

If $\left\{ \int_E f_\alpha d\mu \right\}$ and $\left\{ \int_E g_\beta d\mu \right\}$ are generalized Cauchy sequences in X_3 uniformly in $E \in \mathcal{S}$, then for any entourage W from X_3 there exists α_0 and β_0 so that if $\alpha \geq \alpha_0, \beta \geq \beta_0$ it results that $\left(\int_E f_\alpha d\mu, \int_E g_\beta d\mu \right) \in W$, uniformly in $E \in \mathcal{S}$.

Proof. Given a symmetric entourage W_1 from X_3 so that $W_1^2 + W_1^2 + W_1^2 \subseteq W$ we choose an entourage U from X_1 corresponding to W_1 according to axiom C_1 .

We write $F_{\alpha\beta} = \{S \in \mathcal{S}; (f_\alpha(s), g_\beta(s)) \notin U\}$. From the previous Lemma it results that there exists $\alpha_0, \beta_0, d \in D, K = \text{finite} \subset I$ so that if $F \in \mathcal{S}$ and $\alpha > \alpha_0, \beta > \beta_0, \gamma_i(E) < d, i \in K, E \subset S - F, E \in \mathcal{S}$ we have $\int_E f_\alpha d\mu \in W_1(0)$ and $\int_E f_\beta d\mu \in W_1(0)$

By hypothesis there exist if $\alpha_1 \geq \alpha_0$ and $\beta_1 \geq \beta_0$ so that for $\alpha > \alpha_1, \beta > \beta_1$, we have $\gamma_i(F_{\alpha\beta}) < d, i \in K$. Expressing the pair $\left(\int_E f_\alpha d\mu, \int_E g_\beta d\mu \right)$ in the same way as in the proof of the sufficiency from Lemma 3.3., the result is obtained.

Definition 3.5. The function $f \in X_1^S$ is called Γ_μ -integrable if there exists a generalized sequence $\{f_\alpha$ from $\mathcal{E}(\mathcal{S}, \Gamma_\mu, X_1, X_3)\}$ so that $f_\alpha \xrightarrow{\Gamma_\mu} f$ and $\left\{ \int_E f_\alpha d\mu, \right\}$ is a generalized Cauchy sequence in X_3 , uniformly in $E \in \mathcal{S}$. Then the Γ_μ -integral is the element from \hat{X}_3 the completion of X_3 , defined by: $\int_E f d\mu = \lim_{\alpha} \int_E f_\alpha d\mu$.

From the Corollary 3.4 it results that above Γ_μ -integral is properly defined. We denote by $\mathcal{L}(\mathcal{S}, \Gamma_\mu, X_1, X_3)$ the set of Γ_μ -integrable functions from $\mathcal{M}[\mathcal{S}, \Gamma_\mu, X_1]$.

It is obvious that $\mathcal{E}(\mathcal{S}, \Gamma_\mu, X_1, X_3) \subset \mathcal{L}(\mathcal{S}, \Gamma_\mu, X_1, X_3)$ and the Γ_μ -integral restricted to $\mathcal{E}(\mathcal{S}, \Gamma_\mu, X_1, X_3)$ coincides with the Γ_μ -integral from Definition 3.1.

Theorem 3.6. Relatively to the operation of addition the set $\mathcal{L}(\mathcal{S}, \Gamma_\mu, X_1, X_3)$ is a subsemigroup of X_1^S

(i) For $E \in \mathcal{S}$, the mapping $f \rightarrow \int_E f d\mu$ of $\mathcal{L}(\mathcal{S}, \Gamma_\mu, X_1, X_3)$ in \hat{X}_3 is additive:

$$\int_E (f + g) d\mu = \int_E f d\mu + \int_E g d\mu, f, g \in \mathcal{L}(\mathcal{S}, \Gamma_\mu, X_1, X_3)$$

(ii) For $f \in \mathcal{L}(\mathcal{S}, \Gamma_\mu, X_1, X_3)$ the mapping $E \rightarrow v(E) = \int_E f d\mu, E \in \mathcal{S}$ is additive:

$$v\left(\bigcup_{i=1}^n E_i\right) = \sum_{i=1}^n v(E_i), E_i \cap E_j = \emptyset, i \neq j, v(\emptyset) = 0$$

(iii) For $f \in \mathcal{L}(\mathcal{S}, \Gamma_\mu, X_1, X_3)$ we have: $\lim_{\Gamma_\mu} v(E) = 0$
 $E \xrightarrow{E \in \mathcal{S}}$

The proof follows from Corollary 3.4. and the definition 3.5.

REFERENCES

- [1] N. BOURBAKI: *Éléments de Mathématique, Livre III, Topologie générale*, Chapitre 9, Hermann Paris, 1958.
- [2] L. DREWNOWSKY: *Topological Rings of Sets, Continuous set functions, Integration I, II*, Bull.Acad.Polon.Sci.Math.Astr.Phys 20,4(1972), 269-276, 277-286.

- [3] N.DUNFORD, J. SCHWARTZ: *Linear operators*, Part I, Interscience, New York, 1958.
- [4] O. LIPOVAN: *Some generalization of measurable functions*, Univ. Beograd. Publ. Elektrotehn. Fak. Ser.Math. 7(1996) 25-30.
- [5] O. LIPOVAN: *Elements of Submeasure Theory with Applications*, Monografii Matematice, Nr.46, 1992 Universitatea de Vest Timisoara.
- [6] O. LIPOVAN: Exhausting and order continuous pseudosubmeasures, BUL. St., Univ “Politehnica”, Timisoara, Tom 42 (56),2, Matematica –Fizica 44-49.
- [7] J.C. MASSE: *Integration dans les semigroupes*, Collect. Math 23, Département. De Math. Université Loyal Quebec, 1974.
- [8] E. POPA : *O caracterizare a spatiilor uniforme*. Studii si Cercetari Matematice, 19, 9(1967)1299-1301, Ed. Acad. RSR, Bucuresti.



THE BENDING OF THE FINITE ELASTIC ROD ON ELASTIC FOUNDATION UNDER THE ACTION OF CONCENTRATED LOADS

Wilhelm W. KECS

Department of Mathematics-Informatics, University of Petrosani, ROMANIA

Abstract

The paper gives solution in the distributions space D'_+ for the boundary-value problems regarding the bending of the elastic rods on elastic foundation. The expression of the rod deflection is given with the help of the fundamental solution in D'_+ of the operator which describes the rod bending. We admit that on the rod act uniformly distributed loads of intensity q , as well as a concentrated load of value P . We have considered a straight homogeneous elastic rod of finite length ℓ , and with constant cross-section, supported in point O and with elastic fixing in point A . The rod lies on an elastic foundation of Winkler type. The deflection of the rod as well as the reactions in the rod ends is given.

1. INTRODUCTION

In solving the problem of the bending of the finite elastic rod on elastic foundation under the action of concentrated loads we come across difficulties owing to these concentrated loads and moments.

The general and unitary method to deal with the problems concerning discontinuous loading is the distribution theory. In the framework of this theory a single equation which contains the boundary and jump conditions is obtained.

The distribution theory was used in [2], [6], [7], [8] and [9] for analyzing beams with discontinuities. A bending problem with discontinuities in which the distribution theory isn't systematically applied, being a combination between classical mathematical analysis and the distribution theory, is studied in [10]. In [2] and [6] using the distribution theory in a systematic manner we study the bending problem with discontinuities of a finite elastic rod on elastic foundation under the action of concentrated loads.

In this paper we study the bending of a straight homogeneous elastic rod of finite length, with constant cross-section, supported in the left end and with elastic fixing in the right end, which lies on an elastic foundation of Winkler type.

We determine the deflection of the rod as well as the reactions of the rod ends. The obtained result allows a global analysis of the influence of the each term: support, elastic fixing and the concentrated load.

2. THE STUDY OF THE BENDING OF THE FINITE ELASTIC ROD

Let be OA a straight homogeneous elastic rod of finite length ℓ , and with constant cross-section, supported in point O and with elastic fixing in point A , which lies on an elastic foundation of Winkler type [1]. We admit that on the rod act uniformly distributed loads of intensity q , as well as a concentrated load of value P applied in point $c \in (0, \ell)$.

We shall denote by $v(x), x \in [0, \ell]$ the deflection of the rod. We denote by $\tilde{\partial}_x = \frac{\tilde{d}}{dx}, \partial_x = \frac{d}{dx}$ the derivative in classic sense and the derivative in distribution sense, respectively.

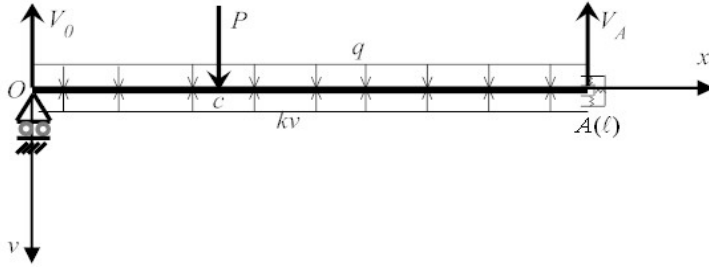


Fig. 2.1. Elastic rod supported on an elastic foundation

$$q_e(x) = -kv(x), \quad x \in [0, \ell], \quad (2.1)$$

where k is called the rigidity coefficient of the elastic foundation.

We shall denote by $D'(\square)$ the distribution (continuous linear functional) defined on the test functions space $D(\square)$, which are indefinite derivable functions with compact support.

We denote by $D'_+ \subset D'(\square)$ the distributions from $D'(\square)$ having the supports on $[0, \infty)$. We mention that the distributions from D'_+ represent a convolution algebra without divisors

of zero. We observe that $\tilde{v}(x) = \begin{cases} v(x), & x \in [0, \ell], \\ 0, & x \notin [0, \ell], \end{cases}$ represents a function type distribution from

D'_+ , because its support is in $[0, \ell] \subset [0, \infty)$.

We denote by the symbol $[\]_a$ the jump of a certain value at point $x = a$.

Due to the way in which the rod is fixed the boundary conditions are

$$\begin{aligned} \tilde{v}(0+0) = 0, \tilde{v}(0-0) = 0, \tilde{v}(\ell+0) = 0, \tilde{v}(\ell-0) = 0, \\ \tilde{\partial}_x^2 \tilde{v}(0+0) = 0, \tilde{\partial}_x^2 \tilde{v}(0-0) = 0, \tilde{\partial}_x^2 \tilde{v}(\ell+0) = 0, EI \tilde{\partial}_x^2 \tilde{v}(\ell-0) = k_1 \tilde{\partial}_x \tilde{v}(\ell-0). \end{aligned} \quad (2.2)$$

From the boundary conditions (2.2) we have

$$\begin{aligned} [\tilde{v}]_0 = \tilde{v}(0+0) - \tilde{v}(0-0) = 0, [\tilde{v}]_\ell = \tilde{v}(\ell+0) - \tilde{v}(\ell-0) = 0, \\ [\tilde{\partial}_x \tilde{v}]_0 = \tilde{v}'(0+0) - \tilde{v}'(0-0) = \tilde{v}'(0+0), [\tilde{\partial}_x \tilde{v}]_\ell = \tilde{v}'(\ell+0) - \tilde{v}'(\ell-0) = -\tilde{v}'(\ell-0). \end{aligned} \quad (2.3)$$

According to [2] for the deflection \tilde{v} we have the expression

$$\tilde{v}(x) = \begin{cases} 0, & x \notin [0, \ell] \\ \frac{q}{4EI\omega^3} \int_0^x u(x-t)dt - \frac{V_0}{4EI\omega^3} H(x)u(x) + \frac{P}{4EI\omega^3} H(x-c)u(x-c) \\ + \frac{1}{4\omega^3} \tilde{v}'(0+0)H(x)u_2(x), & x \in [0, \ell] \end{cases} \quad (2.4)$$

where $\omega = \sqrt[4]{\frac{k}{4EI}}$. We mention that we introduce the real-valued functions $u, u_1, u_2, u_3 \in C^\infty(\square)$

having the expression:

$$\begin{aligned} u(x) &= \cosh \omega x \sin \omega x - \sinh \omega x \cos \omega x, \\ u_1(x) &= u'(x) = 2\omega \sinh \omega x \sin \omega x, \\ u_2(x) &= u''(x) = 2\omega^2 (\cosh \omega x \sin \omega x + \sinh \omega x \cos \omega x), \\ u_3(x) &= u'''(x) = 4\omega^3 (\cosh \omega x \cos \omega x). \end{aligned} \quad (2.5)$$

We have

$$u^4(x) = u_3'(x) = -4\omega^4 u(x).$$

From here results

$$u^{(4k)}(x) = (-4\omega^4)^k u(x), \quad u^{(4k+1)}(x) = (-4\omega^4)^k u_1(x),$$

$$u^{(4k+2)}(x) = (-4\omega^4)^k u_2(x), \quad u^{(4k+3)}(x) = (-4\omega^4)^k u_3(x).$$

Because any natural number $n \geq 4$ can be written under the form $n = 4k + p$, $p = 0, 1, 2, 3$; $k \in \mathbb{N}$, we have:

Any $n \geq 4$ order derivative of the function $u \in C^\infty(\mathbb{R})$ represents a multiple of one of the functions u , $u_1 = u'$, $u_2 = u''$, $u_3 = u'''$ namely

$$u^{(n)}(x) = \begin{cases} (-4\omega^4)^k u(x), & n = 4k \\ (-4\omega^4)^k u_1(x) & n = 4k + 1 \\ (-4\omega^4)^k u_2(x) & n = 4k + 2 \\ (-4\omega^4)^k u_3(x) & n = 4k + 3 \end{cases} \quad k = 1, 2, 3, \dots$$

Using the formula $\int_0^x f(x-t)dt = \int_0^x f(t)dt$ the deflection \tilde{v} can be written under the form

$$\tilde{v}(x) = \begin{cases} 0, & x \notin [0, \ell) \\ \frac{q}{4EI\omega^3} \int_0^x u(t)dt - \frac{V_0 u(x)}{4EI\omega^3} + \frac{\tilde{v}'(0+0)u_2(x)}{4\omega^3}, & x \in [0, c) \\ \frac{q}{4EI\omega^3} \int_0^x u(t)dt - \frac{V_0 u(x)}{4EI\omega^3} + \frac{\tilde{v}'(0+0)u_2(x)}{4\omega^3} + \frac{Pu(x-c)}{4EI\omega^3}, & x \in [c, \ell] \end{cases} \quad (2.6)$$

We observe that in this relation of the deflection \tilde{v} appear only two unknowns, namely: the reaction V_0 in O and the rotation of rod to the right in point O , $\tilde{v}'(0+0)$. These unknowns as well as the unknowns $V_A, m_A, \tilde{v}'(\ell-0)$ representing the reaction and moment in the A as well as the rotation of rod to the left in point A , respectively, will be determined from the following conditions:

$$q \int_0^\ell u(t)dt - V_0 u(\ell) + Pu(\ell-c) + EI\tilde{v}'(0+0)u_2(\ell) = 0, \quad (2.7)$$

$$q \int_0^\ell u_1(t)dt - V_0 u_1(\ell) + Pu_1(\ell-c) + EI[\tilde{v}'(0+0)u_2(\ell) - 4\omega^3 \tilde{v}'(\ell-0)] = 0, \quad (2.8)$$

$$q \int_0^\ell u_2(t)dt - V_0 u_2(\ell) + Pu_2(\ell-c) + 4\omega^3 m_A - 4\omega^4 EI\tilde{v}'(0+0)u(\ell) = 0, \quad (2.9)$$

$$q \int_0^\ell u_3(t)dt - V_0 u_3(\ell) + Pu_3(\ell-c) - 4\omega^3 V_A - 4\omega^4 EI\tilde{v}'(0+0)u_1(\ell) = 0, \quad (2.10)$$

$$m_A = k_1 \tilde{v}'(\ell-0), \quad (2.11)$$

where k_1 represents a proportionality factor.

The relations (2.7)-(2.10) was obtained from the condition that the support of the deflection should be $[0, \ell]$, namely $\text{supp } \tilde{v} = [0, \ell]$.

From the above system of equations we shall obtain the unknowns $V_0, V_A, m_A, \tilde{v}'(\ell-0)$ and $\tilde{v}'(0+0)$.

We have the expression

$$V_0 = \frac{k_1 (b_1 u_2(\ell) - b_0 u_3(\ell)) + EI (b_2 u_2(\ell) + 4\omega^4 u(\ell) b_0)}{EI (u_2^2(\ell) + 4\omega^4 u^2(\ell)) - k_1 (u_3(\ell) u(\ell) - u_2(\ell) u_1(\ell))}, \quad (2.12)$$

$$\tilde{v}'(0+0) = \frac{1}{EI} \frac{EI(b_2u(\ell) - b_0u_2(\ell)) + k_1(b_1u(\ell) - b_0u_1(\ell))}{EI(u_2^2(\ell) + 4\omega^4u^2(\ell)) - k_1(u_3(\ell)u(\ell) - u_2(\ell)u_1(\ell))}, \quad (2.13)$$

$$\tilde{v}'(\ell-0) = \frac{u_2(\ell)(b_1u_2(\ell) - b_2u_1(\ell)) + 4\omega^4u(\ell)(b_1u(\ell) - b_0u_1(\ell)) + u_3(\ell)(b_2u(\ell) - b_0u_2(\ell))}{4\omega^3 [EI(u_2^2(\ell) + 4\omega^4u^2(\ell)) - k_1(u_3(\ell)u(\ell) - u_2(\ell)u_1(\ell))]}, \quad (2.14)$$

$$m_A = k_1 \frac{u_2(\ell)(b_1u_2(\ell) - b_2u_1(\ell)) + 4\omega^4u(\ell)(b_1u(\ell) - b_0u_1(\ell)) + u_3(\ell)(b_2u(\ell) - b_0u_2(\ell))}{4\omega^3 [EI(u_2^2(\ell) + 4\omega^4u^2(\ell)) - k_1(u_3(\ell)u(\ell) - u_2(\ell)u_1(\ell))]}, \quad (2.15)$$

where

$$\begin{aligned} b_0 &= \frac{q}{\omega} - \frac{q}{\omega} \frac{u_3(\ell)}{4\omega^3} + Pu(\ell - c), \\ b_1 &= qu(\ell) + Pu_1(\ell - c), \\ b_2 &= q\omega^2u_1(\ell) + Pu_2(\ell - c), \\ b_3 &= qu_2(\ell) + Pu_3(\ell - c). \end{aligned} \quad (2.16)$$

3. CONCLUSIONS

As it was pointed out in [2] the distribution theory represents the adequate framework to solve the boundary-value problems regarding the bending of the elastic rods on elastic foundation when we have external discontinuities (e.g. discontinuous loading) and internal discontinuities (e.g. owing to the mechanical properties).

In this way the difference between continuous loads and discontinuous loads is vanish.

The classical method of solving the problems in which appear discontinuities is the partition of the rod into segments (which have distinct mechanical and geometrical properties). We obtain a system of boundary (the ends of the segments rod) value problems so that the solution of the problem on each rod segment is continuous. To solve the problem with discontinuities we must take into account the continuity conditions at the interface of the rod segments.

The obtained result allows a global analysis of the influence of the each term: support, elastic fixing and the concentrated load.

REFERENCES

- [1] HETÉNYI, M., *Beams on elastic foundation*, Ann.Arbor: The University of Michigan Press 1946.
- [2] KECS, W. W., *The generalized solution of the boundary-value problems regarding the bending of elastic rods on elastic foundation. II. The generalized solution*, Proceedings of the Romanian Academy – series A: Mathematics, Physics, Technical Sciences, Information Science, (will appeared) 2009.
- [3] KECS, W. W., *Theory of distributions with applications*, The Publishing House of the Romanian Academy, Bucharest, 2003.
- [4] NOWACKI, W., *Dynamics of elastic system*, Chapman Hall L.T.D., London, 1963.
- [5] TOMA, A., *Mathematical methods in elasticity and viscoelasticity* (in Romanian), Editura Tehnica, Bucharest, 2004.
- [6] TOMA, A., *The generalized solution of the boundary-value problems regarding the bending of the elastic rods on elastic foundation. I. The system of generalized equations*, Proceedings of the Romanian Academy – series A: Mathematics, Physics, Technical Sciences, Information Science, nr.2/2008, p.123-128.
- [7] TOMA, A.; KECS, W. W., *A unitary, general method of studying and solving the boundary value problem for the bending elastic rods*, Rev.Roum.Sci.Tech.-Mec. Appl. 44 No.6, 647-661, (1999).
- [8] YAVARI, A.; SARKANI, S.; MOYER, E. T., *On applications of generalized functions to beam bending problems*, Int J Solids Struct 37, 5675-5705, (2000).
- [9] YAVARI, A.; SARKANI, S., *On applications of generalized functions to the analysis of Euler-Bernoulli beam-columns with jump discontinuities*, Int J Mech Sci 43, 1543-1562, (2001).
- [10] YAVARI, A.; SARKANI, S.; REDDY, J. N., *Generalized solutions of beams with jump discontinuities on elastic foundations*, Archive of Applied Mechanics 71, 625-639, (2001).



**ISIRB
2009**
ROMANIA - HUNGARY - SERBIA



Further Considerations on the Formal Verification of Number Theoretical Algorithms *

Laura Kovács¹ and Adalbert Kovács²

¹ EPFL, Switzerland

² University "Politehnica" Timișoara, Romania

Abstract. We discuss experimental results of an automatic approach for inferring polynomial loop invariants of P-solvable loops implementing interesting number-theoretic algorithms. The method relies on techniques from symbolic summation and polynomial algebra, and is implemented in the software package `Alligator` written in *Mathematica*.

1 Introduction

To verify and/or analyze programs containing loops one needs to discover some properties of loops automatically. Such properties are known as loop invariants. Powerful techniques for finding loop invariants are thus crucial for further progress of software verification and program analysis.

Research into methods for automatically generating loop invariants has a long history, starting with the works of [18, 5]. However, due to the limited arithmetic operations among program variables, the problem of invariant inference has recently become a challenging research topic [12, 16, 4, 14, 15, 9].

In [9, 11] we introduced an automatic approach for polynomial invariant generation, that, contrarily to [12, 16, 4] does not use a priori fixed invariant templates, and it is applicable to the a richer class of loops than the one introduced in [15]. These invariants are of the form $p_1 = 0 \wedge \dots \wedge p_r = 0$, where p_1, \dots, p_r are polynomials over the program variables. In the sequel we will call a *polynomial equality* any equality of the form $p = 0$, where p is a polynomial. Thus an invariant is polynomial if it is a conjunction of polynomial equalities.

The loops for which our method automatically infers polynomial invariants are characterized by the following conditions: (i) they contain only assignments to variables and conditional statements; (ii) tests conditions are omitted; (iii) the variables in assignments range over numeric types, such as integers or rationals; (iv) the variables can be expressed as a polynomial of the initial values of variables (those when the loop is entered), the loop counter, and some new variables, where there are algebraic dependencies among the new variables. We call such loops *P-solvable*. There are many natural examples of P-solvable loops in real-life programs.

Our method for invariant generation first translates conditional statements within the loop into a sequence of loops, called inner loops. Then all loop conditions are ignored,

* Work was partly done while the first author was at RISC-Linz, Austria.

turning the loop into a non-deterministic program. Next symbolic summation methods are applied to the inner loops to determine if the output values of their variables can be expressed using symbolic expressions in their input values and inner loop counters. If yes, a collection of potential polynomial invariants is generated using a Gröbner basis algorithm to eliminate loop counters. The invariant property of these polynomials are then checked using the weakest precondition strategy, and valid polynomial invariants of P-solvable loops are thus derived. Moreover, we proved that under some conditions the method computes *all* polynomial invariants, i.e. it computes a Gröbner basis of the ideal of polynomial invariants. However, we could not find any example of a P-solvable loop for which our approach fails to be complete. We thus conjecture that the imposed completeness conditions cover a large class of imperative programs, and the completeness proof of our approach without the additional assumptions is a challenging task for further research.

Exploiting the symbolic manipulation capabilities of the computer algebra system *Mathematica*, our approach is implemented in a new software package called *Aligator* [9]. Using *Aligator*, a complete set of polynomial invariants is successfully generated for numerous imperative programs working on numbers.

The purpose of this paper is to illustrate our approach on examples implementing interesting algorithms working on numbers. Finding invariants for such loops may be a very hard and creative work since non-trivial mathematical knowledge and intuition may be required. The ultimate goal of this paper is to emphasize the value of applying algebraic techniques for computer aided verification. We hope that the experimental results will provide practical justification for the relevance of our method. For technical details and correctness of the approach we refer to [9, 11].

2 P-solvable Loops and Invariants

In this section we first briefly recall fundamental facts from polynomial algebra and recurrence solving. Then our algorithm for P-solvable loops will be presented.

We assume that \mathbb{K} is a field of characteristic zero (e.g. \mathbb{Q} , \mathbb{R} , etc.), and by $\bar{\mathbb{K}}$ we denote its algebraic closure. Throughout this paper, $X = \{x_1, \dots, x_m\}$ ($m > 1$) denotes the set of loop variables with initial values X_0 , and $\mathbb{K}[X]$ is the ring of polynomials in the variables X with coefficients from \mathbb{K} .

Polynomial Ideals and Invariants. As observed in [13], the set of polynomials p such that $p = 0$ is a polynomial invariant forms a polynomial ideal, called *polynomial invariant ideal*. The challenging part in polynomial invariant inference is thus to systematically compute a *basis* of this ideal. For doing so we rely on [1], and try to algorithmically compute a Gröbner basis $\{p_1, \dots, p_r\}$ ($p_i \in \mathbb{K}[X]$) of the polynomial invariant ideal. The conjunction of the polynomial equations corresponding to the polynomials from such a computed basis (i.e. $p_i(X) = 0$) would thus completely characterize the polynomial invariants of the loop. Namely, any other polynomial invariant could be derived as a logical consequence of $p_1 = 0 \wedge \dots \wedge p_r = 0$.

In the process of deriving such a finite basis of the polynomial invariant ideal, we leverage methods from algorithmic combinatorics, as presented below.

Recurrences and Closed Forms. From the assignments statements of a P-solvable loop, recurrence equations of the variables are built and solved, using the loop counter

n as the recurrence index. Solutions of recurrence equations are called *closed-forms*, and they express the value of each program variable in a loop iteration as a function of n and some given initial values.

In our research, we handle special classes of recurrence equations, i.e. those that are either C-finite [19] or Gosper-summable [3]. C-finite recurrences always admit closed forms [2], whereas closed forms of Gosper-summable recurrences can be computed, if they exist, using the decision algorithm given by [3]. For example, the closed form solution of the C-finite recurrence $x[n+1] = 2 * x[n] + 1$ (corresponding to the loop assignment $x := 2 * x + 1$) is $x[n] = 2^n * x[0] + 2^n - 1$, where $x[n]$ denotes the value of variable x at loop iteration n and thus $x[0]$ is the initial value of x (i.e. before entering the loop); whereas the closed form the Gosper-summable recurrence $y[n+1] = y[n] + 2$ (corresponding to the loop assignment $y := y + 2$) is $y[n] = y[0] + 2n$, where $y[n]$ denotes the value of variable y at loop iteration n and $y[0]$ is the initial value of y .

We only consider P-solvable loops whose assignment statements describe Gosper-summable or C-finite recurrences. Moreover, P-solvability of loops requires the existence of *polynomial* closed form solutions of each variable, i.e. closed forms are polynomial expressions in loop counter, initial values and some new variables, where there are polynomial relations, so-called *algebraic dependencies*, among the new variables. Computing the algebraic dependencies reduces once again to compute a Gröbner basis of the ideal of all algebraic dependencies [7]. For example, the ideal of algebraic dependencies among $a = 2^n$ and $b = 4^n$ is generated by the polynomial relation $a^2 - b = 0$; note that this relation holds for any $n \in \mathbb{N}$.

P-solvable Loops and Invariants. We consider P-solvable loops as below.

While[b, s_0 ; If[b_1 Then s_1 Else ... If[b_{k-1} Then s_{k-1} Else s_k ...]; s_{k+1}] (1)

where b_0, \dots, b_{k-1} are boolean expressions, and s_0, \dots, s_{k+1} are sequences of assignments. As mentioned, in our approach to invariant generation all tests are omitted, and the loops are turned into non-deterministic programs [11]. Using regular expression like notation, loop (1) can be thus equivalently written as

$$(S_1 | S_2 | \dots | S_k)^*, \text{ where } S_i = s_0; s_i; s_{k+1} \text{ for all } i = 1, \dots, k. \quad (2)$$

Loop (1) is P-solvable iff the *inner* loops S_i^* from (2) are P-solvable. Namely, the variables of each S_i^* can be expressed as a polynomial of the initial values of variables (those when the loop is entered), the inner loop counter, and some new variables, where there are algebraic dependencies among the new variables. In the sequel we write $S_i^{j_i}$ to mean the j_i -times repeated execution of S_i , where $j_i \in \mathbb{N}$ denotes the loop counter of S_i .

We have now all necessary ingredients to synthesize our invariant generation algorithm for P-solvable loops with assignments and (nested) conditionals. This is achieved in Algorithm 2.1, as given below.

Algorithm 2.1 P-solvable Loops with Nested Conditionals

Input: P-solvable loop (1) with k conditional branches and assignments

Output: Set GI of polynomial invariants for (1) among X with initial values X_0

Assumption: $k \geq 1, j_i \in \mathbb{N}, i = 1, \dots, k$

- 1 Transform loop (1) into loop (2) with k P-solvable inner loops S_1^*, \dots, S_k^*
- 2 for each $S_i^{j_i}$, $i = 1, \dots, k$ do
- 3 Compute the closed form system of the P-solvable loop $S_i^{j_i}$:

$$\begin{cases} x_1[j_i] = q_{i,1}(j_i, y_{i1}, \dots, y_{is}) \\ \vdots \\ x_m[j_i] = q_{i,m}(j_i, y_{i1}, \dots, y_{is}) \end{cases}, \text{ where } \begin{cases} y_{ir} \in \bar{\mathbb{K}}, \\ q_{i,l} \in \bar{\mathbb{K}}[j_i, y_{i1}, \dots, y_{is}], \\ q_{i,l} \text{ are parameterized by } X_0, \\ r = 1, \dots, s, \quad l = 1, \dots, m \end{cases}$$

- 4 Compute the ideal $A_i = I(j_i, y_{i1}, \dots, y_{is})$ of algebraic dependencies for the new variables y_{is} from the closed form of $S_i^{j_i}$
- 5 endfor
- 6 Compute the merged closed form of $S_1^{j_1}; \dots; S_k^{j_k}$:

$$\begin{cases} x_1[j_1, \dots, j_k] = f_1(j_1, y_{11}, \dots, y_{1s}, \dots, j_k, y_{k1}, \dots, y_{ks}) \\ \vdots \\ x_m[j_1, \dots, j_k] = f_m(j_1, y_{11}, \dots, y_{1s}, \dots, j_k, y_{k1}, \dots, y_{ks}) \end{cases}, \text{ with}$$

$f_l \in \bar{\mathbb{K}}[j_1, y_{11}, \dots, y_{1s}, \dots, j_k, y_{k1}, \dots, y_{ks}]$,
 the coefficients of f_l are given by the initial values X_0 before $S_1^{j_1}; \dots; S_k^{j_k}$

- 7 Let $A = \sum_{i=1}^k A_i$
- 8 Compute $PI_1 = ((x_1 - f_1, \dots, x_m - f_m) + A) \cap \bar{\mathbb{K}}[x_1, \dots, x_m]$
- 9 for each permutation $(w_1, \dots, w_k) \neq (1, \dots, k)$ over $\{1, \dots, k\}$ do
- 10 Compute the merged closed form of $S_{w_1}^{j_{w_1}}; \dots; S_{w_k}^{j_{w_k}}$:

$$\begin{cases} x_1[j_1, \dots, j_k] = f_1(j_{w_1}, y_{w_1 1}, \dots, y_{w_1 s}, \dots, j_{w_k}, y_{w_k 1}, \dots, y_{w_k s}) \\ \vdots \\ x_m[j_1, \dots, j_k] = f_m(j_{w_1}, y_{w_1 1}, \dots, y_{w_1 s}, \dots, j_{w_k}, y_{w_k 1}, \dots, y_{w_k s}) \end{cases}, \text{ with}$$

$f_l \in \bar{\mathbb{K}}[j_1, y_{11}, \dots, y_{1s}, \dots, j_k, y_{k1}, \dots, y_{ks}]$,
 the coefficients of f_l are given by the initial values X_0 before $S_{w_1}^{j_{w_1}}; \dots; S_{w_k}^{j_{w_k}}$

- 11 Let $A = \sum_{i=1}^k A_{w_i}$
- 12 Compute $G = ((x_1 - f_1, \dots, x_m - f_m) + A) \cap \bar{\mathbb{K}}[x_1, \dots, x_m]$
- 13 Compute $PI_1 = PI_1 \cap G$
- 14 endfor

- 15 From PI_1 keep the set GI of those polynomials whose conjunction is preserved by each S_1, \dots, S_k :

$$GI = \{p \in PI_1 \mid wp(S_i, p(X) = 0) \in \langle GI \rangle, i = 1, \dots, k\} \subset PI_1, \text{ where } wp(S_i, p(X) = 0) \text{ is the weakest precondition of } S_i \text{ with postcondition } p(X) = 0$$

- 16 *return* GI .

Algorithm 2.1 receives as input a P-solvable loop (1), and transforms it into (2) as its first step. Next, closed forms and algebraic dependencies of each inner loop S_i^t are computed using the methods presented on page 2 (steps 2-5 of Algorithm 2.1). Further, inner loops are taken in all possible $k!$ permutation orders. For each permutation order, closed forms of inner loops are “merged” to express the behavior of a sequence of inner loops as a polynomial system in the inner loop counters, initial values X_0 and some new variables where there are algebraic dependencies among the new variables. Loop counters are next eliminated by Gröbner basis computation, and the ideal of valid polynomial identities after arbitrary inner loop sequences is thus derived (steps 6-12 of Algorithm 2.1). Further, the intersection of the polynomial ideals of all inner loop sequences is computed (step 13 of Algorithm 2.1), and the ideal PI_1 of polynomial relations for the *first iteration* of loop (2) with initial values X_0 is obtained. Finally, using the weakest precondition strategy, the inductiveness property of polynomials from PI_1 is checked, and a set GI of polynomial invariants for (1) is derived (steps 15-16 of Algorithm 2.1).

Note that steps 9-16 are relevant only for P-solvable loops with nested conditionals (i.e. $k > 1$). For loops with assignment statements only, polynomial invariants are computed from the closed form system of the loop by eliminating the variables in the loop counter, using Gröbner basis computation. Moreover, based on the theory of Gröbner bases, the computed set of polynomials is a basis of the polynomial invariant ideal. Hence, our approach for invariant generation in case of P-solvable loops with assignments only is always complete: any further polynomial invariant can be inferred from the computed basis.

Moreover, under additional assumptions on the ideal of polynomial relations among X with initial values X_0 corresponding to sequences of k and $k + 1$ inner loops, in [11] we proved that our method is also complete for a wide class of P-solvable loop with nested conditionals. Namely, it returns a basis for the polynomial invariant ideal for some special cases of P-solvable loops with conditional branches and assignments. It is worth to be mentioned though that these additional constraints cover a wide class of loops, and we could not find any example for which the completeness of our approach is violated.

3 Experimental Results

We now turn our interest on the practical applicability of our method for invariant generation, and illustrate the technique on interesting examples implementing non-trivial number-theoretic algorithms.

Our approach is implemented in a new software package, called *Aligator*[10], written on top of the computer algebra system *Mathematica*. The package combines

algorithms from symbolic summation and polynomial algebra with computational logic in a uniform framework, and is applicable to the rich class of P-solvable loops.

We begin with a loop without conditionals, and illustrate that Algorithm 2.1 is applicable for the special case when $k = 1$ (i.e. loop with only assignments).

EXAMPLE 3.1 Consider the loop implementing an algorithm for computing the integer square root k of a given integer number a [8].

```

k := 0; j := 1; m := 1;
While{(m ≤ a),
    k := k + 1; j := j + 2; m := m + j}.
    
```

By applying Algorithm 2.1, the polynomial invariants are derived as follows.

Step 1: Omitting test conditions.

S_1 : $k := k + 1; j := j + 2; m := m + j$.

Steps 2-5: Closed form computation.

System of recurrences:

Recurrence solving:

$$\begin{cases} k[n+1] = k[n] + 1 \\ j[n+1] = j[n] + 2 \\ m[n+1] = m[n] + j[n+1] \end{cases} \quad \begin{cases} k[n] \stackrel{\text{Cosper}}{=} k[0] + n \\ j[n] \stackrel{\text{Cosper}}{=} j[0] + 2n \\ m[n] \stackrel{\text{Cosper}}{=} m[0] + j[0] * n + n(n+1) \end{cases}$$

where $n \in \mathbb{N}$ is the loop counter with $A = \emptyset$.

$k[0]$, $j[0]$ and $m[0]$ denote respectively the initial values of k , j and m .

Steps 6-8: Variable elimination.

$$PI_1 = \langle k - k[0] - n, j - j[0] - 2n, m - m[0] - j[0] * n - n(n+1) \rangle + A \cap \mathbb{Z}[k, j, m]$$

$$= \langle 2j + j^2 - 4m - 2j[0] - j[0]^2 + 4m[0], -j + 2k + j[0] - 2k[0] \rangle$$

Steps 9-16: Polynomial invariant ideal.

$GI = 2j + j^2 - 4m - 2j[0] - j[0]^2 + 4m[0], -j + 2k + j[0] - 2k[0]$ and $PI_1 = \langle GI \rangle$.

In [11], we proved that affine loops are P-solvable. Note that Example 3.1 is affine, and thus P-solvable. Hence, the correctness of Algorithm 2.1 ensures that the returned set GI of invariants is a basis for the polynomial invariant ideal, and our method is complete: any further polynomial invariant can be derived from GI .

The automatically inferred invariant for Example 3.1 is thus

$$2j + j^2 - 4m - 2j[0] - j[0]^2 + 4m[0] = 0 \wedge -j + 2k + j[0] - 2k[0] = 0,$$

yielding

$$1 + 2j + j^2 - 4m = 0 \wedge 1 - j + 2k = 0$$

by initial values substitutions

Many interesting algorithms implementing special numbers from algebraic combinatorics can be encoded using P-solvable loops, as also illustrated in the next example.

EXAMPLE 3.2 Consider the loop computing the number of HC-polyominoes for $m \geq 2$ [17, 6].

```

g := 1; b := 5/16; a := 3/4; r := 2;
While[i ≤ m,
    s := t; t := r; r := 5 * r - 7 * a + 4 * b;
    a := t; b := s; g := 4 * g; i := i + 1].
    
```

For simplicity, we omit a detailed presentation of the steps of Algorithm 2.1, and discuss only the main results obtained from symbolic summation.

The loop body is described by the recurrence equations:

$$\begin{cases} r[n+3] = 5 * r[n+2] - 7r[n+1] + 4r[n] \\ a[n+3] = r[n+2] \\ b[n+3] = r[n+1] \\ g[n+3] = 4g[n+2] \\ i[n+3] = i[n] + 1 \end{cases}$$

where $n \geq 0$ is the loop counter. The recurrences of r and g are C-finite, and hence they can be solved by the methods presented on page 2. The recurrence of i is both Gosper-summable and C-finite, and thus it admits closed form solution which is computed in our approach by the Gosper-algorithm [3]. The closed forms of r and g yield algebraic exponential sequences in n , whose ideal of algebraic dependencies is derived as discussed on page 2. Further, by Gröbner basis computation for eliminating the variables in n from the closed form system of the loop, we obtain a *basis* of the polynomial invariant ideal, as given below.

$$\{ 31 g a[0]^3 - 69 g a[0]^2 b[0] + 56 g a[0] b[0]^2 - 16 g b[0]^3 - 31 a^3 g[0] + 69 a^2 b g[0] - 56 a b^2 g[0] + 16 b^3 g[0] + 32 a^2 r g[0] - 47 a b r g[0] + 20 b^2 r g[0] - 10 a r^2 g[0] + 7 b r^2 g[0] + r^3 g[0] - 32 g a[0]^2 r[0] + 47 g a[0] b[0] r[0] - 20 g b[0]^2 r[0] - g r[0]^3 + 10 g a[0] r[0]^2 - 7 g b[0] r[0]^2 \},$$

yielding the polynomial invariant

$$496a^3 + 1104a^2b - 896ab^2 + 256b^3 - g + 512a^2r - 752abr + 320b^2r - 160ar^2 + 112br^2 + 16r^3 = 0,$$

by initial values substitutions.

Finally, let us give an example of a P-solvable loop with nested conditionals.

EXAMPLE 3.3 Consider the imperative loop implementing an algorithm for computing the square root q with precision err for a real number a [20].

```

r := a - 1; q := 1; p := 1/2;
While[(2 * p * r ≥ err),
    If[2 * r - 2 * q + p ≥ 0
        Then r := 2 * r - 2 * q - p; q := q + p; p := p/2
        Else r := 2 * r; p := p/2].
    
```

Step 1: Omitting test conditions and loop transformation.

$$S_1 : r := 2 * r - 2 * q - p; q := q + p; p := p/2$$

$$S_2 : r := 2 * r; p := p/2.$$

Steps 2-5: Closed form computation of inner loops.

System of recurrences:

<p>Inner loop $S_1^{j_1}$:</p> $j_1 \in \mathbb{N}$ $\begin{cases} p[j_1 + 1] = p[j_1]/2 \\ q[j_1 + 1] = q[j_1] + p[j_1] \\ r[j_1 + 1] = 2 * r[j_1] - 2 * q[j_1] - p[j_1] \end{cases}$	<p>Inner loop $S_2^{j_2}$:</p> $j_2 \in \mathbb{N}$ $\begin{cases} p[j_2 + 1] = p[j_2]/2 \\ q[j_2 + 1] = q[j_2] \\ r[j_2 + 1] = 2 * r[j_2], \end{cases}$
---	---

where j_1 and j_2 represent the loop counters of the inner loops.

Recurrence solving:

<p>Inner loop $S_1^{j_1}$:</p> $j_1 \in \mathbb{N}$ $\begin{cases} p[j_1]_{C-\bar{f}_{inste}} = \frac{1}{2^{j_1}} * p[0_{j_1}] \\ q[j_1]_{C\bar{o}s\bar{p}e\bar{r}} = q[0_{j_1}] + 2 * p[0_{j_1}] - \frac{1}{2^{j_1-1}} * p[0_{j_1}] \\ r[j_1]_{C-\bar{f}_{inste}} = 2^{j_1} * (r[0_{j_1}] - 2 * q[0_{j_1}] - 2 * p[0_{j_1}]) - \frac{1}{2^{j_1-2}} * p[0_{j_1}] + 2 * q[0_{j_1}] + 4 * p[0_{j_1}] \end{cases}$	<p>Inner loop $S_2^{j_2}$:</p> $j_2 \in \mathbb{N}$ $\begin{cases} p[j_2]_{C-\bar{f}_{inste}} = \frac{1}{2^{j_2}} * p[0_{j_2}] \\ q[j_2] = q[0_{j_2}] \\ r[j_2]_{C-\bar{f}_{inste}} = 2^{j_2} * r[0_{j_2}], \end{cases}$
--	---

where $p[0_{j_1}], q[0_{j_1}], r[0_{j_1}]$ are the initial values of p, q, r before entering the inner loop $S_1^{j_1}$. Similarly, $p[0_{j_2}], q[0_{j_2}], r[0_{j_2}]$ are the initial values of p, q, r before entering the inner loop $S_2^{j_2}$.

Introducing new variables and computing algebraic dependencies:

<p>Inner loop $S_1^{j_1}$:</p> $j_1 \in \mathbb{N}$ $x = 2^{j_1}, y = 2^{-j_1}$ $\begin{cases} p[j_1] = y * p[0_{j_1}] \\ q[j_1] = q[0_{j_1}] + 2 * p[0_{j_1}] - 2 * y * p[0_{j_1}] \\ r[j_1] = x * (r[0_{j_1}] - 2 * q[0_{j_1}] - 2 * p[0_{j_1}]) - 2 * y * p[0_{j_1}] + 2 * q[0_{j_1}] + 4 * p[0_{j_1}] \end{cases}$ $A_1 = \langle x * y - 1 \rangle$	<p>Inner loop $S_2^{j_2}$:</p> $j_2 \in \mathbb{N}$ $u = 2^{j_2}, v = 2^{-j_2}$ $\begin{cases} p[j_2] = v * p[0_{j_2}] \\ q[j_2] = q[0_{j_2}] \\ r[j_2] = u * r[0_{j_2}] \end{cases}$ $A_2 = \langle u * v - 1 \rangle$
---	--

Steps 6-8: Polynomial relations of $S_1^{j_1}; S_2^{j_2}$.

Merging closed forms:

For the inner loop sequence $S_1^{j_1}; S_2^{j_2}$, the initial values of the loop variables $p[0_{j_2}]$, $q[0_{j_2}]$ and $r[0_{j_2}]$ before entering loop $S_2^{j_2}$ are given respectively by the values of the variables $p[j_1]$, $q[j_1]$ and $r[j_1]$ after $S_1^{j_1}$. Thus, by replacing the closed form expressions of $p[j_1]$, $q[j_1]$, and $r[j_1]$ in the closed forms $p[j_2]$, $q[j_2]$ and $r[j_2]$, we get the closed form system for the values of loop variables $p[j_1, j_2]$, $q[j_1, j_2]$ and $r[j_1, j_2]$ after j_1 -times repeated execution of S_1 followed by j_2 -times repeated execution of S_2 . Writing respectively p , q and r instead of $p[j_1, j_2]$, $q[j_1, j_2]$ and $r[j_1, j_2]$, the obtained merged closed form is as follows.

Closed form system of $S_1^{j_1}; S_2^{j_2}$:

$$\begin{cases} p = v * y * p[0] \\ q = q[0] + 2 * p[0] - 2 * y * p[0] \\ r = u * (x * (r[0] - 2 * q[0] - 2 * p[0]) - 2 * y * p[0] + 2 * q[0] + 4 * p[0]) \end{cases}$$

with $A = (u * v - 1, x * y - 1)$,

where $p[0]$, $q[0]$, $r[0]$ are respectively the initial values of the loop variables p , q , r before the first iteration of the P-solvable loop with nested conditionals (i.e. before $S_1^1; S_2^1$). We denote

$$I_1 = (p - v * y * p[0], q - (q[0] + 2 * p[0] - 2 * y * p[0]), \\ r - u * (x * (r[0] - 2 * q[0] - 2 * p[0]) - 2 * y * p[0] + 2 * q[0] + 4 * p[0]) \\ u * v - 1, x * y - 1).$$

Variable elimination:

$$PI_1 = I_1 \cap \mathbb{R}[p, q, r] = (q^2 - q[0]^2 + 2 * p * r - 2 * p[0] * r[0]).$$

Steps 6-8: Polynomial relations of $S_2^{j_2}; S_1^{j_1}$.

Merging closed forms:

Closed form system of $S_2^{j_2}; S_1^{j_1}$

$$\begin{cases} p = y * v * p[0] \\ q = q[0] + 2 * p[0] - 2 * y * p[0] \\ r = x * (u * r[0] - 2 * q[0] - 2 * v * p[0]) - 2 * y * v * p[0] + 2 * q[0] + 4 * v * p[0] \end{cases}$$

with $A = (x * y - 1, u * v - 1)$,

where $p[0]$, $q[0]$, $r[0]$ are the initial values of the loop variables p , q , r before the first iteration of the P-solvable loop with nested conditionals (i.e. before $S_2^1; S_1^1$). We denote

$$I_2 = (p - v * y * p[0], q - q[0] - 2 * p[0] + 2 * y * p[0] \\ r - u * (x * (r[0] - 2 * q[0] - 2 * p[0]) - 2 * y * p[0] + 2 * q[0] + 4 * p[0]) \\ u * v - 1, x * y - 1).$$

Variable elimination:

$$G = I_2 \cap \mathbb{R}[p, q, r] = \langle q^2 - q[0]^2 + 2 * p * r - 2 * p[0] * r[0] \rangle.$$

Polynomial relations of inner loop sequences:

$$PI_1 = PI_1 \cap G = \langle q^2 - q[0]^2 + 2 * p * r - 2 * p[0] * r[0] \rangle.$$

Steps 15-16: Polynomial invariants of P-solvable loop with conditionals.

$$GI = \{q^2 - q[0]^2 + 2 * p * r - 2 * p[0] * r[0]\},$$

and thus $PI_1 = \langle GI_1 \rangle$. The derived set GI is hence a basis of the polynomial invariant ideal, and our method is complete: any further polynomial invariant can be derived from GI .

The automatically inferred polynomial invariant for Example 3.3 is thus

$$q^2 - q[0]^2 + 2 * p * r - 2 * p[0] * r[0] = 0,$$

from which, by substituting the concrete values for the symbolically treated initial values $p[0], q[0], r[0]$, we obtain:

$$a - 2 * p * r - q^2 = 0.$$

4 Conclusions

An automatic approach for polynomial invariant generation for P-solvable loops was discussed, and illustrated on a number of examples implementing non-trivial number-theoretic algorithms. For all examples we could find, and thus in particular for the examples discussed in the paper, a basis for the polynomial invariant ideal was derived by using recurrence solving, polynomial algebra and computational logic. The successful application of our approach underlines the value of using algebraic techniques for computer aided verification.

References

1. B. Buchberger. An Algorithm for Finding the Basis Elements of the Residue Class Ring of a Zero Dimensional Polynomial Ideal. *J. of Symbolic Computation*, 41(3-4):475–511, 2006.
2. G. Everest, A. van der Poorten, I. Shparlinski, and T. Ward. *Recurrence Sequences*, volume 104 of *Mathematical Surveys and Monographs*. American Mathematical Society, 2003.
3. R. W. Gosper. Decision Procedures for Indefinite Hypergeometric Summation. *Journal of Symbolic Computation*, 75:40–42, 1978.
4. D. Kapur. A Quantifier Elimination based Heuristic for Automatically Generating Inductive Assertions for Programs. *J. of Systems Science and Complexity*, 19(3):307–330, 2006.
5. M. Karr. Affine Relationships Among Variables of Programs. *Acta Informatica*, 6:133–151, 1976.
6. M. Kauers. *Algorithms for Nonlinear Higher Order Difference Equations*. PhD thesis, RISC-Linz, Johannes Kepler University Linz, Austria, 2005.
7. M. Kauers and B. Zimmermann. Computing the Algebraic Relations of C-finite Sequences and Multisequences. Technical Report 2006-24, SFB F013, 2006.

8. D. E. Knuth. *The Art of Computer Programming*, volume 2. Seminumerical Algorithms. Addison-Wesley, 3rd edition, 1998.
9. L. Kovács. *Automated Invariant Generation by Algebraic Techniques for Imperative Program Verification in Theorema*. PhD thesis, RISC, Johannes Kepler University Linz, 2007.
10. L. Kovács. *Aligator: A Mathematica Package for Invariant Generation*. In *Proc. of IJCAR*, LNCS, Sydney, Australia, 2008. To appear.
11. L. Kovács. Reasoning Algebraically About P-Solvable Loops. In *Proc. of TACAS*, volume 4963 of LNCS, pages 249–264, Budapest, Hungary, 2008.
12. M. Müller-Otm and H. Seidl. Computing Polynomial Program Invariants. *Information Processing Letters*, 91(5):233–244, 2004.
13. E. Rodríguez-Carbonell and D. Kapur. Automatic Generation of Polynomial Loop Invariants: Algebraic Foundations. In *Proc. of ISSAC 04*, 2004.
14. E. Rodríguez-Carbonell and D. Kapur. Automatic Generation of Polynomial Invariants of Bounded Degree using Abstract Interpretation. *Science of Computer Programming*, 64(1), 2007.
15. E. Rodríguez-Carbonell and D. Kapur. Generating All Polynomial Invariants in Simple Loops. *J. of Symbolic Computation*, 42(4):443–476, 2007.
16. S. Sankaranarayanan, H. B. Sipma, and Z. Manna. Non-Linear Loop Invariant Generation using Gröbner Bases. In *Proc. of POPL 2004*, 2004.
17. R. P. Stanley. *Enumerative Combinatorics*, volume 2 of *Cambridge Studies in Advanced Mathematics* 62. Cambridge University Press, 1997.
18. B. Wegbreit. The Synthesis of Loop Predicates. *Communication of the ACM*, 2(17):102–112, 1974.
19. D. Zeilberger. A Holonomic System Approach to Special Functions. *Journal of Computational and Applied Mathematics*, 32:321–368, 1990.
20. K. Zuse. *The Computer - My Life*. Springer, 1993.

AUTHOR'S ADDRESS:

Dr. Laura Kovács
EPFL
IC-MTC, Station 14
CH-1015 Lausanne
Switzerland
laura.kovacs@epfl.ch

Prof. Dr. Adalbert Kovács
University “Politehnica” of Timișoara
Department of Mathematics
Pta. Victoriei nr. 2, RO-300006 Timișoara
Romania
profdrkovacs@yahoo.com



Considerations on the Calculus Algorithm of the Fluid's Velocity Potential through Profile Grids

Adalbert Kovács¹, Laura Ildikó Kovács²

¹ University "Politehnica" of Timișoara, Romania

² Research Institute for Symbolic Computation, Johannes Kepler University, Linz, Austria

Abstract.

Based on the results of [10] and [11], in this paper we present some practical aspects of the usage of the calculus algorithm for the study of the compressible fluid's stationary movement through profile grids, on an axial-symmetric flow-surface, in variable thickness of stratum.

Keywords: boundary element method, hydrodynamic networks, fluid's velocity potential, Fredholm integral equation, Lagrange interpolation

1 Introduction

In this paper we present practical aspects of the usage of the calculus algorithm for the study of the compressible fluid's stationary movement through profile grids, on an axial-symmetric flow-surface, in variable thickness of stratum. More precisely, we show the applicability of the boundary element methods (BEM) with real values, and the possibility of solving the integral equation of the velocity potential by using the successive approximation method w.r.t. the parameters ρ (fluid's density) and h (thickness variation of fluid stratum), and using the Lagrangian interpolation formula through five points for the calculation of the derivatives of the velocity potential.

The rest of the paper is organized as follows: in section 2 we state the problem and some theoretical considerations that are needed. In section 3 we present the calculus algorithm for the study of the compressible fluid's stationary movement, together with its practical aspects. Section 4 concludes with some ideas for the future work.

2 Presenting the Problem

The fundamental equations (from the CVBEM method) in the problem of the compressible fluid's movement on an axial-symmetric flow-surface, in variable thickness of stratum, could be ([5], [6], [7]):

$$\begin{aligned} w(z) &= \bar{V}_m + \int_{L_0} H(z, \zeta) \bar{w}(\zeta) d\zeta + i \iint_{D_0^-} H(z, \zeta) \hat{q}(\zeta) d\xi d\eta \\ F(z) &= \bar{V}_m \cdot z + \Gamma \cdot G(z, \zeta_A) + \int_{L_0} H(z, \zeta) F(\zeta) d\zeta + i \iint_{D_0^-} G(z, \zeta) \hat{q}(\zeta) d\xi d\eta \end{aligned} \quad (1)$$

where:

- A – is a fixed point on the base profile L_0 ;
- t – is the grid step;
- Γ – is the circulation around L_0 .

$$\begin{aligned} H(z, \zeta) &= \frac{1}{2\pi i} \operatorname{ctg} \frac{\pi}{t} (z - \zeta) \\ G(z, \zeta) &= \frac{1}{2\pi i} \ln \sin \frac{\pi}{t} (z - \zeta) \\ \hat{q}(\zeta) &= 2 \frac{\partial w}{\partial \zeta} = - \left[v_x \frac{\partial \ln p^*}{\partial \xi} - v_y \frac{\partial \ln p^*}{\partial \eta} \right], \quad p^* = \frac{\rho \cdot h}{\rho_0} \end{aligned} \quad (2)$$

where:

- ρ – is the fluid's density;
- h – is a function that represents the thickness' variation of the fluid stratum.
- D_0^- – bounded simple convex domain, defined as:

$$D_0^- : \left[-\frac{t}{2} < \xi < \frac{t}{2}, -\left(t + \frac{l}{2}\right) < \eta < \left(t + \frac{l}{2}\right) \right] \quad (3)$$

where:

- l – is the projection of L_0 profile's frame on the Oy axis.

Our purpose is to solve the fundamental equations (1) (obtained from the CVBEM method) using (BEM) in real variables. For doing so, we consider the fundamental integral-equation of the complex potential $F(z) = \varphi + i\psi$ and transform it into an integral equation with real variables, i.e. we build the integral equation of the velocity potential $\varphi(s)$ ($\psi(s)$ is the flow rate function).

Theorem 2.1. [7], [11] *In the subsonic motion of the compressible fluid through the profile grid, on an axial-symmetric flow-surface, in variable thickness of stratum, the velocity potential $\varphi(s)$, $s \in L_0$ is the solution of the integral equation (4):*

$$\varphi(s) + \int_{L_0} \varphi(\sigma) \frac{dM(s, \sigma)}{d\sigma} d\sigma = b(s) + \iint_{D_0^-} \hat{q}(\sigma) N(s, \sigma) d\xi d\eta \quad (4)$$

where:

- $s(x_0, y_0)$ and $\sigma(\xi, \eta)$ are the curvilinear coordinates of the fixed point A on the L_0 base profile;

$$\begin{aligned}
 b(s) &= 2(x_0 v_{mx} + y_0 v_{my}) + \Gamma M(s, \sigma_A) + \int_{L_0} [\psi(s) - \psi(\sigma)] \frac{dN}{d\sigma} d\sigma \\
 M(z_0, \zeta) &= \frac{1}{\pi} \arctg \frac{th \frac{\pi}{t} (\eta - y_0)}{tg \frac{\pi}{t} (\xi - x_0)} \\
 N(z_0, \zeta) &= \frac{1}{\pi} \ln \sqrt{\frac{1}{2} \left[ch \frac{2\pi}{t} (\eta - y_0) - \cos \frac{2\pi}{t} (\xi - x_0) \right]} \\
 v_{mx}, v_{my} & \text{ are the components of the asymptotic mean velocity } v_m.
 \end{aligned} \tag{5}$$

Proposition 2.1. [10], [11] *In the case of an axial-subsonic movement of a perfect and compressible fluid through profile grids, the flow rate function is determined from the boundary condition (6):*

$$\psi(s) = u_0 \cdot \int_0^s p^*(s) \left(\frac{R}{R_0} \right) ds, \quad u_0 = \omega R_0, \tag{6}$$

where:

- ω is the angular rotation velocity of the profile grid;
- R_0 defines the origin of the axis system related to the turbine's axis.

Equation (4) is an integro-differential equation. In this section, we will show a possibility of solving this equation applying the *method of successive approximation* (the iteration method), using also the result from [8] about the order of the term containing the double integral expression:

$$\varphi_{\bar{q}}(s) = \iint_{D_{\bar{q}}} \bar{q}(\sigma) N(s, \sigma) d\xi d\eta. \tag{7}$$

Proposition 2.2. [10], [9] *In the case of the subsonic movement of the compressible fluid through the profile grid on an axial-symmetric flow-surface, in variable thickness of stratum, the integral equation of the velocity potential $\varphi : D_{\bar{q}} \rightarrow \mathbb{R}$ is solvable by applying the method of successive approximations w.r.t. the parameter $p^* = \frac{p^h}{\rho^h}$.*

Proof. For isentropic processes, by the Bernoulli-equation, we obtain:

$$\rho = \rho_0 \left(1 - \frac{\gamma - 1}{2} \frac{v^2}{c_0^2} \right)^{\frac{1}{\gamma - 1}}, \quad v^2 = v_\tau^2 + v_n^2, \quad v_\tau = \frac{d\varphi}{ds}, \quad v_n = \frac{1}{p^*} \frac{d\psi}{ds} \tag{8}$$

where:

- γ is the adiabatic constant;
- c_0 is the sound velocity in the zero velocity point;
- v_τ and v_n are, respectively, the tangential and normal velocities on L_0 .

In the first approximation it is assumed that $\rho = \rho_0 = \text{constant}$ and $p^* = p^{*(0)} = \text{constant}$. Thus, from (2), it results that $q^{(0)}(\sigma) = 0$. Hence, in the integral equation (4) the double integral (7) is neglected and results the following Fredholme integral equation of second type, with continuous nucleus:

$$\varphi^I(s) + \int_{L_0} \varphi^I(s) \frac{dM(s, \sigma)}{d\sigma} d\sigma = b^I(s) \quad (9)$$

From solving equation (9) we obtain $\varphi^I(s)$, and furthermore from (6), (8), (12) ψ^I , ρ^I are obtained. Finally, using the relation:

$$p^* = \frac{\rho \cdot h}{\rho_0}, \quad \tilde{q}^I(\sigma) = -\text{grad} \rho \cdot \text{grad} \ln p^*, \quad (10)$$

a p^{*I} and $\tilde{q}^I(\sigma)$ are determined.

In the second iteration $p^* = p^{*I}$ is assumed and for the determination of $\varphi^{II}(s)$ the following Fredholme integral equation of second type, with continuous nucleus, will be solved:

$$\varphi^{II}(s) + \int_{L_0} \varphi^{II}(s) \frac{dM(s, \sigma)}{d\sigma} d\sigma = b^{II}(s) + \iint_{D_{\sigma^*}} \tilde{q}^I(\sigma) N(s, \sigma) d\xi d\eta, \quad (11)$$

where a ψ^I and $b^{II}(s)$ are previously calculated from (6) and (5), respectively.

From solving equation (11), we obtain φ^{II} . Furthermore, from (6), (8), (12) and (10) ψ^{II} , ρ^{II} , p^{*II} and $\tilde{q}^{II}(\sigma)$ are obtained, respectively. Next, the third approximation might be done by assuming $p^* = p^{*II}$, and so on. □

Proposition 2.3. [10] *Having given the values of the velocity potential on each element of the L_0 profile's division, the tangential velocity v_{τ} may be calculated in each division element of the L_0 basic profile's boundary by the formula, given by the Lagrange interpolation method through five points:*

$$\begin{aligned} v_{\tau i} &= \varphi'(s_i) = \frac{2}{3h}(\varphi_{i+2} - \varphi_{i-2}) - \frac{1}{12h}(\varphi_{i+4} - \varphi_{i-4}), \\ h &= \Delta s_i = s_{i+1} - s_{i-1}, \\ i &= 1, 3, 5, \dots, 2n - 1, \end{aligned} \quad (12)$$

where n denotes the number of division elements and by s_i we refer to the i^{th} element of the division of L_0 .

To ensure the practical functionality of proposition 2.2, i.e. to indicate the solving method of the Fredholme integral equation of second type obtained in each approximation step (equation (6), (11)), let us formulate and prove two more propositions.

Proposition 2.4. [10], [11] *In the first approximation step, solving the velocity potential's Fredholme integral equation of second type is reduced to the solving of four systems of linear algebraic equations.*

Proof. Using the superposition rule of potential streams, we seek the solution of the Fredholme integral equation of second type (9) to be of the form:

$$\varphi^f = \varphi_1^f v_{mx} + \varphi_2^f v_{my} + \varphi_3^f \Gamma + \varphi_4^f u_0, \quad u_0 = \omega R_0, \quad (13)$$

where φ_k^f , $k = 1 \div 4$ are the solutions of the system (14) of integral equations:

$$\begin{aligned} \varphi_1^f(s) + \int_{L_0} \varphi_1^f(\sigma) \frac{dM(s,\sigma)}{d\sigma} d\sigma &= 2x_0 \\ \varphi_2^f(s) + \int_{L_0} \varphi_2^f(\sigma) \frac{dM(s,\sigma)}{d\sigma} d\sigma &= 2y_0 \\ \varphi_3^f(s) + \int_{L_0} \varphi_3^f(\sigma) \frac{dM(s,\sigma)}{d\sigma} d\sigma &= M(s, \sigma_A) \\ \varphi_4^f(s) + \int_{L_0} \varphi_4^f(\sigma) \frac{dM(s,\sigma)}{d\sigma} d\sigma &= b_4(s) \end{aligned} \quad (14)$$

where:

$$b_4(s) = \int_{L_0} [\psi^f(s) - \psi^f(\sigma)] \frac{dN}{d\sigma} d\sigma. \quad (15)$$

The integral equations (14) could be solved using the Bogoliubov-Krilov method, conform to which, solving each integral equation reduces to solving a system of linear algebraic equations. Conform to the method, using an arbitrary division, we partition the boundary of L_0 in n subintervals $\Delta s = \Delta\sigma$. Note, that the chosen division might be not uniform, for instance at the trailing or the leading edge, where the variation of the function φ_k^f is stronger from point-to-point, the length of subintervals might be shorter. In each subinterval, the function φ_k^f is assumed to be constant and equal to φ_{kj}^f , where j represents the number of the middle-points of the considered subintervals. If the first division-points are debited by even numbers, and the division-points of the middle of the subintervals by odd numbers, then, conform to the approximation method, the integral equations (14) can be approximated by the following systems of linear algebraic equations:

$$\varphi_{kt}^f + \sum_{j=1}^{2n-1} \varphi_{kj}^f \Delta M_{tj} = b_{kt}^f, \quad i = 1, 3, 5, \dots, 2n-1, \quad k = 1, 2, 3, 4, \quad (16)$$

where:

$$\begin{aligned} b_{1t}^f &= 2x_t, & b_{2t}^f &= 2y_t, & b_{3t}^f &= M_{tA}, \\ b_{4t}^f &= \sum_{j=1}^{2n-1} \Delta \psi_{i,j}^f \left(\frac{dN}{d\sigma} \right)_{i,j}, & \Delta \psi_{i,j}^f &= \psi_i^f - \psi_j^f, & \Delta\sigma &= \sigma_{j+1} - \sigma_{j-1}. \end{aligned} \quad (17)$$

Solving the algebraic system (16), we obtain φ_{kt}^f in n distinct point from the boundary of L_0 . Finally, from equations (13), φ_i^f is determined in each point of the boundary's division. \square

Proposition 2.5. [10], [11] *In the second approximation step, the Fredholme integral equation (11) of the velocity potential is reduced to solving four systems of linear algebraic equations.*

Proof. From (8) and (10), a ρ^I and a $\tilde{q}^I(\sigma)$ is determined, respectively. Consequently, using the superposition rule of potential streams, we seek the solution of the Fredholm integral equation of second type (11) to be of the form:

$$\varphi^{II} = \varphi_1^{II} v_{mx} + \varphi_2^{II} v_{my} + \varphi_3^{II} \Gamma + \varphi_4^{II} u_0, \quad u_0 = \omega R_0 \quad (18)$$

where φ_k^{II} , $k = 1 \div 4$ are the solutions of the system 19 of integral equations:

$$\begin{aligned} \varphi_1^{II}(s) + \int_{L_0} \varphi_1^{II}(\sigma) \frac{dM(s,\sigma)}{d\sigma} d\sigma &= 2x_0 + \iint_{D_{\sigma^*}} \tilde{q}^I(\sigma) N(s,\sigma) d\xi d\eta \\ \varphi_2^{II}(s) + \int_{L_0} \varphi_2^{II}(\sigma) \frac{dM(s,\sigma)}{d\sigma} d\sigma &= 2y_0 + \iint_{D_{\sigma^*}} \tilde{q}^I(\sigma) N(s,\sigma) d\xi d\eta \\ \varphi_3^{II}(s) + \int_{L_0} \varphi_3^{II}(\sigma) \frac{dM(s,\sigma)}{d\sigma} d\sigma &= M(s, \sigma_A) + \iint_{D_{\sigma^*}} \tilde{q}^I(\sigma) N(s,\sigma) d\xi d\eta \\ \varphi_4^{II}(s) + \int_{L_0} \varphi_4^{II}(\sigma) \frac{dM(s,\sigma)}{d\sigma} d\sigma &= b_4^{II} \end{aligned} \quad (19)$$

where:

$$\begin{aligned} b_4^{II}(s) &= \frac{1}{u_0} \int_{L_0} \left[\psi^{II}(s) - \psi^{II}(\sigma) \right] \frac{dN}{d\sigma} d\sigma + \iint_{D_{\sigma^*}} \tilde{q}^I(\sigma) N(s,\sigma) d\xi d\eta \\ \psi^{II}(s) &= u_0 \int_0^s \left(\frac{R}{R_0} \right)^2 p^{*I}(s) ds \\ p^{*I} &= \frac{v^I \cdot n^I}{\rho_0} \end{aligned} \quad (20)$$

Using the numeric method presented in proposition 2.4, by applying the Bogoliubov-Kr lov method, solving (19) is reduced to solving systems of linear algebraic equations.

These systems of linear algebraic equations will have the form:

$$\varphi_{ki}^{II} + \sum_{j=1}^{2n-1} \varphi_{kj}^{II} \Delta M_{ij} = b_{ki}^{II}, \quad i = 1, 3, 5, \dots, 2n-1, \quad k = 1, 2, 3, 4, \quad (21)$$

where b_{1i}^{II} , b_{2i}^{II} , b_{3i}^{II} and b_{4i}^{II} are obtained by using the Simpson formula for handling the double integral.

Solving the algebraic system (21), we obtain φ_{kj}^{II} in n distinct point from the boundary of L_0 . Finally, from equations (18), φ_i^{II} ($i = \overline{1, n}$) is determined in each point of the boundary's division. □

3 The Calculus Algorithm of the Fluid's Velocity Potentials through Profile Grids

1. Given are: the entering values into the profile grids of p_1 , $v_{1\infty}$, α_1 and the asymptotic mean velocity \vec{V}_m ; the installation angle λ ; the number of profiles n ; the density ρ_0 and the sound velocity c_0 corresponding to the null-velocity point. The functions $h(\sigma)$ and $\frac{R}{R_0}(\sigma)$ are given by their table of values;

2. Conform to the chosen division, the coordinates $\sigma_i(\xi_i, \eta_i)$, $i = 1, 3, 5, \dots, 2n - 1$ are determined. The circulation Γ is determined from the Jukovschi-Ciaplighin condition [10], [11];
3. From equation (5), the values of $\Delta M_{i,j}$, $\left(\frac{dN}{d\sigma}\right)_{i,j}$, $i, j = 1, 3, 5, \dots, 2n + 1$ are calculated;
4. Using the trapezoid method, ψ_i^I is calculated from the integral equation (6), and, using (17), b_{ik}^I ($k = 1 \div 4$) are determined;
5. The linear algebraic system (16) is solved, and, thus, φ_{ik}^I is obtained. Furthermore, from (13), ρ_i^I is also obtained;
6. Using the Lagrange interpolation formula through five points (12), $v_{\tau_i}^I$ is calculated. Next, from (8), v_i^I is determined, and, furthermore, ρ_i^I is also obtained;
7. Using ρ_i^I and $h = \text{const}$, from the integral (20), by the trapezoid method, a $\psi_i^{II}(\sigma)$ is determined. Using equations (19) and (20), b_{ik}^{II} ($k = 1 \div 4$) are obtained;
8. The integral equations (19) are solved, transforming them first into a linear algebraic system. Furthermore, φ_{ik}^{II} is obtained, and, from (18), ρ_i^{II} is determined;
9. Using the Lagrange interpolation formula through five points (12), $v_{\tau_i}^{II}$ is calculated. Next, from (8), v_i^{II} is determined, and, furthermore, ρ_i^{II} is also obtained. Furthermore, using ρ_i^{II} , the next iteration $\rho_i = \rho_i^{II}$ can be calculated, $h = \text{variable}$, and the algorithm continues.

4 Conclusion and Further Work

We have shown some practical aspects of the usage of the calculus algorithm for the study of the compressible fluid's stationary movement through profile grids, on an axial-symmetric flow-surface, in variable thickness of stratum, namely :

- the usage of the boundary element method with real values;
- the applicability of the successive approximation method w.r.t. the parameters ρ (fluid's density) and h (thickness variation of fluid stratum) for solving the integral equation of the velocity potential;
- the usage of the Lagrangian interpolation formula through five points for calculating the derivatives of the velocity potential.

Regarding practical applicability of our algorithm, our plans for the near future are:

- make more test cases w.r.t. several input (geometrical and hydrodynamical) values of the velocity potentials taken from practical experiments involving profile grids;
- study the possibility of applying the algorithm (i.e. the approximation methods) for the calculation of other fluid-characteristics.

References

- [1] P. Benerji and R. Butterfield. *The Boundary Element Method in Applied Sciences (in russian)*. MIR, Moskow, 1984.
- [2] T. Czibere. *Die Potentialtheorie den zwei Hauptproblemen der Hydrodynamischen Gittertheorie*. Miskolc, 1970.
- [3] B.P. Demidovici and I.A. Maron. *The Mathematical Basis of Numeric Calculus (in russian)*. Nauka, Moskow, 1970.
- [4] T.V. Hromadka II. *The Complex variable boudary element method*. Springer Verlag, Berlin, 1984.
- [5] A. Kovács. Beiträge im Bereich der Anwendung p-analytischer Funktionen in der Hydrodynamik der Netze. *I.P.T.V.T. Scientific and Technical Bulletin*, T.35(49):39–49, 1990.
- [6] A. Kovács. P-analytische Funktionen im Studium der räumlichen Bewegung des kompressiblen Fluids durch Profilnetze. *Bulletins for Applied Mathematics, T.U. Budapest*, T.791(LXI):169–177, 1992. PAMM's Annual Central Meeting, Balatonfüred, 14/17 V.1992.
- [7] A. Kovács. Solving a Basic Hydrodynamic Problem by the Application of the Boundary Element Method with Iterations. *Bulletins for Applied Mathematics, T.U. Budapest*, T. 788(LXI):137–147, 1992. PAMM's Annual Central Meeting, Balatonfüred, 14/17 V.1992.
- [8] A. Kovács. Über die Stabilierung und Bestimmung einer Iterationsformel für einen konexen unendlichen Bereich. In *Proceedings of The 5th Symposium of Mathematics and its Applications, Timisoara*, pages 88–92 pp., 1999. 4-7 November.
- [9] A. Kovács. Mathematische modelle in der hydrodynamik der profilgitter. *Monographical Bookles in Applied and Computer Mathematics PAMM, Budapest*, MB-19:92 pp., 2001.
- [10] A. Kovács and L.Kovács. The Lagrange Interpolation Formula in Determining the Fluid's Velocity Potential through Profile Grids. In *to appear in Bulletins for Applied Mathematics, T.U. Budapest*, page 10, 2005. PAMM's Annual Central Meeting, Balatonalmádi, 26-29 May 2005.
- [11] A. Kovács and L. Kovács. Rechnungsalgorithmus der Potentialintegralgleichung der kompressiblen Fluidgeschwindigkeit durch Profiligitter. In N.Boja, editor, *Proceedings of The 10th Symposium of Mathematics and its Applications, Timisoara*, pages 427–434, 2003. 6-9 November.
- [12] G.V. Viktorov and I.V. Vutchikova. The Calculus of Fluid-Flow through Profile Grids on an Axial-Symmetric Flow-Surface with Variable Thickness of Stratum (in russian). *Izd. ANSSSR, MJG*, (5):96–102, 1969.

Authors' address:

¹University “Politehnica” Timișoara, Department of Mathematics,
 Ro- 300223 Timișoara, Piața Regina Maria Nr.1,
 profdrkovacs@yahoo.com

²Research Institute for Symbolic Computation,
 Johannes Kepler University, A-4040 Linz, Austria
 lkovacs@risc.uni-linz.ac.at



DENSITY OF POLYNOMIAL REPARTITIONS

MAKSAY Stefan, STOICA Diana

"Politehnica" University of Timisoara, Faculty of Engineering of Hunedoara, ROMANIA

Abstract:

The present note tries to use the results of mathematic shaping to determine some probability density of polynomial forms. After the determination of a regression curve by a degree previously given, aided by the method of the smallest squares, it will be selected from this curve a domain of definition in which this function will satisfy the conditions of being a probability density.

Keywords:

Probability density, Density of polynomial repartitions, coefficient of correlation

1. PRELIMINARIES

The present note tries to use the results of mathematic shaping to determine some probability density of polynomial forms.

For example we will consider the following dates, in which the first line represent the independent variable x and second line represent the dependent variable y.

1.663	1.791	1.81	1.864	1.905	1.912	1.976	2.009	2.111	2.135	2.162	2.172	2.183	2.197	2.238
0.334	0.266	0.314	0.306	0.361	0.36	0.29	0.44	0.171	0.268	0.211	0.262	0.261	0.259	0.226

To determine the regression curve of 3rd degree (g=3) will use the following MathCAD program [1]

```

ORIGIN≡ 1      TOL := 10-5  g := 3

xT =
| 1  1.663  1.791  1.81  1.864  1.905  1.912  1.976  2.009  2.111  2.135  2.162  2.172  2.183  2.197  2.238
|-----|
| 1  0.334  0.266  0.314  0.306  0.361  0.36  0.29  0.44  0.171  0.268  0.211  0.262  0.261  0.259  0.226

yT =
| 1  0.334  0.266  0.314  0.306  0.361  0.36  0.29  0.44  0.171  0.268  0.211  0.262  0.261  0.259  0.226
|-----|

n := length(x)      i := 1.. n
xm := min(x)        xM := max(x)
ym := mean(y)       ym = 0.289
j := 1.. 2·g + 1

Sj := ∑i (xi)2·g-j+1  ST = (1.09 × 103  525.332  254.647  124.186  60.957  30.128  15)

k := 1.. g + 1      v := 1.. g + 1

mk,v := Sv+k-1      m =
| 1.09 × 103  525.332  254.647  124.186
| 525.332  254.647  124.186  60.957
| 254.647  124.186  60.957  30.128
| 124.186  60.957  30.128  15

TLk := ∑i yi · (xi)g-k+1  TLT = (34.754  17.235  8.607  4.329)

co := m-1 · TL

```

resulting the coefficients of polynomial correlation

$$co^T = (-0.843 \ 4.14 \ -6.637 \ 3.778) \tag{1}$$

and also the regression curve equation is

$$y = -0.843 \cdot x^3 + 4.14 \cdot x^2 - 6.637 \cdot x + 3.778 \tag{2}$$

which in the nodes has this values

$$kk := 1..g + 1 \quad Su_i := \sum_{kk} co_{kk} \cdot (x_i)^{g-kk+1}$$

$$Su^T = \begin{array}{c|cccccccccccccccc} & 1 & 2 & 3 & 4 & 5 & 6 & 7 & 8 & 9 & 10 & 11 & 12 & 13 & 14 & 15 \\ \hline 1 & 0.311 & 0.325 & 0.327 & 0.329 & 0.328 & 0.327 & 0.321 & 0.315 & 0.282 & 0.271 & 0.257 & 0.251 & 0.244 & 0.236 & 0.206 \end{array}$$

For the polynomial regression of 3rd degree will be obtained the following values for the correlation coefficient and respectively for the deviation from the regression curve

$$r3 := \sqrt{1 - \frac{\sum_i (y_i - Su_i)^2}{\sum_i (y_i - ym)^2}} \quad r3 = 0.615 \tag{3}$$

$$St3 := \sqrt{\frac{1}{n} \cdot \sum_i (y_i - Su_i)^2} \quad St3 = 0.051 \tag{4}$$

Next we will give attention to a domain on which to choose the expression of probability density.

Distribution density must fulfill the conditions [2]:

$$f(x) \geq 0, \quad \int_{-\infty}^{\infty} f(x) dx = 1.$$

Because

$$\int_{xm}^{xM} \sum_{kk} co_{kk} \cdot (x)^{g-kk+1} dx = 0.174 \tag{5}$$

using the next program we will determine the limits of a definition domain for a positive function, marked f3(x), restriction of the regression polynomial, so that the integral on this range will be equal with the unit

$$var1 := 0.15 \quad var2 := 0.8$$

Given

$$\int_{xm-var1}^{xm+var2} \sum_{kk} co_{kk} \cdot (x)^{g-kk+1} dx = 1$$

$$tvar := Find(var1, var2) \quad tvar = \begin{pmatrix} 1.28 \\ 0.141 \end{pmatrix}$$

We will obtain in this way the values

$$tvar_1 = 1.28 \quad tvar_2 = 0.141$$

for which

$$\int_{xm-tvar_1}^{xm+tvar_2} \sum_{kk} co_{kk} \cdot (x)^{g-kk+1} dx = 1 \tag{6}$$

where

$$xm - tvar_1 = 0.383 \quad xm + tvar_2 = 2.379$$

In conclusion, the expression of probability density of 3rd degree is

$$f_3(x) := \text{if} \left[x_m - t_{var_1} < x < x_M + t_{var_2}, \sum_{kk} co_{kk} \cdot (x)^{g-kk+1}, 0 \right], \quad (7)$$

and it's graphic is show in figure 1 with the help of the adjoining program

```
nrnod := 1000          is := 1..nrnod
xvis := xm - (tvar)1 - .35 +  $\frac{is - 1}{nrnod - 1} \cdot [x_M + tvar_2 + .1 - (x_m - tvar_1 - .35)]$ 
```

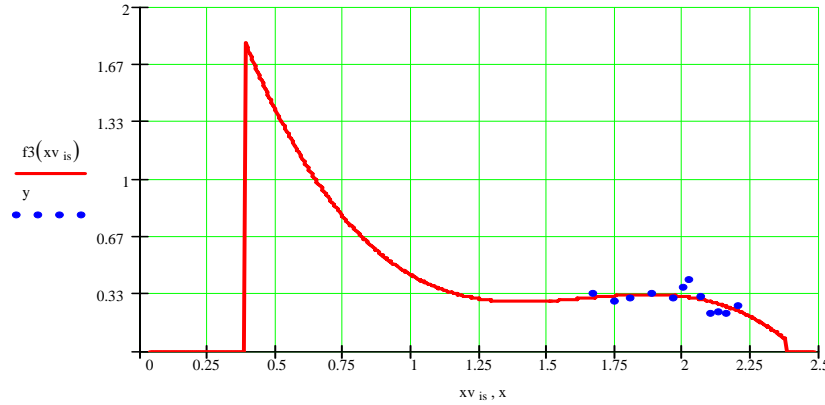


Figure. 1 Probability density of 3rd degree and the distribution of experimental points
The expression of the repartition function is

$$F_{trunc3}(x) := \int_{x_m - t_{var_1}}^x \text{if} \left[x_m - t_{var_1} < u < x_M + t_{var_2}, \sum_{kk} co_{kk} \cdot (u)^{g-kk+1}, 0 \right] du, \quad (8)$$

and it's graphic is shown in Figure 2.

```
wFtrunc3is := Ftrunc3(xvis)
```

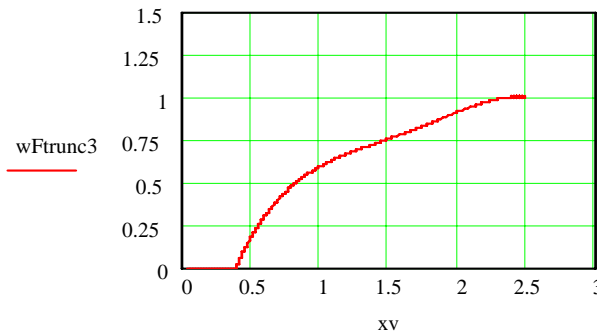


Figure. 2 Repartition function for regression polynomial of 3rd degree

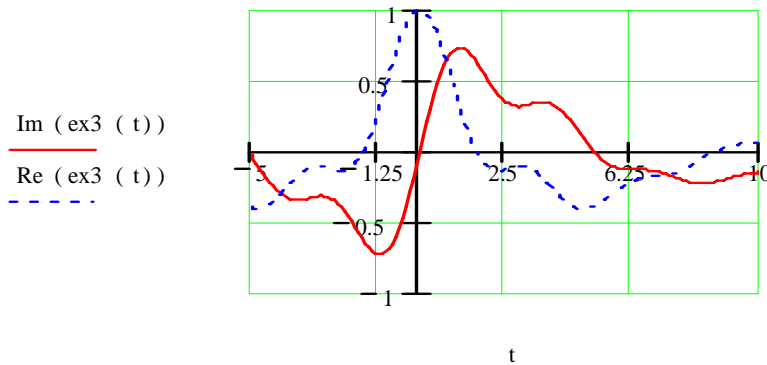


Figure. 3 The real and imaginary part of the characteristic function for the probability density of 3rd degree

The expression of the characteristic function is

$$ex3(t) := \int_{-1}^6 e^{i \cdot t \cdot x} \cdot \left[\text{if} \left[x_{m-} - \text{tvar}_1 < x < x_M + \text{tvar}_2, \sum_{kk} co_{kk} \cdot (x)^{g-kk+1}, 0 \right] \right] dx \quad (9)$$

and it's graphic is shown in figure 3.

If we made a regression of 4th degree (g=4), we will use the program

$$g := 4 \quad j := 1..2 \cdot g + 1 \quad S_j := \sum_i (x_i)^{2 \cdot g - j + 1}$$

$$k := 1..g + 1 \quad v := 1..g + 1 \quad m_{k,v} := S_{v+k-1} \quad TL_k := \sum_i y_i \cdot (x_i)^{g-k+1}$$

$$co := m^{-1} \cdot TL \quad co^T = (42.345 \quad -332.126 \quad 972.561 \quad -1.26 \times 10^3 \quad 609.971)$$

from which results the regression polynomial of the following form

$$y = 42.345 \cdot x^4 - 332.126 \cdot x^3 + 972.261 \cdot x^2 - 1.26 \cdot 10^3 \cdot x + 609.971 \quad (10)$$

which in the nodes has the values

Su ^T =	1	2	3	4	5	6	7	8	9	10	11	12	13	14	15
	0.333	0.282	0.293	0.328	0.348	0.35	0.354	0.343	0.269	0.251	0.235	0.232	0.229	0.229	0.254

For polynomial regression of 4th degree we will obtain the following values for the correlation coefficient and respectively for the deviation from the regression curve

$$r4 := \sqrt{1 - \frac{\sum_i (y_i - Su_i)^2}{\sum_i (y_i - y_m)^2}} \quad r4 = 0.736 \quad (11)$$

$$St4 := \sqrt{\frac{1}{n} \cdot \left[\sum_i (y_i - Su_i)^2 \right]} \quad St4 = 0.044 \quad (12)$$

Because

$$\int_{x_m}^{x_M} \sum_{kk} co_{kk} \cdot (x)^{g-kk+1} dx = 0.171 \quad (13)$$

it will determine the limits of the definition domain for regression density of 4th degree. The program used is likewise with the one from previous case, and it will obtain

$$\text{tvar} = \begin{pmatrix} 0.15 \\ 0.374 \end{pmatrix} \quad \text{tvar}_1 = 0.15 \quad \text{tvar}_2 = 0.374$$

resulting

$$\int_{x_m - \text{tvar}_1}^{x_M + \text{tvar}_2} \sum_{kk} co_{kk} \cdot (x)^{g-kk+1} dx = 1 \quad (14)$$

where

$$x_m - \text{tvar}_1 = 1.513 \quad x_M + \text{tvar}_2 = 2.612$$

In conclusion, the expression of probability density of 4th degree is

$$f4(x) := \text{if} \left[x_m - \text{tvar}_1 < x < x_M + \text{tvar}_2, \sum_{kk} co_{kk} \cdot (x)^{g-kk+1}, 0 \right] \quad (15)$$

and it's graphic is shown in figure 4

```
nrnod := 1000          is := 1..nrnod
xvis := xm - (tvar)1 - .3 +  $\frac{is - 1}{nrnod - 1} \cdot [xM + tvar_2 + .3 - (xm - tvar_1 - .3)]$ 
```

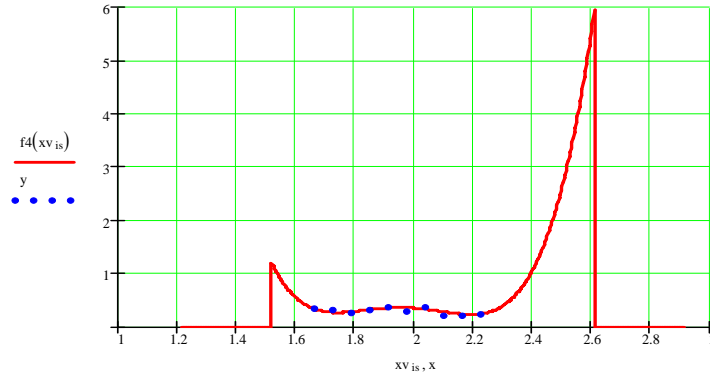


Figure 4. Probability density of 4th degree and the distribution of the experimental points
The expression of the repartition function is

$$Ftrunc4(x) := \int_0^x \left[\text{if} \left[xm - tvar_1 < u < xM + tvar_2, \sum_{kk} co_{kk} \cdot (u)^{g-kk+1}, 0 \right], 0 \right] du, \quad (16)$$

and it's graphic is shown in figure 5

wFtrunc4_{is} := Ftrunc4(xv_{is})

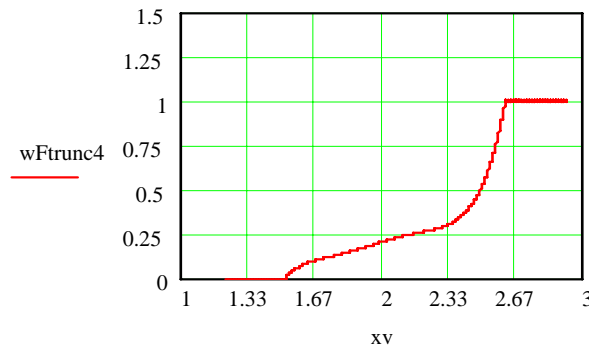


Figure 5. The repartition function for repression polynomial of 4th degree
The characteristic function has the expression

$$ex(t) := \int_{-1}^6 e^{i \cdot t \cdot x} \cdot \left[\text{if} \left[xm - tvar_1 < x < xM + tvar_2, \sum_{kk} co_{kk} \cdot (x)^{g-kk+1}, 0 \right] \right] dx \quad (17)$$

and it's graphic is shown in figure 6

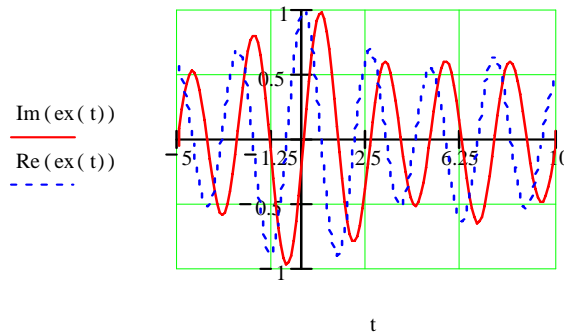


Figure 6. The real and imaginary part of the characteristic function
for probability density of 4th degree

In case that we do a regression of 5th degree (g=5), it results de regression polynomial of the following form

$$y = -119.156 \cdot x^5 + 1212 \cdot x^4 - 4911 \cdot x^3 + 9912 \cdot x^2 - 9962 \cdot x + 3988 \quad (18)$$

which in the nodes has the values

Su ^T	1	2	3	4	5	6	7	8	9	10	11	12	13	14	15
	0.335	0.27	0.289	0.337	0.358	0.359	0.35	0.331	0.259	0.247	0.239	0.238	0.237	0.237	0.244

For polynomial regression of 5th degree we will obtain the following values for the correlation coefficient and respectively for the deviation from the regression curve

$$r5 := \sqrt{1 - \frac{\sum_i (y_i - Su_i)^2}{\sum_i (y_i - ym)^2}} \quad r5 = 0.7462 \quad (19)$$

$$St5 := \sqrt{\frac{1}{n} \cdot \left[\sum_i (y_i - Su_i)^2 \right]} \quad St5 = 0.043 \quad (20)$$

Because

$$Int := \int_{xm}^{xM} \sum_{kk} co_{kk} \cdot (x)^{g-kk+1} dx \quad Int = 0.167 \quad (21)$$

we will determine the limits of the definition domain for the regression density of 5th degree. The program used is likewise with the previous one, and we will obtain

$$tvar = \begin{pmatrix} 0.277 \\ 0.126 \end{pmatrix} \quad tvar_1 = 0.277 \quad tvar_2 = 0.126$$

resulting

$$\int_{xm-tvar_1}^{xM+tvar_2} \sum_{kk} co_{kk} \cdot (x)^{g-kk+1} dx = 1 \quad (22)$$

where $xm - tvar_1 = 1.386$, $xM + tvar_2 = 2.364$.

The expression of probability density of 5th degree is

$$f5(x) := \text{if} \left[xm - tvar_1 < x < xM + tvar_2, \sum_{kk} co_{kk} \cdot (x)^{g-kk+1}, 0 \right] \quad (23)$$

and the graphic is shown in figure 7

$$\begin{aligned} nrm := 1000 \quad is := 1..nrm \\ xv_{is} := xm - (tvar)_1 - .7 + \frac{is - 1}{nrm - 1} \cdot [xM + tvar_2 + .7 - (xm - tvar_1 - .7)] \end{aligned}$$

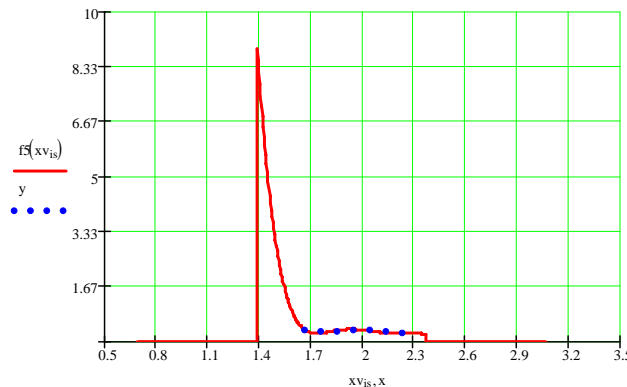


Figure 7. Probability density of 5th degree and repartition of the experimental points

The expression of the repartition function is

$$F_{trunc5}(x) := \int_0^x \left[\text{if} \left[x_m - t_{var1} < u < x_M + t_{var2}, \sum_{kk} c_{o_{kk}} \cdot (u)^{g-kk+1}, 0 \right] du \right] \quad (24)$$

and it's graphic is shown in figure 8

$$wF_{trunc5_{is}} := F_{trunc5}(xv_{is})$$

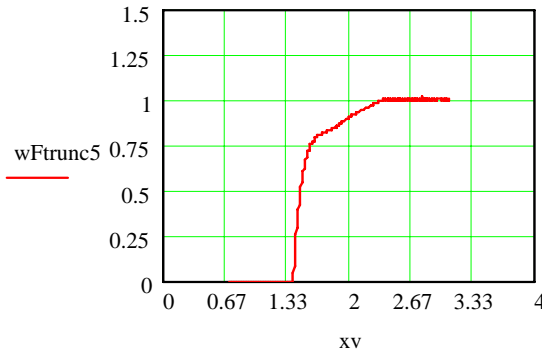


Figure 8. Repartition function for the regression polynomial of 5th degree
The characteristic function has the expression

$$ex(t) := \int_{-1}^6 e^{i \cdot t \cdot x} \cdot \left[\text{if} \left[x_m - t_{var1} < x < x_M + t_{var2}, \sum_{kk} c_{o_{kk}} \cdot (x)^{g-kk+1}, 0 \right] \right] dx \quad (25)$$

and it's graphics is shown in figure 9

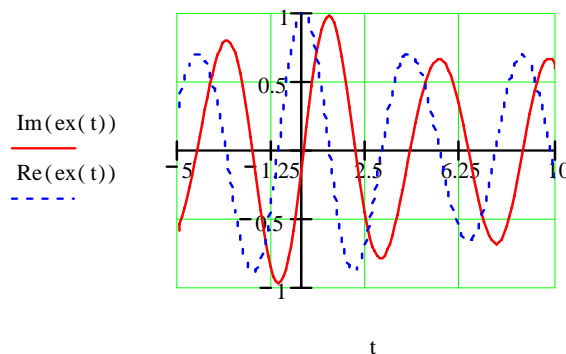


Figure 9. The real and imaginary part of the characteristic function
for probability density of 5th degree

2. OBSERVATIONS

For the regression polynomial of 2nd degree we will obtain the regression parable of the following form

$$y = -0.778 \cdot x^2 + 2.874 \cdot x - 2.323. \quad (26)$$

In this case we will obtain the following values for the correlation coefficient and respectively for the deviation from the regression curve

$$r2 := \sqrt{1 - \frac{\sum_i (y_i - S_{u_i})^2}{\sum_i (y_i - y_m)^2}} \quad r2 = 0.6131 \quad (27)$$

$$St2 := \sqrt{\frac{1}{n} \cdot \left[\sum_i (y_i - Su_i)^2 \right]} \quad St2 = 0.051 \quad (28)$$

Analyzing the form of the parable, shown in figure 10, it's obvious that, on the domain in which the function is positive, the condition cannot be satisfied that integral from it to be equal with the unit.

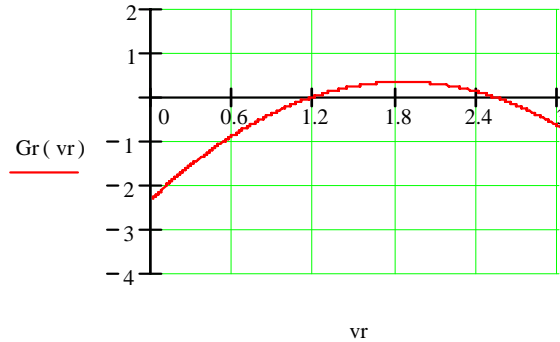


Figure 10. Regression parable

Results that this set of dates, which is obvious a modeling of 2nd degree, it does not accept an appropriate probability density. From the same reason does not accept also probability density of 6th degree.

3. CONCLUSIONS

The advantage of polynomial modeling is the fact that from passing from an inferior grade to a superior grade appears every time new coefficients, and by determines this coefficient the regression curve moulds better and better the experimental figures. By increasing the polynomial grade it will be more accurate the modeling, so it's increasing the value of correlation coefficient.

We specify also the fact that the condition that the integral from probability density must be equals with the unit admission, in possible cases, for a fast grade, much more solutions regarding of the pair of the integrating limits (from which one can be predefine). All the obtained densities mould the experimental domain dates identically. Although, in any form of the function of chosen density, the probability that the random variable to take a value into a range, is the same. In generally we are not interested in modeling on relative big ranges, so the modeling is useful, for example, on a range centered in mean value of a independent variable and the length until the 3rd time deviation from the square mean.

REFERENCES

- [1] Jalobeanu, C., Rasa, I., *MathCAD. Probleme de calcul numeric si statistic*, Editura Albastra, Cluj-Napoca, 1995;
- [2] Maksay, St., Stoica, D., *Calculul probabilitatilor*, Editura Politehnica, Timisoara, 2005.
- [3] Maksay, St., Stoica, D., *Considerations on Modeling Some Distribution Laws*, Applied Mathematics and Computation, 175, 2006, pag. 238-246.



NUMERICAL METHOD FOR SPATIAL STABILITY ANALYSIS OF A VORTEX STRUCTURE AT HIGH REYNOLDS NUMBERS

Diana A. BISTRIAN, Ștefan MAKSAY,

”Politehnica” University of Timisoara, Faculty of Engineering Hunedoara, ROMANIA

Abstract

The investigations concerned the values of parameters for which the vortex become unstable may imply a large amount of measurement, thus one must resort to numerical techniques.

We developed in this paper a spatial stability analysis of a Q type vortex subject to infinitesimal perturbations.

First, the eigenvalue problem governing the linear stability analysis of the non axi-symmetric Q vortex (one of the few known exact solutions to the full Navier-Stokes equations) against normal mode perturbations is investigated for the case of high Reynolds numbers using a spectral collocation technique.

The accuracy of the method is assessed underlying the necessity for the construction of a certain class of interpolant functions satisfying the boundary conditions.

Graphical representations of the spatial eigenfunctions amplitudes are given offering a visualization of the differences between perturbed velocity fields developed for the first unstable axial wavenumber and the least stable one.



BOUNDARY ADAPTED SPECTRAL APPROXIMATION FOR SPATIAL STABILITY OF BATCHELOR VORTEX

¹Diana A. BISTRIAN, ²Ioana F. DRAGOMIRESCU

¹Department of Electrical Engineering and Industrial Informatics,
Engineering Faculty of Hunedoara, "Politehnica" University of Timisoara, ROMANIA

²Department of Mathematics, "Politehnica" University of Timisoara, ROMANIA

Abstract:

The main goal of this paper is to develop a methodology for analyzing the non-axisymmetrical swirling flows with helical vortex breakdown by means of linear stability analysis. For the case of high Reynolds numbers the eigenvalue problem governing the linear stability analysis of the Batchelor vortex is investigated using a boundary adapted spectral collocation technique. A symmetrization is performed eliminating all geometric singularities on the left-hand sides of the governing equations set. The method provides a fairly accurate approximation of the spectrum without any scale resolution restriction.

Keywords:

swirling flow, Batchelor vortex, spectral collocation

1 Introduction

Most of the vortex stability analyses concerned axisymmetrical vortices with axial flow [1] in order to explain the vortex breakdown phenomenon observed experimentally for the first time on delta wings [2], in pipes [3] and in cylinders with rotating ends [4]. Obviously, the axial symmetry hypothesis is a major simplification having the main benefit of dramatically reducing the computational cost [5]. On the other hand, it introduces important limitations as far as the three-dimensionality and unsteadiness of the flow are concerned.

The present paper focused on developing an analytical and numerical technique for analyzing the eigenvalue problem governing the linear stability of an inviscid swirling fluid flow under small perturbations. This problem is characterized by a system of ordinary differential equations with variable coefficients.

In most cases, the spatially or temporal stability (classified for open flows as in [6]) under infinitesimal perturbations is reduced to the study of an algebraic eigenvalue problem of this type. The study leads to a dispersion relation connecting in fact the growth rate ω and the axial wavenumber k as a consequence of the condition that nontrivial eigenvalues to exist. Most of the investigations [1], [7] concerned the values of these nondimensional parameters for which the vortex become unstable in the case of either a spatial stability or temporal stability investigation. Since the investigation of this aspect may imply a large amount of measurement, one must resort also to numerical techniques. Although a spatial stability analysis implies the investigation of a nonlinear eigenvalue problem this type of analysis directly provides the frequency ranges of the most unstable modes. In this paper we consider a more general mathematical model for swirling flow stability analysis, starting with the unsteady Euler equations in cylindrical coordinates. In doing so, we can examine both unsteady and circumferentially variable perturbations.

The paper is organized as follows. The eigenvalue problem governing the linear stability analysis for inviscid swirling flows against normal mode perturbations is defined in Section 2. The third section a new radial spectral approximation is proposed and in Section 4 the

method is applied for the Batchelor vortex case and the actual numerical procedure is presented. The main advantages of the proposed methods are pointed out in Section 5.

2. PROBLEM FORMULATION

The governing equations in the case of incompressible and inviscid flow are the Euler equations

$$\nabla \cdot \underline{V} = 0, \frac{\partial \underline{V}}{\partial t} + (\underline{V} \cdot \nabla) \underline{V} = -\frac{1}{\rho} \nabla p \quad (1)$$

The following flow fields decomposition are used: velocity $\underline{V} + \underline{v}$, pressure $p + \pi$ where (\underline{V}, p) is the base flow, and (\underline{v}, π) is the perturbation considered small.

Since the base flow obey the Euler equations (1) the evolution of such small perturbations of the basic flow is governed by the linearized Euler equations

$$\nabla \cdot \underline{v} = 0, \frac{\partial \underline{v}}{\partial t} + (\underline{V} \cdot \nabla) \underline{v} + (\underline{v} \cdot \nabla) \underline{V} = -\frac{1}{\rho} \nabla \pi \quad (2)$$

In the linearization process the second order terms in the small perturbations were neglected. Assuming a steady columnar flow the velocity profile is written

$$\underline{V}(r) = [U(r), 0, W(r)] \quad (3)$$

where U represents the axial velocity component W the azimuthal component of the velocity both depending only on radius. Next, we consider the following factorization of the small perturbations

$$[\underline{v}(t, z, r, \theta), \pi(t, z, r, \theta)] = [F(r), iG(r), H(r), P(r)] \exp[i(kz + m\theta - \omega t)] \quad (4)$$

Introducing the factorization form (4) into the linearized Euler equations (2) we obtain the following system of first order differential equations

$$krF + G + rG' + mH = 0 \quad (5a)$$

$$kUG - \omega G + \frac{mWG}{r} + \frac{2WH}{r} - P' = 0 \quad (5b)$$

$$rHkU - rH\omega + m(HW + P) + WG + rGW' = 0 \quad (5c)$$

$$FkU - F\omega + \frac{FmW}{r} + U'G + kP = 0 \quad (5d)$$

where prime denotes differentiation with respect to the radius. This homogenous first order differential system is completed with the following boundary conditions at axis and the far field

$$\begin{cases} G(0) = H(0) = 0, F(0), P(0) \text{ finite}, (m = 0), \\ H(0) \pm G(0) = 0, F(0) = P(0) = 0, (m = \pm 1), \\ F(0) = G(0) = H(0) = P(0) = 0, (|m| > 1), \\ F, G, H, P \rightarrow 0, (r \rightarrow \infty) \end{cases} \quad (6)$$

Equations (5) and (6) represent an eigenvalue problem.

3. BOUNDARY ADAPTED RADIAL SPECTRAL APPROXIMATION

The pseudospectral - collocation method is one of the most used technique for the numerical investigations in hydrodynamic stability problems. Many researchers have demonstrated the applicability of this method with high degree of accuracy to eigenvalue problems governing the linear stability of swirling flows [9-11].

The difference between the classical method and the modified version proposed here is given by the selected spaces involved in the discretization process motivated by the need to adapt the grid points to the singularities of the underlying solution.

In fact the boundary conditions (6) at infinity are applied at a truncated radius distance r_{\max} selected large enough such that the numerical results do not depend on this truncated distance.

Following [9] we define the boundary-adapted functions $\{\phi_k\}$, $k = 1, \dots, N$ of *modal* type, i. e. each function provides one particular pattern of oscillation

$$\phi_k(r) = \left(1 - \frac{r}{r_{max}}\right) \cdot r \cdot T_k^*(r), \quad \{\phi_k\}, k = 1, \dots, N \quad (7)$$

with T_k^* the shifted Chebyshev polynomials on $[0, r_{max}]$. These type of polynomials defined on the physical space are used in order to optimize the interpolative procedure. The choice is based on the condition that the values of the grid points are given by the same elementary analytic expression for all values of N and they did not have to be computed numerically for every N .

The linear transformation that maps the standard interval $\xi \in [-1, 1]$ into the physical range of our problem $r \in [0, r_{max}]$ and preserves the clustering rate of collocation nodes is defined by the linear transformation

$$r(\xi) = \frac{r_{max}}{2} \xi + \frac{r_{max}}{2} \quad (8)$$

while the inverse transformation is defined

$$\xi(r) = 2 \frac{r}{r_{max}} - 1 \quad (9)$$

The proposed method allowed us to discard the first and last collocation nodes, expansion functions satisfying the boundary conditions from the construction of our modal boundary-adapted basis. In this way the critical singularities which occurred in evaluating terms like $1/r$ for the numerical treatment of the eigenvalue problem were eliminated. Then the solution is approximated with respect to this expansion set of functions,

$$(F, G, H, P) = \sum_{k=1}^N (u_k, v_k, w_k, p_k) \phi_k(r) \quad (10)$$

A modified Chebyshev Gauss grid $\Xi = (\xi_j)_{0 \leq j \leq N-1}$ in $[-1, 1]$ was constructed

$$\xi_j = \cos\left(\pi + \frac{2j\pi}{2N-2}\right), \quad \xi_j \in [-1, 1], \quad j = 0..N-1 \quad (11)$$

In our case the collocation nodes clustered near the boundaries diminishing the negative effects of the Runge phenomenon. Another aspect is that the convergence of the interpolant on the clustered grid towards unknown function is extremely fast.

Each of the basis functions from (7) meet the relations

$$\begin{aligned} \phi_k(r_1 = 0) &= \phi_k(r_N = r_{max}) = 0, \\ \phi_k(r_j) &\neq 0, \quad j = 1..N, \quad k = 2..N-1 \end{aligned} \quad (12)$$

which implies that each functions F, G, H, P satisfy the boundary conditions (6).

With (10) the mathematical model takes the form

$$kr \sum_{k=1}^N u_k \Phi_k(r) + \sum_{k=1}^N v_k \Phi_k(r) + rG' + m \sum_{k=1}^N w_k \Phi_k(r) = 0 \quad (13a)$$

$$\left(ku_z - \omega + \frac{mu_\theta}{r}\right) \sum_{k=1}^N v_k \Phi_k(r) + \frac{2u_\theta}{r} \sum_{k=1}^N w_k \Phi_k(r) - P' = 0 \quad (13b)$$

$$(rku_z - r\omega) \sum_{k=1}^N w_k \Phi_k(r) + m \left(u_\theta \sum_{k=1}^N w_k \Phi_k(r) + \sum_{k=1}^N p_k \Phi_k(r)\right) + (u_\theta + ru_\theta') \sum_{k=1}^N v_k \Phi_k(r) = 0 \quad (13c)$$

$$\left(ku_z - \omega + \frac{mu_\theta}{r}\right) \sum_{k=1}^N u_k \Phi_k(r) + u_z' \sum_{k=1}^N v_k \Phi_k(r) + k \sum_{k=1}^N p_k \Phi_k(r) = 0 \quad (13d)$$

Let us denote by $[r] = \text{diag}(r_i)$, r_i given by (8), $i = 0, \dots, N-1$, $[\phi] = (\phi_{ij})_{\substack{1 \leq i \leq N, \\ 1 \leq j \leq N}}$, $\phi_{ij} = \phi_j(r_i)$, $[U] = \text{diag}(U(r_i))$, $[W] = \text{diag}(W(r_i))$, $1 \leq i \leq N$. The system (13) can be written $(kM_k + \omega M_\omega + m M_m + M_0)\bar{s} = 0$ with $\bar{s} = (\bar{f} \ \bar{g} \ \bar{h} \ \bar{p})^T$ and the matrices M_k , M_ω , M_m and M_0 having the following explicit forms

$$M_k = \begin{pmatrix} [r][\phi] & 0 & 0 & 0 \\ 0 & [U][\phi] & 0 & 0 \\ 0 & 0 & [rU][\phi] & 0 \\ [U][\phi] & 0 & 0 & [\phi] \end{pmatrix} \quad (14); \quad M_\omega = \begin{pmatrix} 0 & 0 & 0 & 0 \\ 0 & -[\phi] & 0 & 0 \\ 0 & 0 & -[r][\phi] & 0 \\ -[\phi] & 0 & 0 & 0 \end{pmatrix} \quad (15)$$

$$M_m = \begin{pmatrix} 0 & 0 & [\phi] & 0 \\ 0 & \left[\frac{W}{r}\right][\phi] & 0 & 0 \\ 0 & 0 & [W][\phi] & [\phi] \\ \left[\frac{W}{r}\right][\phi] & 0 & 0 & 0 \end{pmatrix} \quad (16); \quad M_0 = \begin{pmatrix} 0 & [\phi] + [r]D & 0 & 0 \\ 0 & 0 & 2\left[\frac{W}{r}\right][\phi] & -D \\ 0 & [W][\phi] + [rW'][\phi] & 0 & 0 \\ 0 & [U'][\phi] & 0 & 0 \end{pmatrix} \quad (17)$$

By differentiating (10) results

$$F'(r) = \sum_{k=1}^N \left\{ \left(1 - \frac{2r}{r_{\max}}\right) u_k T_k^*(r) + \left(1 - \frac{r}{r_{\max}}\right) r u_k T_k^{*'}(r) \right\} \quad (18)$$

For $k = 1$ we have $T_1^{*'}(r) = 0$ and rewriting (18) we have

$$F'(r) = \left(1 - \frac{2r}{r_{\max}}\right) u_1 T_1^*(r) + \sum_{k=2}^N \left\{ \left(1 - \frac{2r}{r_{\max}}\right) u_k T_k^*(r) + \left(1 - \frac{r}{r_{\max}}\right) r u_k T_k^{*'}(r) \right\} \quad (19)$$

The shifted Chebyshev polynomials meet the recurrence relation

$$T_n^{*'}(r) = \frac{r_{\max}}{4} \frac{(n-1)}{r(r_{\max} - r)} [T_{n-1}^*(r) - T_{n+1}^*(r)], \quad n \geq 2 \quad (20)$$

thus

$$F'(r) = \left(1 - \frac{2r}{r_{\max}}\right) u_1 T_1^*(r) + \sum_{k=2}^N u_k \left\{ \left(1 - \frac{2r}{r_{\max}}\right) T_k^*(r) + \left(1 - \frac{r}{r_{\max}}\right) r \frac{r_{\max}}{4} \frac{(k-1)}{r(r_{\max} - r)} [T_{k-1}^*(r) - T_{k+1}^*(r)] \right\} \quad (21)$$

The interpolant derivative matrix D from (17) was evaluated by

$$D = \begin{pmatrix} \left(1 - \frac{2r_1}{r_{\max}}\right) T_1^*(r_1) & E_2(r_1) & E_3(r_1) & \dots & E_N(r_1) \\ \left(1 - \frac{2r_2}{r_{\max}}\right) T_1^*(r_2) & E_2(r_2) & E_3(r_2) & \dots & E_N(r_2) \\ \dots & \dots & \dots & \dots & \dots \\ \left(1 - \frac{2r_N}{r_{\max}}\right) T_1^*(r_N) & E_2(r_N) & E_3(r_N) & \dots & E_N(r_N) \end{pmatrix} \quad (22)$$

where

$$E_k(r) = \left(1 - \frac{2r}{r_{\max}}\right) T_k^*(r) + \frac{k-1}{4} [T_{k-1}^*(r) - T_{k+1}^*(r)], \quad k \geq 2 \quad (23)$$

This algorithm allows us to obtain the eigenvalue, the eigenvector, the index of the most unstable mode, the maximum amplitude of the most unstable mode and the critical distance where the perturbation is the most amplified.

The main advantages of the proposed method consist in reducing the computational time by reducing the matrices order to $(4N - 8)^2$ and for a certain spectral parameter N we obtain an exponential decreasing error.

4 NUMERICAL RESULTS FOR BATCHELOR VORTEX

The above presented method was tested on a particular benchmark model: the Batchelor or q-vortex [7].

The flow field is characterized by the velocity field $\underline{V}(r)=[U(r),0,W(r)]$ [4],

$$U(r) = a + e^{-r^2}, \quad W(r) = \frac{q}{r}(1 - e^{-r^2}) \quad (24)$$

where q represents the swirl number defined as the angular momentum flux divided by the axial momentum flux times the equivalent nozzle radius and a provides a measure of free-stream axial velocity.

In [7] the numerical investigation of the two-point boundary value problem was based on a shooting method. The properties of the Batchelor vortex are pointed out by considering them as functions of the swirl ratio q and the external flow parameter a .

The computed spectrum of the eigenvalue problem is depicted in Figure 1. Graphical representations of the spatial eigenfunction amplitudes of the most unstable mode are given in the Figure 2. For a stabilization of the Gibbs phenomenon a Lanczos type σ factor [10] was used,

$$\sigma_k = \frac{\sin \frac{2\pi k}{N}}{2\pi k} \cdot \frac{1}{N}, \quad 1 \leq k \leq N \quad (25)$$

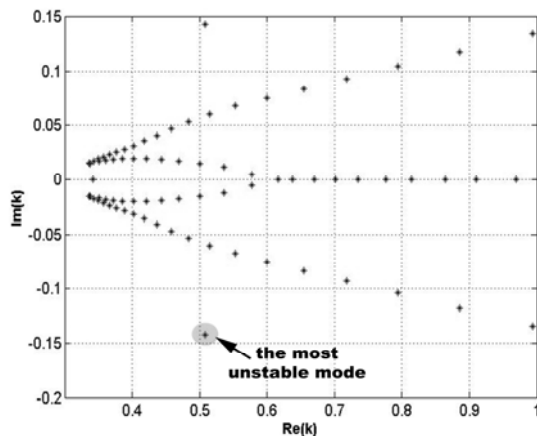


Figure 1. Spectra of the hydrodynamic eigenvalue problem computed at $\omega = 0.01$, $m = -3$, $a = 0$, $q = 0.1$, $N = 150$.

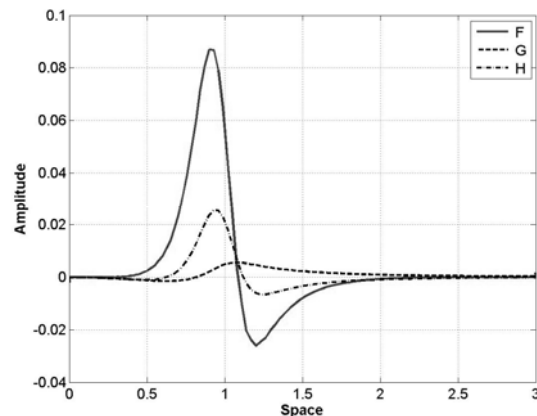


Figure 2. Values of eigenfunction amplitudes of the most unstable mode $\omega = 0.01$, $m = -3$, $a = 0$, $q = 0.1$, $N = 150$, $k = 0.50842 - 0.14243i$.

Table 1. Convergence behaviour of the critical distance for the most unstable mode with $\omega = 0.01$, $a = 0$, $q = 0.1$ and $m = -3$.

N	Axial wavenumber k	Critical distance r_c
100	0.64887-3.7433i	0.00302
150	0.50842-0.14243i	0.90051
180	0.50847-0.14232i	0.92294
250	0.50854-0.14216i	0.95451
300	0.50857-0.14209i	0.93874

5. CONCLUSION

In this paper we developed a spectral numerical procedure to investigate the spatial stability of a swirling flow subject to infinitesimal perturbations. Using a spectral collocation technique our numerical procedures directly provided relevant information on perturbation

amplitude for stable or unstable induced modes, the maximum amplitude of the most unstable mode and the critical distance where the perturbation is the most amplified.

The accuracy of the methods is assessed underlying the necessity for the construction of a certain class of orthogonal expansions functions satisfying the boundary conditions. The key issue was the choice of the grid and the choice of the modal trial basis, the scheme based on shifted Chebyshev polynomials provided good results.

REFERENCES

- [1] Khorrami M. R., Malik M.R., Ash R.L., 1989, “Application of spectral collocation techniques to the stability of swirling flows”, *J. Comput. Phys.*, Vol. 81, pp. 206–229.
- [2] Peckham, D.H., Atkinson, S.A., “Preliminary results of low speed wind tunnel tests on a gothic wing of aspect ratio 1.0”, *Aero. British Res. Council*, 1957, CP 508, pp. 16-17.
- [3] Sarpkaya, T., 1971, “On stationary and travelling vortex breakdown”, *J. of Fluid Mech.*, Vol.45, pp.545-559.
- [4] Escudier, M., 1984, “Observations of the flow produced in a cylindrical container by a rotating endwall”, *Experiments in Fluids*, Vol.2, pp.189-196.
- [5] Susan-Resiga R., Muntean S., Stein P., Avellan F., 2008, “Axisymmetric Swirling Flow Simulation of the Draft Tube Vortex in Francis Turbines at Partial Discharge”, *Proc. of the 24th IAHR Symp. on Hydraulic Machinery and Systems, October 27-31, Foz do Iguassu, Brasil*, Paper No 13.
- [6] Huerre P., Monkewitz, P.A., 1990, “Local and global instabilities in spatially developing flows”, *Annu. Rev. Fluid Mech.*, Vol. 22, pp. 473-537.
- [7] Olendraru C., Sellier A., Rossi M., Huerre P., 1999, “Inviscid instability of the Batchelor vortex: Absolute-convective transition and spatial branches”, *Physics of Fluids*, Vol. (11) 7, pp. 1805-1820.
- [8] Susan-Resiga R., Ciocan G.D., Anton I., Avellan F., 2006, “Analysis of the Swirling Flow Downstream a Francis Turbine Runner”, *Journal of Fluids Engineering*, Vol. 128 (1), pp. 177-189.
- [9] Batchelor, G.K, Gill, A.E., 1962, “Analysis of the stability of axisymmetric jets”, *J. Fluid Mech.*, Vol. 14, 529 -551.
- [10] Canuto, C., Hussaini, M.Y., Quarteroni, A., Zang, T.A., 2007, “Spectral methods - Evolution to complex geometries and applications to fluid dynamics”, Springer, New York.
- [11] Trefethen, L.N., 2000, “Spectral methods in Matlab”, SIAM, Philadelphia.
- [12] Mason, J.C., Handscomb, D.C., 2002, “Chebyshev polynomials”, Chapman & Hall, New York, NY, CRC, Boca Raton.
- [13] Lessen M., Paillet F., (1974) “The stability of a trailing line vortex. Part 2. Viscous theory”, *J. Fluid Mech.*, 65, pp. 769-779.
- [14] Loiseleux T., Chomaz J.M., Huerre P., (1998) "The effect of swirl on jets and wakes : Linear instability of the Rankine with axial flow", *Physics of Fluids*, (10)5, pp. 1120-1126.
- [15] Olendraru C., Sellier A., 2002, “Absolute-convective instabilities of the Batchelor vortex in the viscous case”, *J. Fluid Mech.*, Vol. 459, pp. 371–396.
- [16] Parras L., Fernandez-Feria R., 2007, “Spatial stability and the onset of absolute instability of Batchelor’s vortex for high swirl numbers”, *J. Fluid Mech.*, Vol. 583, pp. 27– 43.